Etude expérimentale des hétérodéformations dans les moirés des bicouches de graphène

Florie Mesple

THÈSE

Pour obtenir le grade de

DOCTEUR DE L'UNIVERSITÉ GRENOBLE ALPES

École doctorale : PHYS - Physique
Spécialité : Physique de la Matière Condensée et du Rayonnement
Unité de recherche : PHotonique, ELectronique et Ingéniérie QuantiqueS

Etude expérimentale des hétérodéformations dans les moirés des bicouches de graphène

Experimental study of heterostrain in moiré superlattices of graphene bilayers

Présentée par :

Florie MESPLE

Direction de thèse :

Vincent RENARD Université Grenoble Alpes	Directeur de thèse
Claude CHAPELIER Université Grenoble Alpes	Co-directeur de thèse

Rapporteurs :

Joseph A. STROSCIO
NIST/Physical Measurement Laboratory
Mikhail KATNELSON
PROFESSEUR, Radboud University (NL)

Thèse soutenue publiquement le **21 décembre 2022**, devant le jury composé de :

Joseph A. STROSCIO DIRECTEUR DE RECHERCHE, NIST/Physical Measurement Laboratory	Rapporteur
Mikhail KATNELSON PROFESSEUR, Radboud University (NL)	Rapporteur
Rebeca RIBEIRO PALAU CHARGE DE RECHERCHE, CNRS	Examinatrice
Clemens WINKELMANN MAITRE DE CONFERENCE, Université Grenoble Alpes	Examinateur
Laurence MAGAUD DIRECTEUR DE RECHERCHE, CNRS	Présidente
Jérôme LAGOUTE DIRECTEUR DE RECHERCHE, CNRS	Examinateur

Remerciements

First of all I would like to thank all my members, Joseph Stroscio and Mikhail Katsnelson for agreeing to evaluate my PhD manuscript, as well as Rebeca Palau-Ribeiro, Clemens Winkelmann, Laurence Magaud, and Jérôme Lagoute for their interest in my work.

During this PhD, I was lucky to benefit from a lot of fruitful discussions and expertise from colleagues and collaborators.

I would like to thank in particular Guy Trambly de Laissardière, along with Ahmed Missaoui, who followed most of this work through important discussions and numerical works regarding chapters 2, 3 and 4 of this work. Paco Guinea and Tommaso Cea, for interesting discussions and for calculations regarding chapters 3 and 4. Niels Walet, for his important inputs and his efficiency in calculating huge systems from chapter 4.

In addition, I would like to thank Colin Paillet and Adrien Michon for making samples, and Djordje Došenović and Hanako Okuno for doing TEM measurements on our samples.

Je voudrais chaleureusement remercier les personnes à l'origine de ce travail, mes encadrants de thèse Vincent et Claude. Vous m'avez d'emblée investie de votre confiance tout en restant disponibles, vous avez toujours été généreux en conseils avisés, sur le plan scientifique tant que sur le plan humain. Vous m'avez encouragée et soutenue pour participer à des conférences et écoles d'été. Je vous en suis très reconnaissante, et j'espère que nous garderons ce contact enrichissant dans les années futures. J'ai la chance de pouvoir dire que c'est à vos côtés que j'ai attrapé la "névrose" du STM.

Vincent, je voudrais te remercier pour ton optimisme à toute épreuve, ta curiosité contagieuse qui nous fait nous poser les "bonnes" questions. J'ai toujours admiré ta connaissance profonde de la physique qui te permet d'avoir une compréhension quasi intuitive de phénomènes complexes et qui te permet de "d'extraire tout le jus" des données à ta disposition. Tu m'as appris à faire de la recherche, a travers des collaborations notamment, mais tu m'as aussi et surtout appris à parler de la recherche et à l'écrire. Claude, je voudrais te remercier pour ta bienveillance, tes conseils et ta disponibilité. Tu n'as jamais hésité à interrompre ton travail pour prendre le temps de m'apporter une partie de ta grande expertise technique, sur le STM, avec solidworks, ou pour partager une de tes histoires. J'aime aussi l'exigence et l'intégrité que tu accordes à ton travail, en prenant "le temps de la recherche" et en n'hésitant jamais à poser les questions qui fâchent.

Tu sais voir l'excellence chez tes étudiant-es, ce qui nous motive et nous pousse à donner le meilleur.

J'ai travaillé au sein du Laboratoire de Transport Électronique Quantique et Supraconductivité (LaTEQS) du CEA, où j'ai pu interagir avec plaisir avec de nombreuses personnes. J'y ai eu accès à de très bonnes conditions de travail, notamment grâce au travail de Jean-Pascal, Xavier, Manuel, François et son expertise dans les journées de labo, Marielle toujours disponible et efficace face à l'adversité de l'administration du CEA. Michel, qui m'a fourni (presque sans rechigner) les nombreuses pièces de deux cellules de déformation. Fred, et Fred, qui ont résolu leur part de problèmes que j'ai pu rencontrer, de même que Jean-Luc, qui est toujours là quand on a besoin de lui, et ce même alors qu'on ne le sait pas. Iulian fameux cryogéniste, qui a toujours une chose intéressante à raconter et expliquer. Gérard, Karine et Christophe du D5 avec qui j'ai eu la chance d'interagir lors de nombreuses croissances d'échantillons. Bien sûr je voudrais remercier aussi Loïc et Thomas, mes deux thésards modèles qui m'ont beaucoup appris : les croissances, le STM, le git, python, le ski et j'en passe. Je voudrais remercier tous les collègues de bureau et de labo que j'ai croisé de près ou de loin, qui ont pu distraire les journées à midi, autour d'un débat, d'une partie de fléchettes ou d'une bière. Ralbert, Estelle, Axel, Nathan et Chotivut, Cécile, Gonzalo, Estelle, Marion, et les nouveaux et nouvelles arrivant-es à qui je souhaite le meilleur pour la suite.

J'ai aussi eu la chance de pouvoir passer une partie de mon temps au meilleur STM ultra-vide de l'institut Néel. Je voudrais remercier Pierre et Jean-Yves de m'avoir accueillie au sein de leur équipe, d'avoir partagé avec moi leur savoir encyclopédique de l'art du STM, et quelques secrets de l'ultra-vide.

Enfin, parce que ces trois années de thèses sont aussi trois années de vie, je voudrais remercier toutes les personnes avec qui j'ai partagé ce bout de chemin, de près ou de loin. Et avec qui j'espère continuer à cheminer ensemble !

Synopsis grand public

Etude expérimentale des hétérodéformations dans les moirés des bicouches de graphène

Le graphène est le premier cristal purement bidimentionnel a avoir été exfolié à partir du graphite, un matériau très courant qui peut être retrouvé jusque dans les mines des crayons à papier. C'est aussi un matériau très solide et résistant avec des propriétés conductrices exceptionnelles. On a même découvert récemment que des phases exotiques de la matière se forment en superposant deux couches de graphène tournées d'un angle particulier surnommé l'angle *magique*.

Dans cette thèse on utilise la microscopie à effet tunnel pour étudier ce système de deux couches de graphène. Cette technique permet en effet de déterminer l'empilement relatif des couches ainsi que de mesurer les propriétés électroniques de l'ensemble.

On étudie en particulier l'effet des *hétérodéformations*, c'est à dire les déformations relatives des couches, sur les propriétés électroniques des bicouches de graphène tournées. On s'intéresse aussi à un nouveau type de réorganisation microscopique des atomes induite par les hétérodéformations biaxiales, la *relaxation en tourbillon*. On présente aussi le développement expérimental d'un microscope à effet tunnel permettant l'application de déformations à l'échantillon pendant la mesure afin de contrôler les heterodéformations.

Experimental study of heterostrain in moiré superlattices of graphene bilayers

Graphene is the first purely two dimentional crystal that has been exfoliated from a very common material, graphite, that can be found in pencil leads for example. It is also a very strong and stiff material with exceptional conducting properties. Exotic phases of matter were recently discovered by stacking two layers of graphene with a specific angle between them, the so called *magic* angle.

In this thesis, we use Scanning Tunneling Microscopy measurements to study this bilayer graphene system. This technique is indeed a great tool to determine the exact stacking arrangement of two layers of graphene while probing the electronic properties of the system.

We focus in particular on the effects of *heterostrain*, in other words the relative strain between the layers, on the electronic properties of

twisted bilayers of graphene. We also focus on a new type of slight atomic rearrangements induced by a biaxial heterostrain, the *swirl relaxation*. We also present the experimental developement of a straining Scanning Tunneling Microscope in order to control heterostrain during measurements.

Résumé

Superposer deux couches de graphène l'une sur l'autre avec une rotation donne lieu à la formation d'un moiré. Ce moiré conserve la dispersion linéaire des porteurs de charge mais leur vitesse de Fermi est renormalisée. Celle-ci s'annule même pour un angle dit *magique*, donnant lieu à un nouveau type de localisation des électrons, induite par le moiré. Cette dernière donne lieu à la formation de phases fortement corrélées telles que la phase supraconductrice découverte récemment et qui a soulevé un grand intérêt dans la communauté de la matière condensée.

Dans cette thèse, on s'intéresse à l'effet de l'empilement relatif entre les couches sur les propriétés électroniques du système. En utilisant des données de microscopie et spectroscopie à effet tunnel, on montre que les déformations relatives entre les couches, nommées *hétérodéformations*, contrôlent la physique des bicouches de graphène tournées d'un angle proche de l'angle magique. L'arrangement exact entre les couches, comprenant les hétérodéformations, est suffisant pour expliquer la variabilité des proprétés électroniques observées expérimentalement d'un échantillon à l'autre.

A plus petit angles encore, il est nécessaire de prendre en compte les déformations locales liées à la *relaxation* du système à l'échelle atomique. On s'intéresse à un nouveau type moiré dans les bicouches de graphène relaxées, induit par les hétérodéformations biaxiales et dans lequel se développe un mode de relaxation particulier que l'on nomme *tourbillon*.

Enfin, dans le but d'utiliser les déformations comme une sonde, on présente la fabrication et les tests d'une cellule de déformation compatible avec un STM qui opère à température ambiante ou cryogénique. Un tel appareil peut être utilisé sur toute une variété de matériaux, dont les bicouches de graphène tournées.

Abstract

Stacking two layers of graphene on top of each other with a twist gives rise to a moiré pattern. This moiré does not affect the linear dispersion of the charge carrier, but renormalises their Fermi velocity. The latter even cancels for an so called *magic* angle, triggering a new type of electron localisation which is induced by the moiré. This localisation gives rise to strongly correlated phases, such as the recently discovered superconducting phase that created intense interest in the condensed matter community.

In this thesis, we investigate the effect of the relative stacking between the layers on the electronic properties of the system.

By using Scanning Tunneling Microscopy and Spectroscopy data from the literature we show that the relative strain between the layers, so called *heterostrain*, controls the physics of twisted bilayers of graphene near the superconducting twist angle regime. The exact stacking arrangement including heterostrain is enough to explain the sample to sample variability that has been observed in recent experiments.

At lower angles, in addition to the exact stacking arrangement, local deformations related to *relaxation* processes of the system on the atomic scale must be taken into account as well. We investigate a new type of moiré induced by biaxial heterodeformations, in which occurs a peculiar relaxation mode that we call a *swirl* relaxation pattern.

Last, aiming at using strain as a tool, we show the building and testing of a strain cell compatible with an Scanning Tunnaling Microscope that operates at room and cryogenic temperatures. Such a device can be used on a variety of materials in addition to twisted graphene layers.

Contents

Introduction

Atoms forming crystals are organized following a long range order in all three directions of space. They have fascinated mankind for centuries, and more recently condensed matter physicists as they progressed in the understanding of their cristallography down to the smallest scale, as well as the understanding of their electronic properties. The surface of crystals are another constant source of interest, as they have characteristics than can be quite different from the bulk of the crystal. The study of surfaces deepened and extended with the invention of Scanning Tunneling Microscopy, because it enables to probe the structural arrangement of a surface while giving information on its electronic properties.

The reduced dimentionality of a surface can be pushed to its limit when considering an atomically thick material. This challenge was first answered with the first isolation of graphene in 2004 [1], a purely 2-D material that can be exfoliated from graphite. It was followed by the exfoliation of many layered crystals such as $NbSe_2$, $MoSe_2$ along with many others, among the hundreds of other stable single-layer materials that are predicted. These 2-D materials can be isolated by the exfoliation of bulk layered materials or by bottom-up synthesis with methods similar to Chemical Vapor Deposition. In the case of graphene, both methods are demonstrated to work efficiently.

These materials are surprisingly stable as they do not break upon mechanical or thermal fluctuations, although some of them need to be encapsulated. Instead, graphene for example is extremely strong and stiff, with a Young modulus above 1TPa [2], which permits measuring it even when it is completely suspended.

As the thickness of a crystal gets lower than the electron wavelength, the degree of freedom of electrons is reduced and their quantum character can be expressed in different ways. Single-layer materials can thus host electronic properties that originate from bulk crystals (conducting, isolating, semiconducting, superconducting, ...), but exotic electronic effects originating from their 2D character can also emerge. A striking example is the demonstration of quantum hall effect at room temperature in graphene only three years after its first isolation [3]. Another example is the indirect to direct bandgap transition in MoS_2 upon reduction of the number of layers [4], which is also observed in other Transition Metal Dichalchogenides (TMDs).

In addition, 2-D materials offer the possibility to form new crystals by stacking them on top of each other, both layers being held

by weak van der Waals forces. This stacking can be done in various ways and can involve any 2-D material, offering a new way to design a whole variety of thin materials, new crystals with unique electronic properties. By twisting two layers of graphene on top of each other for example, STM measurements reveal that the *moiré* that forms between the two periodicities can confine electrons in specific regions of the sample [5]. Furthermore, superconductivity can emerge in the system and can be tuned by changing the twist angle or the strength of the interlayer interaction [6, 7]. The relative strain, or *heterostrain* between the layers has also been found to affect the electronic properties of the system [8]. All in all, not only the type of material that are stacked together but also the precise stacking arrangement of the layers matter in determining the electronic properties of a 2-D van der Waals material, which makes this family of materials very versatile.

The topic at stake in this thesis is to investigate experimentally in detail the effects of relative stacking between two layers of graphene. This investigation is done at the local scale, mainly by using STM measurements. We start by introducing notions on twisted bilayers of graphene in Chapter 1. Then we turn to the expected effect of strain on the electronic properties of the system in Chapter 2. We take advantage of STM measurements to understand these effects at the local scale, in Chapter 3. Next, we turn to studying a peculiar relaxation mode in Chapter 4, which we call the *swirl* relaxation pattern. It arises in TBLGs when the moiré pattern is induced by biaxial heterostrain. Last, we present the experimental development of a straining STM aiming at using strain as a tool to investigate *in situ* the modifications of the electronic properties of a system under strain.

1

Introductive notions on twisted bilayers of graphene

Contents

Graphene and its derivates have always triggered intense interest. In this introductive chapter, we do not try to be exhaustive, particularly in such a rapidly evolving field, but rather to give a brief overview of the understanding of graphene and its bilayers in the low energy limit. Then we focus on the twisted bilayers of graphene (TBLG) and in particular the low and very low twist angle regimes.

1.1 Graphene

Graphene has a particular honeycomb symmetry that comes from the hybridization of the $2s$, $2p_x$ and $2p_y$ orbitals of carbon into so called sp^2 orbitals that posses C_3 symmetry. Each carbon atom is thus connected to three neighbors with in-plane covalent σ bonds each of them at a distance $\delta_{1,2,3} = a_0 = 0.142$nm.

The remaining $2p_z$ orbital are not modified. Their overlap is small, and thus they create a so called π state delocalized over the lattice. The electronic properties of graphene emerge from these $2p_z$ orbitals that each provide one electron to the graphene Fermi sea. To retrieve a good dercription of graphene, it is thus enough to take only

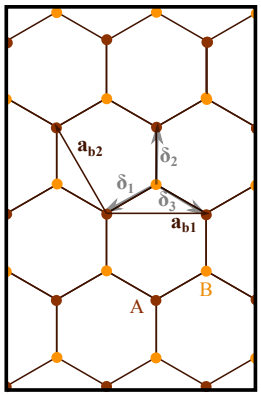

Figure 1.1: Definitions of the triangular graphene lattice. The unit cell contains two unequivalent carbon atoms, with $\boldsymbol{a}_{b1} = a \cdot (1, 0)$ and $\boldsymbol{a}_{b2} = a \cdot (-1/2, \sqrt{3}/2)$ and the crystal parameter $a = a_0\sqrt{3}$.

these electrons into account : this is the tight-binding approach. This justifies the second quantization Hamiltonian of graphene :

$$H = t \sum_{<i,j>} c^+_{\alpha,i} c_{\beta,j} + h.c. \tag{1.1}$$

Each particle on site i and sublattice β has a probability t to jump on its nearest neighbor j with opposite sublattice α, and vice versa.

All the electronic properties of the system are described by this Hamiltonian. In the following, we give a brief derivation of its low energy limit description that is sufficient to grasp important properties of graphene. This derivation is done first by going to Fourier space. For this, one develops the creation (annihilation) c^+ (c) operators in k space :

$$\begin{aligned} H &= t \sum_{<i,j>} \sum_{\boldsymbol{k},\boldsymbol{k}'} c^+(\boldsymbol{k})_{\alpha,i}\, e^{i\boldsymbol{k}\boldsymbol{R}_i}\, c(\boldsymbol{k}')_{\beta,j}\, e^{-i\boldsymbol{k}'\boldsymbol{R}_j} + h.c. \\ &= t \sum_{\delta_{ab}} \sum_{\boldsymbol{k},\boldsymbol{k}'} c^+(\boldsymbol{k})_{\alpha,i}\, e^{i\boldsymbol{k}\boldsymbol{R}_i}\, c(\boldsymbol{k}')_{\beta,j}\, e^{-i\boldsymbol{k}'(\boldsymbol{R}_i+\delta_{ab})} + h.c. \end{aligned} \tag{1.2}$$

where $\delta_{ab} = \delta_{1,2,3}$ (see figure 1). This reduces into :

$$H = t \sum_{\delta_{ab}} c^+(\boldsymbol{k})_{\alpha,i}\, c(\boldsymbol{k})_{\beta,j}\, e^{-i\boldsymbol{k}\delta_{ab}} + h.c. \tag{1.3}$$

In matrix form in the sublattice space, H writes :

$$H = \begin{pmatrix} 0 & t\sum_{\delta_{ab}} e^{-i\boldsymbol{k}\delta_{ab}} \\ t\sum_{\delta_{ab}} e^{i\boldsymbol{k}\delta_{ab}} & 0 \end{pmatrix} = \begin{pmatrix} 0 & f(\boldsymbol{k}) \\ f^*(\boldsymbol{k}) & 0 \end{pmatrix} \tag{1.4}$$

It is useful to derive the low energy limit around Dirac cone $\xi = \pm 1$, valid for all wavevectors q around K_ξ with $q << K_\xi$ [9] :

$$\begin{aligned} f(\boldsymbol{k}) &= f(\boldsymbol{K}_\xi + \boldsymbol{q}) \\ &= t \sum_{\delta_{ab}} e^{-i\boldsymbol{K}_\xi\delta_{ab}}\, e^{-i\boldsymbol{q}\delta_{ab}} \\ &\simeq t \sum_{\delta_{ab}} e^{-i\boldsymbol{K}_\xi\delta_{ab}}(1 - i\boldsymbol{q}\delta_{ab}) \\ &= -i\boldsymbol{q}t \sum_{\delta_{ab}} \delta_{ab}\, e^{-i\boldsymbol{K}_\xi\delta_{ab}} \\ &= -i\boldsymbol{q}t \sum_{\delta_{ab}} \delta_{ab}\, cos(\boldsymbol{K}_\xi\delta_{ab}) - \boldsymbol{q}t \sum_{\delta_{ab}} \delta_{ab}\, sin(\boldsymbol{K}_\xi\delta_{ab}) \end{aligned} \tag{1.5}$$

We follow G. Montambaux [10] in defining $\boldsymbol{u_x}$ and $\boldsymbol{u_y}$ so that f writes :

$$f^\xi(\boldsymbol{K}_\xi + \boldsymbol{q}) = -it\frac{a\sqrt{3}}{2}\boldsymbol{q}\boldsymbol{u}_y + t\frac{a\sqrt{3}}{2}\xi\boldsymbol{q}\boldsymbol{u}_x \tag{1.6}$$

So that the Hamiltonian can eventually be written in the form of a 2*2 matrix :

$$H^\xi = t\frac{a\sqrt{3}}{2}\begin{pmatrix} 0 & \xi q_x - iq_y \\ \xi q_x + iq_y & 0 \end{pmatrix} = \hbar v_F \boldsymbol{q}\cdot\boldsymbol{\sigma} \tag{1.7}$$

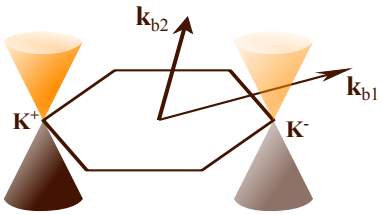

Figure 1.2: Schematic dispersion of monolayer graphene around K_+ and K_- dirac points. It shows the massless property of graphene electrons, as well as its semimetal property.

Small refinements to this low energy limit model can be done to improve our understanding of the system. In particuler, adding the second nearest neighbors hopping to the Hamiltonian results in the electron-hole assymetry of the dispersion [9] ; and the low energy derivation to higher orders in q reveals the threefold direction dependent dispersion, so called *warping*.

With the Fermi velocity (first calculated by P. R. Wallace [11]) is given, for $t = 3.7eV$, by :

$$v_F = \frac{a\sqrt{3}t}{2\hbar} = 1.1 \cdot 10^6 m/s \tag{1.8}$$

Equation 1.7 is reminiscent of a massless Dirac-like Hamiltonian (*Weyl-Hamiltonian*). Close to K_ξ, the wavefunction obeys Dirac equation [9]

$-i\hbar v_F \boldsymbol{\sigma} \cdot \nabla \Psi(\boldsymbol{r}) = E\Psi(\boldsymbol{r})$

Solving this equation yields the famous Dirac cone dispersion $E_\pm = \pm\hbar v_F |\boldsymbol{q}|$. The corresponding eigenstates are :

$$\Psi_\pm^\xi(\boldsymbol{k}) = \frac{1}{\sqrt{2}}(e^{-\xi i\theta_k/2}, \pm e^{+\xi i\theta_k/2}) \tag{1.9}$$

Equation 1.9 enables us to define *pseudospin* in graphene as the angle that weights the density on the two sublattices : $\theta_q = arctan(q_x/q_y)$. This new degree of freedom for graphene electrons is at the root of many interesting properties of graphene, such as *Chiral tunneling* [13].

One can plot the k-space dependent pseudospin texture in the Brillouin zone (BZ) as shown on Fig. 1.3. In agreement with equation 1.9, the pseudospin turns around the K_+, K_- points in opposite directions depending on the chirality ξ.

With that, we can introduce the topological *winding number* $\mathscr{W}$ of graphene : the number of times the pseudospin rotates by 2π when we rotate the wavefunction around a Dirac singularity. It is a topological number because it only depends on the Hilbert space defined by the wavefunctions. In other words, it only depends on geometrical considerations : In our case, the geometrical equivalent of the BZ of graphene is a torus.

More generally, a topological quantity related to the curvature of a surface, the so called *Chern number*, can always be defined. In our specific case of condensed matter physics, the Chern number can be understood in terms of the *Berry phase* acquired by the Bloch wavefunctions when evolving in momentum space, as showed by M. L. Berry [14].

A sketch of this Berry phase over several contours in the BZ given on fig. 1.4, showing that the total Chern number of graphene is 0, as it is the sum of the winding number of the wavefunctions of sublattice A or B.

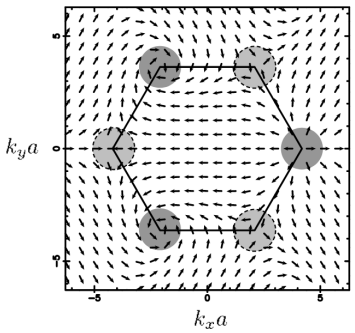

Figure 1.3: Pseudospin texture in the Brillouin Zone of monolayer graphene from [12].

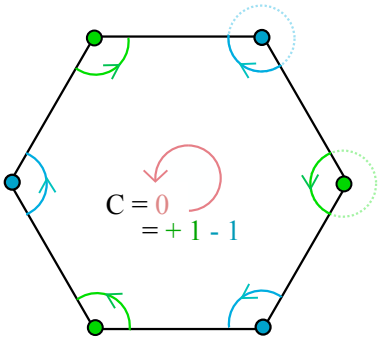

Figure 1.4: Sketch of the Berry phase acquired by evolving the wavefunction around closed paths in the BZ.

1.2 *Bilayers of graphene*

The most straightforward way to stack two aligned layers of graphene is to put atoms resting on each other : this is the so called AA stacking. In that case, the interlayer coupling shifts appart the Dirac cones in energy. In terms of magnitude, this shift corresponds to the tunneling probability t_0 between atoms that are stacked on top of each other [15]. By diagonalization of the 4*4 Hamiltonian of the sys-

tem, one finds that the Fourier bands of the system disperse like $E_\pm = \pm\hbar v_F|\boldsymbol{q}|+t_0$, $E_\pm = \pm\hbar v_F|\boldsymbol{q}|-t_0$.

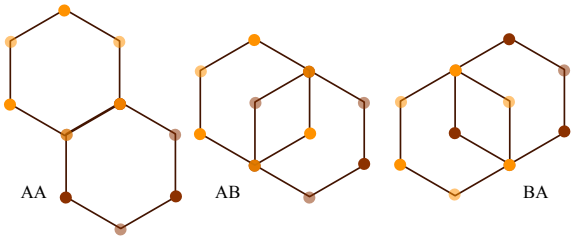

Figure 1.5: Definitions of the AA (left) and Bernal (right) stackings. The unit cell contains Fourier atoms, A_i and B_i from layer $i = 1, 2$.

However, this stacking is energetically costly and has few experimental realizations [16, 17].

Bernal stackings, namely AB or equivalently BA stackings, are energetically favored by $20meV$ per atom with respect to the AA stacking [18]. They correspond to the natural arrangement of graphite crystals discovered by J.D. Bernal in 1924 [19] (see Fig. 1.5). The low energy description yields $E_\pm = \pm\frac{\hbar^2 v_F^2|\boldsymbol{q}^2|}{t_0}$ for electron states on inequivalent sublattices of each single layer A_1/B_1 or A_2/B_2. Higher energy bands $E_\pm = \pm\frac{\hbar^2 v_F^2|\boldsymbol{q}^2|}{t_0} \pm t_0$ are also present, corresponding to electron states on the dimers from A_1/B_2 or A_2/B_1 orbitals.

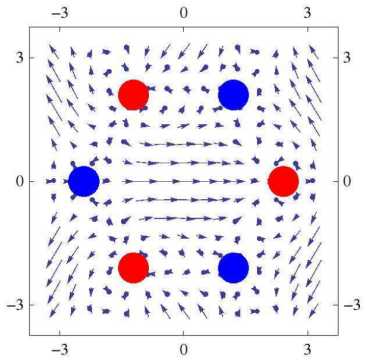

Figure 1.6: Pseudospin texture of AB stacked bilayer of graphene in its Brillouin Zone. From [20].

Close to the K_ξ point, the parabolic dispersion of AB stacked bilayers of graphene results from the supperposition of two Dirac cones, so that their winding number can be thought of as the addition of the winding numbers of two individual monolayers which yields $\mathscr{W} = \pm 2$ [20] as shown on the pseudospin texture in Fig. 1.6.

Many high quality samples of such stacking have been studied. This has led to experimental estimations of graphene hopping parameters using techniques such as infrared spectroscopy and Raman scattering [21, 22, 23]. These estimate the nearest neighbor hopping to be $t \simeq 2.9 - 3.7eV$. The strongest interlayer coupling is estimated to be $t_0 \simeq 0.45$ eV, much lower than t because the orbitals overlap much less significantly due to interlayer separation which is about $0.335nm$.

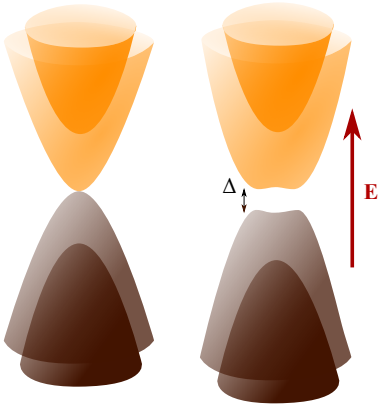

Figure 1.7: Schematic dispersion of bilayer graphene, with (right) and without (left) electric field.

The electronic properties of the system can be tuned by the application of an external field that breaks the symmetry of the layers. It enters in the Hamiltonian in the form of a potential V so that the conduction and valence bands are written in a low energy limit

$$E_\pm = \pm\sqrt{(eV/2)^2 + \left(\frac{\hbar^2 v_F^2|\boldsymbol{q}^2|}{t_0}\right)^2} \tag{1.10}$$

Thus, the potential results in a gap oppening Δ as shown by E. McCann *et al.* [24]. This gap is due to Coulomb interactions and thus is dependent on the relative doping of the individual layers, which can also be taken into account [25]. In most experiments the external field originates from an external gate, and thus such relative doping of the layers is likely to happen from screening and charge reorganization of the layers. In addition, the low energy limit of equation 1.10 is sufficient to describe the gapped dispersion from the experiments

as $V << t_0$. All in all, this approach well describes experimental results such as the ARPES (angle-resolved photoemission spectrocopy) measurement of a doped bilayer on SiC [26].

1.3 *Twisted bilayers of graphene (TBLG)*

Two layers of graphene can also be stacked with an interlayer twist θ_{int}. In that case, the periodicity of the system can be quite enhanced as the short range translational symmetry is broken. The appearance of a new superlattice in graphitic systems triggered intense attention since its first observation in the 80's and was soon referred to as *moiré period* in reference to the optical phenomenon of the interference between two non equivalent periodicities [5].

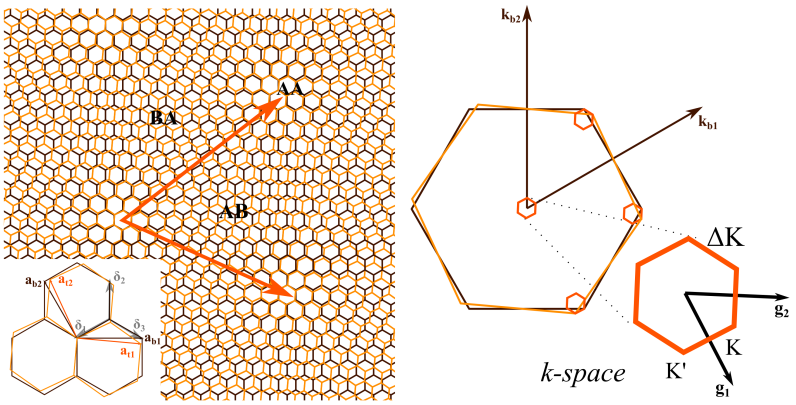

Figure 1.8: Real space (**left**) sketch of a twisted bilayer of graphene (TBLG). With the inset showing both graphene periodicities. The moiré periodicity $\boldsymbol{a}_{m1}$ and $\boldsymbol{a}_{m2}$ connecting two nearest neighbors AA zones is shown in dark orange. In reciprocal space (**right**) this periodicity is referred as $\boldsymbol{g_1}$ and $\boldsymbol{g_2}$, that are the generators of the moiré Brillouin zone (mBZ) shown in dark orange.

This moiré pattern is not only a peculiar optical phenomenon, but has in fact tremendous impact on the physics of the system. We will see in the following that this moiré can confine electrons, forcing them to interact, favouring the emergence of correlated phenomena such as superconducting and correlated insulating phases [6, 27], magnetic phases [28], and strange metal behaviour [29, 30].

A sketch of a twisted bilayer system is given on Fig. 1.8. In real space, the larger periodicity is visible in the moiré period connecting two AA stacking regions that are surrounded by AB and BA stackings. The effect of the twist between the lattices is also visible in Fourier space : the BZ of both lattices are twisted with respect to each

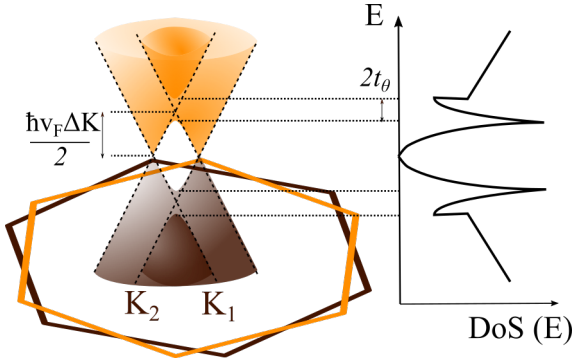

Figure 1.9: Anticrossing of the Dirac cones from first and second layers K_1 and K_2. Van Hoove singularities are visible in the density of states at the saddle point energies.

other, so that the Dirac cones of the first and second layer are separated by ΔK thereby defining the moiré Brillouin zone (mBZ). This quantity is proportional to the moiré periodicity and can be directly linked to the rotation angle by :

$$\Delta K = 2|\boldsymbol{k}_D| sin(\theta_{int}/2) \tag{1.11}$$

with $\boldsymbol{k}_D$ the position of the monolayer Dirac cone.

The low energy physics of each graphene layer is greatly modified by the hybridization of the Dirac cones from each layer. Particularly, the anticrossing of the Dirac cones leads to a saddle point in the dispersion : It features a maximum in the direction of ΔK and a minimum in the perpendicular direction. Leon van Hove [31] showed that such feature in the dispersion of a 2D system leads to a logarithmic divergence of its local density of states : $LDOS \propto log(1 - \frac{E}{E_{saddle}}) \xrightarrow[E=E_{saddle}]{} \infty$. The energy separation of these so called *van Hove singularities* (vHs) depends on the distance ΔK between Dirac points in k-space in the following way :

$$\Delta E_{vHs} = \hbar v_F \Delta K - 2t_\theta \tag{1.12}$$

with $t_\theta = 0.108eV$.

The vHs can be measured in the local density of states (LDOS) by STM and were first reported by Li *et al.* [33] with this technique. More details are given in section 3.1. The linear dependency of ΔE_{vHs} as a function of $sin(\theta_{int}/2)$ has been demontrated experimentally by I. Brihuega *et al.* [32] using a STM technique, as shown on Fig. 1.10.

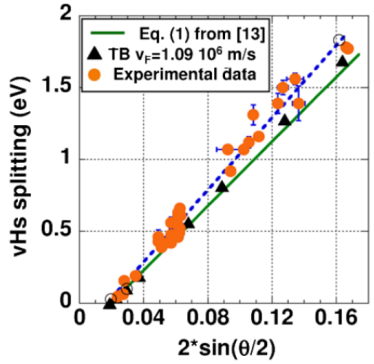

Figure 1.10: Energy separation of the vHs. The tight-binding calculations (black triangles) and equation 1.12 (green solid line) fit well the STM experimental data (orange dots). From [32].

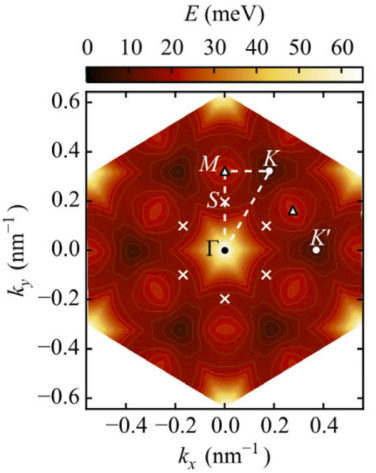

Figure 1.11: Colormap in the mBZ of the first conduction band for a 1.2°TBLG. The K and K' points at the corners of the mBZ show local minima that correspond to the Dirac-like features originating from the folding of Dirac cone $K_{\xi,1}$ and Dirac cone $K_{\xi,2}$, $\xi = \pm 1$. Saddle points are indicated at the vHs energy at the S points. Adapted from [8].

1.3.1 *Exact calculations : An iterative method*

The unit cell of our TBLG system is now that of the moiré and can contain more than several thousands of atoms for low angles. Thus, the diagonalization of the tight-binding Hamiltonian can no longer be done analytically. Numerical methods can be used, such as the *Lanczos algorithm* that calculates iteratively the wavefunctions of the system for a given Hamiltonian, until convergence is achieved. This calculation is accurate but can be time consuming. It has been used in several works to investigate the electronic properties of TBLG. In the following, we focus on this model as developed in the work of G. T. de Laissardière *et al.* [34].

Previoulsly, we have defined hopping parameters independently, because each combination of orbitals overlapp in different ways. In this model, we consider a more general description in which the hoppings depend on the distance and the angle between the orbitals.

$$t_{ij} = n^2 V_{pp\sigma}(r_{ij}) + (1 - n^2) V_{pp\pi}(r_{ij}) \tag{1.13}$$

The angle between the orbitals is taken into account in t_{ij} through the term $n = cos(< O_z, (\boldsymbol{r}_j - \boldsymbol{r}_i) >)$ that is equal to 0 (resp. 1) when the vector between atoms i and j is perpendicular (resp. parallel) to the out-of-plane direction O_z and t_{ij} is thus a purely $V_{pp\pi}$ (resp. $V_{pp\sigma}$) tunneling process.

The distance between the orbitals is taken into account by the *Slater-Koster* parameters $V_{pp\pi}$ and $V_{pp\sigma}$:

$$V_{pp\pi} = -\gamma_0 e^{q_\pi(1-\frac{r_{ij}}{a_0})}, \quad V_{pp\sigma} = \gamma_1 e^{q_\sigma(1-\frac{r_{ij}}{a_1})} \tag{1.14}$$

where their exponential decay are arbitrarily set to be the same : $\frac{q_\sigma}{a_1} = \frac{q_\pi}{a_0} = 2.218\text{Å}^{-1}$, with $a_0 = 1.418\text{Å}$ the interatomic distance and $a_1 = 3.349\text{Å}$ the interlayer distance.

In this model, the important parameter to be tuned is the hopping t. Previously, it was either derived from *ab initio* calculations or estimated from experimental techniques as described in section 1.2. In the work of I. Brihuega *et al.* [32], efforts were made to fit these calculations to experimental datas. It was done by taking advantage of the previously mentioned linear dependency of the vHs spacing ΔE_{vHs} over $sin(\theta_{int}/2)$, with a slope that is proportional to t according to equations 1.11 and 1.12. The calculations that fits best the data are obtained with a monolayer Fermi velocity of $1.09 \cdot 10^6 m/s$ (shown on Fig. 1.10 in black triangles), in agreement with the value previously mentioned. This Fermi velocity corresponds to taking a hopping parameter of $t = 3.7eV$, which is higher than expected from *ab initio* calculations. Using the same values we also obtain a good estimation of the strongest interlayer hopping parameter $t_0 = 0.48eV$.

With these calculations, the dispersion of TBLG can be retrieved, as shown on Fig. 1.11 for the first conduction band.

Such calculations also give access to the Fermi velocity, as defined in a low energy limit, near the Dirac cones. In agreement with the initial continuum calculations by J. M. B. Lopez dos Santos *et al.*[35], one can retrieve with that description that the Fermi velocity is renormalized for small twist angles. The Fermi velocity is reduced with interlayer twist and even cancels for small twist angles near 0.9°as shown on Fig. 1.12. This can be intuitively expected from Fig. 1.9 because the anticrossing of the Dirac cones happen closer to charge neutrality with decreasing θ_{int}.

In addition, this model also predicts that the velocity renormalization comes along a confinement of the 2D electron gaz : wavefunctions tend to localize in AA regions [34].

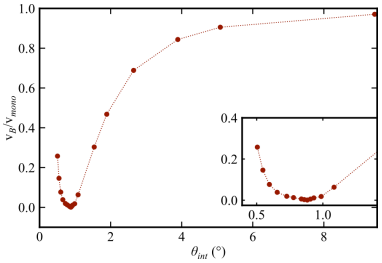

Figure 1.12: Fermi velocity in twisted graphene bilayer. Calculated ratio of the Fermi velocity of a bilayer system v_{Bi} to that of the monolayer ($v_{mono} = 1.1.10^6 m/s$). The inset shows a close up near 0.9°.

1.3.2 *Low energy description : Continuum model*

Despite their accuracy, the calculations described in the previous section can be quite time expensive. Indeed, they rely on the iterative exact diagonalization of the Hamiltonian, whose size directly depends on the number of atoms. In particular, convergence time increases for decreasing angles because the number of atoms increases in the moiré unit cell.

A good description of TBLG systems can be achieved with lower computational cost, if one relies on a low energy limit approximation. This kind of approach, so called continuum model, was introduced in Refs. [35, 36, 37].

In this description, the moiré acts as an additional potential on

the system and varies slowly over the graphene period. The Hamiltonian of the system can thus be viewed as a combination of the two individual layers Hamiltonians H_1 and H_2 and an interlayer potential Hamiltonian $H_\perp$.

$$H = \begin{pmatrix} H_1 & H_\perp \\ H_\perp^\dagger & H_2 \end{pmatrix} \tag{1.15}$$

Each intralayer Hamiltonians H_l, $l = 1,2$ can be written in the low energy limit because intervalley wavevectors are neglected for sufficiently low twist angles (tipically below 10°). Additionally, the twist is taken into account as a layer dependent shift of the Dirac cone position. The Hamiltonians H_l are thus similar to the one derived in equation 1.7, with a layer dependent shift $\boldsymbol{q} \rightarrow \boldsymbol{q} + (-1)^l \Delta K/2$.

The Hamiltonian $H_\perp$ that couples the layers depends on the interlayer hopping $t_\perp$. The latter is seen as continuous over the moiré cell. One can thus integrate these hoppings over the moiré cell.

In Fourier space, the contributions to $t_\perp(\boldsymbol{K} + \boldsymbol{q})$ are found to decay exponentially in $\boldsymbol{q}$. This is why the Hamiltonian can be drastically truncated to keep only the smallest harmonics in the moiré cell. Around the K point, these are 0, $\boldsymbol{g_1}$ and $\boldsymbol{g_2}$ with $\boldsymbol{g_i}$ the moiré period in Fourier space connecting two equivalent Dirac cones as sketched on Fig. 1.13. The same can be done around the moiré K' point.

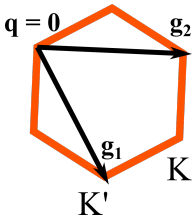

Figure 1.13: Sketch of the geometry of the moiré Brillouin zone.

$$H_\perp = \sum_{\boldsymbol{k}=0,\boldsymbol{g_1},\boldsymbol{g_2}} e^{i\boldsymbol{k}\cdot\boldsymbol{r}} \begin{pmatrix} u_1 & u_2 \\ u_2 & u_1 \end{pmatrix} \tag{1.16}$$

where the parametrization of the continuum model is commonly given by $u_1 = u_2 = 0.11$eV [36, 38]. The u_i parameters can also be set to different values, accounting for corrugation effects [39]. The representations of the Hamiltonian are not the same at each equivalent K point and are related by $H(\boldsymbol{k} + \boldsymbol{g_1}) = MH(\boldsymbol{k})M^{-1}$ and $H(\boldsymbol{k} + \boldsymbol{g_2}) = M^{-1}H(\boldsymbol{k})M$ with $M = \begin{pmatrix} e^{i2\pi/3} & 0 \\ 0 & e^{-i2\pi/3} \end{pmatrix}$ [12]. In the details of the calculation, a phase has thus to be added in the off-diagonal term of the matrix for two terms of the sum.

All in all, the Hamiltonian is then reduced to a 12*12 matrix, much easier to diagonalize.

Many physical quantities can be derived from these calculations. R. Bistritzer *et al.* [36] were the first to show that the Fermi velocity vanishes when twist angle is reduced to 1.1°: the so called *magic angle*. They were also able to go to even lower angle and predicted a sequence of magic angles below the first one, as shown on Fig. 1.14.

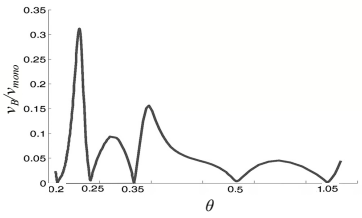

Figure 1.14: Fermi velocity in twisted graphene bilayer. Calculated ratio of the Fermi velocity of a bilayer system v_B to that of the monolayer ($v_{mono} = 1.1.10^6 m/s$). Adapted from [36].

1.4 *Low twist angle regime*

In the following, we non exhaustively overview experimental evidences of the correlated physics at play in low twist angle TBLG.

1.4.1 *Ordered states in the low twist angle regime*

A decrease of the Fermi velocity comes along with a flattening of the lower energy bands, as $v_F \propto \frac{1}{\partial E/\partial k}$. This was first probed by Scanning Tunneling Microcopy and Spectroscopy (STM/STS) [32, 33, 42]. This effect is particularly remarkable when the crossing energy between the Dirac cones is comparable to the anticrossing energy. This happens when the Fermi velocity cancels near $\sim 1°$: the bands can become extremely flat.

In this regime one expects that the electron-electron interactions play a huge role, because in these flat bands the charge carriers do not possess enough kinetic energy to escape Coulomb interactions with each other. Ordered states in such a system were thus soon predicted [36]. However, these were not detected in the first STM/STS experiments, because correlated physics are only expected when the chemical potential of the system lies in the flat bands. These low energy valence and conduction bands each have 4 flavours, 2 for valley and 2 for spin degeneracies : this represents 8 charge carriers per moiré cell, the latter containing tens of thousands of atoms.

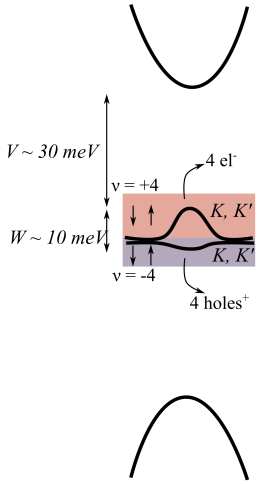

Figure 1.15: Principle sketch of the flat bands of TBLG with typical energy scales [40, 41].

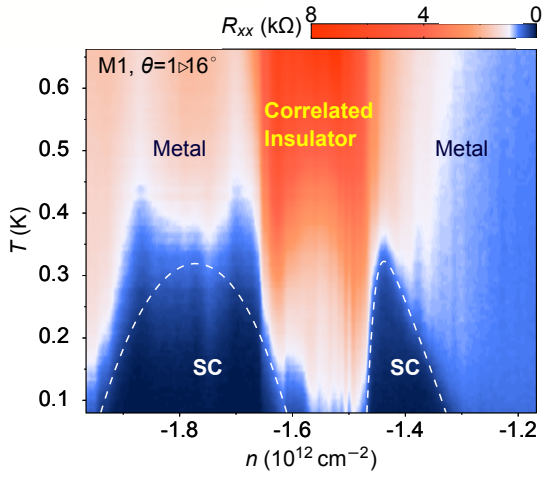

Figure 1.16: First evidence in transport experiments of superconducting domes at low temperature close to the correlated insulating state which occurs at half filling of the flat valence band. Adapted from [6].

Experimental evidence of such correlated states were first measured in transport experiments, where the TBLG system was encapsulated in hBN layers. Y. Cao *et al.* [6, 27] measured superconducting and correlated insulating phases near half filling of the first valence band ($\nu = -2$). They were able to achieve this by tuning the filling of the flat bands with a back gate. This result was reproduced several times : we know that the typical temperature for the correlated insulating state is $\sim$ 4K and the superconducting state can arise below temperatures as high as $\sim$ 3K. Yet another ordered phase was measured by A. Sharpe *et al.* [28] showing evidence of ferromagnetism

near filling $\nu = 3$

The importance of interactions in the emergeance of these physics can be also be evidenced by tuning interlayer distance, thereby influencing superconductivity as predicted by S. Carr *et al.* [43]. M. Yankowitz *et al.* [44] experimentally detected pressure induced superconductivity for a TBLG whose angle was above the magic angle. In their experiment, they changed the interlayer distance using hydrostatic pressure.

Superconducting state has been also measured in twisted trilayers of graphene [45, 46, 47], where the experiments support a scenario where the system is a strongly coupled superconductor and hosts unconventional superconductivity. In this system, the magic twist angle is increased with respect to a TBLG system by a factor $\sqrt{2}$. This trilayer behaviour was predicted by E. Khalaf *et al.* [48] who also predicted other magic angle physics up to 6 graphene layers, stacked in peculiar fashions. Up to now, following this theoretical prediction, experimental evidence of superconducting states relying on electronic correlations were observed in devices up to 5 layers by Y. Zhang *et al.* [49].

Another observation in TBLG which is reminiscent of unconventional superconductors is the strange metal behaviour [29, 30, 50], namely the linear temperature dependency of the longitudinal resistivity of the system that cannot be explained by a Boltzmann description.

Despite numerous experimental and theoretical works that point towards unconventional superconductivity, the origin of these ordered phases is still under investigation.

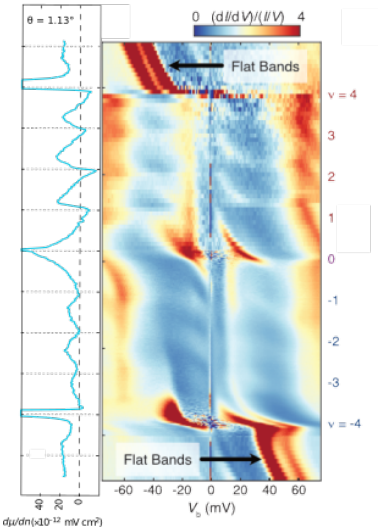

Figure 1.17: **Left** Inverse electronic compressibility $\partial\mu/\partial n$ of a 1.13°device measured with a scanning nanotube based single electron transistor (SET). An abrupt decrease in the compressibility is measured each time the system polarizes in one spin/valley flavour. Adapted from [51]. **Right** Colormap LDOS of a 1.06°device measured by STS. A shift in position of the flat bands upon doping can be followed with the central peaks that correspond to the van Hove singularities (vHs). The higher energy bands detected at higher voltage bias also shift their positions upon polarisation of the system. From [52].

1.4.2 *Broken symmetries in the low twist angle regime*

Since interesting ordered phases rise in TBLG when the chemical potential lies in the flat bands of the system, a further look at this range of fillings can teach us on how to understand the physics in TBLG.

The system experiences spin/valley symmetry breakings in this range of doping energy. The 4-fold degeneracy is lifted at each integer filling of the system, as it polarizes into spin and/or valley flavours. This polarization can be detected in the LDOS by STS [52, 53, 54, 55] where the position of the bands in voltage bias is reset to the charge neutrality point (CNP) at integers fillings $\nu = 1, 2, 3$ (see Fig. 1.17, right). It is also visible in transport experiments [45, 51, 56, 57], up to temperatures as high as a $100K$. In these experiments, electronic compressibility shows a Dirac-like character near the CNP where all 4 flavours are filled altogether upon increasing gate voltage. At each integer fillings, the system experiences a transition, so called *Dirac-revival*, where the electrons fill only one flavour and the system resets to its Dirac-like character which is visible in Fig. 1.17 (left).

These polarized states could be at the roots of certain ordered

phases detected in the system [58]. In particular, they support the emergence of magnetization [28, 51]. Also, the measured quantized anomalous Hall effect [59] is believed to arise directly from such spin and valley polarization of electrons.

1.4.3 *Inhomogeneities in the low twist angle regime*

Experimental data present discrepancies in their features. In transport experiments, it is particularly striking, as the physics that are probed can be completely different from one sample to the other. Fig. 1.18 gives a review of several similar samples, some of them featuring insulating states at half filling, while others with similar twist angle do not. The work of R. Polski *et al.* [58] also puts into perspective the "magic angle" requirement, since superconductivity, cascade transitions and strange metal behaviours were detected over a large twist angle range ($0.8° < \theta_{int} < 1.23°$) in very homogeneous samples.

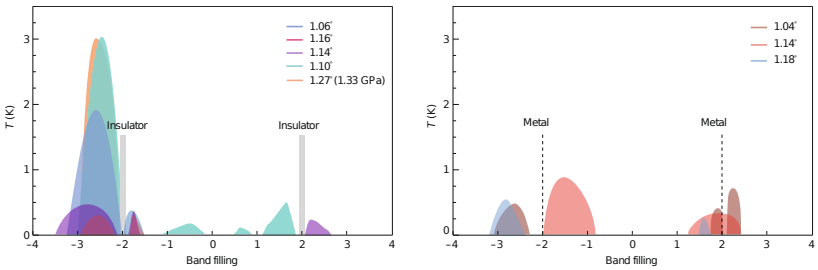

Figure 1.18: Phase diagram sketchs of several TBLG samples characterized by their angle of rotation. The colored dome corresponds to the superconducting phase. The left (resp. right) plot gathers the sample that present (resp. do not present) a correlated insulating state at half filling of each band. From [60].

The sample to sample variability from transport experiments can in part be explained by the different fabrication process and designs, and in particular the detailed electrostatic environment of TBLG that can play a role in the screening of electronic interactions [60].

Another non negligible aspect is the sample inhomogeneities that have been found to be ubiquitous in stacked samples [61]. These inhomegeneities can be unveiled for example by SQUID on tip measurements, [51, 62]. For example, blister-type defects (wrinkles, bubbles) often arise during the commonly used tear and stack processes and their number can be reduced by "squeezing" the device [63].

This inhomogeneity can be quantified in several ways. The most common one is to quantify this in terms of twist angle inhomogeneity, as the electronic properties are often calibrated in terms of twist angle. For example, a mapping over the sample of the local twist angle $\theta_{int}(\boldsymbol{r})$ can be done by relating it to the local charge density $n_s(\boldsymbol{r})$, as when the bands are filled, a moiré cell of surface area A contains 4 electrons [62] : $n_s(\boldsymbol{r}) = \frac{4}{A} = \frac{8\theta_{int}^2}{\sqrt{3}a^2}$. The local charge is extracted from the Landau Level structure.

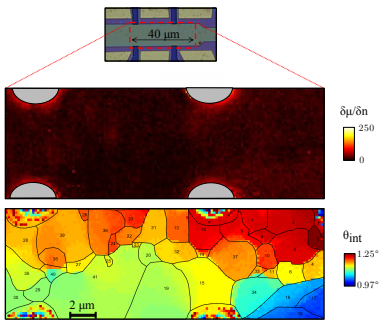

Figure 1.19: Angle mapping using a scanning SQUID. Image from [64].

One illustration of such mapping is given in Fig. 1.19. One can easily imagine that such a rigid evolution of twist angle has to be refined as two regions that have a given twist angle are either separated by a boundary, which are often found to induce strain [65], or

evolve continuously from one to the other, which means one has to include continuous strain from one region to the other.

Moreover, this so called *twist angle disorder* has an important effect on the local density of states of the system. As argued in Ref. [66], this disorder is always accompanied with strain because of the breaking of C_3 symmetry, and results in a smoothing of LDOS features such as a broadening and weakening of the vHs and a filling of states in the gaps above the flat bands. In the low energy limit however, the Dirac cone velocity is conserved upon this symmetry breaking.

Inhomogeneities may be one of the origins of the sample to sample variability in transport experiments. In particular, superconductivity could be destroyed more easily in the most inhomogeneous samples, which would explain the variability of temperature and filling ranges in which the system enters a superconducting regime.

1.5 Minimal twist angle regime

We now turn to even lower twist angles in TGLB, that are also interesting from the structural and electronic points of view. These systems referred to as minimally or marginally twisted bilayers, have angles typically below 1°.

1.5.1 Relaxation into Domain Walls

We have seen that AB stacking is energetically favored with respect to AA stacking. The whole energetic stacking pattern of TBLG was calculated quite soon by A. M. Popov *et al.* [18] as shown in Fig. 1.20.

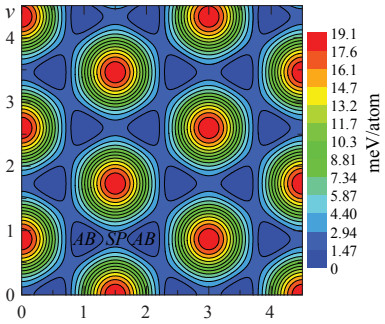

Figure 1.20: Calculations of the bonding energy of rigidly twisted bilayers of graphene. AA regions are about $20meV$ more costly than AB/BA stackings. Intermediate regions form a saddle point in energy and are thus referred to as SP. From [18].

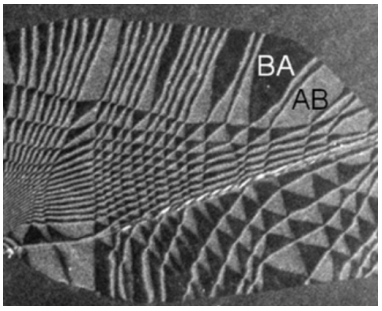

Figure 1.21: Dark Field TEM image of TBLG on copper showing an array of relaxed structures forming AB/BA stacked triangular regions. Defects and boundaries create spatial inhomogeneities in the local twist and reconstruction that can even form arrays of linear domains. Adapted from [67].

To favor the minimization of this stacking energy, also called *binding energy* U_B, the atoms can move from their original position in the single layer to maximize AB/BA stacking regions. Locally, it creates slight changes in atomic length and an increase in the elastic energy U_E of the system, which also tends to be minimized. This whole *relaxation* process forms a lattice of domain walls (DW), also called *reconstructed structure*, that conserves the initial moiré periodicity while minimizing the total energy $U = U_B + U_E$ of the system. The energy that is payed at the domain walls where the relaxation creates a concentration of local strain is compensated by the energy gain in increased AB/BA regions.

This relaxation happens at all angles, and is in fact responsible for the decoupling of the lower energy bands of magic angle TBLG from the higher energy bands [40, 68] favoring the strongly correlated states in magic angle TBLG. Nevertheless, relaxation is most critical and visible at minimal twist angle regimes below 1°. The work of Alden *et al.* [67] shown on Fig. 1.21 gives a large scale experimental evidence that minimally twisted TBLG relaxes into an array of Domain Walls that separate maximally extended AB and BA stacked regions, and meet into shrinked AA stacked regions. Such patterns were noticed on graphite for the first time in 1960 by

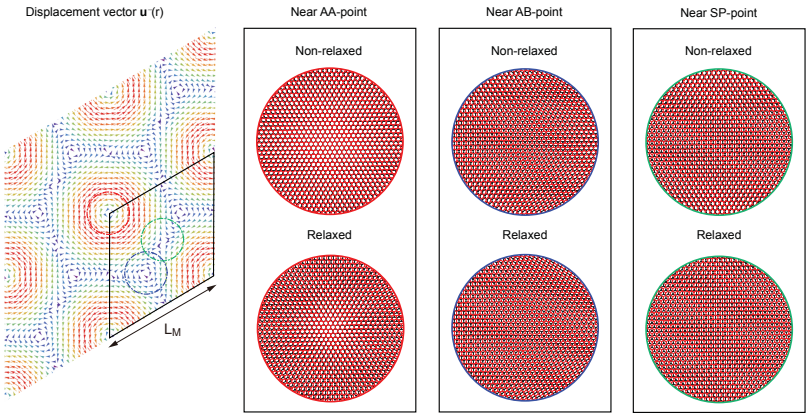

Figure 1.22: Self consistent relaxation calculations from minimisation of $U = U_B + U_E$. On the left is given the position dependent relative atomic displacement $\boldsymbol{u}_{-}(\boldsymbol{r})$ of layer 1 $\boldsymbol{u}_1(\boldsymbol{r})$ with respect to layer 2 $\boldsymbol{u}_2(\boldsymbol{r})$. Initially, the layers are rigidly twisted by $\theta_{int} = 1.05°$. The three panels on the right show that during such relaxation, AA regions tend to shrink while AB regions to expand. The SP (saddle point in terms of stacking energy pattern) regions tend to anisotropcally expand and form domain walls connecting neighboring AA zones. From [40].

TEM [69], and shortly after at a more local scale by STM experiments [70, 71] in which triangular patterns were noticed.

Despite these structures can be quite impressive because they involve the collective movement of numerous atoms, the actual displacement of individual atoms remains small. M. M. van Wijk *et al.* [72] demontrated that such displacement can be theoretically estimated by calculating the minimal stacking configuration of realistic structures using molecular dynamics. The general idea of such calculations relies on the minimization of the total energy of the system, starting from rigid atomic positions with given binding energy parameters, and allowing in-plane and out-of-plane movements of the individual atoms during minimization. Such relaxation calculation is presented on Fig. 1.22 for a low angle TBLG, where a significant reduction of AA stacking region size is induced by small rotation of individual atoms around it. In order to investigate theoretically the relaxation of free standing graphene layers, several different atomistic potential models exist. Although calculations agree qualitatively, the results can vary slighty depending on the choice of the model and the parameters used. Some theoretical works calculated that the maximal displacement of individual atoms does not go above $a_0/10$ in-plane and $a_g/5$ out-of-plane for $\theta \to 0°$[73]. According to Ref. [74], in the case of a twist angle of 0.76°, atoms can move up to 0.25Å $\sim a_g/10$ in-plane. In the work of Ref. [40], the maximal relative in-plane displacement is calculated to be about $a_g/4$ for $\theta_{int} = 0.55°$.

The choice of the potential defining the exact binding energies of the atoms in the system is thus critical to perform accurate calculations. F. Guinea and N. Wallet [75] show a careful comparison of such atomical potentials and show that LCBPO-II (long-range carbon bond-order potential-II) [76] and AIREBO (Adaptive Intermolecular Reactive Empirical Bond Order potential) [77] in combination with the Kolmogoreov-Crespi (KC) potentials as used in [78] describe most accurately the results from Alden *et al.* [67]. The former, such as the AREBO potentials, give a description of C-C bonds, in terms of energies and length in particular, giving a good a description of

a whole array of hydrocarbon molecules. The KC potentials, on the other hand, provide a treatment of interlayer interactions, which are critical in the case of bilayer graphene. All in all, such calculations should always be compared to experimental results.

A significant amount of experimental techniques are able to investigate the large scale structure of such DW lattices. Most, like the previously mentioned STM technique, are suitable to investigate TBLG directly on the surface but other can investigate TBLG encapsulated in hBN.

Optical techniques such as Low Energy Electron microscopy techniques [79, 80] or 4D Scanning Transmission Electron Microcopy using bragg interferometry [81] can be particularly efficient because they can give information on the exact local stacking over large scales. Dark Field Transmission Electron Microscopy can also be used [82], even when the encapsulation consists in one hBN layer if it is misaligned with the graphene [83].

Piezoresponse Force Microscopy can also be used, as it relies on the electro-mechanical response of the sample to out-of-plane electric field, which is different close to the DWs because of the strain gradients that are localized there [84]. One of the perspectives of such a technique is to characterize and investigate the homogeneity of transport TBLG samples, by taking advantage of the relaxation that is present even in the case of twists close to the magic angle.

Other techniques that rely on optical methods are capable of investigating encapsulated devices : nano Raman scanning can probe the DW by measuring the lattice dynamics (*e.g.* phonons) [85], nano scanning near field optical microscopy (s-SNOM) combined with an infrared light excitation reveal the different absorption coefficient from different regions [86], [87].

Such measurements show that although the local displacements of individual atoms are small, the consequences on the electronic properties can be significant.

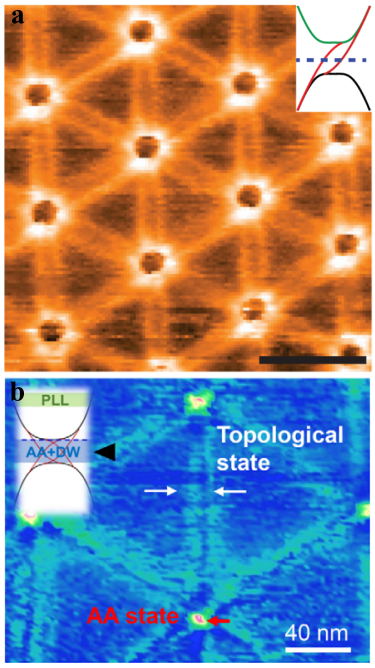

Figure 1.23: **a** STM imaging ($V_b = -0.11V$, $I_t = 200pA$) from Ref. [88] of helical edge states in a 0.245°marginally twisted bilayer graphene (scale bar is $50nm$). **b** Similar helical edge states for a 0.12°system ($V_b = -40meV$, $I_t = 150pA$) from Ref. [89].

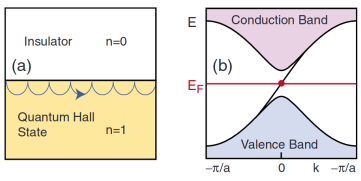

Figure 1.24: From [94].

1.5.2 *Localized states at the Domain Walls*

The domain walls (DW) between AB and BA stacking regions are not only a structural curiosity, where strain is concentrated. In fact, they can also host edge states that were evidenced by STM measurements [88, 89, 90] (see Fig. 1.23) and in transport experiments by a measure of the conductance of a single DW [91] or by measuring a conductance interference pattern that originates from topologically protected modes [92].

These physics are reminiscent of the edge states in the Landau Level Quantum Hall Effect [93] that arise notably in topological insulators as reviewed in Ref. [94]. In this type of materials, the physics is influenced by geometrical considerations : their Chern invariant related to the curvature of their Hilbert space is non trivial (*i.e.* $C \neq 0$).

In the case of an interface between two regions of different Chern number, the resolution of the Haldane model imposes that a state

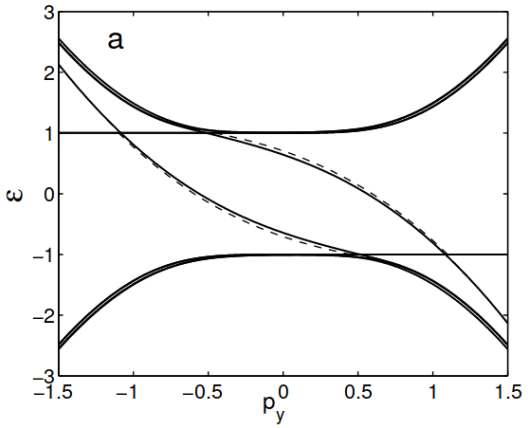

Figure 1.25: Dispersion bands estimated from continuum numerical calculations (solid line) and with an analytical approximation (dashed line) around Dirac point K_ξ. The DW between regions of different topological number is chosen along y. There are two localized bands near a particular Dirac point, propagating in the same direction. At the other Dirac cone, two other modes propagate in the opposite direction. Figure from [95]. These results are in agreement with more accurate calculations from a tight-binding model [96].

has to cross the Fermi level at that interface as shown on Fig. 1.24. Indeed, upon crossing of the interface, the Chern number has to go for example from +1 in one region to -1 in the other, thereby forcing a gap "sign change" at the interface that corresponds to this Fermi energy crossing state.

The possibility of topologically protected edge states in AB/BA bilayer graphene was investigated early because of the well known gap oppening that arises upon the application of an electric field $\boldsymbol{E}$ as reminded in section 1.2. Edge states were predicted if a sign change of the electric field was engineered between adjacent regions of a bilayer [95, 96]. This can be understood as changing $\boldsymbol{E}$ into $-\boldsymbol{E}$ creates a sign change of the gap around K and K' points. At these points, the curvature is peaked around each unequivalent Dirac cone, and a *valley Chern number* that corresponds to the *winding number* introduced in section 1.1 can be defined [97]. Thus, upon the crossing of the DW, the winding number changes sign in a given valley from $+\mathscr{W}_\pm$ in one region to $-\mathscr{W}_\pm$ and forces the appearance of low energy topological edge modes.

Calculations shown on Fig. 1.25 find that at the interface of AB/BA bilayer DW, two edge modes originating from valley K_+ propagate in one direction, and two others from valley K_- propagate in the opposite direction. They are called *helical* edge states in reference to their valley and spin polarization. This is in agreement with topological requirements that the total Chern number cannot change, being determined by the topological structure of the bulk states as :

$C = N_{left} - N_{right} = 0$

Where $N_{left} = N_{right} = 2$ are the numbers of right and left moving edge modes. The equation that is valid around a given valley is written [97] : $\mathscr{W}_\pm = N_{left\pm} - N_{right\pm} = \pm 2$ which agrees with the band calculations.

The topological character of these helical edge states around each valley makes them robust against valley-preserving disorder [95]. In particular, a low energy channel going in one direction determined by the velocity of the band can only be backscattered at the expense of changing its valley index. Such graphene systems are thus de-

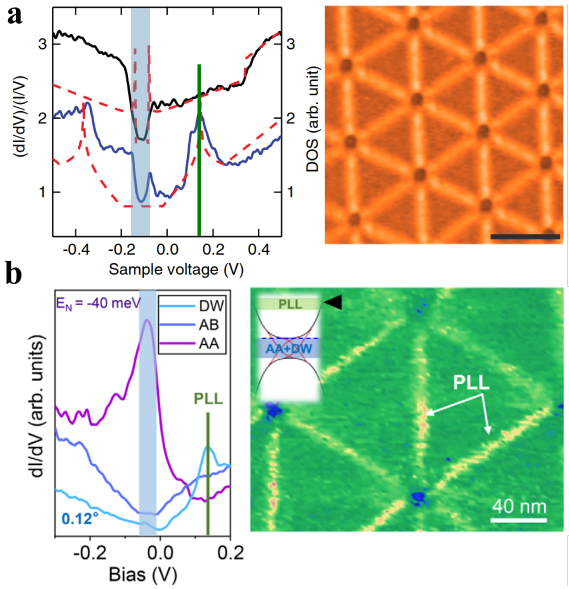

Figure 1.26: STM evidence of localized states at the domain walls outside of the gap. The gap is highlighted with grey region in the STS spectra (left) and a spatially resolved image (right) is taken at the energy of the peak highlighted with the green line. **a** Data from [88] showing peaks at $\pm 250meV$ around charge neutrality point. **b** Data from [89] showing a peak at $+130meV$.

sirable in the context of device fabrication, for example valley filters or valley valves using biased AB/BA domain walls can be imagined [95, 96].

Wright *et. al* [98] also noticed that edge states should appear in the case of a uniform $\boldsymbol{E}$ where the change in winding number comes from the mirror symmetry between AB and BA regions. The situation is thus equivalent to an edge state induced by gate polarity. Such a domain wall can be achieved by applying a differential strain to the layers, in the form of shear or uniaxial strain [99, 100], the former being similar to the DW arising during the relaxation of a minimally twisted system. In the work of P. San-Jose *et al.* [101], the authors argue that the formation of such AB/BA solitons in real devices may be at the origin of insulating / metallic switching of the global transport properties.

In the case of marginally twisted bilayers, helical edge states can organize into domain wall networks that can also be interesting for device fabrication [102]. Their early investigation revealed in-gap states with complex behavior [100], but in that case relaxation was not taken into account. A recent paper [103] including controlled relaxation shows that its effect significantly changes the spectrum close to charge neutrality in the marginal twist cases (typically $\theta_{int} < 0.5°$). In that case, upon the application of voltage, a significant amount of bands are gaped around charge neutrality, leaving a set of linearly dispersing channels in the gap localized into quasi-1D states along the DW, that are expected to experience little scattering. These calculation permit to approach an understanding of STM measurements. In addition, they also predict a whole family of dispersing channels that could arise in the system, which were not experimentally detected.

In STM experiments, localized states near the Domain Walls have also been detected at energies *outside* of the gap, as shown in Fig.

1.26.

Such features have been understood for the measurements of S. Huang *et al.* [88] in a continuum model picture [104], where the electronic properties are described locally, without the twist angle parameter. Because the stacking is modified at the DW, the local bands are modified with respect to the AB/BA stacking and feature two saddle points around charge neutrality, that are translated into vHs in the LDOS. This results points towards the importance of the local stacking on the electronic properties.

In the experiment by Q. Zheng *et al.* [89], there is only one peak in the DOS out of the gap, at positive energies. The authors interpret it in terms of pseudo-Landau levels (PLL), as predicted by A. Ramirez and J. Lado [105] for the unrelaxed marginally twisted bilayer in the presence of an electrical field, and as measured in marginally twisted bilayers near AA regions [106]. The absence of negative energy and second positive PLL is attributed to the local strain concentrated at the DW as induced by relaxation. Indeed, previous works predict strong electron hole assymmetry that can significantly reduce the PLLs [107, 108].

In both scenarios, the localized states in marginally twisted bilayers of graphene are sensitive to the precise relaxation.

1.6 Conclusion

A prolific amount of interesting physics arise in graphene bilayers, spanning from ordered states in TBLG to topological modes near domain walls of graphene bilayers. In TBLG, these physics are triggered by the high tunability of the system with the twist angle. But we have seen that this tunability also means that the system is highly sensitive to inhomogeneities. This sensitivity is evidenced by the sample to sample variability in transport experiments.

In the following chapter, we will thus focus on *heterostrain*, the relative strain between the layers, as a source of inhomogeneity in graphene bilayers. We will comment further on sample to sample variability even in STM/STS experiments and see that it can be explained by heterostrain in Chapter 3.

In the case of long wavelength moirés in graphene bilayers, we will see in Chapter 4 that biaxial heterostrain can also be a source of stacking reorganisations in the system.

With that in mind, but beyond the scope of this thesis, it would be useful to correlate inhomogeneities and electronic properties extracted from transport experiments, by combining them with imaging techniques such as STM/STS, pseudo force microscopy or SQUID on tip experiments. Another perpective is the experimental in situ tuning of strain in such systems, that will be the focus of Chapter 5.

2
Strain in graphene and its twisted bilayers

Contents

Graphene being a perfectly 2D material, it is tempting to study how it reacts to stress and to mechanical deformations. There is thus a large amount of studies on this matter, as well as some reviews [109].

Some early studies focused on studying its mechanical properties in particular through the suspended monolayer graphene [2, 110, 111]. The high stiffness and strength of graphene enables it to withstand strains up to 25% [2] which explains that it can bend, create ripples, or adapt to external factors without breaking such as surface inhomogeneities, AFM and STM scanning tip, external pressure, among others. This has interest to us, as strain affects the electronic properties of graphene. In this chapter, we will see that strain not only affects monolayer graphene, but also twisted bilayers graphene (TBLG) in a complex way.

2.1 Monolayer of graphene

2.1.1 Homogeneous in-plane strain Hamiltonian

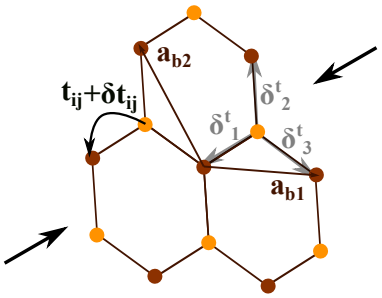

Figure 2.1: Sketch of a deformed bravais lattice.

Straining graphene implies changing the Carbon-Carbon lengths δ_i of its bravais lattice, as shown on Fig. 2.1. The induced change in the overlap of the orbitals modifies the nearest neighbor (NN) hopping parameters.

On first order the correction of the hopping parameter can be written : $t = t_0 + t_0 \frac{\partial t_0}{\partial a}$. In Fourier space, it translates into the distorsion of the graphene Brillouin zone. This change in C-C length can be position depend, in the case of inhomogeneous strain or when one takes relaxation into account for example. In the following we consider homogeneous static strain.

To describe this effect, we follow Ref. [9, 112, 113] in writing it as a correction on the Hamiltonian from equation 1.1. This correction includes the neighbor dependent change in the hopping parameters from atom i of sublattice a to atom j of sublattice b : δt^{ab}_{ij}.

$$H = t \sum_{<i,j>} c^+_{a,i} c_{b,j} + h.c. + \sum_{<i,j>} \delta t^{ab}_{ij} c^+_{a,i} c_{b,j} + h.c. \tag{2.1}$$

Adding the correction on the next-nearest neighbor hoppings (NNN) by going to higher orders in δt does not have dramatic impact on the physics (see [114]).

We know from section 1.1 that the first term yields in the low energy Dirac fermion dispersion $\hbar v_F \boldsymbol{\sigma} \cdot \boldsymbol{q}$. Developing in the same way the second term around the Dirac cone $\boldsymbol{K}_\xi$ gives the following matrix element with $\delta^t_{ij} = \delta^t_i$, $i = 1, 2, 3$ the deformed NN vector.

$$\begin{aligned} \delta f(\boldsymbol{K}_\xi + \boldsymbol{q}) &= - \sum_{i=1,2,3} \delta t_i e^{-i\boldsymbol{K}_\xi \cdot \delta^t_i} e^{-iq\delta^t_i} \\ &\simeq - \sum_{i=1,2,3} \delta t_i e^{-i\boldsymbol{K}_\xi \delta^t_i} \end{aligned} \tag{2.2}$$

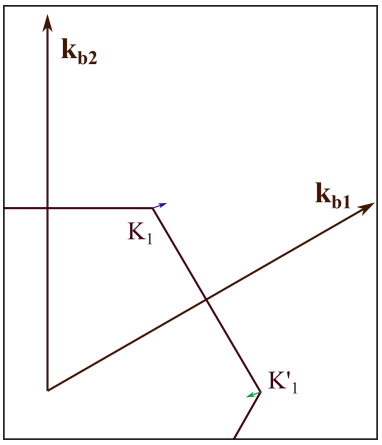

Figure 2.2: Sketch of a deformed monolayer graphene BZ. The blue and green arrows show the effect of the strain induced gauge field on the Dirac cones. They are shifted in opposite directions depending on their chirality. The strain induced distortion of the BZ is negligible with respect to the gauge field amplitude.

which can be written in the same way as for equation 1.6 :

$$\delta f(\boldsymbol{K}_\xi + \boldsymbol{q}) = - \underbrace{\sum_i \delta t_i cos(\boldsymbol{K}_\xi \delta^t_i)}_{e\hbar v_F A_x} + i \underbrace{\sum_i \delta t_i sin(\boldsymbol{K}_\xi \delta^t_i)}_{\xi e\hbar v_F A_y} \tag{2.3}$$

In matrix form, the correction to the 2*2 Hamiltonian is written:

$$\delta H^\xi = -\xi e\hbar v_F \begin{pmatrix} 0 & \xi A_x - iA_y \\ \xi A_x + iA_y & 0 \end{pmatrix} = -\xi e\hbar v_F \boldsymbol{A} \cdot \boldsymbol{\sigma} \tag{2.4}$$

So that in the low energy limit around Dirac cone K_ξ :

$$H^\xi = \hbar v_F (\boldsymbol{q} - \xi \boldsymbol{A}) \cdot \boldsymbol{\sigma} \tag{2.5}$$

This equation shows that strain not only distorts the graphene lattice but also introduces - as showed in Refs. [112, 113] - a Gauge Field to the Dirac-like Hamiltonian. This additional effect can be visualized in Fourier space as a chirality dependent shift of the Dirac cone as shown on Fig. 2.2. This field is written:

$$\begin{aligned} A(\boldsymbol{r}) &= \frac{1}{e\hbar v_F} \sum_i \delta t_i(\boldsymbol{r}) e^{-i\delta^t_i K_\xi} \\ &= A_x - i\xi A_y \end{aligned} \tag{2.6}$$

$$\boldsymbol{A} = (A_x, A_y) \tag{2.7}$$

The pseudovector $\boldsymbol{A}$ can be associated to the strain induced *pseudo-magnetic field* (PMF) as it mimics the effet of a magnetic field in shifting the wavevector in the Hamiltonian. For example, the Hamiltonian of a particle of charge e in a magnetic field of vector potential $\boldsymbol{A}$ writes $(\boldsymbol{q} - e\boldsymbol{A})^2$, by substituting $\boldsymbol{q} \rightarrow \boldsymbol{q} - e\boldsymbol{A}$. The same kind of substitution is also valid in the case of tightly bound electrons in a magnetic field, and is referred to as the *Peierls substitution*.

The low energy developement can be done around the Dirac cones of the distorted BZ $\boldsymbol{K}_\xi$ or of the undistorted BZ $\boldsymbol{K}'_\xi$. This choice has no impact on the pseudovector potential. However, the derived low energy Dirac equation is going to be affected by this choice and with it the calculations of physical quantities such as the Fermi velocity [115, 116].

A complete description of such effect of strain on monolayer graphene is given in Ref. [117].

The direction of the pseudovector induced shift depends on the chirality ξ of the Dirac cone. This is clear in the derivation of equation 2.5 but can also be viewed in terms of conservation of time reversal symmetry [9] : the unequivalent Dirac cones of graphene are linked through time reversal symmetry, which in practice means that an electron in a cone can go to the other one by keeping the same position while taking the opposite direction for its wavevector such that $\boldsymbol{r} \rightarrow \boldsymbol{r}$, $\boldsymbol{q} \rightarrow -\boldsymbol{q}$. Applying this transformation to the strained graphene Hamiltonian yields $(-\boldsymbol{q} - e\boldsymbol{A})^2$. This does not preserve the Hamiltonian unless the pseudovector potential $\boldsymbol{A}$ also changes sign when changing valley, giving another argument for the chiral dependency.

2.1.2 *Strain effect in monolayer graphene*

Early experiments have been able to detect significant effects of strain on the phonons of monolayer graphene [118, 119], encouraging both experimental and theoretical works to study whether the bands of graphene could be engineered by strain.

In particular, in the presence of uniaxial strain the hopping anisotropy creating pseudomagnetic field can in principle engineer the merging of two unequivalent Dirac cones. This produces a topological transition in which the topological winding number introduced in section 1.1 goes from ± 1 to 0 [120]. This topological transition has profound effects on the electronic properties as the system goes from semi-metallic to band insulating state [10, 121]. However, such a situation can only be reached with strains above 20% [121, 122] which makes it extremely challenging experimentally. According to Pereira *et al.* [121], it is the sign that the Dirac spectrum is indeed robust in the presence of small perturbations and thus confirms its "topologically protected" nature.

In [124], the authors show that a more realistic strain of about 10% can create a uniform $10T$ pseudomagnetic field if it is applied along graphene's cristallographic directions. This gave motivation to investigate pseudo-Landau level (pLL) quantization in the experiments. Levy *et al.* [123] showed for the first time that such pLL could be detected in STM experiments, by measuring the spatially varying LDOS on a graphene nanobubble (see Fig. 2.3). Zhu *et al.* [125] evidenced that an STM tip on suspended graphene can engineer strain that creates such pLL. STM measurements from Meng *et al.* [126], Bai *et al.* [107], Banerjee *et al.* [127], and S-Y. Li *et al.* [108] show they can also appear on a monolayer of graphene strained in the presence of ripples, and Jiang *et al.* [128] in the presence of engineered pillars.

Other physical properties can be engineered through strain, such as a local modifications of its Fermi velocity [129, 130] or at a device

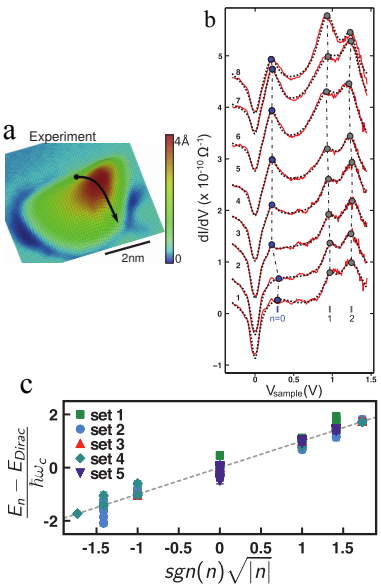

Figure 2.3: **a** STM image of a graphene nanobubble **b** STS spectra showing the LDOS featuring Landau levels whose positions in energy follow a typical $\sqrt{n}$ trend (**c**) with n the number of a given Landau level. Figure from [123].

scale its mobility and residual doping [131, 132, 133].

The experimental engineering of graphene electronic properties remains difficult despite years of experimental efforts because of the high strains it requires. We will see this strain engineering can be easier in the case of TBLG.

2.2 *Twisted Bilayers of graphene*

When considering the twisted bilayers of graphene, the parameter of the twist θ between the layers is quite important. In addition to twist, strain can also be taken into account, by regarding it as a relative deformation of one layer with respect to the other referred to as *heterostrain*, or considering simultaneous strain on both layers which is referred to as *homostrain* as introduced by Huder *et al.* [8].

In the following, we first consider *heterostrain*. Its effect can be complex and to understand it we focus on a low energy limit description. We will also use results from exact diagonalisation calculations of the Lanczos algorithm in which the effects of strain are intrinsically taken into account (see section 1.3.1).

These descriptions give insight on how heterostrain can engineer the flat bands of TBLG, which could have an impact on the strongly correlated electron physics.

2.2.1 *Geometrical effect of Heterostrain*

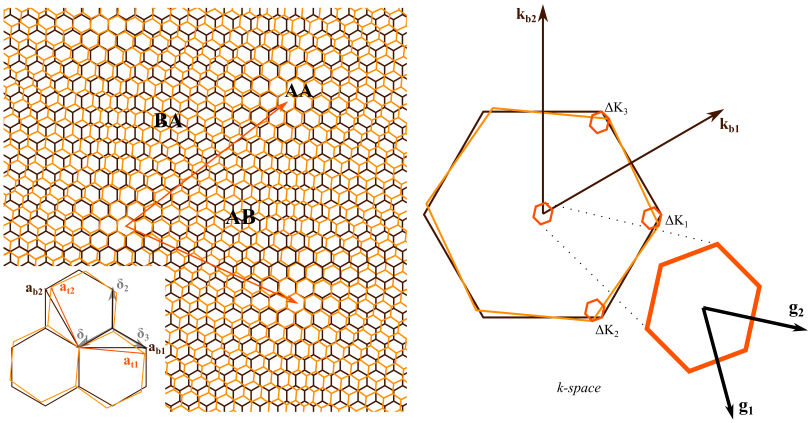

Figure 2.4: Real space (left) sketch of a twisted and heterostrained bilayer of graphene (TBLG), the inset showing both graphene periodicities. In reciprocal space (right) the moiré periodicity is referred to as g_1 and g_2, the generators of the moiré Brillouin zone (mBZ) whose side lengths ΔK_i $i = 1, 2, 3$ are different due to strain application.

In Fig. 2.4 a principle sketch of a TBLG containing heterostrain is shown, where the bottom (brown) layer is left unstrained, and the top (orange) layer is slightly deformed in addition to its rotation. It is clear that the top layer BZ is going to be deformed. This can be written as a modification of its BZ corners position $\boldsymbol{K}_i^d = \boldsymbol{K}_i + \delta\boldsymbol{K}_i$ for $i = 1, ..., 6$. The mBZ (dark orange) corresponding to the real periodicity of the 2 rotated layers system and defined from lengths $\boldsymbol{K}_i^d - \boldsymbol{K}_i^r = \Delta\boldsymbol{K}_i$, is thus distorted.

In this geometrical approach, one can predict the shape of the deformed moiré Brillouin Zone (mBZ). The size of the mBZ sides $\delta\boldsymbol{K}_i$

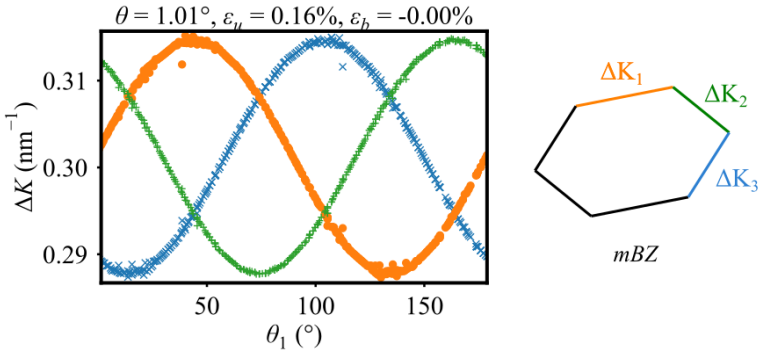

Figure 2.5: Geometric description of the mBZ periodicity length ΔK_i changes as a function of the direction of application θ_1 of a 0.16% uniaxial strain. As expected, we retrieve 60° periodicity. For illustrative purposes, on the sketch on the right was constructed by multiplying both interlayer angle and uniaxial heterostrain by a factor 10.

change as a function of the angle of application of uniaxial strain. This is shown on Fig. 2.5 for a heterostrain configuration corresponding to a 0.16% uniaxially strained layer, rotated by 1.01°.

If these geometrical considerations are important because they allow to define the Brillouin zone in the presence of heterostrain, it does not describe the distance between the two unequivalent Dirac points and thus fails to describe the vHs splitting [134, 135] that is given by the Dirac cone crossing energies as derived in Chapter 1 in the case of the unstrained system.

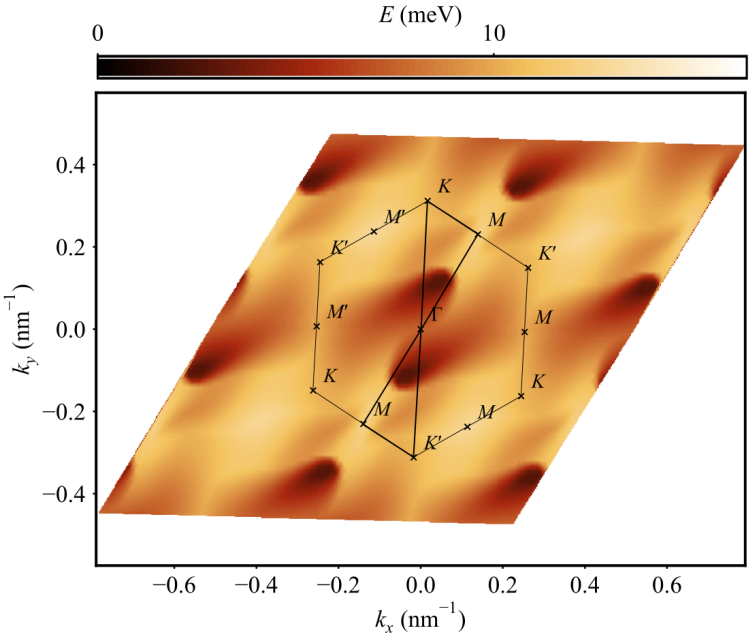

Figure 2.6: Calculation of the conduction flat band, for the heterostrain configuration : $\theta = 1.01°$, $\varepsilon_{uni} = +0.16\%$, $\varepsilon_{bi} = 0.0\%$, $\theta_1 = -\theta_s = 26°$. This configuration was chosen because it matches the experimental situation of Ref. [136]. The calculation is obtained by Lanczos algorithm. The minima in the band correspond to the *Dirac nodes* of the system that originate from each layers Dirac cones and are pushed away from the mBZ corners (visualized by K, K' marks) by heterostrain.

To illustrate that, Fig. 2.6 shows a calculation of the first conduction flat band of a $\theta = 1.1°$ twisted system for a heterostrain of 0.16% along the direction $\theta_s = -26°$. Following the geometrical effect, the mBZ length from Fig. 2.6 lengths match those calculated on 2.5 at $\theta_1 = 26°$: $\Delta \boldsymbol{K}_i \sim \{0.30, 0.31, 0.29\}\, nm^{-1}$. However, the two low en-

ergy regions inside the geometrically deformed BZ corresponding to the *Dirac nodes* are clearly not at the corners of the mBZ. They are shifted away in opposite directions depending on their chirality, effect that is reminiscent of a PMF effect as derived in section 2.1.1 for the monolayer, and this similarly finds its origin in the atomic length changes of the deformed layer.

Moreover, the Dirac nodes on Fig. 2.6 do not feature circular isoenergetic curves. This is explained by the Fermi velocity anisotropy [115, 116, 137] that arises when two directions are unequivalently stretched. A higher Fermi velocity is to be found in the direction of the stretch and thus the isoenergetic curves will result in an ellipse directed in the direction perpendicular to it [115].

2.2.2 *Heterostrain induced Pseudo Magnetic Field*

Due to the existence of the moiré periodicity, the PMF effect is, for a given strain, stronger for TBLG than for monolayer graphene. One can understand this in Fourier space : the pseudo-vector $\boldsymbol{A}$ does not depend on the system periodicity, which implies it is bigger in proportion to the periodicity of the system in TBLG than in the monolayer graphene . This is visualized on Fig. 2.7, where the ratio between pseudo-vector length and periodicity is clearly bigger than in the monolayer case in Fig. 2.2. One can also understand it in terms of flux of the pseudo magnetic field, as a given amount of strain creates a given "pseudo flux" in each graphene unit cell. For the TBLG case, the total flux in the moiré unit cell can be rather big because of the high number of graphene unit cells in the moiré period.

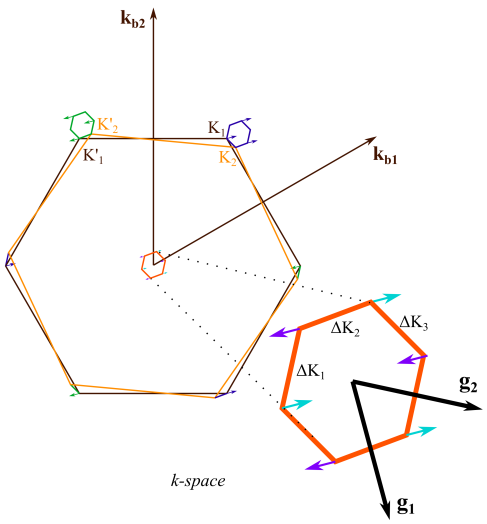

Figure 2.7: Sketch of the deformed (brown) and twisted undeformed (orange) graphene BZ, as well as the definition of the TBLG mBZ. Small arrows represent the pseudo-vector $\boldsymbol{A}$ of the deformed layer. The blue and the green mBZ are folded into the orange mBZ in the center. They are all the same up to a shift in k-space, showing that applying strain in one layer is the same than applying a balanced strain in the two graphene layers, in opposite directions.

This PMF effect makes the prediction of the vHs energy unintuitive, because it means that the saddle points are shifted in energy and away from *M* points.

In the following we derive the stacking dependent shift of the Dirac node and show it cannot actually describe the shift predicted

in the calculations.

Such derivation is interesting because the Dirac cones merging that is experimentally challenging in the case of monolayer graphene could in principle be achieved more easily in the case of TBLG. However, there is here a major difference. As argued in [138], the two Dirac points are coming from graphene Dirac points of the same valley, and thus K and K' have the same chirality and cannot pair-annihilate. From these topological considerations we can predict interesting effects on the bands when the Dirac cones are brought closer together.

From equation 2.6 we know the pseudo-vector depends on nearest neighbor (NN) hoppings t_i, $i = 1, 2, 3$. To express it, we write the change in NN carbon bond length δu_i, so that the NN hopping term writes :

$$\begin{aligned} t_i^{ab} &= t_0 + \delta t_i^{ab} \\ &= t_0 + \frac{\partial t^{ab}}{\partial a}\delta u_i \end{aligned} \tag{2.9}$$

In [117], the quantity $\frac{\partial t^{ab}}{\partial a}$ can be obtained by a Raman spectroscopy estimation [118] of the Grüneisen parameter $\beta = -\frac{\partial ln(t^{ab})}{\partial ln(a)} = \frac{\partial t^{ab}}{\partial a} \cdot \frac{a}{t^{ab}} \simeq 2$. In some continuum models, a higher value is however more commonly used by estimating $\beta \sim a_0/r_0 \sim 3.14$ [40] with r_0 the decay length of the hopping integral.

With the tight binding model parameters defined in section 1.3.1, we find that

$$\frac{\partial t}{\partial r}|_{a_0} = \gamma_0 q_\pi e^{q_\pi(1-\frac{r_{ij}}{a_0})}/a_0|_{a_0} \tag{2.8}$$

With $\gamma_0 = 3.7eV$ and $q_\pi = a_0 \cdot 2.218$Å, it leads to $\beta = 3.15$ which corresponds to the value used in the literature for continuum models.

This change in length can be written in terms of local effective lattice displacement $\boldsymbol{u(r)} = (u_x, u_y)$ as done in Refs. [9, 139] :

$$\begin{aligned} \delta u_i &= \frac{\boldsymbol{\delta}^{ab}}{a}(\boldsymbol{\delta}^{ab} \cdot \nabla)\boldsymbol{u(r)} \\ &= \frac{\boldsymbol{\delta}^{ab}}{a}(\boldsymbol{\delta}^{ab} - \boldsymbol{\delta}_i^t) \end{aligned} \tag{2.10}$$

With $\boldsymbol{\delta_i^t}$ the three unequivalent strained NN vectors. One can thus find that the gauge field $\boldsymbol{A}_{j,\xi}$ ($j = 1, 2, 3$) in the low energy limit around $K_{j,\xi}$ is :

$$A_{j,\xi} = \frac{2\pi}{\hbar v_F}\frac{\partial t^{ab}}{\partial a}\sum_{i=1,2,3}\frac{\boldsymbol{\delta}^{ab}}{a}(\boldsymbol{\delta}^{ab} - \boldsymbol{\delta}_i^t)e^{-i\boldsymbol{\delta}_i^t K_{j,\xi}} = A_x + i\xi A_y \tag{2.11}$$

Using equation 2.11 and the model parameters $v_F = t_0^{(ab)} a_0 3/2\hbar = 1.1 \cdot 10^6$ m.s^{-1}, the $A_{j,\xi}$ vectors can be calculated and the Dirac node separation in k space DK can be determined for any heterostrain configuration. Such a heterostrain configuration can be defined by four parameters as developped in section 2.3.1 : the interlayer angle θ, the uniaxial strain ε_{uni} and biaxial strain ε_{bi} and the angle of application of uniaxial strain θ_s.

Fig. 2.8 shows the evolution DK as a function of uniaxial strain amplitude and direction of application, with fixed twist angle $\theta = 1.1^\circ$ and biaxial strain $\varepsilon_{bi} = 0\%$. The shift of the Dirac cone due to $\boldsymbol{A}$ is comparable to that of the shift due to the geometrical effect for uniaxial strains above 2%. This confirms that in the TBLG system, a Dirac Cone merging could be much easier to achieve than in the monolayer graphene (above $\sim 20\%$!). However, a closer look at Fig. 2.8 shows that the condition $DK \to 0$ is never reached. The lowest DK in the deformed mBZ is shown on the lower right sketch of Fig. 2.8.

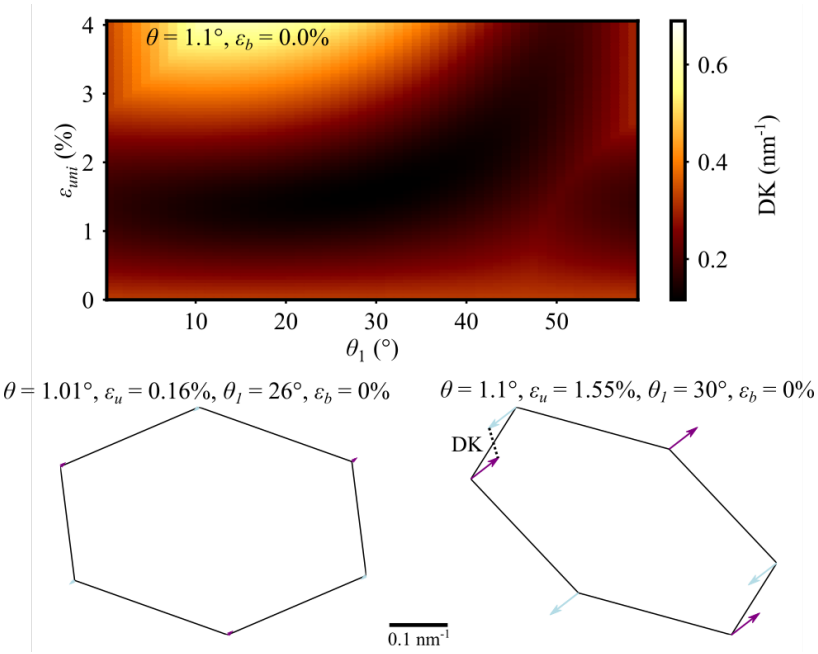

Figure 2.8: **Top :** Colormap of the distance between the Dirac nodes as a function of uniaxial strain amplitude (y-axis) and direction of application (x-axis). Interlayer angle and biaxial strain are fixed : $\theta = 1.1°$, $\varepsilon_{bi} = 0.0\%$. **Bottom :** k-space representation of the deformed mBZ with arrows representing the chiral gauge field A_ξ, for two different heterostrain configurations : The left one corresponds to the configuration of Fig. 2.6, and the right has the lowest Dirac node separation DK in this parameters range.

Comparing our prediction of the Dirac node position given on the lower left sketch of Fig. 2.8 with the Lanczos algorithm calculation shown on Fig. 2.6, a clear discrepancy is found. For the same heterostrain configuration, with $\varepsilon_{uni} = 0.16\%$, the pseudo-vector shift is 10 times smaller than the geometrical effect shift, and the predicted Dirac node separation is different in amplitude and direction.

This discrepancy does not mean that we cannot rely on low energy limit approximation. In fact, it rather comes from us neglecting the effect of the interplay between strain and the moiré modulation, which we discuss now.

2.2.3 *Heterostrain PMF combined with the moiré*

Continuum calculations including heterostrain [38, 140] rely on the low energy limit and are in agreement with Lanczos algorithm calculations as will be shown in Chapter 3. This agreement comes from the fact that an additional effect of strain is taken into account in the off-diagonal term of the Hamiltonian 1.15 as $H_\perp$ depends on the distorted moiré vectors $\boldsymbol{g}_i = M_{strain}^T \cdot \boldsymbol{g}_i^{undistorted}$.

In particular, Fig. 2.9 shows a very rapid shift of Dirac nodes away from K points when a very small amount of strain is applied, and then a slow shift when strain is varied to higher values.

This reminds of the effect of a brutal transition that could be attributed to a symmetry breaking as investigated in Ref. [141], in the present case the C_3 symmetry. Such sensitivity in Dirac node position is also observed for TBLG where C_3 symmetry is broken by an in-plane magnetic field [142].

This shift can be estimated analytically by writting the Hamiltonian in the lowest band by including both the interlayer modulation

The dependance of $H_\perp$ on $\boldsymbol{g}_i$ was described in equation 1.16:

$$H_\perp = \sum_{k=0,\boldsymbol{g_1},\boldsymbol{g_2}} e^{i\boldsymbol{k}\cdot\boldsymbol{r}} \begin{pmatrix} u_1 & u_2 \\ u_2 & u_1 \end{pmatrix} \quad (2.12)$$

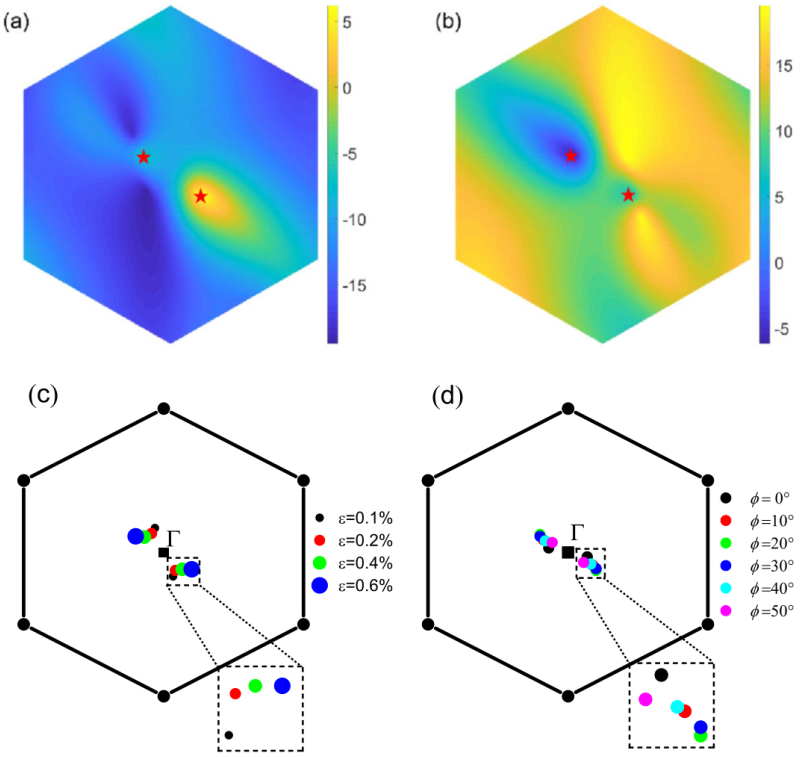

Figure 2.9: Continuum calculations of the valence **(a)** and conduction **(b)** flat bands of a relaxed TBL graphene system with $\theta = 1.05°$, $\varepsilon_{uni} = 0.6\%$, $\theta_1 = 30°$. Stars show the position of the Dirac nodes. Their positions are also plotted as a function of strain magnitude **(c)** and direction of application **(d)**. The distorted mBZs have been deformed to match an hexagon and ease comparison. Figure from [140].

and the intralayer Dirac Hamiltonian. Using calculations similar to the model of Ref. [36], Ohad Antebi *et al.* [147] showed that, in the low energy and low strain limit, the Dirac node displacement can be written :

Such derivation including all the physics are done in Refs. [143, 144, 145, 146]

$$\delta \boldsymbol{K}_i = \frac{3w^2}{1-3w^2}\left(1 + \frac{u^2}{w^2}\frac{|\boldsymbol{K}_i|a_0}{\beta}\right)\boldsymbol{A}_i \tag{2.13}$$

Where the dimentionless tunneling parameters are $w = \frac{u_1}{\hbar v_F |\boldsymbol{K}_i| \theta_{int}}$ and $u = \frac{u_2}{\hbar v_F |\boldsymbol{K}_i| \theta_{int}}$, which are equal in the abscence of corrugation because $u_1 = u_2$. In this equation, the term in the parenthesis is close to 1 for low angles. However, the prefactor in front of the parenthesis can be quite big, in particular close to the magic angle. As an example, for typical parameters ($w = \frac{0.11eV}{\hbar v_F 0.3nm^{-1} 0.9°} = 0.32$) we find a prefactor higher than 20. This supports the high sensitivity of the position of the Dirac nodes even with small amounts of strain.

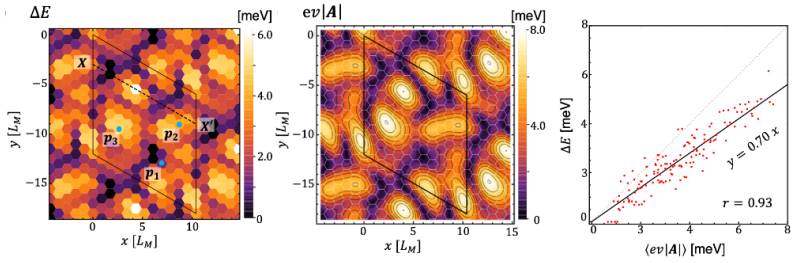

Figure 2.10: Calculations from Ref. [144] showing a colormap in real space of ΔE the spacing energy between the peaks in the DOS **(left)** and of $\hbar v_F |\boldsymbol{A}|$ the amplitude of the pseudo gauge field **(middle)**. The **right** panel shows that these two values averaged over the moiré unit cell are correlated, heterostrain controlling almost exclusively the spacing energy.

The strong sensitivity of the position of the Dirac cones on strain means that the electronic properties will also strongly depend on the strain, as we will find in Chapter 3. The work of N. Nakatsuji [144] shows that the distance between the high DOS peaks is proportional to the pseudo-vector $\boldsymbol{A}$, in agreement with the low energy analytical equation 2.13. These calculations also support a local description of the flat bands of TBLGs.

2.2.4 *Homostrain*

In contrast to heterostrain, homostrain consists in applying the same strain to both layers. In [8], it was found that its effect is much less critical than for heterostrain.

This is due to a cancellation of the relative pseudomagnetic field from both layers. The dramatic shift in the Dirac nodes is proportional to the difference between the pseudo-vectors [147] :

$\delta \boldsymbol{K}_i \propto \boldsymbol{A}_i = \boldsymbol{A}_i^{l=2} - \boldsymbol{A}_i^{l=1}$

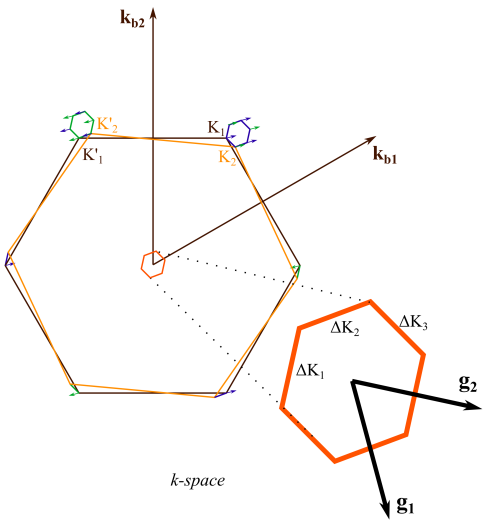

Figure 2.11: Sketch of the effect of homostrain in the mBZ. The strain in one layer shifts the Dirac nodes in one direction (green vectors), and the strain in the other layers shifts the Dirac nodes of opposite chirality in the same direction. The blue and the green mBZ are folded into the orange mBZ in the center. They are all the same up to a shift in k-space, showing that in terms of PMF, applying a similar strain to both layer is the same as applying no strain.

This can also be sketched in the mBZ as shown on Fig. 2.11 : the deformation of the first layer shifts a Dirac node in one direction, while the other layer deformation shifts the other Dirac nodes in that same direction. As a result, the positions of the Dirac nodes in the mBZ is equivalent to their positions in an unstrained mBZ.

As a consequence, only the geometrical deformation of the mBZ in the case of homostrain has an effect on the electronic properties of TBLG and it requires higher amounts of strain to affect the bands significantly.

2.3 *Heterostrain effect in low angle TBLG*

Analytical and low energy approximations give us a lot of information on the effect of strain, in particular we know that we should focus on heterostrain and that small strains are already interesting to

study.

To go beyond the low energy limit, we collaborate with the theory group of G. Trambly de Laissardière, in order to investigate how the flat bands of TBLG are affected by heterostrain. We use calculations relying on an exact diagonalization method as introduced in section 1.3.1 and performed by A. Missaoui and G. Trambly de Laissardière.

In order to perform such calculations, we provide them with moiré unit cells containing all atomic positions. The challenge is thus to produce cells that are periodic while containing a controlled heterostrain. This is done with the method we describe now.

2.3.1 *Commensurate periodic cells with arbitrary heterostrain for tight-binding calculations*

Definition of commensurability

In the simpler case of unstrained TBLG moiré pattern, the periodization of the moiré unit cell can be obtained in the commensurate case. It happens if the rotation can be characterized by two integers (m, n), that define the moire periodicity $\boldsymbol{a}_{mi}$ with respect to the graphene peridicity : $\boldsymbol{a}_{mi} = m\boldsymbol{a}_{b1} + n\boldsymbol{a}_{b2}$ [34, 148]. This condition is realized at a few intergers (m, n) only, if one considers the simple solution in which the unit cell contains only one AA region (or *beating*).

This condition is also called *first order commensurability* as it implies that $m - n = 1$ and can be realeased if one considers that two (or more) neighboring beatings can be unequivalent. This yields a whole family of unit cells containing various numbers of beatings as shown in the work of Artaud *et al.* [149] (see on the sketch in the margin).

This means that one can model almost any angle for a couple (m, n). The price to pay, as shown on Fig. 2.12, is the increased number of atoms in the given unit cell for angles where no low order cell (N small) can be found. As the calculations can be costly in time, it is interesting to notice that the physics lie mainly in the $N = 1$ cell. In other words, a given angle can be satifyingly decribed by the closest first order approximant. In Ref. [8], the commensurate cell was thus reduced from order $N = 3$ to its first order approximant without significant impact on the electronic properties. An intuition of this can be found in Fig. 2.12 where an increasing density of first order cells per twist angle unit is found below 10°, the range of angles where the electronic properties are mosly affected by the twist.

Even if the stacking does not consist in a pure rotation, one can always find a commensurate approximant close enough to any given stacking. In the following we describe a method that can be used to find such commensurate approximant in the most general case of the stacking of two layers that include relative strain and twist.

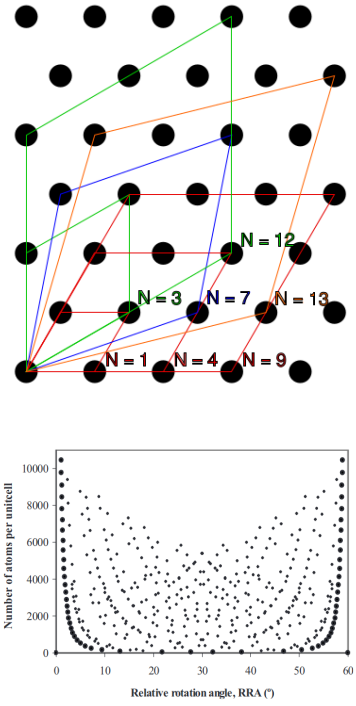

Figure 2.12: Number of atoms in a commensurate moiré unit cell with respect to the twist between the layers. There is a discrete number of first order cells, which are shown in bold dots. From [148].

General description for strain

A given stacking arrangement including heterostrain and interlayer twist can be written as a link between an unstrained bottom layer - of unitary vectors in the orthonormal basis $(\boldsymbol{a_{b_1}}, \boldsymbol{a_{b_2}})$ - and a twisted-strained top layer - of unitary vectors $(\boldsymbol{a_{t_1}}, \boldsymbol{a_{t_2}})$:

$$\begin{pmatrix} \boldsymbol{a_{t_1}} \\ \boldsymbol{a_{t_2}} \end{pmatrix} = R(\theta_2)M(p_{an})R(\theta_1)M(p_{iso}) \begin{pmatrix} \boldsymbol{a_{b_1}} \\ \boldsymbol{a_{b_2}} \end{pmatrix} \tag{2.14}$$

With $R(\theta) = \begin{pmatrix} cos\theta & sin\theta \\ -sin\theta & cos\theta \end{pmatrix}$ a rotation, $M(p_{an}) = \begin{pmatrix} p_{an} & 0 \\ 0 & 1 \end{pmatrix}$ a uniaxial deformation and $M(p_{iso}) = \begin{pmatrix} p_{iso} & 0 \\ 0 & p_{iso} \end{pmatrix}$ a biaxial deformation. These parameters are related to uniaxial ε_{uni} and biaxial ε_{uni} heterostrain levels that can be extracted experimentally. In that framework, the direction of application of strain is $\theta_s = -\theta_1$.

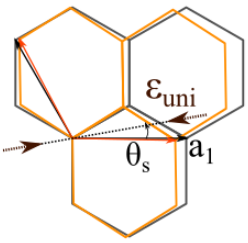

Figure 2.13: Definition of the angle of application of uniaxial strain θ_s with respect to the graphene axis.

This description can be simplified by performing a simple matrix multiplication that yields the *Park Madden* matrix as introduced by A. Artaud *et al.* [149].

$$\begin{pmatrix} \boldsymbol{a_{t_1}} \\ \boldsymbol{a_{t_2}} \end{pmatrix} = \begin{pmatrix} a & b \\ c & d \end{pmatrix} \begin{pmatrix} \boldsymbol{a_{b_1}} \\ \boldsymbol{a_{b_2}} \end{pmatrix} \tag{2.15}$$

Construction of the park madden matrix

In practice, the Park Madden matrix is determined starting from the first layer graphene vectors written in the orthonormal basis : $\boldsymbol{a}_{b1} = (1, 0)$ and $\boldsymbol{a}_{b2} = (-1/2, \sqrt{3}/2)$.

The second layer is then constructed with chosen heterostrain parameters.

$$\begin{pmatrix} a_{t_i,x} \\ a_{t_i,y} \end{pmatrix} = \begin{pmatrix} cos\theta_2 & sin\theta_2 \\ -sin\theta_2 & cos\theta_2 \end{pmatrix} \begin{pmatrix} p_{an} & 0 \\ 0 & 1 \end{pmatrix} \begin{pmatrix} cos\theta_1 & sin\theta_1 \\ -sin\theta_1 & cos\theta_1 \end{pmatrix} \begin{pmatrix} p_{iso} & 0 \\ 0 & p_{iso} \end{pmatrix} \begin{pmatrix} a_{b_i,x} \\ a_{b_i,y} \end{pmatrix} \tag{2.16}$$

Equation 2.16 is equivalent to equation 2.14 which is written in matrix form.

The Park Madden matrix parameters (a, b, c, d) are determined from the input $(p_{iso}, p_{an}, \theta_1, \theta_2)$ parameters identifying Eq. 2.14 and Eq. 2.15 .

In practice, it is easier to work in the hexagonal basis where $\boldsymbol{a}_{b_1,hex} = (1, 0)$ and $\boldsymbol{a}_{b_2,hex} = (0, 1)$, and to replace $\boldsymbol{a}_{b_i,\perp}$ by $\boldsymbol{a}_{b_i,hex}$ in equation 2.16 :

$$\begin{pmatrix} a_{t_1,1} \\ a_{t_1,2} \end{pmatrix}_{hex} = P^{-1} \begin{pmatrix} a_{t_1,x} \\ a_{t_1,y} \end{pmatrix} = \begin{pmatrix} a \\ b \end{pmatrix} \tag{2.17}$$

$$\begin{pmatrix} a_{t_2,1} \\ a_{t_2,2} \end{pmatrix}_{hex} = P^{-1} \begin{pmatrix} a_{t_2,x} \\ a_{t_2,y} \end{pmatrix} = \begin{pmatrix} c \\ d \end{pmatrix} \tag{2.18}$$

with P the matrix that links hexagonal and orthonormal basis :

$$P = \begin{pmatrix} 1 & -\frac{1}{2} \\ 0 & \frac{\sqrt{3}}{2} \end{pmatrix} \tag{2.19}$$

Finding the commensurate approximant

Commensurability requires that we find integers relating the graphene (top and bottom) periodicity and the moiré periodicity.

On first order, the moiré unit vectors can be written $\boldsymbol{k_{m_i}} = \boldsymbol{k_{t_i}} - \boldsymbol{k_{b_i}}$ which can be devellopped using 2.15:

$$\begin{aligned}\begin{pmatrix}\boldsymbol{k_{m_1}}\\ \boldsymbol{k_{m_2}}\end{pmatrix} &= \begin{pmatrix}\boldsymbol{k_{t_1}}\\ \boldsymbol{k_{t_2}}\end{pmatrix} - \begin{pmatrix}\boldsymbol{k_{b_1}}\\ \boldsymbol{k_{b_2}}\end{pmatrix}\\ &= \left(\begin{pmatrix}1 & 0\\ 0 & 1\end{pmatrix} - \begin{pmatrix}a & c\\ b & d\end{pmatrix}\right)\begin{pmatrix}\boldsymbol{k_{t_1}}\\ \boldsymbol{k_{t_2}}\end{pmatrix}\\ &= \begin{pmatrix}1-a & -c\\ -b & 1-d\end{pmatrix}\begin{pmatrix}\boldsymbol{k_{t_1}}\\ \boldsymbol{k_{t_2}}\end{pmatrix}\end{aligned} \tag{2.20}$$

Which yields in real space :

$$\begin{pmatrix}\boldsymbol{a_{t_1}}\\ \boldsymbol{a_{t_2}}\end{pmatrix} = \begin{pmatrix}1-a & -b\\ -c & 1-d\end{pmatrix}\begin{pmatrix}\boldsymbol{a_{m_1}}\\ \boldsymbol{a_{m_2}}\end{pmatrix} \tag{2.21}$$

And thus :

$$\begin{pmatrix}\boldsymbol{a_{m_1}}\\ \boldsymbol{a_{m_2}}\end{pmatrix} = \frac{1}{(1-a)(1-d)-bc}\begin{pmatrix}1-d & b\\ c & 1-a\end{pmatrix}\begin{pmatrix}\boldsymbol{a_{t_1}}\\ \boldsymbol{a_{t_2}}\end{pmatrix} \tag{2.22}$$

The commensurability is forced by rounding the coefficients of the matrix to the nearest integer i, j, k, l, that is:

$$i = round\left(\frac{1-d}{(1-a)(1-d)-bc}\right) \tag{2.23}$$

$$j = round\left(\frac{b}{(1-a)(1-d)-bc}\right) \tag{2.24}$$

$$k = round\left(\frac{c}{(1-a)(1-d)-bc}\right) \tag{2.25}$$

$$l = round\left(\frac{1-a}{(1-a)(1-d)-bc}\right) \tag{2.26}$$

Enabling us to relate top graphene and moiré periodicities with integers.

$$\begin{pmatrix}\boldsymbol{a_{m_1}}\\ \boldsymbol{a_{m_2}}\end{pmatrix} = \begin{pmatrix}i & j\\ k & l\end{pmatrix}\begin{pmatrix}\boldsymbol{a_{t_1}}\\ \boldsymbol{a_{t_2}}\end{pmatrix} \tag{2.27}$$

We also express the relation between the moiré and the bottom layer as

$$\begin{pmatrix}\boldsymbol{a_{m_1}}\\ \boldsymbol{a_{m_2}}\end{pmatrix} = \begin{pmatrix}i & j\\ k & l\end{pmatrix}\begin{pmatrix}\boldsymbol{a_{t_1}}\\ \boldsymbol{a_{t_2}}\end{pmatrix} = \begin{pmatrix}ia+jc & ib+jd\\ ka+lc & bk+ld\end{pmatrix}\begin{pmatrix}\boldsymbol{a_{b_1}}\\ \boldsymbol{a_{b_2}}\end{pmatrix} \tag{2.28}$$

from which we force commensurability by rounding the coefficients of the matrix to the nearest integers m, n, q, r as:

$$m = round\,(ia + jc) \tag{2.29}$$

$$n = round\,(ib + jd) \tag{2.30}$$

$$q = round\,(ka + lc) \tag{2.31}$$

$$r = round\,(bk + ld) \tag{2.32}$$

Relating the bottom graphene and moiré periodicities :

$$\begin{pmatrix} \boldsymbol{a_{m_1}} \\ \boldsymbol{a_{m_2}} \end{pmatrix} = \begin{pmatrix} m & n \\ q & r \end{pmatrix} \begin{pmatrix} \boldsymbol{a_{b_1}} \\ \boldsymbol{a_{b_2}} \end{pmatrix} \tag{2.33}$$

The multiplet (i, j, k, l, m, n, q, r) defines a commensurate unit cell with a relative arrangement between the layers close to the one defined by the inputs.

When doing $N\boldsymbol{k_m} = \boldsymbol{k_{t1}} - \boldsymbol{k_{b1}}$, we make the assumption that the moiré periodicity is aligned with the moiré beating. However, as noted by A. Artaud *et al.* [149], this is not always the case. It means that we will sometimes overestimate the minimum cell size required to describe adequately a given stacking configuration.

Order of commensurability

One has to check if the heterostrain parameters of the newly created commensurate cell (refered to as *produced* parameters) match the ones from the input (referred to as *init* parameters). The determination of the heterostrain parameters ($\varepsilon_{uni} = p_{an} - 1$, $\varepsilon_{bi} = p_{iso} - 1$, $\theta_1 = -\theta_s$, $\theta = \theta_{int} = \theta_1 - \theta_2$) is done as described in [149] by identification of the matrixes from equation 2.14 and equation 2.15. If the approximation is found to be too crude, a refined description of the system can be calculated by considering the Nth order cell.

$$N\boldsymbol{k_{m_i}} = \boldsymbol{k_{t_i}} - \boldsymbol{k_{b_i}} \tag{2.34}$$

We achieve the desired level of approximation when N is such that the values of heterostrain matches the one imposed in the initial Park Madden matrix within a given precision.

Fig 2.14 illustrates the process for the determination of the unit cell. It displays the values of the produced cell parameters as a function of the initial angle of application of uniaxial strain, all other parameters being fixed.

The figure shows that some configurations require a unit cell of order 10 to match the correct precision while for others the $N = 1$ approximation is already good. Because they are commensurate, these unit cells are fit to perform calculations in which periodic boundary conditions are necessary.

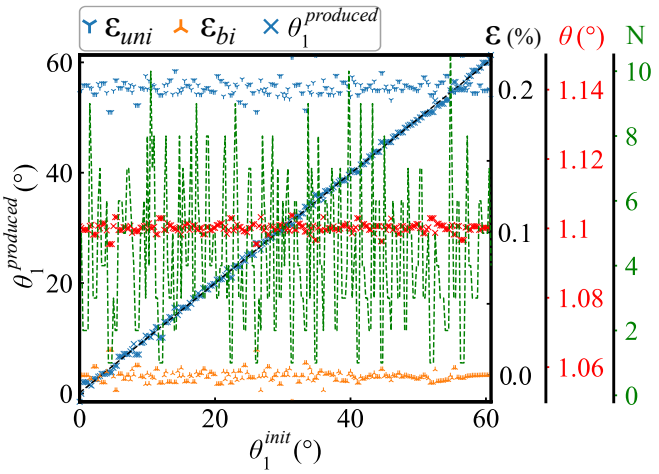

Figure 2.14: Commensurate approximation of moiré unit cells used for the calculation with their final corresponding heterostrain parameters (ε_{uni}, ε_{bi}, $\theta_1^{produced}$, θ) ; for a given target stacking arrangement with various angle of application $\theta_s = -\theta_1^{init}$ of uniaxial heterostrain. The target uniaxial heterostrain is $\varepsilon_{uni} = 0.2\%$ and biaxial heterostrain $\varepsilon_{bi} = 0.0\%$. The interlayer rotation is $\theta_{int} = 1.1°$. The dashed green line shows the order of the unit cell needed to produce each configuration within a given precision.

Fig 2.14 was produced with a precision on the strain $|\varepsilon_{uni}^{init} - \varepsilon_{uni}^{produced}| < 2.10^{-4}$, $|\varepsilon_{bi}^{init} - \varepsilon_{bi}^{produced}| < 3,5.10^{-4}$. Of course, the better the precision the larger the produced commensurate cell which imposes a trade off between the precision and calculation time.

With the moiré unit cells produced as decribed above, the computation of the LDOS can be done relying on the tight binding model and Lanczos algorithm as devellopped by Guy Trambly de Laissardière *et al.* [34] and described in section 1.3.1.

In the paragraphs below is presented our investigation of the effect of the different parameters of heterostrain on the electronic properties of TBLG near the magic angle, starting with the effect of the angle of application of strain.

2.3.2 *Effect of the angle of application of strain on the flat bands of TBLGs*

Fig. 2.15 shows a colormap of the LDOS for various stacking configurations. For each angle of application θ_s of a 0.4% uniaxial strain on a 1.1°twisted TBLG, a commensurate unit cell was produced and the LDOS calculated.

As expected from the C3 symmetry of unstrained graphene layers, the LDOS is 60° periodic in θ_s. Moreover, the spacing of the van Hove singularities (vHs) as measured from the separation between the outermost peaks, does not vary with θ_s, a finding also supported by Fig. 2.17 for different strain magnitudes.

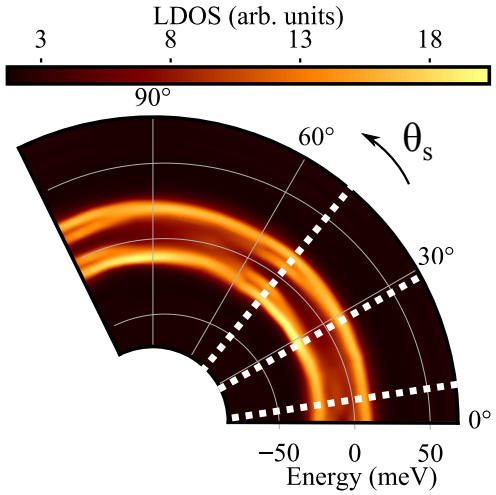

Figure 2.15: **a** Calculated local density of states in AA regions for a 0.4 % uniaxial heterostrain applied along varying direction θ_s. The white dotted lines indicate three typical behaviours of the LDOS.

Instead, the angle of application controls continuously the splitting of the peaks, featuring three main behaviours. Near 10°, the LDOS features a zero energy peak that was first observed by L. Huder *et al.* [8] and was later observed in other works [106, 150]. Near 30°, the LDOS is the simplest : it features the regular two peaks correponding to the vHs that have been observed very often since their first detection [33]. Near 50°, the LDOS features a splitting of both peaks that, to our knowledge, hasn't been reported experimentally yet.

These behaviours are stable when varying the amplitude of strain, as shown in Fig. 2.16.

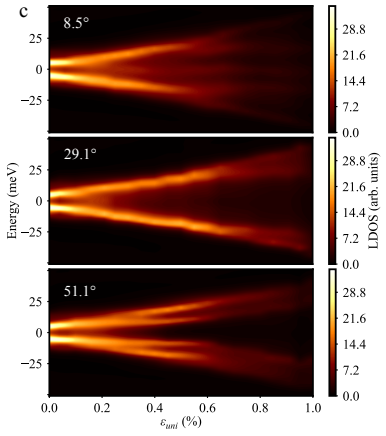

Figure 2.16: Tight-binding prediction for the local density of states in AA regions as function of energy and for increasing uniaxial heterostrain. The variations are plotted for three different angles θ_s of application of heterostrain that define the principal bahaviours of the LDOS. These typical angles are highlighted with white dotted lines on Fig. 2.15 .

2.3.3 *Effect of the amplitude of strain on the flat bands of TBLGs*

Upon an increase of the uniaxial heterostrain amplitude, the van Hove singularities separate linearly for all angle θ_s of application of heterostrain (Fig. 2.16), in agreement with calculations of the continuum model [38, 140, 144]. For strains below 0.1%, the system remains in a state close to the purely twisted system, with only two vHs close to one another. It continuously evolves towards the three different behaviours decribed above, which are completely formed around 0.4% of strain and makes them easier to spot.

For higher strains, starting between 0.6% and 0.7%, the description in terms of vHs peaks starts to collapse. Indeed, the bandwidth increases with strain and starts to destroy the saddle points. This effects comes along with a smoothing of the energy localization, but not of the spatial localisation of the DOS in AA zones, even at strains as high as 1%. This is confirmed by the work of H. Shi *et al.* [106], in which a TBLG with 0.78% of strain was measured in STM/S, showing a lowering in energy localization, but a remaining spatial localisation in AA regions

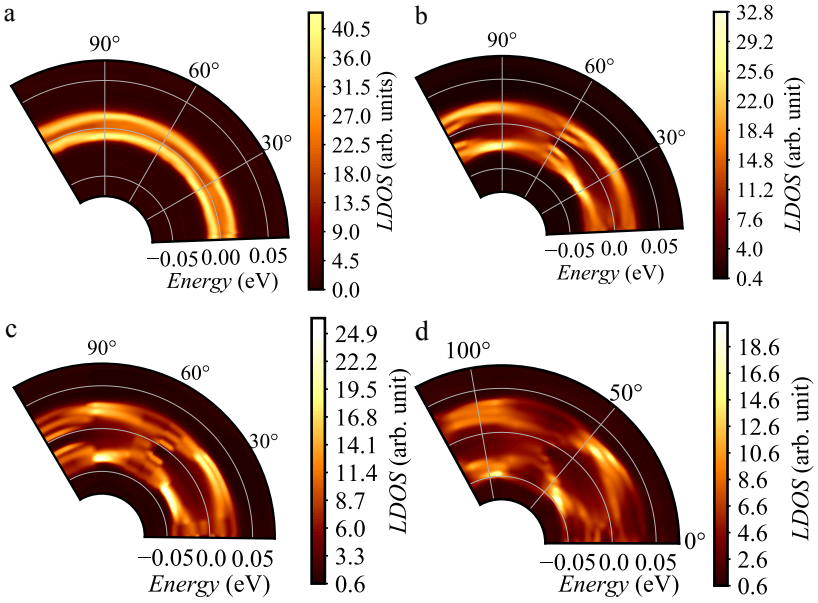

Figure 2.17: Calculated effect of heterostrain on the LDOS in AA region of twisted graphene bilayers. Color maps of the LDOS of TBLG as a function of the angle of application of uniaxial heterostrain, for zero biaxial heterostrain and for a twist angle of 1.1°. For each figure, the uniaxial strain ε_{uni} is fixed at 0.2% in **a**, 0.6% in **b**, 0.8% in **c**, 1% in **d**.

2.4 *Conclusion*

Strain affects the electronic properties of monolayer graphene. It can induce pseudo-Landau levels, changes in Fermi velocity, modifications of mobility and doping. Although interesting physics can be probed, this remains an experimental challenge due to the relatively high strains that have to be applied to reach significant effect (typically $\sim 20\%$).

In that aspect, TBLG can be very interesting because strains as small as 0.1% can affect the electronic properties. This is due to the

combined effect of strain induced geometrical changes in the BZ, pseudo magnetic field, and moiré periodicity. The breaking of $C3$ symmetry is at the root of such a deep effect, similarly to the case of in-plane magnetic fields. Heterostrain, the relative strain between the layers, is the relevant parameter to consider as opposed to homostrain where an equal strain is applied to both layers.

Heterostrain tunes the flat bands of TBLG by increasing linearly their bandwidth. This finding will be confirmed by analysis of STM measurements in Chapter 3. The direction of application of strain with respect to the cristallographic directions of TBLG is also an important parameter to explain some features in the LDOS.

Such low values of strain that are relevant in the case of TBLG induce very small changes in the position of atoms. One could wonder about the difficulty of experimentally detecting such small atomic displacements. Fortunately, we will see in Chapter 3 that the moiré acts as a magnifying glass for heterostrain, which enables to accurately deduce strain values in the system measured by STM. Additionally, such strain values are easily reached in typical straining setups, as will be further shown in Chapter 5, opening perspectives to probe these physics *in situ*.

3
Imaging native strain in TBLG with STM

Contents

In this Chapter, we investigate experimentally the strain dependent electronic properties of twisted bilayers of graphene. We use a Scanning Tunneling Microscope (STM) which allows to access both structural and electronic properties. We will first explain its working principle. Then, how it can be used to quantify local relative strain between TBLG. Finally, we will take advantage of STM versatility by combining this strain study with an analysis of its impact on the electronic properties of the system.

3.1 Scanning Tunneling Microscopy technique at 4K

Scanning Tunneling Microscopy is a technique that was developed in the early 1980s by G. Binning and H. Röhrer [151] for which they received the Nobel prize in 1986. Their instrumental development was made in the context of the search towards vacuum tunneling, that was meant to be used for local spectroscopy measurement. But what made a difference was they realizing that this technique would also enable to perform scanning with atomic resolution [152]. This makes the strength and interest of this technique that is now commonly used to combine topographic (Scanning Tunneling Microcopy) and spectroscopic (Scanning Tunneling Spectroscopy) information of surfaces.

3.1.1 Tunneling through vacuum

STM technique relies on the quantum tunneling of charge carriers between a conducting tip and a conducting surface that creates a tunneling current when these are separated in energy by the bias V_b. The tunneling through vacuum between these conductors happens if the wavefunctions of their electrons are overlapping, which occurs for distances of few angstroms. The probability of quantum tunneling and thus the current decays exponentially with the tip height z : $I_t(z) \propto e^{-kz} = T(V_b, z)$. Where k is the decay of the wave function of the electron $k = \sqrt{\frac{2m\Phi}{\hbar^2}}$ and depends on the materials through their effective work function (or mean barrier height) $\Phi = \frac{\Phi_s - \Phi_t + eV_b}{2}$.

A variation of height of 1Åresults in a one order of magnitude transmission probability (for a barrier height of $4eV$), which explains how precise subnanometer determination of tip height can be achieved with STM technique.

The tunneling current not only varies with height but also with the local density of states (LDOS) of the tip ρ_t and the sample ρ_s. At finite temperature, the distribution of electrons at a given energy $f(E)$ is also to be taken into account. The tunneling current can be written as :

$$I_t(V_b) \propto |M|^2 \int_{-\infty}^{+\infty} \rho_s(E + V_b)\rho_t(E)(f(E + V_b) - f(E))dE \tag{3.1}$$

Where I_t is also proportional to all tunneling events that occur with probability M, the tunneling matrix element that can be calculated using Fermi golden rule and yields the previously mentioned e^{-kz} dependency. Assuming that $k_bT << eV$ so that the Fermi dirac distribution becomes a step function ; and that the density of states of the tip is constant ($\rho_t(E) = \rho_t$), a simplified expression of the tunneling current is :

$$I_t(V_b) \propto T(V_b, z) \int_{E_F}^{E_F + V_b} \rho_s(E + V_b)dE \tag{3.2}$$

3.1.2 Tunneling Spectroscopy

To perform a spectrocopic measurement of the LDOS we have to get rid of the integral over the energy of the LDOS in the tunneling current. This can be done by derivating tunneling current with respect to applied bias tension :

$$\frac{dI_t(V_b)}{dV_b} \propto T(V_b,z)\rho_s(E_F+V_b) + \frac{dT(V_b,z)}{dV_b}\int_{E_F}^{E_F+V_b}\rho_s(E+V_b)dE \quad (3.3)$$
$$= T(V_b,z)\rho_s(E+V_b) + BI$$

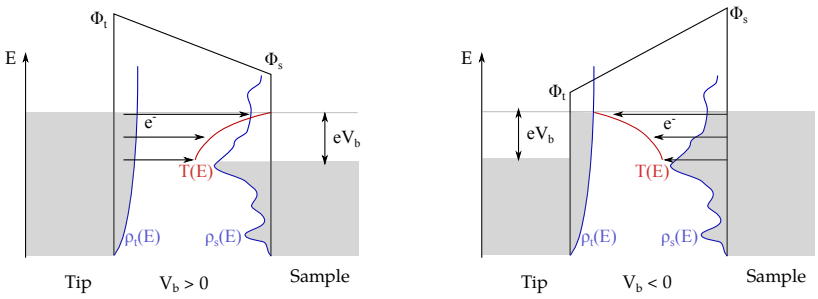

Figure 3.1: Energy diagram showing the tunneling of electrons between the tip and sample for positive (left) and negative (right) bias of the sample.

The LDOS of the sample is thus proportional to the derivated current as long as the background integral term BI can be neglected. In [153], G. Hörmandinger shows this is the case for $V_b < 0.2eV$ or for higher energies when the contributing states to the tunneling are sufficiently smooth over V_b.

Experimentally, this Scanning Tunneling Spectroscopy (STS) is achieved by adding an AC modulation to the sample bias, and measuring the resulting modulation of the tunneling current with a lock-in amplifier. By ramping V_b, we measure the LDOS of the sample as a function of the energy.

Because of its exponential dependence on distance, the tunneling occurs in a very local region below the tip. This also makes the strength of STM technique because it means one can perform spatially resolved spectroscopies, even down to the atomic scale.

3.1.3 *Scanning Tunneling Microscopy*

Scanning the surface enables to retrieve spatially resolved features of the surface electronic states. These correspond to a convolution between topographic and electronic effects.

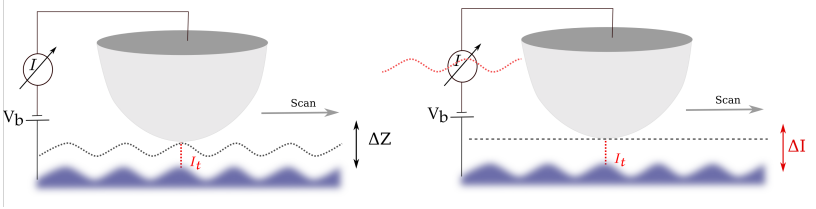

Figure 3.2: Schematic principle for two different scanning modes. In Z mode (left) tip extension is recorded, and in I mode (right) tunneling current variations are recorded.

There are two ways to record surface states, presented in Fig. 3.2. The first scanning mode consists in recording the tip extension -ie the distance between tip and sample- as the tip is scanned over the surface while maintaining the tunneling current constant with a feedback loop. Another possibility is to keep a constant tip height while scanning and recording the changes in tunneling current. In real life,

scanning is never a hundred percent "Z" nor "I" mode : one has to adapt feedback loop and scan speed values so that the tip does not crash on the sample, achieves atomic resolution, while performing scans in a realistic amount of time.

3.1.4 *STM of twisted bilayers of graphene*

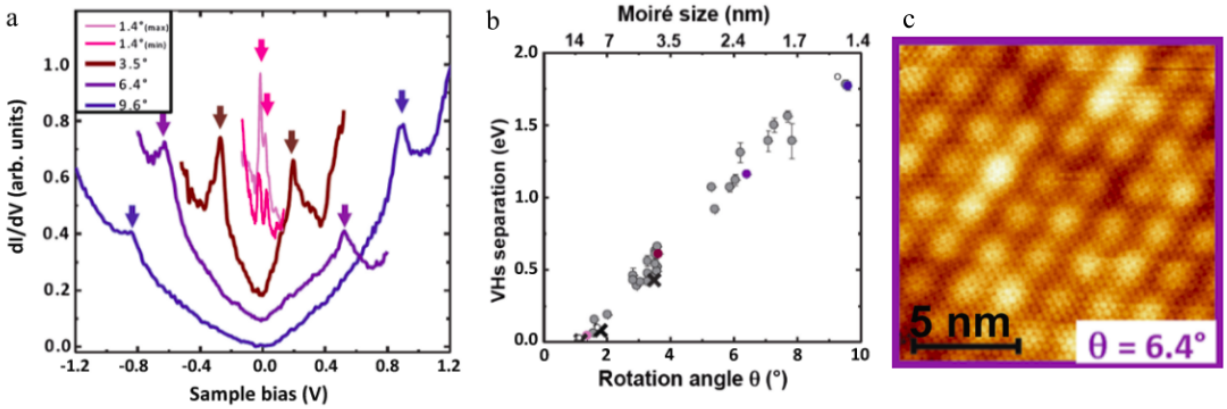

Figure 3.3: **a** Experimental LDOS for several twist angles. van Hoove singularities (vHs) are emphasized with arrows. **b** vHs spacing as a function of twist angle and moiré periodicity. **c** STM image of a 6.4°moiré, with visible atomic resolution. Adapted from [32].

Moiré and graphene periodicities can be imaged by scanning the surface of TBLG as shown on Fig. 3.3c for a twist angle of 6.4°. The visible corrugation between AA regions and AB regions results from a combination of *(i)* topography, as the interlayer distance is higher in AA regions than in AB regions [68, 154], and *(ii)* density of states, as the electrons are localized in AA regions [34].

Spectroscopy of the system gives information on the energy of the saddle points. These are detected in the LDOS by the vHs, whose separation decreases with the twist angle (Fig. 3.3b). The localization of electrons in AA regions was noted in the early experiments by Z. Y. Rong and P. Kuiper [155]. This observation is supported by LDOS measurements as the vHs amplitude is bigger (resp. smaller) in AA (AB) regions as shown in light pink (resp. dark pink) on Fig. 3.3a.

Last, STM measurements teach us about spatial variations of the moiré periodicity. These are particularly pronounced near defects and grain boundaries as shown on Fig. 3.4. They are due to relative deformations of the layers, which we call *heterostrain* following Ref. [8]. This heterostrain significantly modifies the moiré, the latter acting as a strain magnifier. [156, 157, 158, 159]

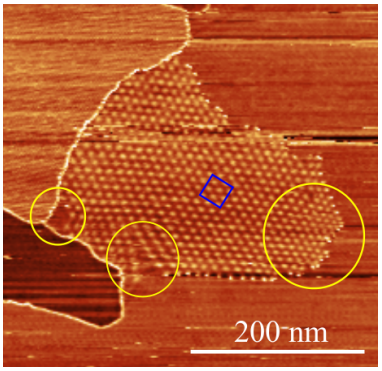

Figure 3.4: STM topography ($V_b = -500mV, I_t = 1nA$) of a 1.2°moiré pattern (as measured from the homogeneous region in the blue square). The boundaries around the grain that are common in such graphene on the C-face of SiC sample create native strain in the TBLG, detected by the inhomogeneous moiré periodicity as emphasized by the yellow circles. Adapted from [8].

3.2 *Quantifying native heterostrain*

The physics of TBLG rely on the precise arrangement between the layers. In particular, heterostrain is ubiquitous in TBLG samples and has to be taken into account. Though the local arrangement varies through space due to inhomogeneities and relaxation processes it is often possible to find homogeneous regions in heterostrain and twist

angle. Moreover, the properties of TBLG are determined by the local arrangement as shown in the work of N. Nakatsuji and M. Koshino [144]. It means we can rely on the local analysis of homogeneous regions of TBLG in order to describe the physical system.

To quantify local native heterostrain and twist angle, STM is a good method because one can image simultaneously both atomic and moiré periodicities.

It is even more interesting because with STM we can make a direct link between local stacking and local electronic properties.

We will now describe how the relative arrangement can be determined from STM topographic images of Moiré.

3.2.1 *Determination of heterostrain using commensurability study*

Relative arrangement and Heterostrain

Quantifying local in-plane homogeneous heterostrain means we have to quantify the relative arrangement between the layers.

This link between the bottom layer $(\boldsymbol{a_{b_1}}, \boldsymbol{a_{b_2}})$ and top layer $(\boldsymbol{a_{t_1}}, \boldsymbol{a_{t_2}})$ periodicities, following the work of A. Artaud *et al.* [149], can be written in the form of a so called Park Madden matrix, so that:

$$\begin{pmatrix} \boldsymbol{a_{t_1}} \\ \boldsymbol{a_{t_2}} \end{pmatrix} = \begin{pmatrix} a & b \\ c & d \end{pmatrix} \begin{pmatrix} \boldsymbol{a_{b_1}} \\ \boldsymbol{a_{b_2}} \end{pmatrix} \tag{3.4}$$

This matrix includes, in the most general stacking arrangement, a pure rotation between the layers and an additional heterostrain.

$$\begin{pmatrix} \boldsymbol{a_{t_1}} \\ \boldsymbol{a_{t_2}} \end{pmatrix} = R(\theta_2)M(p_{an})R(\theta_1)M(p_{iso}) \begin{pmatrix} \boldsymbol{a_{b_1}} \\ \boldsymbol{a_{b_2}} \end{pmatrix} \tag{3.5}$$

With $R(\theta) = \begin{pmatrix} cos\theta & sin\theta \\ -sin\theta & cos\theta \end{pmatrix}$ a rotation matrix, $M(p_{an}) = \begin{pmatrix} p_{an} & 0 \\ 0 & 1 \end{pmatrix}$ the matrix for uniaxial deformation and $M(p_{iso}) = \begin{pmatrix} p_{iso} & 0 \\ 0 & p_{iso} \end{pmatrix}$ the matrix for biaxial deformation.

The four stacking parameters $(p_{an}, p_{iso}, \theta_1, \theta_2)$ are obtained by identification of Equation 3.4 and Equation 3.5 following Ref. [149], as described in section 2.3.1.

These parameters are related to more physical quantities by defining uniaxial heterostrain $\varepsilon_{uni} = p_{an} - 1$ and biaxial heterostrain $\varepsilon_{bi} = p_{iso} - 1$.

Experimental determination of Park Madden Matrix

Finding the link between the two graphene layer periodicities over the imaged regions is done in Fourier space, where the top (resp. bottom) layer periodicity is referred as $\boldsymbol{k}_{t_i}$ (resp. $\boldsymbol{k}_{b_i}$), $i = 1, 2$. A fast Fourier Transform (FFT) of the experimental data gives us an average of the periodic arrangements. By fitting a grid on the moiré periodicity in the FFT, as done on Fig. 3.7 one finds the integers that

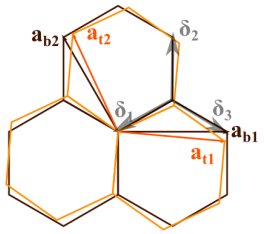

Figure 3.5: Definitions of bottom layer periodicity (untwisted, brown hexagons) and top layer periodicity (twisted and deformed, orange hexagons).

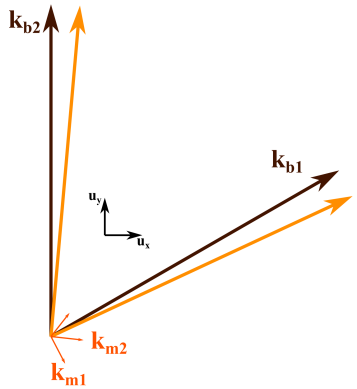

Figure 3.6: The use of the grid is optional : it is enough to write $\boldsymbol{k}_{t_i}$ and $\boldsymbol{k}_{b_i}$ in the same basis. By using the grid, we have the benefit of retrieving a commensurate system that is fit for tight binding Lanczos algorithm calculations as presented in section 2.3.2. This sketch shows two possible basis in which both graphene periodicities can be expressed, $(\boldsymbol{u}_x, \boldsymbol{u}_y)$ and $(\boldsymbol{k}_{m1}, \boldsymbol{k}_{m2})$.

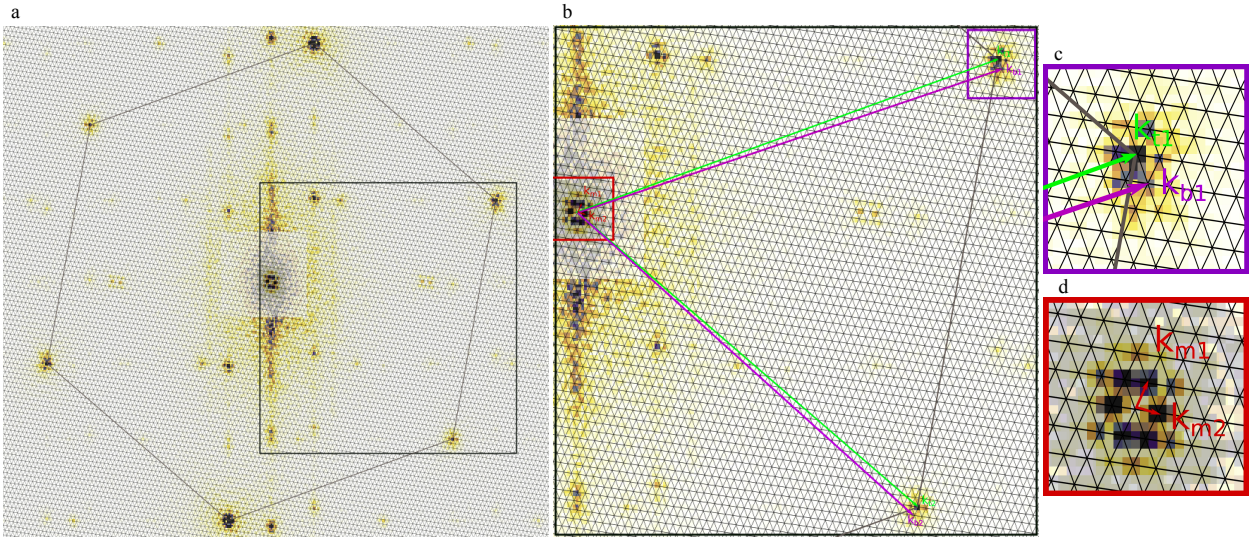

Figure 3.7: **a** Fast Fourier Transform of a low angle TBLG imaged in STM and published in ref [160]. The reciprocal points of the top graphene layer are emphasized by the black hexagon and the moiré periodicity is emphasized with the black grid. **b-d** Zooms of the FFT with the reciprocal moiré vectors shown in red, the top layer graphene periodicity in green and the bottom layer graphene perodicity in purple.

link both graphene periodicities to the moiré periodicity. In the case of Fig. 3.7, we have

$$\begin{pmatrix} \boldsymbol{k}_{t_1} \\ \boldsymbol{k}_{t_2} \end{pmatrix} = \begin{pmatrix} i & k \\ j & l \end{pmatrix} \begin{pmatrix} \boldsymbol{k}_{m_1} \\ \boldsymbol{k}_{m_2} \end{pmatrix} = \begin{pmatrix} 29 & 34 \\ -23 & 66 \end{pmatrix} \begin{pmatrix} \boldsymbol{k}_{m_1} \\ \boldsymbol{k}_{m_2} \end{pmatrix} \tag{3.6}$$

$$\begin{pmatrix} \boldsymbol{k}_{b_1} \\ \boldsymbol{k}_{b_2} \end{pmatrix} = \begin{pmatrix} m & q \\ n & r \end{pmatrix} \begin{pmatrix} \boldsymbol{k}_{m_1} \\ \boldsymbol{k}_{m_2} \end{pmatrix} = \begin{pmatrix} 28 & 35 \\ -24 & 66 \end{pmatrix} \begin{pmatrix} \boldsymbol{k}_{m_1} \\ \boldsymbol{k}_{m_2} \end{pmatrix} \tag{3.7}$$

Which enables us to calculate the Park Madden Matrix.

$$\begin{pmatrix} \boldsymbol{k}_{b_1} \\ \boldsymbol{k}_{b_2} \end{pmatrix} = \begin{pmatrix} a & c \\ b & d \end{pmatrix} \begin{pmatrix} \boldsymbol{k}_{t_1} \\ \boldsymbol{k}_{t_2} \end{pmatrix} \tag{3.8}$$

Along with the heterostrain parameters : $(\varepsilon_{uni}, \varepsilon_{bi}, \theta_{int}, \theta_s)$ = (-0.55%, 0.13%, 1.1°, 34°).

This analysis has the advantage of describing the *relative* arrangement of the layers, and thus getting rid of experimental artifacts, that could emerge from a miscalibration of the piezoelectric scanning tube or the thermal drift for example. In that sense, the method is very robust.

3.2.2 *Analysis at the moiré scale*

When imaging low angle TBLG, the moiré can easily reach periods above $10nm$. It means that imaging several moiré periods while achieving atomic resolution is time consuming. That is why several groups image low angle TBLG at the moiré scale.

At that scale, we only have access to the next nearest neighbor AA sites distances as shown on Fig. 3.8. We can still retrieve information on the heterostrain, as these distances are significantly modified for small atomic displacements, the moiré acting as a strain magnifier.

A. Kerelski et al. [160] showed that heterostrain can be extracted using graphene's Poisson ratio estimate $\delta = 0.16$. In that description,

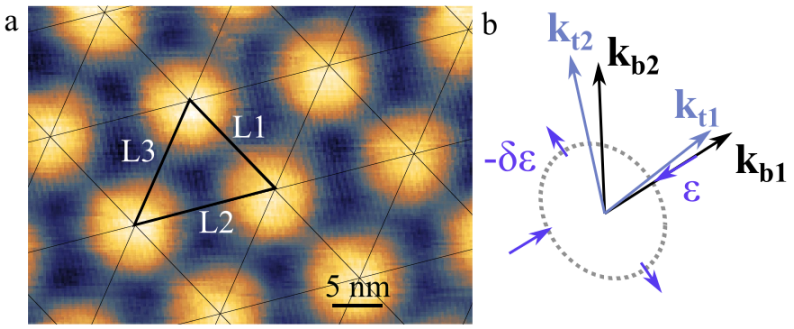

Figure 3.8: **a** Topography of a low angle TBLG without atomic resolution. The grid emphasizes the slight deformation of the moiré periodicity with $L1 \neq L2 \neq L3$ resulting from heterostrain. Adapted from [161]. **b** Sketch in Fourier space of heterostrain described in the form of Poisson behaviour.

one layer is stretched (squeezed) in one direction by an amount ε and squeezed (stretched) in the opposite direction by an amount $-\delta\varepsilon$. This situation is sketched in Fig. 3.8b. In matrix form, this writes :

$$\begin{pmatrix} \boldsymbol{k_{t_1}} \\ \boldsymbol{k_{t_2}} \end{pmatrix} \tag{3.9}$$
$$= \begin{pmatrix} cos\theta_s & -sin\theta_s \\ sin\theta_s & cos\theta_s \end{pmatrix} \begin{pmatrix} \frac{1}{1+\epsilon} & 0 \\ 0 & \frac{1}{1-\delta\epsilon} \end{pmatrix} \begin{pmatrix} cos\theta_s & sin\theta_s \\ -sin\theta_s & cos\theta_s \end{pmatrix} \begin{pmatrix} cos\theta & sin\theta \\ -sin\theta & cos\theta \end{pmatrix} \begin{pmatrix} \boldsymbol{k_{b_1}} \\ \boldsymbol{k_{b_2}} \end{pmatrix}$$

In other words, the reduced number of degrees of freedom ($L1, L2, L3$) forces us to neglect the separation of heterostrain into pure biaxial strain ε_{bi} and pure uniaxial strain ε_{uni}, as well as forcing $\theta_s = -\theta_1 = \theta_2$.

The distances between next nearest neighbor AA sites ($L1, L2, L3$) are extracted experimentally. The experimental stacking configuration is then found by minimizing the function that relates the heterostrain configuration to the experimental values of ($L1, L2, L3$).

In practice, one starts from an arbitrary heterostrain configuration $(\varepsilon, \theta_s, \theta)$. The corresponding distances $(L1_{calc}, L2_{calc}, L3_{calc})$ are calculated from the simple relation $\boldsymbol{K_{mi}} = \boldsymbol{k_{ti}} - \boldsymbol{k_{bi}}$. A numerical minimisation process then gives the experimental stacking configuration.

3.2.3 *Comparison between moiré scale and commensurability methods :*

Although the framework describing heterostrain at the moiré scale is less general as it does not take into account effects that are not described by Poisson behaviour, we will see in the following that we find good agreement when describing one sample with both models.

In order to give some intuition for this, we write a general strain matrix that includes Poisson strain behaviour with its parameters (ε, δ) **and** pure biaxial strain E_b.

$$StrainMatrix = \begin{pmatrix} (1+\varepsilon)(1+E_b) & 0 \\ 0 & (1-\delta\varepsilon)(1+E_b) \end{pmatrix} \tag{3.10}$$

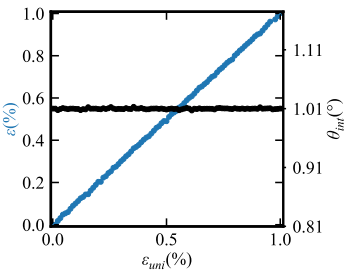

Figure 3.9: Moiré scale approach is used to calculate parameters ε and θ_{int} from ($L1, L2, L3$) lengths. The latter are calculated first using commensurability method with parameters $\delta = 0.16$, $E_b = 0$, $\theta_{int} = 1.01°$, and varying ε_{uni}. Good agreement is found.

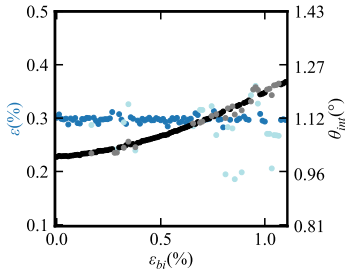

Figure 3.10: Same as Fig. 3.9 with parameters $\delta = 0.16$, $\varepsilon_{uni} = 0.3\%$, $\theta_{int} = 1.01°$, and varying E_b. With pure biaxial heterostrain, the moiré scale description quickly overestimates the twist angle. Below 0.2%, this approach is still satisfying.

The lengths ($L1, L2, L3$) are first calculated using the commensurability method, considering any general stacking. Moiré scale approach is then applied on the obtained lengths ($L1, L2, L3$) to retrieve the best fitting configuration.

Fig. 3.9 shows that for any uniaxial strain amplitude, when biaxial strain is zero, the moiré scale approach retrieves the good stacking parameters. When biaxial strain is increased at constant uniaxial strain (Fig. 3.10), the moiré scale approach cannot describe the system fully and the twist angle is artificially increased in order to fit best ($L1, L2, L3$) parameters. Such a behaviour could be corrected by determining the direction of graphene period with respect to that of the moiré period.

These methods can be quantitatively compared satisfyingly when pure biaxial strain is smaller than 0.2%.

3.3 *Effect of heterostrain on the flat bands of TBLG*

An STM systematic experimental study of heterostrain in TBLG can be quite challenging, because samples where the twist angle is controlled are difficult to achieve, in particular if we want accessible and clean surfaces suited for STM measurements.

In order to overcome this difficulty, we survey already published STM measurements from different groups. This kind of meta-analysis means that we do not control all parameters as the samples are measured in different experimental conditions and setups. We must thus carefully consider all these parameters in our analysis. However, if a general trend is found, it gives the study more weight as it means the identified trend is reproducible through all different samples and experimental setups.

In the following, we will discuss such an analysis of several samples of TBLG near the magic angle, from different already published data.

Depending on the response of the authors to our data request we could use their raw data for our survey or not. We could use the raw data of Refs. [8, 136, 162]. For Refs. [52]a, [53, 54, 160, 161] we used topographic STM images digitized from the corresponding manuscripts. For Refs [163], [52]b, [52]c, we did not have the data to do our own strain analysis and used the values of heterostrain provided by the authors.

When the published images had atomic resolution, we extracted local heterostrain from the commensurability method described in subsection 3.2.1. For Refs. [161, 162] [52]a, [53, 54], the stacking configuration was retrieved using the moiré scale method as in subsection 3.2.2. We checked both methods provided very similar estimates of uniaxial heterostrain for the data of Refs. [8, 136, 160]. Indeed, biaxial heterostrain is usually much lower that uniaxial heterostrain, which satifies the empirical criteria for the validity of the moiré scale approach presented in paragraph 3.2.3.

In the following, for easier representation, we will use the correspondence :

1 : L. Huder *et al.* [8]
2 : A. Kerelski *et al.* [160]
3 : Y. Choi *et al.* [136]
4 : Y. Jiang *et al.* [162]
5 : M. Xie *et al.* [161]

6 : Z. Zhang *et al.* [163]
7 : D. Wong *et al.* [52]
8 : Y. Choi *et al.* [53]
9 : K. Nuckolls *et al.* [54]

We will show that in those samples which are all near the magic twist angle, the relative deformations between the layers are predominant over twist angle in determining the flat bands of the system.

3.3.1 *Characterisation of the flat bands in the non correlated regime*

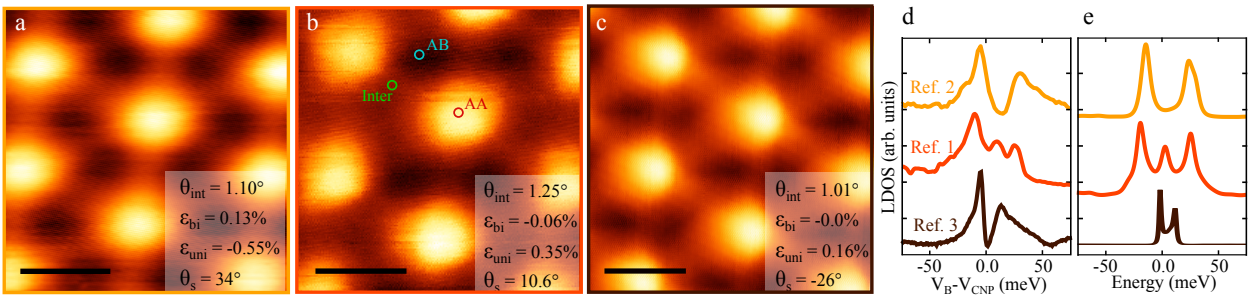

Figure 3.11: Panels **a**, **b** and **c** present STM images of twisted graphene layers near the magic angle adapted from Refs. [160], [8] and [136] respectively. The scale bar is 10 nm in each image. Topographies were taken at ($0.5V$, $30pA$), ($0.4V$, $50pA$), and ($0.5V$, $50pA$) respectively. Insets present the heterostrain parameters extracted with the method of subsection 3.2.1, in good agreement with estimates of the original studies. **d** Local density of states measured in the AA regions for the samples of panels **a**, **b** and **c**. **e** Corresponding tight-binding calculation of the LDOS including heterostrain.

Figure 3.11 presents typical STM images collected from Refs. [8, 136, 160]. These STM images can seem very similar, which is not surprising as they have a twist angle very close to one another. However, this similarity is only apparent as evidenced by the variety of the local density of states measured from the STS measurements on Fig. 3.11d. We expect that the flat-bands should merge at the magic angle, as discussed in Chapter 1. But the spectra of Ref. [160] and [136] show two van Hove singularities that are spaced by an amount ΔE_{exp} that proves that the flat bands are still separated and are not flat. In addition, despite the samples have a twist angle differing by only 0.15°, their vHs spacing differ by a factor 2-3.

The variety of spectroscopic features of Fig. 3.11d can be explained by intrinsic heterostrain. Its values are extracted from a commensurability method, and shown in the inset of each panel. It reveals that biaxial heterostrain is always smaller than uniaxial heterostrain, the latter varying by a factor over 3. By generating commensurate cells that include strain and performing tight binding calculations simiarly to the method presented in paragraphs 2.3.1 and 2.3.2, we show on Fig. 3.11e that including strain in the system is enough to explain the main LDOS features, the number of peaks and their spacing.

We find that the phenomenology described in section 2.3.2 is retrieved experimentally. Namely, for increased uniaxial strain amplitudes, the flat bands separation is increased. Also, the importance of the angle of application of strain is revealed by the LDOS on Fig. 3.11b featuring a third peak at zero energy that was also emphasized in section 2.3.2.

Sample to sample variation is obvious from other published STM data [52, 53, 54, 161, 162, 163] but also significant in transport experiments [60].

3.3.2 *Effect of electron-electron interactions*

In addition to the effect of heterostrain, the vHs spacing ΔE_{exp} is doping dependent which has been attributed to electron-electron interactions [52, 136, 160, 161, 162, 163].

Interactions are tuned by changing the doping of the sample - or filling factor of the bands -, and varied experimentally using the backgate of samples when the heterostructure is deposited on $Si/SiO2$ wafers using tear and stack methods as done in Refs. [52, 53, 54, 136, 160, 161, 162, 163].

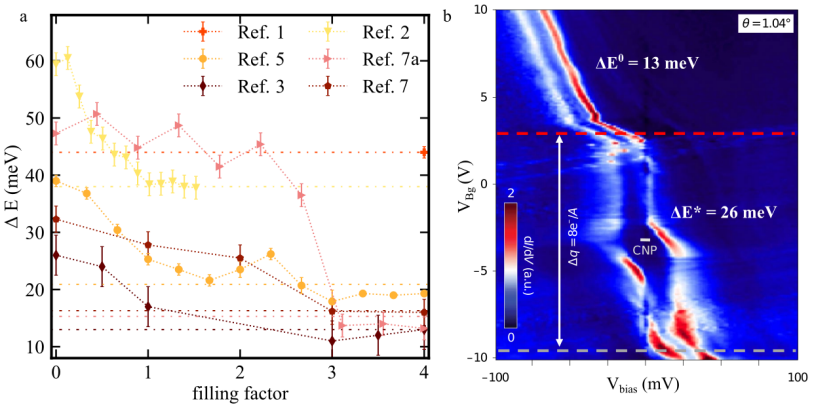

Figure 3.12: **a** Experimental van Hoove singularity spacing as measured from the outermost pics in the STS local density of states, as a function of filling. The horizontal dotted lines correspond to the vHs spacing calculated using commensurate cells that include heterostrain. Error bars correspond to the uncertainty related to width of the van Hove singularity peaks as measured from the digitized data. **b** Colormap of a STS measurement adapted from [136]. vHs peaks are visible in red and white colors and their spacing varies with the backgate (y axis), showing a maximum spacing near charge neutrality point also referred to as zero electron filling.

When the charge carriers fill the flat bands, their Fermi velocity goes to zero, thereby boosting the Coulomb to kinetic energy ratio which is a measure of interactions. The flat bands spacing and width is thus increased which translates into an increased vHs spacing in the STS spectra that is maximum at charge neutrality point (CNP) (*i.e.* zero filling), where electronic interactions express most.

This behaviour is examplified on Fig. 3.12b for one specific experiment. A quantitative comparison of several samples on Fig. 3.12a shows that ΔE_{exp} can be increased significantly at zero filling. At full filling of the flat bands, it converges to the non-interacting situation modeled by tight binding calculations ΔE_{TB} emphasized by the doted line.

3.3.3 *Combined effect of heterostrain and interactions within the continuum model*

Calculations including interactions in the recursive tight binding approach are very time consuming for such system sizes : a 1° moiré cell contains more than 10 thousand atoms. A single point DOS calculation, when including interactions, sometimes takes several weeks to achieve good convergeance. Indeed we have seen the tight binding approach calculates wavefunctions at the atomic scale, meaning it deals with big Hamiltonians.

We thus turn to a continuum model which has lower computational cost as seen in section 1.3.2 this model to describe TBLG systems including both heterostrain and interactions. These calculations

are performed by our theoretician colleagues Francisco Guinea and Tommaso Cea.

The effects of uniaxial heterostrain that were absent in the initial continuum model from L. Dos Santos *et al.* [35] can be introduced in the Hamiltonian relying on the low energy limit approximation, as shown by Z. Bi *et al.* [38].

In Chapter 2, we have seen heterostrain enters as a shift in Dirac cone positions. This shift depends on the strain induced pseudo gauge field that was introduced in subsection 2.1.1.

Here previous works can be followed [40, 121, 124, 139] to define the effective gauge field, as :

$$\boldsymbol{A}_l = \frac{(-)^{l-1}\varepsilon\sqrt{3}\beta(1+\delta)}{4a}\,(\cos 2\theta_s, \sin 2\theta_s) \tag{3.11}$$

where $\beta \simeq 3.14$ [40] is the Grüneisen parameter and ε is the heterostrain magnitude in a Poisson behaviour approximation.

We have seen heterostrain also affects the interlayer Hamiltonian $H_\perp$, because it enters as a geometrical factor on the reciprocal lattice of the TBLG :

$\boldsymbol{G}_i = \mathcal{E}^T \boldsymbol{g}_i$.

Where $\mathcal{E}$ is a heterostrain matrix applied symmetrically on both layers. In our case, the calculations consider a matrix that uses the moiré description for heterostrain decribed in subsection 3.2.2. For small twist angles, it is thus written :

$$\mathcal{E} = \varepsilon \begin{pmatrix} -\cos^2\theta_s + \delta\sin^2\theta_s & (1+\delta)\cos\theta_s\sin\theta_s \\ (1+\delta)\cos\theta_s\sin\theta_s & -\sin^2\theta_s + \delta\cos^2\theta_s \end{pmatrix} + \theta_{int}\begin{pmatrix} 0 & -1 \\ 1 & 0 \end{pmatrix} \tag{3.12}$$

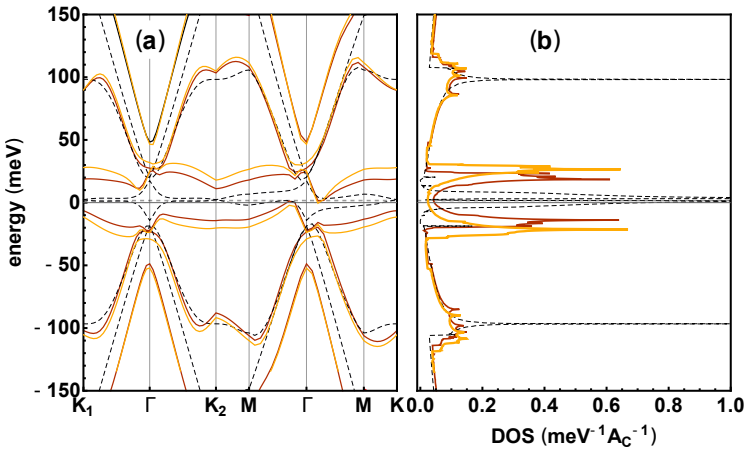

Figure 3.13: **a** Band structure along the high symmetry path of the BZ obtained with continuum calculations at charge neutrality. The unstrained stucture without electronic interactions is given as a reference with the black dotted curve. The calculation for a heterostrain configuration of $\varepsilon = 0.6\%$, $\theta_s = 29°$ and $\theta_{int} = 1.10°$ is given in solid line. The yellow (resp. red) curve shows the situation with (resp. without) interactions. The dielectric constant is set to $\epsilon = 5\epsilon_0$ for the interacting situation. **b** Corresponding DOS. The Fermi energy shown as the dashed grey line is at charge neutrality.

Coulomb interactions are included in the model using a Hartree-Fock approach, as detailed in [164].

Within this framework, the interacting Hamiltonian includes in a mean field approximation the Hartree term H^H that accounts for the onsite potential (including spin and valley degeneracy) U quantify-

ing the overlapping energy of two wave functions on the same site i.

The Hamiltonian also includes the Fock term H^F that accounts for the exchange potential $V_{\boldsymbol{k}}$ between two wavefunctions on neighboring sites i and j.

All in all the Hamiltonian can be written :

$$H^{HF}_{TBLG} = H_{TBLG} + H^H + H^F, \tag{3.13a}$$

$$H^H = \sum_{\boldsymbol{k}\boldsymbol{G}\boldsymbol{G}'} \sum_i |\boldsymbol{k}+\boldsymbol{G}, i\rangle\, U\left(\boldsymbol{G}-\boldsymbol{G}'\right) \langle \boldsymbol{k}+\boldsymbol{G}', i|\,, \tag{3.13b}$$

$$H^F = \sum_{\boldsymbol{k}\boldsymbol{G}\boldsymbol{G}'} \sum_{ij} |\boldsymbol{k}+\boldsymbol{G}, i\rangle\, V_{\boldsymbol{k}}\left(\boldsymbol{G}, \boldsymbol{G}'; i, j\right) \langle \boldsymbol{k}+\boldsymbol{G}', j|\,, \tag{3.13c}$$

Because the system always has a substrate, the electronic interactions can be screened by a dielectric substrate. The Hartree and Fock terms thus depend on a coulomb potential that is assumed to behave like a double metalic gate : $v_c(\boldsymbol{q}) = \frac{2\pi e^2}{\epsilon|\boldsymbol{q}|}\tanh\left(|\boldsymbol{q}|d\right)$, where e is the electron charge, the distance of the sample from the gate is set to $d = 40$nm and the dielectric constant of the environment in the most common case of a hBN substrate is typically $\frac{\epsilon}{\epsilon_0} \sim 4-7$, ϵ_0 being the dielectric constant of the vacuum.

Figure 3.13 shows the continuum calculations in this framework, confirming that heterostrain increases the bandwidth and the flat bands spacing. In addition, they show that the electronic interactions further renormalize the flat bands.

3.3.4 *Effect of strain on the flat bands of TBLG : low interactions regime*

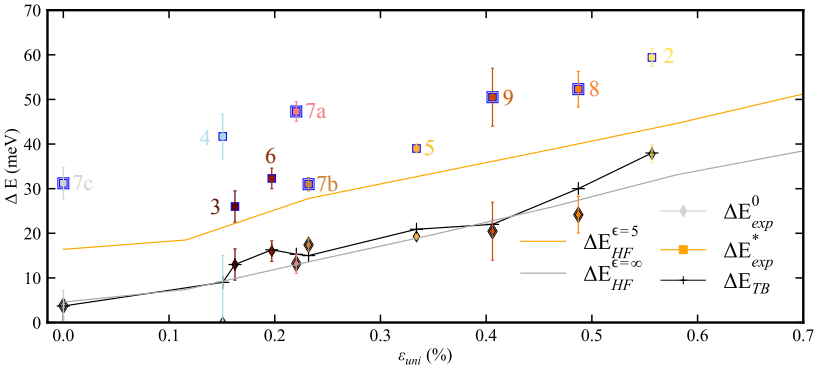

Figure 3.14: van Hoove singularity spacing as a function of uniaxial strain from STM measurements at large doping (ΔE^0_{exp}) and zero doping (ΔE^*_{exp}), from theoretical tight-binding (ΔE_{TB}), and from the Hartree-Fock approach in the continuum model in the regime of low ($\Delta E^{\epsilon=\infty}_{HF}$) and large ($\Delta E^{\epsilon=5}_{HF}$) interactions. The measurements where a cascade of electronic transitions was measured are indicated by a double border.

A quantitative comparison of vHs spacing ΔE for several experimental results, including corresponding tight binding and continuum calculations is given on Figure 3.14.

The linear dependency of experimental ΔE as a function of ε_{uni} both at high filling (diamonds) and near CNP (squares) establishes that heterostrain controls the flat bands of twisted graphene layers near the magic angle. The agreement of tight binding calculations ΔE_{TB} with experiments at high doping ΔE^0_{exp} is very good, as expected for calculations based on the precise stacking arrangement

extracted as in section 3.2.1. They also explain the small deviations of the data from a purely linear strain dependence, as the twist angle and biaxial strain amplitude can slightly vary from one sample to the other.

Quantitative agreement is also retrieved for continuum calculations at negligible interactions $\Delta E_{HF}^{\epsilon=\infty}$ (i.e. where the dielectric constant is set to high values) with increasing heterostrain ε. These calculations are performed for a twist angle of 1.1° and the direction of application of uniaxial strain is set to $\theta_s = 30°$. Despite this angle does not always match the experimental situation, we have seen in Fig. 2.15 the weak dependence of ΔE (spacing between the outermost singularities) on θ_s.

The relevance of this linear behaviour can be emphasized by plotting the data from Fig. 3.14 as function of the interlayer twist angle as shown on Fig. 3.15. Previous studies show that the twist angle is critical in determining the electronic properties [32, 165] in the $0 \rightarrow 60°$ range. Here, we can refine this statement. Indeed, the weak correlation of the data with twist angle shows that in a 0.2°range around magic angle, θ_{int} is a second order parameter in determining the flat bands of the system. We plot in Fig. 3.16 the vHs spacing as a function of interlayer angle for various stacking configurations in commensurate structures produced similarly to those from section 2.3.1. In agreement with the low energy model [38] and the experimental data from Fig. 3.15, these calculations show that the system is mostly insensitive to θ_{int} in the range from 0.7° to 0.9° up to $\varepsilon_{uni} = 0.3\%$. This trend continues for higher strains but within a narrower range of twist angles, ΔE_{vHs} eventually becoming linearly dependent on the twist angle at large heterostrain, as the description of the system in terms of vHs starts to collapse above 0.6% (see also Fig. 2.17).

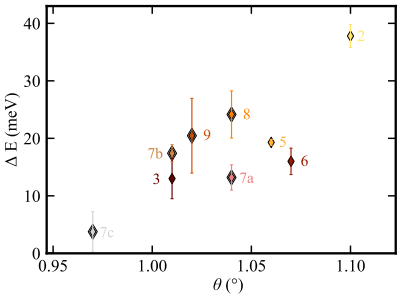

Figure 3.15: Plot of the Experimental spacing of the van Hoove singularities as a function of interlayer twist angle. Each point represents a different sample. The correspondance of the numbers to references in the literature is given at the beginning of this section.

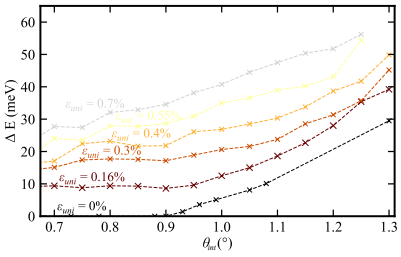

Figure 3.16: The spacing of van Hove singularities extracted from the DOS calculated using commensurate structures that include strain is plotted as a function of twist angle. Each color represents a different value of uniaxial strain, written on the left. In these calculations relying on the model presented in section 1.3.1, the magic angle is lower than 1.1°.

3.3.5 *Further comments for the effect of strain in the highly interacting regime*

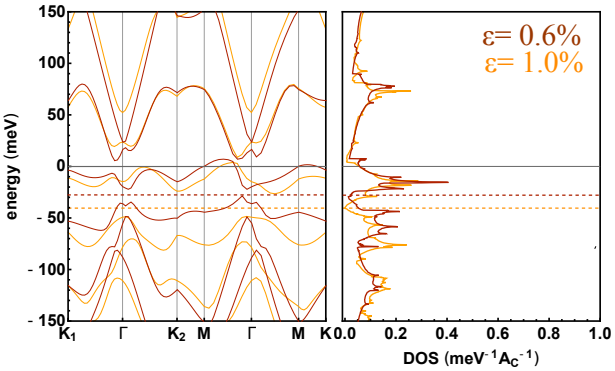

Figure 3.17: **left** Band structure along the high symmetry path of the BZ obtained with continuum calculations at charge neutrality, with strong interactions : the dielectric constant is set to $\epsilon = 4\epsilon_0$. The calculation are done for a heterostrain of $\varepsilon = 0.6\%$ (resp. $\varepsilon = 1.0\%$) as shown by a red solid line (resp. a yellow sold line). **right** Corresponding DOS with vHs that are not well defined anymore.

In the regime of low doping, when the interactions are strong, Fig. 3.14 shows that the bandwidth is significantly increased by uniaxial heterostrain for all samples. The Hartree-Fock calculations including strain and interactions reproduce well that trend, but underestimate

the peak spacing ΔE^*_{exp}. The realistic dielectric constant chosen here $\epsilon = 5\epsilon_0$ could be decreased in order to fit better the experimental data and describe even higher interactions. However this does not yield a better agreement because the vHs are no longer well defined, especially at large strains, when the low energy bands start to merge into the continuum of higher energy bands as shown on Fig. 3.17.

So called cascade of electronic transitions refers to the spontaneous polarization of the system into of valley and/or spin states. They are directly linked to the strong interactions and arise at intermediate fillings. These polarized states are detected in STM [52, 53, 54, 55] and in transport experiments [45, 51, 56, 57].

Another limit to our description at high interactions is the large data scatter of experimental ΔE^*_{exp}. Several external sources for that scatter can be considered : twist angle, heterostrain value or angle of application, bandwidth of the bands measured from the FWHM of van Hove singularities, tunneling resistance, temperature, and detection of a cascade of electronic transitions in the sample.

In particular, we can focus on the effect of tunneling resistance, that can modify the local stacking [44] and induce strain in the layer [166]. Previous measurements for the sample from Ref. [8] show that when the tip is closer to the sample, mechanical interactions with the tip can be induced and affect the measured LDOS, as discussed also in the work of L. Huder [134]. Specifically, we find that the vHs spacing deviates significantly from the tight binding calculations for low tunneling resistance, when the tip is closer to the sample (Fig. 3.18a). Tip trend is visualized for sample from Ref.1 on Fig. 3.18b showing a decrease in vHs spacing with decreasing tunneling resistance. For Ref.3 on Fig 3.18c-d, a decrease in vHs spacing is observed for increasing tunneling resistance. This strong sample dependence on the response can be attributed to the experimental setup (Cryogenic vacuum for sample of Ref.1 versus ultra high vacuum for sample of Ref. 3) as well as to the microscopic structure of the tip that can induce heterostrain as well as homostrain, vertical displacement, local rotation, in various fashions.

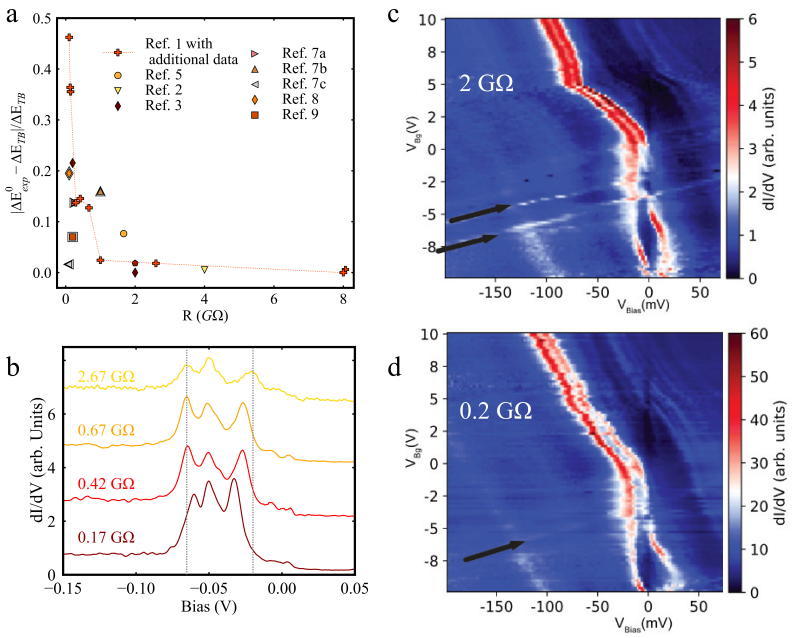

Figure 3.18: **a** Relative deviation of ΔE^0_{exp} to ΔE_{TB} as a function of the tunneling resistance $R_t = V_b/I_t$. **b** DOS for various tunneling resistance corresponding to sample from Ref.1 ([8]). **c** Gate dependent DOS colormap for a $R_t = 2G\Omega$, corresponding to sample from Ref.3 ([136]). **d** Same as **c** for $R_t = 0.2G\Omega$.

3.3.6 Perspectives

We have showed that TBLG near magic angle are most sensitive to heterostrain by relying on the systematic study of TBLG with various strain amplitudes. For this, we take advantage of the ubiquitous native strain that exists in each sample, that provided us with a relevant set of data. Another path would be to tune strain *in situ*, which requires the development of a new experimental platform. We will explain the design and fabrication of such a setup in Chapter 5.

This work also reveals that electronic correlations are very sensitive to some additional experimental parameters beyond those investigated here, or a complex combination of these. As an example, one could consider further the effect of the substrate or more generally the detailed electrostatic environment as is suggested in the review by A. Balents *et al.* [60], or investigate the effect of atomic lattice relaxation [83].

In addition, the strong impact of heterostrain on the flat bands of magic angle twisted bilayers of graphene is also pointed in theoretical works [38, 144]. Altogether, it motivates a future systematic investigation of its influence on the strongly interacting phases of twisted graphene layers, and on other moiré materials.

4
Atomic swirl in graphene bilayers

Contents

We have seen in previous chapters that the physics of TBLG depend on the precise relative arrangement of the layers. A slight homogeneous strain can have significant importance on the physics of the system. In this Chapter, we turn to another type of changes in the relative arrangement of the layers, namely atomic relaxation. These in-plane or out-of-plane local deformation of the atomic lattice are common in marginally twisted TBLGs.

In this Chapter we discuss a new type of relaxation in bilayers of graphene and discuss its possible origin. We then focus on understanding its low energy electronic properties. Before that, we will present the samples used in this study.

4.1 Graphene on SiC samples

4.1.1 Growth of Graphene on SiC

In the following, we study a sample of graphene grown on the Si face of Silicon Carbide (SiC). The synthesis of epitaxial graphene on SiC was first achieved by C. Berger *et al.* in 2004 [167], although graphitization of annealed SiC substrate was detected as soon as 1975 [168].

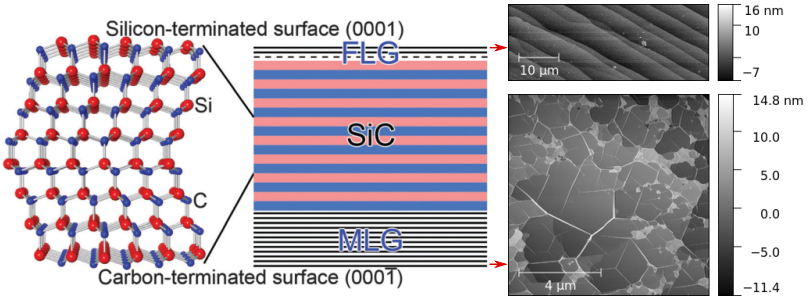

Figure 4.1: A sketch of the atomic structure of SiC is given on the left. Upon heating, the SiC substrates undergoes thermal decomposition and Carbon atoms that remain on the surface organize into few (resp. multi) graphene layers on the Si terminated (resp. C terminated) face. The AFM images on the right show typical topographies of both faces : the Si terminated face features regular steps and the C terminated face is flatter and features many domains separated by grain boundaries.

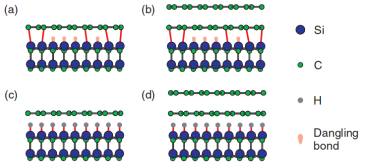

Figure 4.2: Side view sketch of epitaxial (top) and hydrogen intercalated (bottom) monolayer (left) and bilayer (right) graphene. When there is no intercalation, bonds between the first layer graphene layer and the Si atoms of the substrate are formed following the so called $(6\sqrt{3} \times 6\sqrt{3})R30°$ reconstruction of SiC(0001) (As observed in STM in Ref. [175]). The figure is from [176].

The growth of graphene on that material relies on the thermal decomposition of SiC that happens upon annealing. Graphene typically starts to grow at temperatures above 1000°C, as the Si atoms that have a lower vapour pressure than Carbon sublimate, and the Carbon atoms reorganize on the surface. The material is usually available in the industry with two unequivalent faces. These are described on Fig. 4.1 along with their respective topographies after graphene growth.

Graphene grown in such annealing process fully covers the substrate and is very clean, which is favorable for STM measurements. In typical annealing recipes, the surface characteristics on both faces can be controlled by varying temperature rates and pressure during the growth. In particular, the surface features inhomogeneities and domains that appear during the growth, and thus one can investigate with STM various regions hosting different structural and electronic properties on the same sample [169, 170].

The sample we study here is grown in CRHEA (Centre de Recherche sur l'Hétéro-Epitaxie et ses Applications), in a CVD reactor using two different gases at high temperatures [171, 172, 173, 174].

The first gas consists in a mixture of Hydrogen and Argon. In most annealing processes, Hydrogen is used to improve the surface quality of graphene by etching [177], before any graphene grows on the surface. In CVD growth, it can also be used to decouple the graphene layers from the substrate during the growth of graphene, as the Hydrogen atoms bond with Silicon atoms of the substrate and can be used to form quasi-free-standing graphene layers [176] as shown in Fig. 4.2 (bottom).

Upon reaching temperatures over 1500°C, a flow of propane is added in the growth chamber, that acts as an additional source of Carbon and allows to use lower growth temperatures. All in all, this method is closer to annealing processes than to regular CVD, but the propane flow provides an additional parameter to control the aspect of the surface. Such growth process usually makes the sample more homogeneous, in particular in terms of number of layers.

4.1.2 *Graphene on the Si terminated face of SiC*

The Si face of SiC has been extensively studied by STM since its synthesis [169, 170, 175, 178, 179, 180]. It typically features a low num-

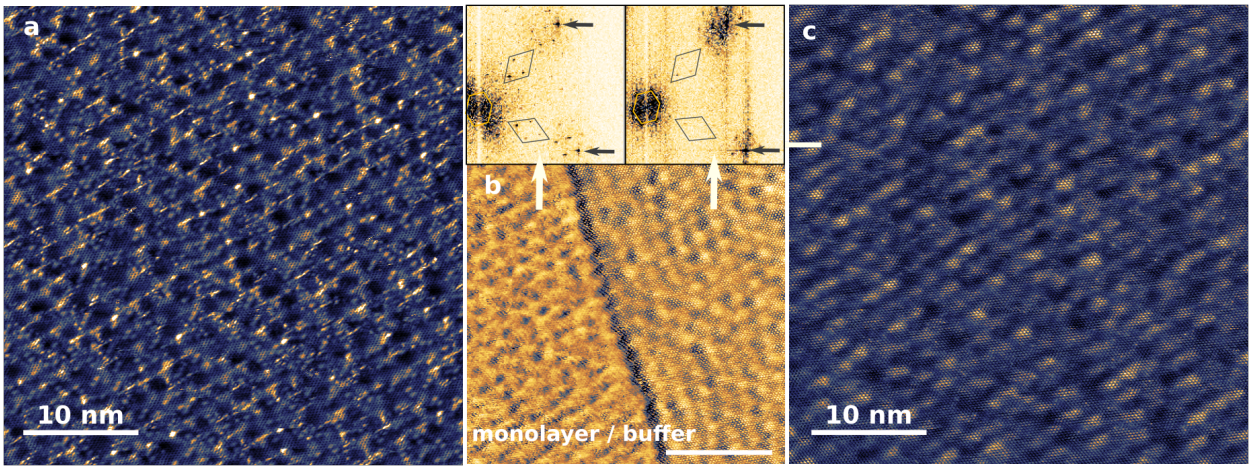

Figure 4.3: STM images of **a** Monolayer graphene on buffer ($V_b = -600mV$, $I_t = 80pA$), **b** Monolayer / Bilayer graphene interface ($V_b = +700mV$, $I_t = 250pA$), **c** Bilayer graphene on buffer ($V_b = -600mV$, $I_t = 80pA$). Insets correspond to the FFT of monolayer on buffer (left) and bilayer graphene (right). Dark arrows correspond to the graphene periodicity. Orange hexagons mark the 6×6 superlattice modulation from the SiC reconstruction, and the losanges surround the $2 \times 2 - G$ match between graphene and the reconstructed lattice.

ber of graphene layers (one or two) on top of a so-called *buffer layer* decoupling the topmost graphene layers from the SiC surface. The buffer layer corresponds to a graphene layer with sp_2 sigma bonds, but no π delocalized states. Indeed, one third of the carbon atoms form bonds with the Si atoms from the reconstructed SiC interface as sketched in Fig. 4.2. Due to these bonds, the Si terminated face of SiC strongly modifies the morphology of the buffer layer that acquires a $6\sqrt{3} \times 6\sqrt{3}R30$ periodicity from the substrate reconstruction.

This reconstruction is visible in STM images even when imaging monolayer or bilayer graphene as shown on the STM images from Fig. 4.3. The reconstruction is characterized by the 6×6 superlattice modulation that can be seen in both real space STM images and their FFT (orange hexagons). It comes along with a periodicity corresponding to the match between the graphene lattice and the reconstructed SiC interface lattice, that is visible in the FFT midway from the graphene spots (black losanges) and referred to as $2 \times 2 - G$ (see [175]). The top layer is smooth over the surface, which can be seen for example in Fig. 4.3b in the case of a bilayer/monolayer on buffer interface.

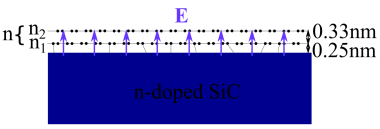

Figure 4.4: Sketch of monolayer on buffer graphene including doping and typical interlayer distances.

Because of the low number of layers of graphene on the Si face of SiC, the top layer graphene is quite close to the substrate and a charge transfer from the n-doped substrate is expected to dope the sample. The corresponding doping induced potential changes measured by STM (or ARPES) in graphene can reach $-100meV$ to $-500meV$. In addition, the top layer and (intercalated) buffer are expected to have a slight differential doping due to charge screening and charge reorganization in the layers. This doping difference creates an electric field $\boldsymbol{E}$ in the system. The overall situation is sketched in Fig. 4.4. In addition, the mobility of graphene is affected by the buffer layer which could act as a source of scattering. Mobilities up to $2 \cdot 10^3 cm^2 V^{-1} s^{-1}$ were measured [181] in graphene on SiC samples, two orders of magnitude lower than the mobility measured in suspended graphene layers reaching $2 \cdot 10^5 cm^2 V^{-1} s^{-1}$ [182]. Indeed, the buffer layer morphology is very dependent on the SiC interface

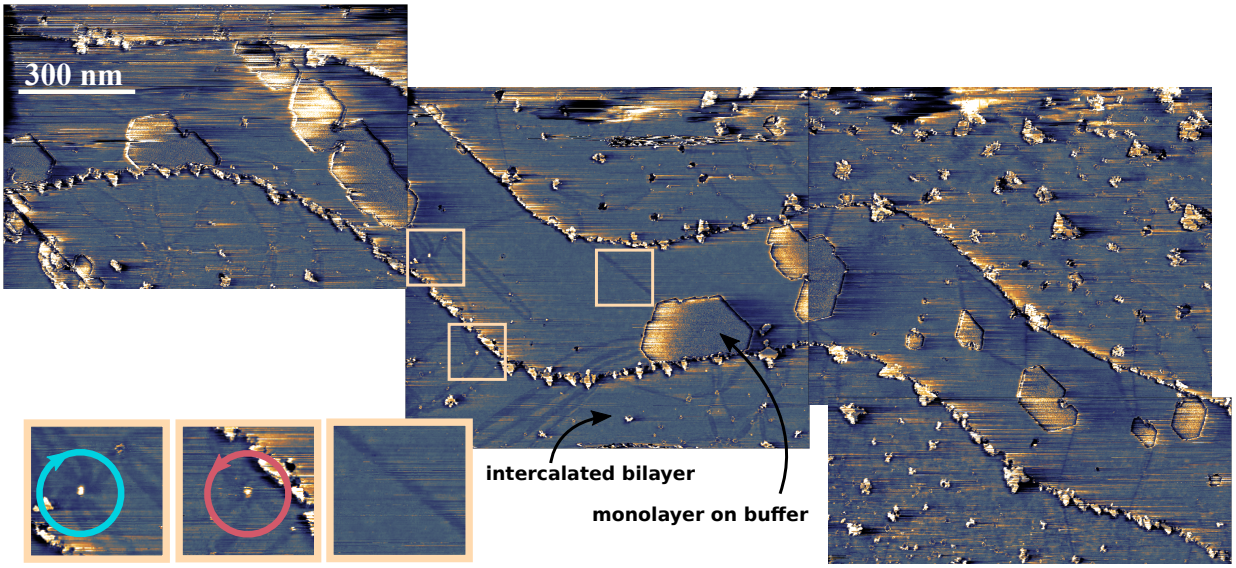

Figure 4.5: STM imaging $(V_b, I_t) = (-230mV,\ 350pA)$ of a mostly intercalated SiC terrasse. The three insets are zooms of the image that highlight the presence of domain walls (right) and swirl relaxation features that rotate clockwise (left) or anticlockwise (middle).

and its distance from the substrate is typically $0.25nm$, lower than the $0.33nm$ distance between two graphene layers. Although graphene on SiC is very clean, it is not referred to as high quality graphene because of its inherent doping and lower mobility.

4.1.3 Intercalation of graphene

To produce high quality quasi-freestanding graphene, a possible path is to intercalate graphene grown on SiC. Over the years, such intercalation was demonstrated with several techniques, including Hydrogen [176, 183, 184, 185], Fluorine [186], gold [187], or Nitrogen [188, 189].

The most studied case is that of Hydrogen, as it is easily achieved from Hydrogen exposure of the sample in a furnace. This intercalation occurs at temperatures above 700°C, as the atoms need sufficient thermal activation to pass the potential barrier required to intercalate below the graphene layers and form bonds with the Si atoms of the reconstructed SiC interface. The buffer layer is thus decoupled, forming a quasi-freestanding graphene layer (see bottom of Fig. 4.2). Most of the time, this intercalation is not homogeneous over the surface and starts near defects or step edges.

The intercalation of our sample was done using a gas mixture of H_2/NH_3 as a source of Hydrogen. The sample was exposed during 30mn at 150mbar and 1100°C. The resulting surface is shown on Fig. 4.5. The imaged terrasse is mostly intercalated, with several regions where a monolayer on buffer structure remains. The distance between the Hydrogen passivated SiC interface and the liberated bottom-most graphene layer is increased to $0.44nm$ as determined from Scanning Transmission Electron Microscopy (see annex A for more details), which is typical for hydrogen intercalated graphene

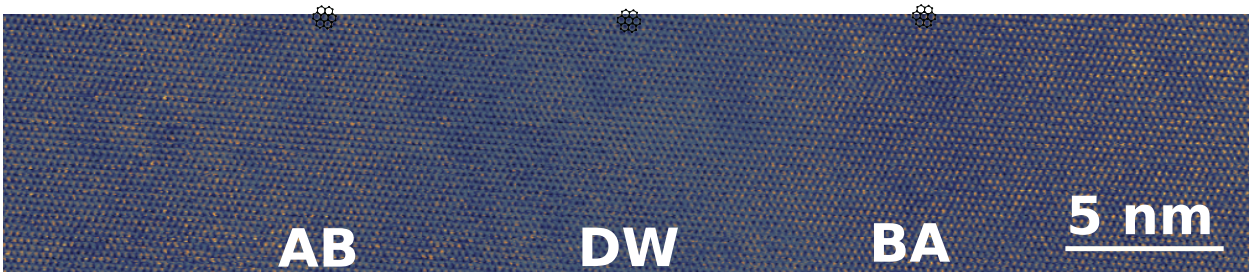

Figure 4.6: STM imaging $(V_b, I_t) = (-500mV,\ 200pA)$ perpendicular to a line of Fig. 4.5 featuring triangular contrasts : one third of carbon atoms are visible which is typical in STM for AB stacking ; and honeycomb contrast in the center : the atomic lattice resembles more to a circle, as all atoms are visible which in STM is typical of a decoupled graphene layer.

[185].

The surface also features several "lines" emphasized in the insets of Fig. 4.5, that at some places meet into clockwise or anticlockwise rotating "flowers", which we call *swirl* in the following. A close examination of these lines is shown in the atomically resolved STM image in Fig. 4.6 showing that the stacking types alternate between AB and honeycomb. These lines can thus be attributed to domain walls (DW) between AB and BA stackings, as introduced in section 1.5 and similarly to previous STM measurements that reported such stacking dependent contrast [90, 190].

In the following, we first turn to understanding the origin of the apparition of these DW features and of their *swirl* on the surface. Then, we focus on their electronic properties.

4.2 *Swirl pattern in relaxed bilayer graphene*

4.2.1 *Experimental evidence of swirl patterns*

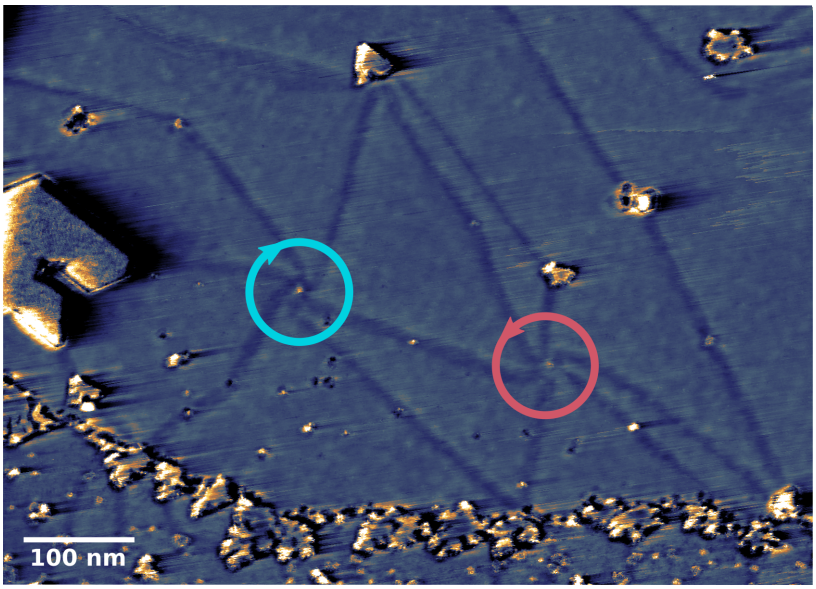

Figure 4.7: STM imaging $(V_b, I_t) = (-300mV,\ 250pA)$ of a small lattice of domain walls featuring clockwise (cyan) and anticlockwise (magenta) rotating swirl relaxation patterns on intercalated bilayer graphene on SiC.

An examination of Fig. 4.7 reveals that the DW can organize in an array that resembles the relaxed marginally twisted bilayers introduced in section 1.5 that have already been extensively studied

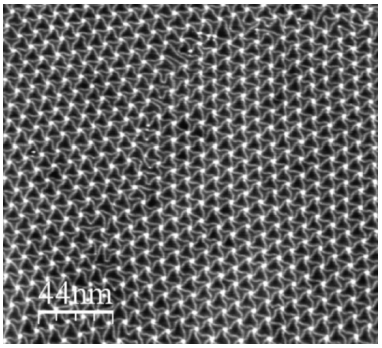

Figure 4.8: STM image ($0.1nA$, $-1V$) of the swirl lattice originated from the reconstructed lattice of $Au(111)$ with Gd adsorbates. From [193].

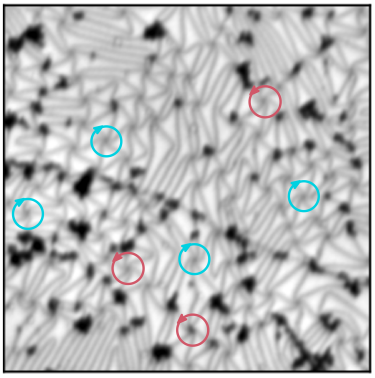

Figure 4.9: Bright Field LEEM image of intercalated bilayer graphene grown on the Si face of SiC, featuring a large area swirl relaxation lattice. The direction of rotation of several swirls are emphasized with magenta (anticlockwise) and cyan (clockwise) colors. From Ref. [201].

[81, 82, 83, 84, 87, 191, 192]. In that case, because of the small rotation, relaxation occurs in the system to maximize the size of AB/BA regions and concentrates heterostrain locally at the DWs that appear as lines connecting two closest AA stacked regions. These AA regions form at the vertices between six DWs and tend to localize the electrons, which explains why they appear as a bright spot in STM experiments. In our case, the moiré size is $\sim 200nm$, which would correspond to a 0.07° twist angle, one of the smallest angle ever observed in TBLG.

However, differences with previous experiments can be noted. In particular, the domain walls stabilize around the AA region into a so-called *swirl* that rotates anticlockwise (magenta) or clockwise (cyan) as shown on Fig. 4.7. It is this pattern that we will discuss now. We understand it as a result of the atomic relaxation of a new type of moiré : not that of a twist but rather that of a biaxial heterostrain.

Such a *swirl* feature was already observed in other 2D materials such as graphene trilayers [194], TaS_2 bilayers [195], or WS_2 bilayers [196]. But also in polyatomic metallic surfaces, such as $Au(111)$ including Na adsorbates [197], epitaxial Cu on $Ru(0001)$ [198], $Ru(0001)$ etched by graphene [199], or $Au(111)$ including Gd adsorbates [193]. Although the origin of this swirl is not always commented in the case of the previously mentioned 2D materials, in the metallic surface case the swirl is understood as originating from a lattice mismatch between the top layer periodicity and the bulk periodicity. This lattice mismatch can be described as a biaxial heterostrain as done in the calculations of Ref. [200]. In the case of Cu epitaxial layers, this mismatch is intrinsic as crystals of Ru and Cu do not have the same lattice constant. This swirl feature thus disappears when a higher number of layers are deposited, and the strain is released. In the case of $Ru(0001)$ etched by graphene, additional Ru atoms are displaced by the graphene growth from a step edge to the first layer of $Ru(0001)$, inducing a slight excess of Ru atoms in that layer and a lattice mismatch between the first and second $Ru(0001)$ layers. In the case of Au with adatoms, the top gold layer undergoes a lattice reconstruction induced by the potential of the adatoms, thereby changing the top layer lattice constant and inducing these features.

In the case of graphene bilayers, this feature is unobserved in graphene on $h-BN$ although reconstructed lattices of minimal angle TBLG have been extensively measured [81, 82, 83, 84, 87, 192]. However, both simple domain walls and swirl features similar to what we observe were recently measured in low-energy electron microscopy (LEEM) experiments on graphene grown on Si face SiC [80, 201] as shown on Fig. 4.9.

The structural characteristics of the structure in Fig. 4.7 can be compared to other bilayer graphene relaxation lattices [67, 81, 88]. The domain walls width is $30 \pm 7nm$, bigger than previous experiments. The size of the AA stacked region has a diameter of $9 \pm 2nm$, strikingly smaller than the DW width. This behaviour is different from previously measured twisted graphene relaxation lattices

where the AA region has a similar size to the DW size, in a $3-10nm$ range, indicating that the $\sim 90 \pm 10nm$ wide swirl of the domain walls observed in this case allows a more efficient reduction of staking energy than the straight domain wall case.

4.2.2 *Relaxation morphology of the swirl pattern*

These experimental observations point towards strong effect of the SiC substrate on the emergence of the swirl relaxation.

Biaxial heterostrain can be considered as a likely explanation for such relaxation pattern, as investigated in theoretical works for different materials [200, 202, 203]. In such a scenario, biaxial strain would arise during the growth process. Indeed, the covalent bonds that form between the buffer layer and the SiC lattice reconstruction force the graphene layer to adapt its lattice parameter to the SiC lattice, thus applying biaxial strain to the graphene lattice. In other words, because of the SiC reconstruction the buffer layer acquires an increased lattice constant, and thus contains a lower number of atoms than pristine graphene on a given surface. This phenomenon is probably highly dependent on temperature, as discussed in Ref. [171].

Upon intercalation, the graphene layer remains biaxially strained because the number of carbon atom it contains does not change. In addition, as noticed in Fig. 4.5, the layer is still attached to the SiC in the several non-intercalated regions so that it cannot relax in-plane to relieve this biaxial strain. In the intercalated regions, the graphene bilayer is thus biaxially heterostrained. On the other hand, as $h-BN$ and graphene interact through van der Waals forces, the lattice mismatch between both is not enough to induce relative biaxial strain between the graphene layers which would explain why the swirl reconstruction mode has never been observed in TBLG/$h-BN$.

Another possible scenario for this swirl pattern is a broken layer-mirror symmetry in the out-of-plane relaxation of the layers, as calculated in the case of TBLG by S. Dai *et al.* [204]. Although most calculations consider layer-mirror symmetric buckling near AA regions and expect it to be no bigger than 0.3Å [205], a much higher out-of-plane relaxation -typically multiplied by a factor 10- is found by allowing layer-mirror symmetry breaking. This scenario was also studied in Ref. [206] where the authors show that this type ot out-of-plane relaxation induces corrugations of the order of the angström, significantly affecting the bandwidth of the flat bands in low angle TBLG and inducing partial filling of the bands on a $\sim 0.1°$ range of twist angles. Such buckling is visualized on Fig. 4.10, which also demonstrates that such a high buckling is accompanied with a small biaxial strain near AA stacked regions. The work of Ref. [206] also quantifies the interatomic bond length changes induced by such buckling at AA regions which yields a $\sim 0.1\%$ biaxial strain.

Both scenarios are most likely intricate, and point towards the importance of biaxial heterostrain in the layers. In order to under-

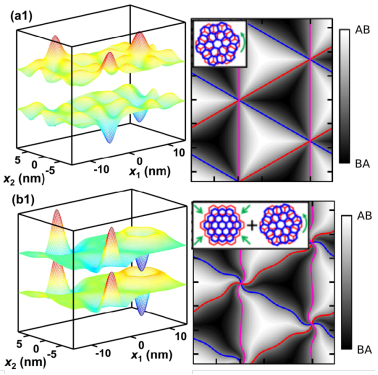

Figure 4.10: Possible relaxation modes with (top) and without (bottom) layer mirror symmetry. From Ref. [204]. The left pictures show the buckling shape of both layers and the right picture shows the atomic stacking after relaxation, with the inset showing the typical movement of the atoms near the AA region.

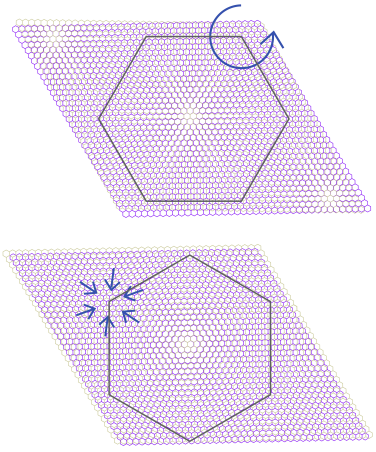

Figure 4.11: Real space stacking in a moiré arising from pure twist (top) or pure biaxial strain (bottom). Arrows sketch the lowest energy movement of atoms around AB/BA regions that is expected when closely looking at the image. The dark hexagon represents the Wigner Seitz moiré cell.

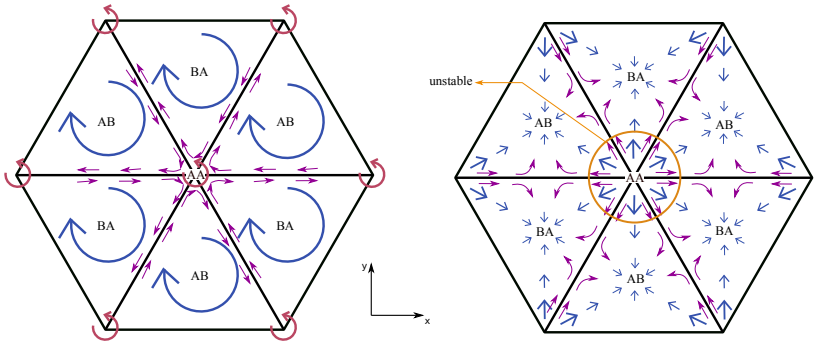

Figure 4.12: Qualitative sketch of expected atomic displacement directions upon relaxation in the large moiré regime, where the stacking fraction of AB regions is much bigger than the AA region. **a** Relaxation in the case of marginally twisted layers. **b** Relaxation in the case of slighly biaxially heterostrained layers. The DWs connecting AA regions are represented by black lines.

stand it, one can look more closely at the movement of individual atoms upon relaxation. The relaxation process starts from a given stacking and tends to concentrate strain at the domain walls of the relaxed pattern, by extending AB stacked regions and shrinking AA stacked regions. Marginal twist and slight biaxial strain both create a six-fold symmetric moiré that may seem similar at the large scale, but whose precise local stackings are different as evidenced on Fig. 4.11. Starting from a marginally twisted moiré or a slighly biaxially heterostrained moiré, the movement of the atoms upon relaxation is thus expected to be different.

The expected atomic movements upon relaxation in both cases are sketched on Fig. 4.12 for two different stacking configurations, in the regime where the area fraction of AB stacking is much bigger than the fraction of AA stacking.

In the case of relaxation starting from a marginally twisted moiré, local heterostrain is accumulated in the domain walls in the form of shear strain in the armchair direction as shown by the purple arrows on Fig. 4.12a. This shear is created with the rotation of atoms around AB regions in order to maximize their area. This rotation and shear is also visible in the calculations from Ref. [40, 72] presented in paragraph 1.5, although it corresponds to a relatively high twist angle (close to 1°), thus in the regime where the area fraction of AA and AB regions are comparable.

In the case of relaxation starting from a slightly biaxially heterostrained moiré, we expect the atoms around AB/BA regions to shrink towards their center. The DW in the regions where AB and BA stackings are closest is thus purely uniaxially strained in the direction perpendicular to the DW. This uniaxial strain is decreased to the profit of a uniaxial strain parallel to the DW, as the atoms get closer to AA stacked regions.

The latter relaxation mode results in importantly strained graphene lattice near the AA region center, which is energetically costly and thus unstable. Instead, shear would be more favorable, as it is less energetically costly [200]. Indeed, it resembles most to a twist which is the lowest possible energy configuration [18]. Given this observation, the apparition of the swirl can now be understood by closely studying on Fig. 4.13 the differences between a purely strained DW

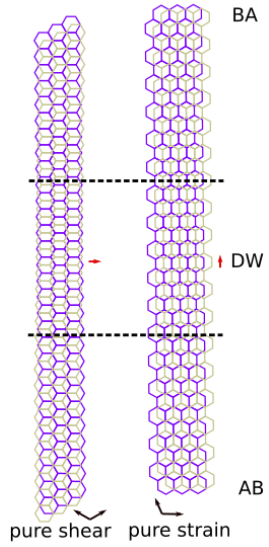

Figure 4.13: Sketch of the two possible AB / BA domain walls, delimited by the dashed lines. The gray layer is either strained or sheared by the amount given by the Burger vector (in red). The pure shear has a Burger vector parallel to the graphene armchair direction and parallel to the DW direction. The pure strain has a Burger vector perpendicular to the DW direction. The crystallographic directions are shown in black arrows.

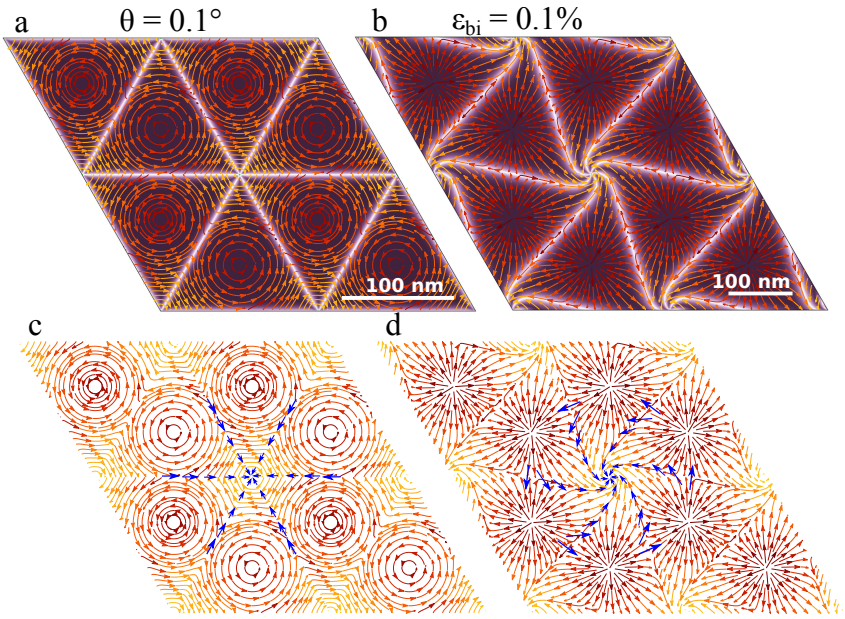

Figure 4.14: Stacking parameter of relaxed structures starting from a twist angle of 0.1° (**a**), and a biaxial strain of 0.1% (**a**). Calculations are performed by Niels Walet as described in Ref [75]. The yellow and red arrows correspond to the calculated flow of atomical motions between unrelaxed and relaxed positions, for the top layer. In the bottom layer, the atoms move in the opposite directions. **c** and **d** show the same streamlines, with local Burger vectors in blue along the domain walls.

and a purely sheared DW that separates the AB and BA regions. For that, it is useful to consider the *Burger vector*, that quantifies the shift of the lattice across a dislocation : the DW can be seen as such a dislocation [82, 207]. We find that the direction of a purely uniaxially strained DW is oriented perpendicular to the Burger vector and the zigzag graphene cristallographic direction. On the other hand, a purely sheared DW is necessarily parallel to the Burger vector and the armchair graphene direction.

In biaxially heterostrained bilayers the swirl induces a gradual rotation of the Burger vector from the center of the domain wall towards AA region. This allows to relax elastic energy more efficiently as it induces a transition from the energetically costly uniaxial DW to the more favorable sheared DW. This has the advantage of further reducing the size of AA region to gain more elastic energy.

The apparition of the swirl can be investigated theoretically. For this we turn to the relaxation models as presented in section 1.5 and performed by Niels Wallet following previous works [75, 103]. In this case, the potential model is a modified version of the AIREBO potentials as proposed in Ref. [208] (modeling the intralayer binding energies), in combination with the Kolmogorov Crespi potential [78] (modeling the interlayer interactions). In addition, a flat layers approximation is considered.

The results are presented on Fig. 4.14, where the colormap corresponds to the quality of the stacking $w = w_{AA} - w_{AB}$: green color corresponds to AA stacked regions and dark purple to AB/BA stacked regions. The stacking alignment functions are explained in Ref. [75].

We first turn to the relaxation pattern of a purely marginally twisted system with large wavelength, namely $\theta = 0.1°$ on Fig. 4.14 a. We find the system does not relax into a swirl, therefore twist alone can-

The function w_{AA} quantifies the in-plane (δ normalized) distance between the interlayer nearest neighbors of an atom i at its position $\boldsymbol{r}_i$ and at positions $\boldsymbol{r} + \boldsymbol{\delta}_{AB}$, with $\boldsymbol{\delta}_{AB} = (\delta_1, \delta_2, \delta_3)$. The function w_{AB} does a similar thing but calculates two interlayer nearest neighbor distances and takes the minimal one : - the distances at position $\boldsymbol{r}_i$ and $\boldsymbol{r}_i - \boldsymbol{\delta}_{AB}$; - the distances at positions $\boldsymbol{r}_i + \boldsymbol{\delta}_{AB}$ and $\boldsymbol{r}_i - \boldsymbol{\delta}_{AB}$. The calculations yield for AA and AB/BA stackings the extremal values : $w(AA) = 0 - 3 = -3$ and $w(AB) = 3 - min\{0, 3\} = 3$ and $w(BA) = 3 - min\{3, 0\} = 3$.

not explain our observations. The local displacements of the atoms upon relaxation create a shear strain at the domain walls following the predictions of the qualitative sketch of Fig. 4.12, which can be understood by plotting the local Burger vectors in blue arrows on Fig. 4.14 c.

Then, we turn to a moiré system with large moiré wavelength containing small biaxial heterostrain of $\varepsilon_{bi} = 0.1\%$. We find on Fig. 4.14 b that relative pure biaxial strain is sufficient to induce the apparition of swirl relaxation pattern. The local displacements of the atoms upon relaxation clearly create an uniaxial strain domain wall in between AA regions. This can be described by a Burger vector perpendicular to the DW direction as shown in Fig. 4.14 d. This Burger vector gradualy rotates when the DW gets closer to the AA region, as the DW slowly shifts into a shear type DW where the Burger vector is parallel to DW direction. We find that the swirl pattern fits well the experiment with its diameter close to $90nm$. This was not the case in the calculations of S. Dai [204] where the swirl is found to be smaller than $15nm$ independently of the moiré length.

We verify on Fig. 4.15 that no swirl is observed for a pure biaxial strain of 0.8%. This suggests that there exists a critical moiré length at which the swirl can develop, and below which the DWs remain straight. This moiré wavelength should be over $100nm$, which corresponds to a pure biaxial strain of $\varepsilon_{bi} = 0.245\%$.

In order to verify that there exists a critical moiré length for swirl relaxation, and verify if the size of the swirl can vary with the value of biaxial strain, other cells with biaxial strains between 0.1% and 0.8% should be calculated.

In addition, the effect of uniaxial strain on the swirl pattern should be investigated, as it is most likely present in our experimental stacking as well, given the strong anisotropy of the triangles visible on Fig. 4.7.

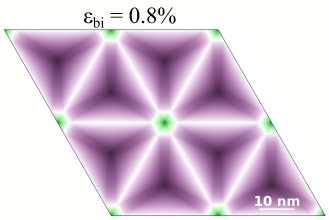

Figure 4.15: Stacking parameter of a relaxed structure starting a biaxial strain of 0.8%.

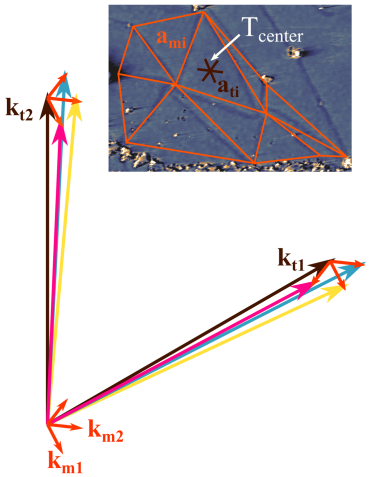

Figure 4.16: Sketch of the possible stackings of the bottom graphene periodicity (yellow, blue and red) for a given top graphene periodicity $\boldsymbol{k}_{ti}$ (brown) and moiré periodicity (orange) $\boldsymbol{k}_{mi}$, $i = (1,2,3)$. The inset shows the swirl relaxation pattern with its top layer graphene cristallographic directions in brown and the rigid triangular lattice in orange. The central triangle T_{center} is chosen as the most representative and we focus on it the following.

4.2.3 *Experimental minimal twist and heterostrain*

It is thus of interest to determine what is the original stacking type of our relaxed pattern. In other words, we want to know what is the *unrelaxed* experimental stacking, either twist-like, biaxial strain-like, or a more general stacking where both minimal twist and heterostrain is present in the moiré. This can be done by measuring the moiré period, which does not change upon atomic relaxation. However, in our experiment the moiré period is clearly position dependent as evidenced by the position dependent length of the DWs. To overcome that difficulty, we estimate the local unrelaxed experimental stacking at the scale of a triangular region defined by the domain walls. The determination of relative stacking in each triangular pattern is done with a method close to the commensurabitlity method presented in section 3.2.1 that we describe now.

In Fig. 4.16 we define the triangular network from which the local moiré vectors $\boldsymbol{a}_{mi}$, $i = (1,2,3)$ are defined. The graphene periodic-

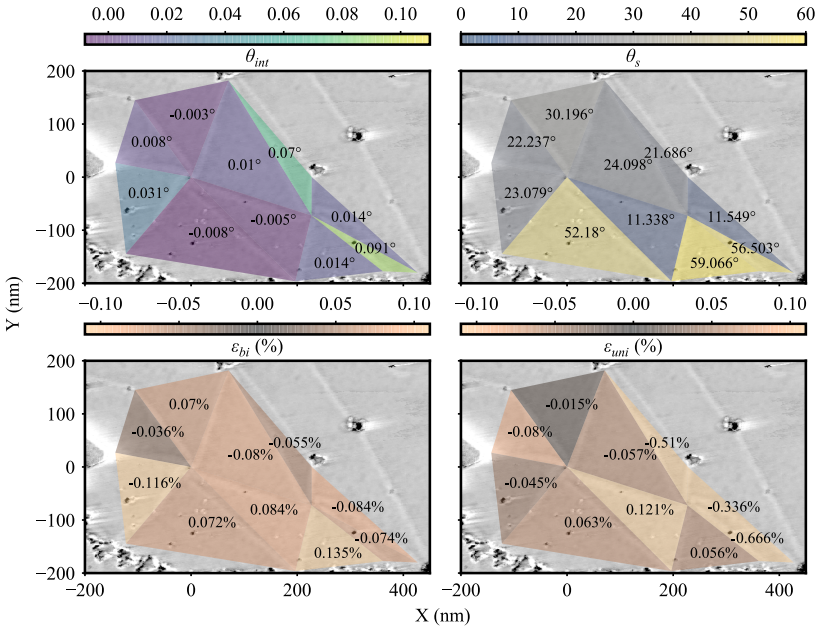

Figure 4.17: Local commensurability analysis performed as explained in the text. For each triangle, the relative stacking parameters (θ_{int}, ε_{bi}, ε_{uni}, θ_s) are determined in the case where twist angle is the lowest. Background is taken from Fig. 4.7.

ity of the top layer measured from STM images is also shown. Its orientation is provided from atomically resolved STM images in the AB region. This orientation actually does not vary at the scale of the image, even close to the domain walls where the directions don't tilt by more that 0.5°, although it is there that strain is accumulated.

The periodicities can be conveniently represented in Fourier space as done on Fig. 4.16. The moiré periodicity shown in orange can be replicated at the top layer and define the bottom layer $\boldsymbol{k}_{bi}$, $i = (1, 2, 3)$. In the most general case $\boldsymbol{k}_{bi}$ can be defined in three diferent ways given here in yellow, cyan and magenta colored arrows, that we cannot discriminate *a priori* in such a relaxed system. The relative stacking corresponding to these three solutions can correspond to mostly twisted layers including some biaxial heterostrain, mostly biaxially heterostrained layers with some twist, or a balanced combination of both. In addition, uniaxial strain can always be present on top of that biaxial strain and twist.

The commensurate indexes and physical heterostrain parameters including twist angle, biaxial strain, uniaxial strain, and its angle of application (θ_{int}, ε_{bi}, ε_{uni}, θ_s) are determined as decribed in section 2.3.1. In practice, we first need to retrieve the Park Madden matrix, which is done by using its definition (see section 2.3.1) with the previously determined top graphene layer and bottom graphene layer periodicities :

$$\begin{pmatrix} a & c \\ b & d \end{pmatrix} = \begin{pmatrix} \boldsymbol{k_{t_1}} \\ \boldsymbol{k_{t_2}} \end{pmatrix} \begin{pmatrix} \boldsymbol{k_{b_1}} \\ \boldsymbol{k_{b_2}} \end{pmatrix}^{-1} \tag{4.1}$$

The three possible relative stacking arrangements are shown on Figs. 4.17 and 4.18. There is a configuration in which the twist angle is very small with a significant biaxial heterostrain (Fig 4.17). In the

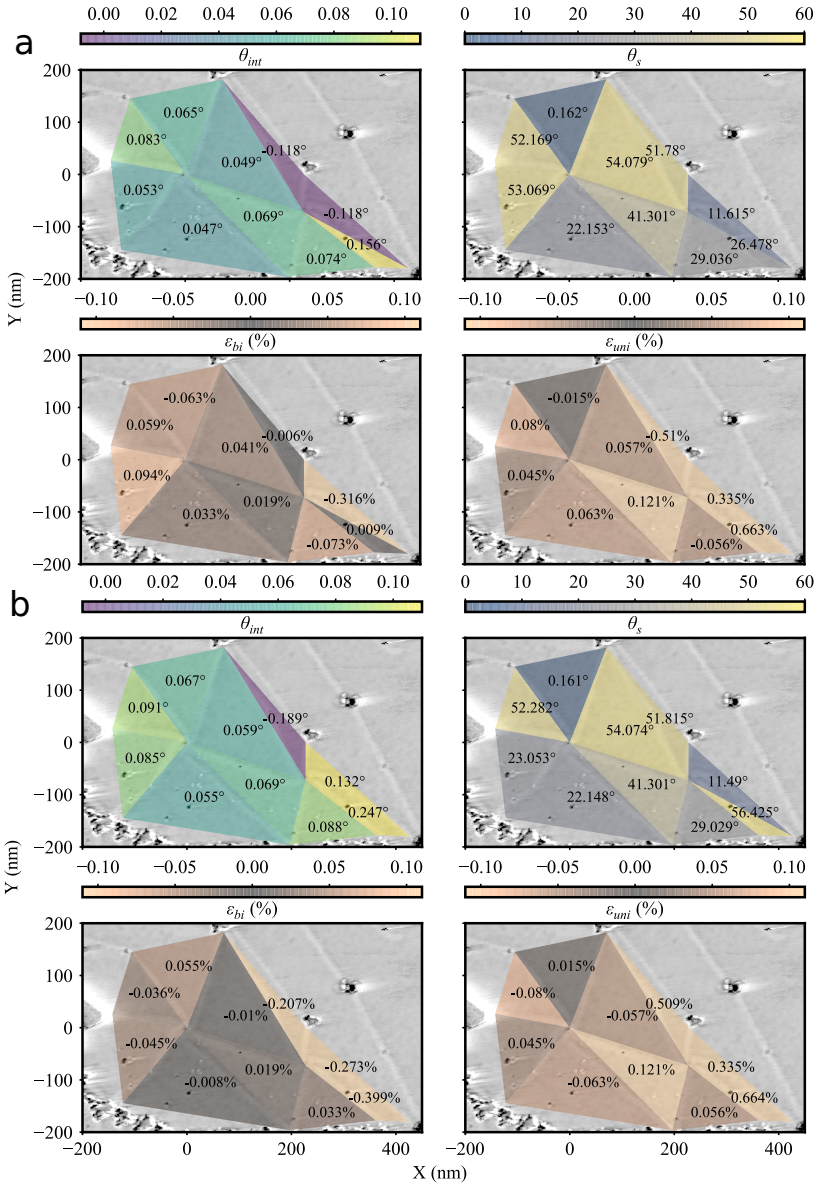

Figure 4.18: Local commensurability analysis performed as explained in the text. For each triangle, the relative stacking parameters (θ_{int}, ε_{bi}, ε_{uni}, θ_s) are determined in the case where twist angle value is the biggest. **a** and **b** panels correspond to increasing interlayer twist angle. Background is taken from Fig. 4.7.

two other possible configurations the twist angle is bigger and biaxial heterostrain is smaller than in the first configuration (Fig. 4.18). Some uniaxial heterostrain is always present, and can be quite high (up to 0.7%) in the triangles most right, which is expected from their longitudinal shape. We therefore focus on the triangles of the clockwise rotating swirl relaxation pattern, in particular we define in Fig. 4.16 the most representative triangle in the center of the swirl pattern which we call T_{center} in the following.

In the case of the lowest angle configuration, the twist angle is typically 0.01°, with some small uniaxial heterostrain (typically 0.06%), but also biaxial heterostrain about 0.08%.

In the case of Fig. 4.18 a and b, the twist angle reaches 0.08° and 0.09° respectively, which comes along a decrease of biaxial heterostrain which this time is about 0.05% and 0.03%.

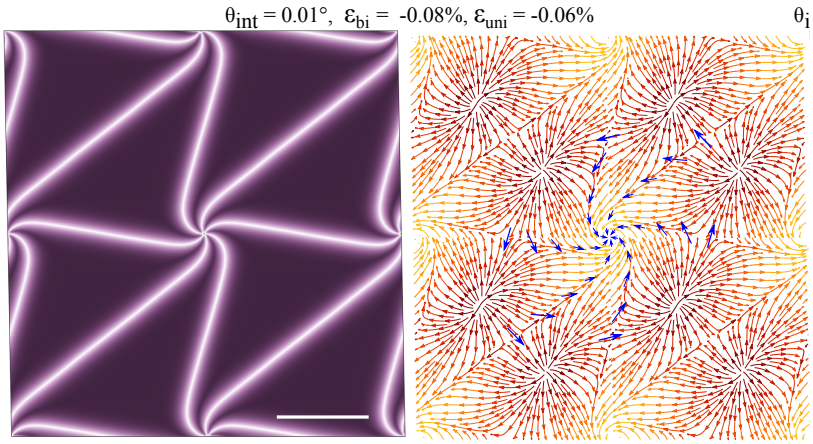

Figure 4.19: **left** Stacking parameter of the relaxed T_{center} structure from Fig. 4.17 with a twist angle of 0.01°, a biaxial heterostrain of -0.08%, and a uniaxial heterostrain of -0.06%. The scale bar is $100nm$. **right** Calculated flow of the atomic motions between the relaxed and unrelaxed positions, for one layer. The blue arrows are the local Burger vectors for the domain walls.

The uniaxial heterostrain is the same in all three configurations, as it is a measure of the anisotropy of the triangle. Instead, the twist angle and biaxial strain are scaling factors of the size of the triangle, which explains why one increases when the other decreases for a given triangle.

In the clockwise swirl, the average biaxial strain from Fig. 4.17 is 0.08%, which is surprisingly close to the expected Gr/SiC lattice mismatch $\varepsilon_{Gr/SiC} = 0.075\%$. The latter corresponds to the ratio between the SiC superperiod and the (integer) number of Graphene atoms (13) that can be fitted in that superperiod : $\varepsilon_{Gr/SiC} = 1 - \frac{13a_{Gr}}{6\sqrt{(3)}a_{SiC}}$ [201], with $a_Gr = 0.2456nm$ and $a_{SiC} = 0.307nm$. It thus gives another argument for biaxial heterostrain arising during the growth, from the covalent bonds between the buffer layer and the SiC reconstruction lattice that induces a lattice constant change as discussed in paragraph 4.2.2.

We use the rigid triangle T_{center} with heterostrain configuration from Fig. 4.17 ($\theta_{int} = 0.01°$, $\varepsilon_{bi} = -0.08\%$, $\varepsilon_{uni} = -0.057\%$, $\theta_s = 24°$) to calculate the corresponding relaxed structure as done in the previous section. The minimization process yields a swirl pattern shown on Fig. 4.19 with swirl diameter of almost $100nm$, an AA stacked region diameter of $3 \pm 1nm$ and DW width of $20 \pm 10nm$. These values agree with the experimental findings, except for the AA region that is underestimated by a factor ~ 3. A possible reason for this discrepancy is that corrugation is neglected in these calculations, and we expect out-of-plane atomic movements to be biggest in these AA stacked regions.

The relaxation pattern of the two other heterostrain configurations of T_{center}, given on Fig. 4.18, are also calculated and shown on Fig. 4.20. These calculations show that the (anti)clockwise direction of the swirl can be controlled by the sign of the biaxial heterostrain. More strikingly, they show that a lower biaxial heterostrain to the profit of an increased twist angle decreases the bending behaviour of the DW, because the uniaxial heterostrain character of the DW decreases with increasing twist angle and decreasing biaxial heterostrain. This

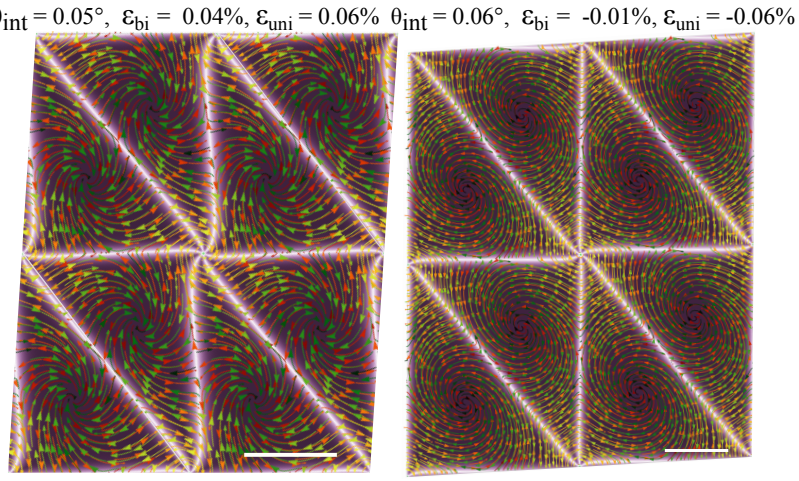

Figure 4.20: Stacking parameter of the relaxed T_{center} structure from Fig. 4.18 with (**left**) a twist angle of 0.05°, a biaxial heterostrain of 0.04%, and a uniaxial heterostrain of 0.06% ; and with (**right**) a twist angle of 0.06°, a biaxial heterostrain of -0.01%, and a uniaxial heterostrain of -0.06%. The orange and red (resp. the yellow and green) arrows show the calculated flow of the atomic motions between the relaxed and unrelaxed positions, for the top (resp. bottom) layer. The scale bar are $100nm$.

is further illustrated by the flow of atomic motions that resemble more and more to the twist relaxation flow presented on Fig. 4.14 a and c. The typical length scales of the DWs, swirl diameter and AA region diameter are, within errorbars, the same independently of twist angle and biaxial heterostrain values.

To sum up, we can understand the structure of our swirl relaxation pattern by taking into account biaxial heterostrain in the system, that originates most likely from the growth process during which the buffer layer bonds to the SiC reconstruction and adapts its lattice parameter accordingly. This relative strain produces a domain wall morphology which is quite different from the pure twist angle case, and which is energetically less favorable, thereby inducing the swirl phenomenon. The relaxation calculations are able to reproduce the experiments, except for the estimated size of the AA stacked region which is underestimated. As we expect AA regions to experience the highest corrugation, it is most likely the cause of this discrepancy and in future calculations out-of-plane relaxation of the layers should be included. A systematic investigation of how the size and the direction of rotation of the swirl depends on out-of-plane relaxation, biaxial heterostrain intensity, and uniaxial heterostrain would also be useful. Finally, an investigation of the electronic properties could give us an additional experimental argument to understand the precise local stacking of the structure.

4.3 *Electronic properties of the system*

Thanks to STM, we not only investigate the structural properties of the surface but we also get information on the electronic properties, by measuring the local density of states.

4.3.1 *Electronic properties from spatially resolved LDOS*

By combining scanning and DOS measurements, we can obtain *differential conductance maps* that give spatially resolved information of

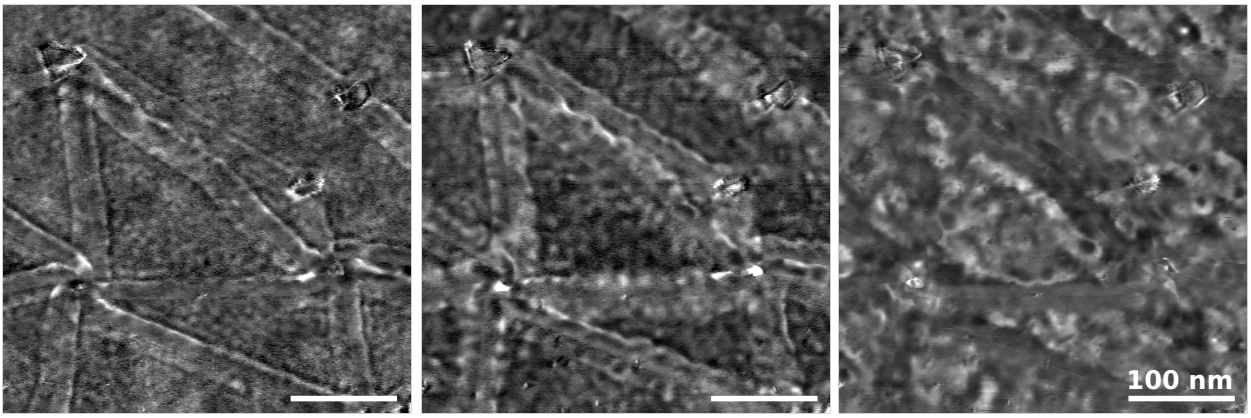

Figure 4.21: Conductance maps of the swirl pattern measured at (V_b = $-190meV$, I_t = $250pA$) (**left**), (V_b = $-150meV$, I_t = $250pA$) (**middle**) and (V_b = $-91meV$, I_t = $250pA$) (**right**). The Lock-in modulation is set to $4meV$ at frequency $379Hz$. The Lock-in timescale is set to $30ms$, which makes each image over 2hours long.

the DOS at a given energy. Such a measurement is performed by measuring the differential conductance dI/dV with a Lock-in. Its time constants are set to fit scanning speed and resolution parameters, so that differential conductance is measured at each pixel along the scanning, at the energy of the scan V_b. Such differential conductance maps can be very useful as they enable to get highly resolved information on the conductance, at a single energy.

This is illustrated on Fig. 4.21 where three conductance maps are taken at the swirl pattern location. At $-190meV$, states at the edges of the domain walls are clearly visible. At lower bias ($90meV$), these states are no longer visible, but an irregular pattern which we associate to confined modes - or scattering interferences - inside the irregular triangle. At an intermediate filling ($-150meV$), AA stacked regions show a very high density of states. At this energy, both disordered scattering and states at the edges of the DW are visible. The low energy properties of the system is thus quite rich and needs to be studied carefully. In order to investigate these features in detail, we first need more information on their energy dependence.

We turn to another measurement technique that combines the spatial resolution of STM with spectroscopic measurements (STS, see section 3.1.2). This is done using a common procedure called Current-Imaging Tunneling Spectroscopy (CITS). In a CITS, imaging is done at a given setpoint (V_b, I_t). The imaging stops regularly in the image and records STS spectra at the scanning setpoint. This technique thus provides spatially resolved DOS with high energy resolution, at the expense of spatial resolution if one wants to measure during a reasonnable timescale, since each spectrum requires a finite time to record. One of the main advantages of this method is that the tip height is kept constant during the bias sweep, which enables to get information on the low energy states while minimizing the tip interaction. The latter can be noticed in particular at low bias in the center of the DWs where strain is concentrated, for example on Fig. 4.21 (right). In the following, we thus choose this technique to investigate the swirl relaxation pattern.

We average LDOS spectra in specific regions from the CITS mea-

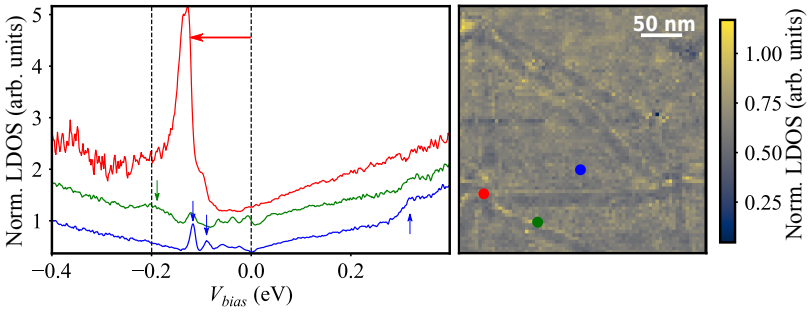

Figure 4.22: CITS of the swirl relaxation pattern. The setpoint is (V_b = +300meV, I_t = 250pA). Blue, Green, and Red spectra are normalized STS spectra averaged around regions respectively in AA stacking, close to a domain wall, and in AB stacking. Spectra are shifted vertically fore clarity. The red arrow illustrates the doping of graphene from zero bias (gray line). The green arrow highlights the energy of the states localized at the DW. Blue arrows highlight a gap opening in AB region near charge neutrality ; and a step like feature in the spectrum near +300meV. The CITS map on the right showing the spatial resolution is plotted at −200meV (black line). For the sake of comparison, this CITS is about 2.5 days long.

surement as shown on Fig. 4.22. The STS spectra point towards a −125meV doping of the bilayer graphene, that originates from the SiC substrate as explained above.

The LDOS at the AA stacked region (Fig. 4.22, red) features a high density of state peak that is similar to the localisation of electrons expected in relaxed minimally twisted samples.

In AB stacked regions, two main features that are typical of a gapped graphene bilayer can be noted (see Fig. 4.22, blue and fig. 4.23). Two peaks close to charge neutrality correspond to a gap induced by the electric field that arises upon differential doping of the bilayer. Here the gap is Δ = 26meV, which corresponds to a difference of potential of the layers such that $eV \sim \Delta$ in the limit (valid here) where $t_0 >> \Delta$ [209]. For an interlayer separation of 0.33nm, the corresponding electric field is $\boldsymbol{E} \sim 78mV/nm$.

As the gap should depend on the doping, we estimate a value of the doping of the bilayer, by numerically integrating the DOS between the Fermi energy V_b = 0meV and the Dirac energy $V_b \sim -110 \pm 10meV$: $n = \int_{E_D}^{E_F} \frac{\partial n}{\partial E} dE$. The DOS is approach by the parabolic-like expression from section 1.2. In that case, the doping per unit area determined from the integral is $n = 1.3 \cdot 10^{12} cm^{-2}$. In a model taking into account the screening of the electric field as done in Ref. [210], this doping corresponds to a gap of $\Delta \sim 20meV$. This value is also consistent with the spectroscopic measurements from Ref. [211].

In addition, a step feature in the spectrum can be noticed $\sim 450meV$ above charge neutrality, which is consistent with the filling of a higher energy band in AB bilayer, comparable with other experiments [88, 170, 179, 180], and confirming the theoretical prediction of t_0 = 450meV.

Last, two interesting features can be noticed in the spectrum. States localized at the edge of the domain walls that are visible in the differential conductance map in Fig. 4.21 are attributed to the broad peak near −200meV in the green STS spectrum of Fig. 4.22. We emphasize that this peak is outside of the gap and thus has a different origin than helical edge states discussed in section 1.5.2. We will discuss these localized states in section 4.3.3. The second interesting feature is a set of peaks between charge neutrality and zero bias, which are visible both in the spectrum close to the DW (green spectrum) and in AB stacked region (blue spectrum). These correspond

In the following we also call the charge neutrality *Dirac energy*, E_D, in reference to the monolayer graphene case where charge neutrality lies exactly at the Dirac energy, where the dirac cone closes.

The 2D DOS including spin using equation 1.10 is written $\frac{\partial n}{\partial E} = \frac{\partial n}{\partial k}\frac{\partial k}{\partial E} = 2\frac{k}{2\pi}\frac{\partial k}{\partial E} = \frac{t_0}{2\pi(\hbar v_F)^2}\frac{E}{\sqrt{E^2-(\frac{eV}{2})^2}} \sim \frac{t_0}{2\pi(\hbar v_F)^2}$

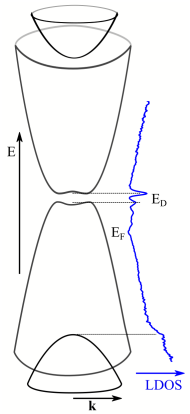

Figure 4.23: Sketch of the gapped bilayer bands along the corresponding STS spectrum with characteristic features (gap, higher energy band step) emphasized with dashed lines.

to the scattering waves noticed in Fig. 4.21. We now discuss these confined states in more details.

4.3.2 *Confined states in AB/BA regions*

Real space differential conductance images show that standing waves of energy dependent wavelength can be observed in AB/BA stacked regions, above the gap and up to slightly above the Fermi energy. These standing waves result from the confinement of states induced by back-scattering at the DW. Fig. 4.24 shows such standing waves at energy $\sim 120meV$ above charge neutrality, in the triangle at the top of the swirl.

The energy dependence of these standing waves is shown on Fig. 4.25(2), where a cut across the triangle is performed and the LDOS is plotted for each bias voltage. The confined states can be visualized by the size of the oscillations between the DWs edges. These states have a decreasing wavelength for increasing energies. Although the signal is reduced near zero bias, which is typical for phonon-induced tunneling suppression at these energies [212], these oscillations are visible up to $50meV$.

Similar quasiparticle interferences have been extensively used to image the Fermi surface of electrons and reconstruct the dispersion of surface bands in many materials [213]. We proceed in the same way to retrieve the conduction band of this AB bilayer graphene.

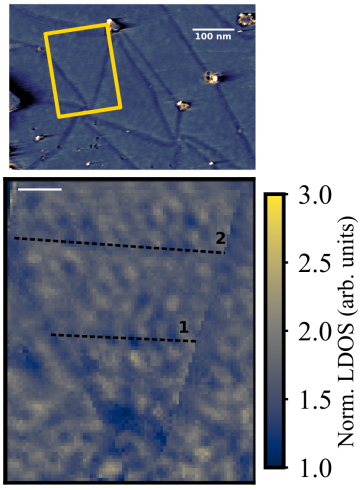

Figure 4.24: CITS map taken at $V_b = -7.3meV$ centered on the topmost triangle of the flower. The setpoint is ($V_b = +150meV$, $I_t = 250pA$). The dashed lines correspond to the spatial cuts shown on Fig. 4.25. The scale bar is $20nm$.

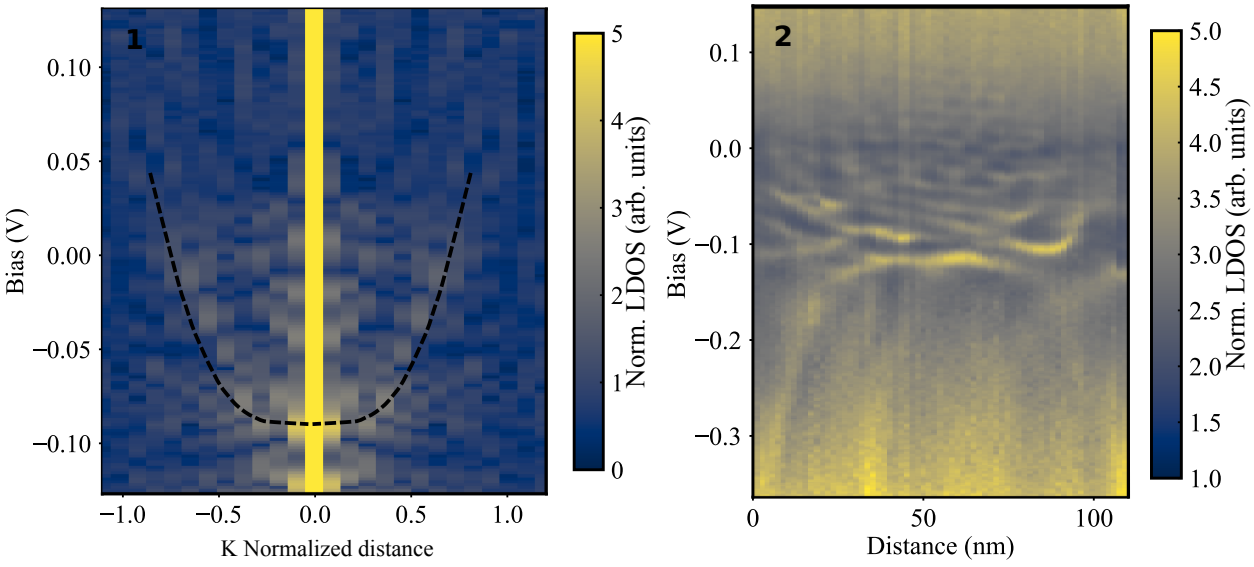

Figure 4.25: **(left)** Fourier transform of the LDOS spatial line cut **1** from Fig. 4.24. The dashed line corresponds to equation 1.10 with $V = -110meV$. **(right)** Line cut **2** from Fig. 4.24. E_D is close to $-110 \pm 10meV$.

The Fourier transform of a cut across the triangle is plotted on Fig. 4.25(1) and gives a direct visualization on the parabolic-like conduction band above charge neutrality. The dotted line is plotted from equation 1.10 in this range of energies. The single adjustable parameter is the vertical position of the band resulting from doping

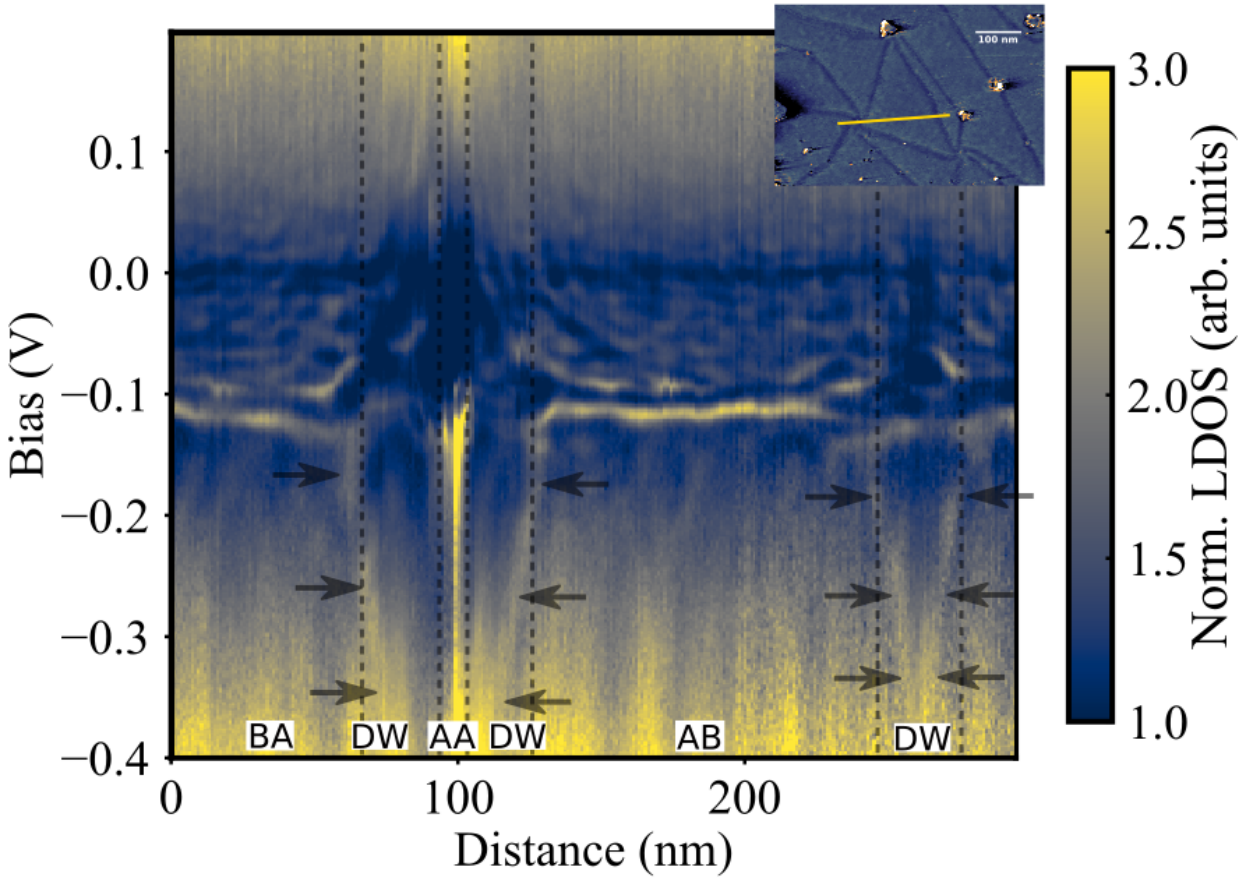

Figure 4.26: LDOS spatial line cut across the top central triangle as shown on inset. The setpoint is (V_b = +200meV, I_t = 250pA). The cut features confined states in AB regions above the electric field induced gap at E_D. This gap is tracked by the two peaks around $\sim -110meV$. A high density of state peak is visible in the AA region. As shown by the vertical dashed lines guiding the eyes, the cut also crosses part of the domain walls (DWs) surrounding one AA stacked region, and one DW between AB and BA region. Black arrows highlight the localized states outside the gap.

which is consistent with the value of the gap as explained above. The low energy limit model thus describes satisfyingly the data.

A 2D Fourier transform over the whole confined area could also be performed, in order to visualize the Fermi surface in k-space and retrieve the band dispersion with a better signal to noise ratio than in the 1D cut of Fig. 4.25. However, due to the spatial irregularity of these standing waves, the periodicity is lost on average in such a 2D Fourier transform. This disorder is mainly due to the irregularity of the triangular pattern. Slight charge reorganizations that occur on the surface also play a role in that disorder, by creating both doping variations and gap changes. Indeed, such disorder potential variations have been previously measured in graphene on $SiO2/Si$ substrates [190, 214], revealing that it can lead to important spatial fluctuations of the electronic properties, such as the formation of interacting quantum dots. In our sample, such a spatial modulation of charge neutrality is reasonable and has already been measured in non-intercalated similar samples [180].

4.3.3 *States at the domain walls*

Conductance maps on Fig. 4.21 have revealed the presence of localized states near the DW. We now turn to describing these states as

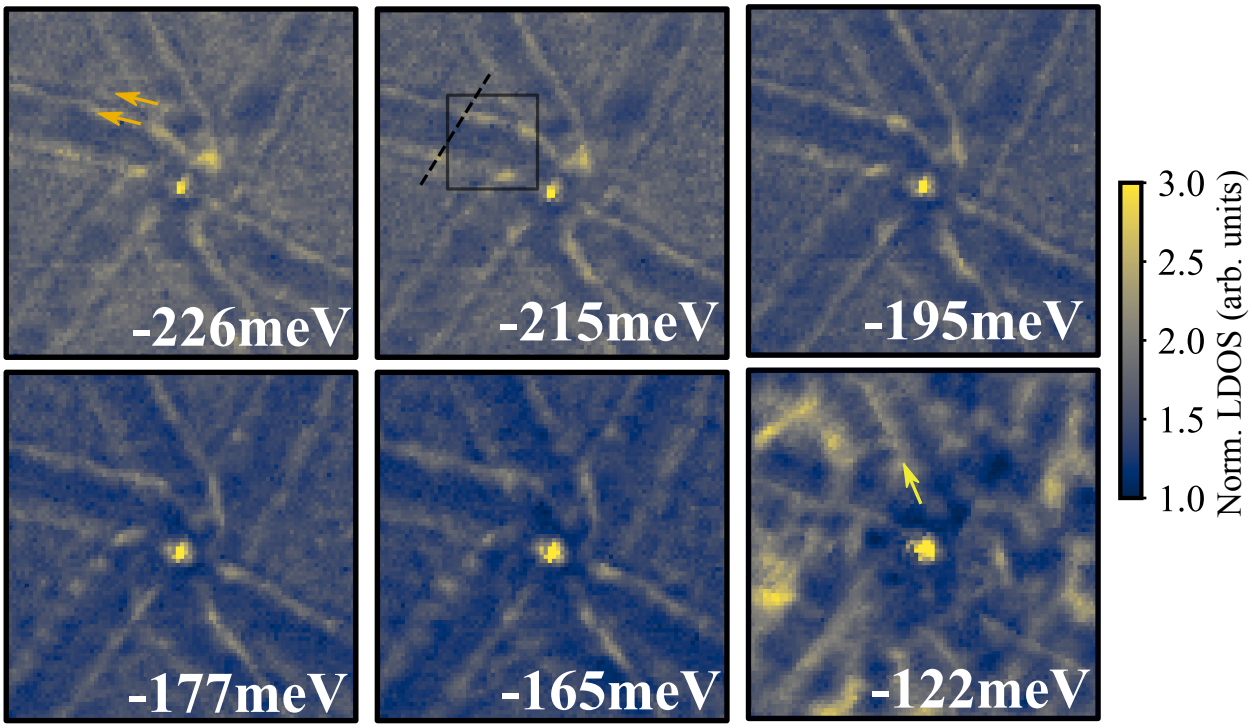

Figure 4.27: Differential conductance images for various energies. The set-point is (V_b = +200meV, I_t = 250pA). They feature an energy peak at charge neutrality in the middle of the DW highlighted by a yellow arrow in the $V_b = -122meV$ differential conductance map. They also shows that a second edge state can be detected at some domain walls, as highlighted by orange arrows on the $V_b = -226meV$ map.

well as giving a preliminary understanding, although they are yet to be understood in the light of a more complete model.

Localized states outside of the gap

We have argued that the most visible localized states have energies outside the gap. Thus, they have a different origin than helical edge states discussed in section 1.5.2, whose energy lies in the gap.

Such localized states near the DW at energies outside of the gap have already been reported in marginally twisted bilayers (see section 1.5.2). These have been understood either in a local stacking picture, where the local bandstructure features saddle points that give rise to two LDOS peaks energetically symmetric around charge neutrality [88], or by considering the apparition of strain induced pseudo-Landau levels [89, 106].

An energy resolved plot of these states is given on Fig. 4.26, across the top right triangle of the clockwise swirl. This plot shows once again the irregular confined states all over the triangle above charge neutrality $E_D \sim -110 \pm 10meV$. The spatially localized edge states noticed in Fig. 4.21 are also visible at energies below E_D, both near the AB/BA DW on the right and near the DW that meet close to the AA region.

These states have increasing energy when getting spatially closer to the DW center, as highlighted with the black arrows on Fig. 4.26.

In order to understand these edge states better, we plot the differential conductance as a function of the voltage bias in Fig. 4.27. These maps confirm that the localized states appear closer to the domain

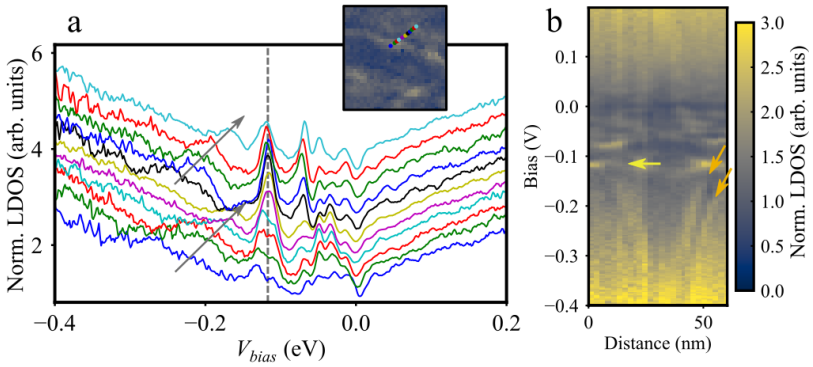

Figure 4.28: **a** STS spectra taken at the edge of the domain wall. The blue to purple spectra are taken regularly from the inner part of the DW edge to the outer part of the DW edge. The gray arrows highlight the energetically varying localized peaks and the gray dashed line the chage neutrality peak not varying in energy. The inset is a zoom from the black square of Fig. 4.27 showing the positions around which the STS spectra are averaged. **b** LDOS spatial cut performed along the black dashed line of the conductance map from Fig. 4.27. It features a peak at charge neutrality in the DW highlighted by the yellow arrow. It also features the two localized peaks indicated with orange arrows.

wall center as the bias is sweeped away from charge neutrality. In addition, further from the DW center, a dip in conductance followed by a second localized peak at energies close to $-200meV$ appear in the conductance maps. Both localized states are highlighted by the orange arrows in Fig. 4.27. The STS spectra of Fig. 4.28 taken regularly from the inner part of the DW edge to the outer part of the DW edge show that the energy of the localized states change with position. When getting closer to the DW center, this energy slowly shifts away from charge neutrality and the corresponding peak gets broader. A second peak on the outer part of the DW is also visible for certain energies, in agreement with the spatial observation in Fig. 4.27.

These observations reveal that the local electronic properties are closely linked to the local morphology of the domain wall.

We expect that the domain walls features concentrated and position-dependent heterostrain. Thus, a possible assumption is that these edge states come from strain induced pseudo Landau-levels.

In that description, the peak at the energy of the gray dashed line in Fig. 4.28 a is the zeroth pseudo Landau-level (0-pLL) localized at charge neutrality, and the localized peaks, whose energy shifts is highlighted by the gray arrows, corresponds to the first and second pseudo Landau-levels (1-pLL, and 2-pLL). The LDOS spatial cut on Fig. 4.28 b supports this observation. The yellow arrow highlights the 0-pLL and the orange arrows highlight the 1-pLL, and 2-pLL, showing that the distance between the peaks increases with the distance to the DW center.

Such a variation of the edge state peaks, getting away from E_D when approaching the DW, is consistent with the expected local strain distribution. Indeed, the latter should be bigger at the inner part of the DW edge, and decrease from there down to zero strain in AB/BA stacked regions, because of the relaxation process. As the strain decreases the strain induced pseudo magnetic field B decreases and the energy spacing of the 0-pLL (E_0) and the 1-pLL (E_1) should depend on B following a square root dependency $(E_1 - E_0)^2 \propto B$.

In this scenario, the absence of negative pLL can be attributed to

the strong electron hole asymmetry of strain induced pLL that was detected in previous experiments [107, 108].

Finally, the specific relaxation morphology of the uniaxial heterostrain DWs must not be neglected, and might give an alternative explanation to these out of the gap states. In particular they do not have the same direction with respect to the crystallographic directions than their shear-like counterparts, as discussed in section 4.2.2. Calculations of the local band structure and electronic properties of the different types of domain walls will thus be very informative for the understanding of this system.

In-gap helical edge states

In this system, one also has to consider the presence of helical edge states in the bilayer gap, that are expected in marginally twisted bilayers, as discussed in section 1.5.2. They should appear on each side of the domain walls and we expect two of them on each side, polarized in spin and valley.

In the presence of an electric field, a sign change of the gap near a given valley K_ξ occurs when crossing between AB and BA regions. This forces the apparition of two in-gap helical edge states (four edge states in total) [95, 100].

These states are hardly noticed in the spatially resolved differential conductance map of Fig. 4.27 a (see map at $V_b = -122meV$). Still, one can notice faint localized states in the gap at the DW position, in the energetically resolved cuts from Fig. 4.26 and Fig. 4.28 b. Whether these states correspond or not to helical edge states is still to be determined. However, in such a scenario, their lack of spatial localization could be explained by a small disorder potential that could induce valley scattering events between the helical edge states and bulk states and destroy the spatial localization of these states. Indeed, such scattering is not prevented by topology as discussed in other contexts by Refs. [215, 216] and [191].

In addition, the behavior of helical edge states in the case of a swirl DW should be studied theoretically to check whether they are affected by the DW specific structure.

4.4 Conclusion

In this Chapter, we have focused on a peculiar relaxation pattern that occurs in bilayer graphene on SiC substrate.

The morphology of this so called *swirl* relaxation pattern can be understood from biaxial heterostrain between the layers, a likely scenario in graphene grown on SiC because of the growth process in which covalent bonds form between graphene and the substrate. Further investigations of the morphology of the swirl pattern should focus on the effect of out-of-plane relaxation and uniaxial heterostrain.

The measurements of the electronic properties of the swirl relaxation pattern reveal a rich phenomenology having some similarities and differences with what has been observed in marginally twisted graphene layers. In particular we are at the moment not able to determine de precise nature of the one dimensional states localized near

the domain walls. Since these domain walls have a new structure showing a gradual change from a uniaxial to a sheared boundary between AB and BA regions, this calls for a detailed theoretical investigation of the electronic properties of such domain walls.

The experimental observation of the swirl pattern can be useful to theoreticians as it helps finding the relevant parameters in relaxation models along their typical scales. In addition, the precise understanding of atomic movements could gives additional information on how van der Waals forces and local strain interact. It also informs us on the growth process of graphene on SiC, by providing quantitative information on a scenario in which the buffer layer is biaxially stretched with respect to pristine graphene.

5
Extrinsic strain application

Contents

In condensed matter, strain can be used as a tool to probe the physical properties of a wide range of materials. During this thesis, a strain cell was designed and fabricated. The novelty of our design is to combine strain application based on longitudinal piezostacks with 4K STM measurements. In this Chapter, we present our setup and its characteristics at room temperature and cryogenic temperatures.

5.1 State of the art strain apparatus

Strain apparatus are extensively used to probe the structural and electronic properties of many materials. In condensed matter physics, to understand the effect of strain on the electronic and optical properties, we are interested in studying *in situ* strain at the local range.

In the early work (1988) by F. K. Men *et al.*, the authors designed a cantilever bar that could apply strain to Si(100) samples through bending while measuring LEED (Low Energy Electon Diffraction) patterns at high temperatures [217]. In that particular design, the strain variation was spatially resolved, as the cantilever applies a strain gradient to the sample.

This approach of straining by bending a sample is often used. In particular, a common design is the three point bending method shown on Fig. 5.1 that enables to tune the engineered strain by changing the distance between a pushing wedge and the counter supports. The wedge is usually a screw, but can also be a spring or a longitudinal piezostack.

Thanks to this design, several groups have studied slips, cracks and other dislocations in different materials using local probes. For example, strain in NaCl, LiF, or NiAl were studied using Atomic

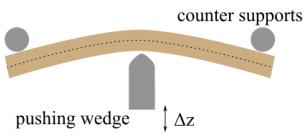

Figure 5.1: principle sketch of a 3 point bending setup.

Force Microscopy (AFM) [218, 219]. Detailed analysis of the surface can also be achieved in STM. Surface strain and dislocations on $Ag(111)$ on mica were for example studied in Ref. [220] in an ultra-high vaccuum STM with a 3-point bending system that could apply strains up to 0.5%. In a similar system, strain up to 0.16% in Si wafers was also studied in Ref. [221].

A very different setup for in-plane in situ strain in a UHV STM was built by Y. Nahas *et al.* [222]. In that setup high strains can be applied by external motors that can be declutched from the STM, in temperatures in the range $90 - 600K$. With that setup, plastic deformation ranges can be reached in a more controlled manner than in three point bending methods.

Another common method to tune strain *in situ* in STM is to glue a thin sample on a piezo material. This method takes advantage of differential thermal contraction between piezo and sample, that can even apply uniaxial strain by using materials with anisotropic thermal contractions. In addition, a voltage can be applied to the piezoelectric material to increase and tune the strain.

In this kind of setup, the experiments rely on the very small thickness of the glued sample, so that strain can be transmitted to the surface that is measured in STM. The maximal strain achieved in such experiments is about 0.3% [223], and the additional strain applied with voltages on the piezoelectrics is typically 0.05% maximum for 100μm thick samples [224].

With such small strains, the plastic deformation range is not reached and the atomic displacements are almost imperceptible, even with STM. This approach is thus suitable to studying symmetry breaking phases, in particular strain induced electronic reorganisation of electons for which STM is perfectly suited. Strain induced changes in Charge Density Waves were observed in $NbSe_2$ [225]. Other symmetry breaking phases were observed, such as a smectic electronic order in $LiFeAs$ [223] and a strain stabilized charge ordered state in $Fe_{1+x}Te$ [226].

Of course, such small strains can also be detected by STM in moiré materials as slight changes in atomic distances can induce significant moiré modifications. The control of heterostrain is particularly desirable in the context of such materials as it widens the parameter space that can tune the moiré, whose changes in turn tune the electronic properties of moiré materials.

We have seen that non tunable strain can be induced in such materials with complex substrate engineering, such as the use of engineered pillars [128], ripples [108, 126, 127], or microscale holes filled with a gas [228]. External strain tuning can also be achieved with external tip interactions in particular in suspended graphene [125]. But these tip induced strains can be hard to interprete because tip interaction can have multiple effects [44, 166].

Most recent efforts also focus on designing setups that can *in-situ* tune strain in exfoliated crystals, offering the perspective of applying tunable strain to moiré materials. L. Wang *et al.* [229] used the

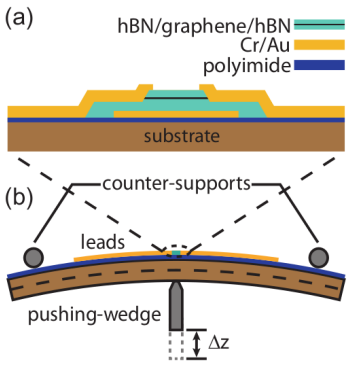

Figure 5.2: Encapsulated graphene on a bendable substrate. Good adherence of the flakes to the substrate is ensured by gold paddings. From [227].

common three point bending system to apply a 0.38% average strain in monolayer graphene encapsulated in hBN. To ensure strain is actually applied to the layers, gold paddings are added to ensure good clamping of the exfoliated layers on the bending substrate. Also, variable distance to the gate due to bending must be corrected in such transport experiments. V. Pasquier *et al.* [230] demonstrated strain application on a $MoSe_2$ flake, up to 1.6%. In that case, the strain is engineered by a slightly modified bending method in which a $NiTi$ alloy plate is attached to four clamps so that biaxial strain can also be applied. The challenge of clamping the flake is met by encapsulating the flake in PMMA deposited on a lift-off resist, or alternatively by 30nm thick Au/Ti strips if metal is needed.

Last, the specificity of 2D materials allows for original strain tuning methods investigated very recently. As an illustration, M. Kapfer *et al.* [231] use *in situ* bending of a graphene ribbon to spatially tailor the moiré supperlattice. Such bending is achieved by taking advantage of interlayer friction to clamp monolayer graphene between a still region and a movable graphite manipulator that can be moved by an AFM tip. Another method that also relies on the interlayer mechanical coupling has been demonstrated on $MoSe_2$ and twisted bilayers of graphene by T. Peña *et al.* [232, 233]. Strain is induced through interfacial friction by depositing stressed thin films on top of the material of interest.

In the following, we focus on the design of a cell that would enable to strain moiré materials, namely graphene on SiC, in a 1% strain range. The experimental challenge lies in the straining of a very hard material : the Young modulus of SiC is $E_{SiC} = 450GPa$. However, it offers large scale surfaces of clean graphene easily obtained from commercially available wafers, that feature moiré patterns at its surface. The experimental bet is that the specific structure of graphene on SiC [234] offers large domains interrupted by defects, step edges or big ripples that are believed to be directly connected to the substrate, and should thus transmit strain to the surface domains.

5.2 *Strain cell compatible with an STM*

Designing idea

Our strain cell is based on the design by A. Mackensie *et al.* [235]. The uniaxial strain application is based on longitudinal piezostacks. It demonstrated strains above 1% for samples with Young modulus similar to that of SiC. Most recently, a design similarly based on a sample bridged between piezostacks was demonstrated to be able to apply a 3% strain on a mechanically exfoliated $MoSe_2$ crystal [236] which is less stiff.

Our main interest in that design is its symmetry, that enables to go to low temperature while avoiding the application of uncontrolled strain from differential thermal contractions. Both extremities of the sample are clamped to titanium moving plates. Strain is achieved by

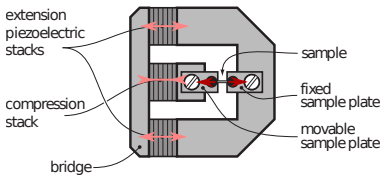

Figure 5.3: Design of a uniaxial strain cell based of longitudinal piezostacks, from the work of A. Mackensie *et al.* [235]. The uniaxial strain extention of the sample sketched in red arrows can be achived by applying a positive (resp. negative) voltage on the extention (compression) stacks, as sketched in pink arrows.

changing the length of the piezostacks that puts the titanium plates into motion in opposite directions. As the piezostacks of opposite titanium plates have the same length, their thermal contractions upon cooling are completely compensated.

This type of strain cell has been extensively used as a source of symmetry breaking to investigate unconventional superconductivity in materials such as (cuprates or pnictides) $YBCO_{6.67}$ [237], Sr_2RuO_4 [238], $Ba(Fe_{1-x}Co_x)_2As_2$ [239], or $Fe_{1+x}Te$ [226].

Our Strain cell Design

Our version of the strain cell is shown on Fig. 5.4. Its design is such that that STM operation can be conducted while applying strain to the sample. The sample is placed at the center of a $\varnothing$ = 46mm Titanium body, so that the tip of our STM falls on the sample when the strain cell and the STM head are assembled. Such assembling is shown on Fig. 5.5.

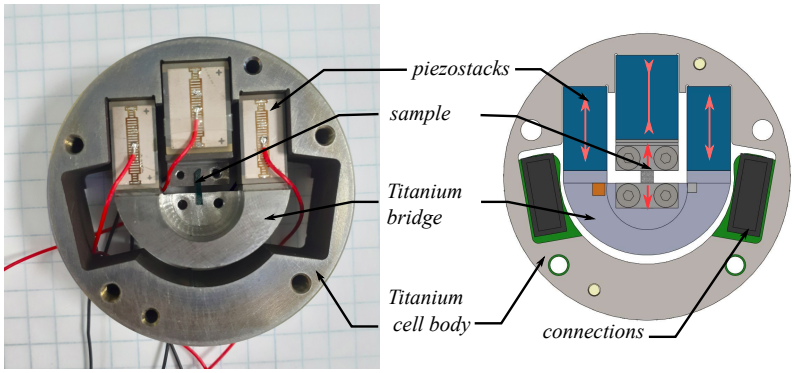

Figure 5.4: Experimental setup of our uniaxial strain cell. The left picture shows the cell with a sample in place and unclamped. Right sketch details the stretching operation of a clamped sample by applying a positive voltage on both outer piezostacks and a negative voltage on the inner piezostack.

The tip is placed within a 1mm range of the sample using optical visualization with a $\times(20-200)$ magnification in combination with a sub-millimeter screw device that enables to place the tip apex within a 50μm precision in the z direction.

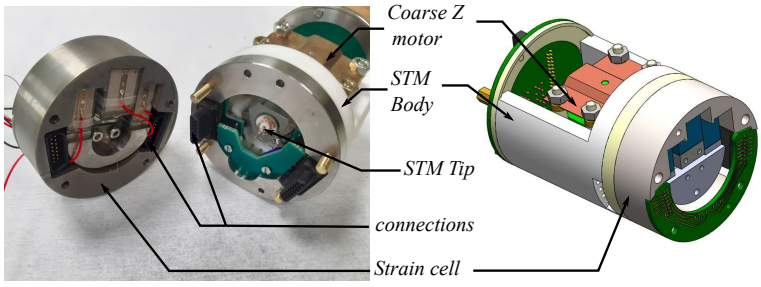

Figure 5.5: Experimental setup of our Scanning Tunneling Microscope equipped with a strain cell. Left picture shows the disassembled two components, and right sketch shows the system ready for operation, with the STM tip facing the sample.

Z coarse motor

In addition, the tip is approached within tunneling distance with a Z coarse motor relying on piezostacks located in the STM head. In our case the design for the coarse motor is compact, as sketched on Fig.

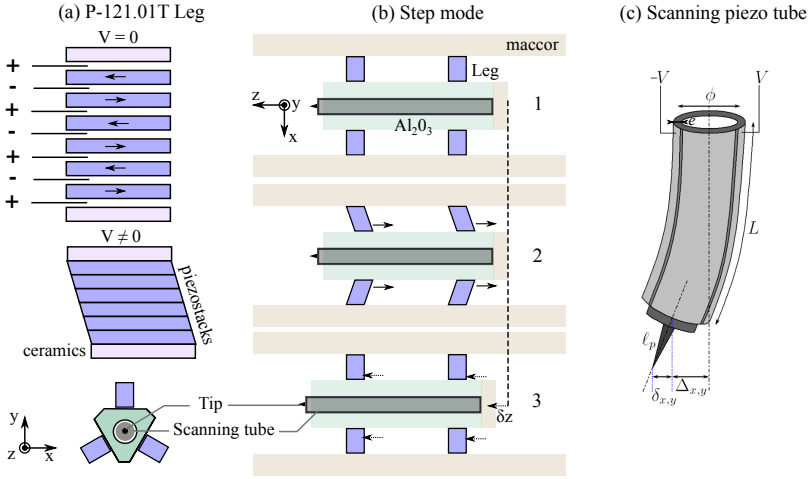

Figure 5.6: (**a**) Sketch of shear piezostacks as a function of voltage. (**b**) Sketch of the coarse motor in inertial mode. Z approach is achieved by applying an alternance of quick (2) and a slow (3) voltage ramps on the piezostacks.

5.6. The STM tube is glued on a maccor base, together with a Al_2O_3 prism. They are set into motion by six commercial shear piezostack "legs" (Fig. 5.6a) that are controlled by voltage ramps in a so called *inertial* mode in which during a fast ramp of voltage the stacks are bent and slide on the prism ; and during a slow ramp of voltage the stacks return to their initial position, dragging the prism and STM tube by friction (Fig. 5.6b). Between each step, the scanning tube in expanded to check whether the tip has reached a distance where tunneling is possible.

Scanning tube

The tube expansion and scanning are controlled by 5 electrodes (X^+, X^-, Y^+, Y^-, Z) that cover a piezoelectric material, namely $PbTi_{1-x}Zr_xO_3$ (with x close to 0.5), in the shape of a tube as sketched on Fig. 5.6c. Tube expansion or contraction is achieved by applying a differential voltage between the inner electrode Z and all outer electrodes. $\Delta_z = \frac{1.8 V_z d_{31} L}{e}$ where L and e are tube characteristics defined in Fig. 5.6 and d_{31} is the piezoelectric coefficient of the material.

Tube scanning is achieved by applying a differential voltage V between two facing electrodes that bends the tube so that the end of the tube shifts over the distance $\Delta_{(x,y)}$. In a low angle approximation, it is written $\Delta_{x,y} = \frac{1.8 V_{x,y} d_{31} L^2}{\Phi e}$ where Φ, L and e are tube characteristics defined in Fig. 5.6 and d_{31} is the piezoelectric coefficient of the material.

The scanning calibrations are done by changing, in the control electronics, the ratios $\Delta_{(x,y)}/V_{x,y}$ and Δ_z/V_z, which are extracted from imaging data on well known samples such as pristine graphene.

The maximum voltage that can be applied on the electrodes determines the scanning window of our experiment. In our case, with a tube length $L \sim 30mm$ and tip length typically $l_P \sim 2mm$, the scanning window width reaches over 5μm at 4K. This is quite large for low temperature STM measurements, which is an advantage when looking for evidence of strain on the surface.

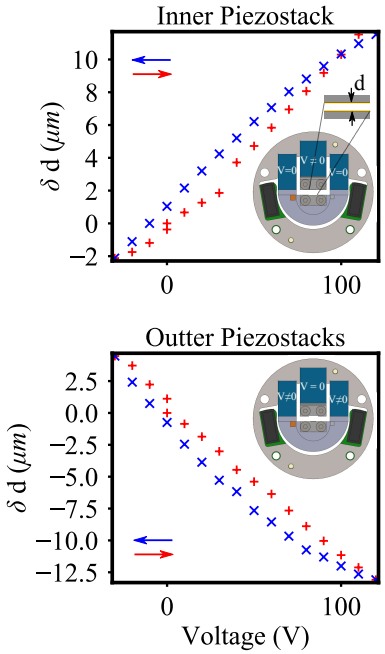

Figure 5.7: Relative displacement δd of $(100 \pm 2)\mu$m spaced metalic plates upon voltage application on the inner (**top figure**) or outer (**bottom figure**) piezostacks. Voltages are ramped from $0V$ to $120V$ (red) then to $-30V$ (blue) and ramped back to $0V$ (red) and show typical hysteresis. The plates consist in gold sputtered SiO_2 wafers of area $A = 3cm^2$, each of them attached to the strain cell moving titanium plates. The error on δd ($\sim 1\mu$m) is mainly due to the error on the determination of the initial distance between the plates d.

5.3 *Operating our strain cell*

Stress from piezoactuators

Strain application relies on longitudinal piezostacks that determine how much stress is applied between both titanium moving parts. A trade-of between the piezostacks dimensions for design requirements and strain application capabilities has to be made. The piezostacks chosen, namely $P887.31/P888.31$, are 13.5mm long stacks with blocking force above $1700N$ and typical displacement range $11\mu m$. Additional characteristics are given in [240].

The blocking force of the stacks in sufficient even for hard SiC samples with Young modulus $E_{SiC} = 450GPa$. Indeed, the force required to apply $\varepsilon = 1\%$ of strain in $1mm$ long samples with typical geometries of $(1 \cdot 0.35)mm^2$ is $F = \sigma \cdot S = \varepsilon \cdot E_{Sic} \cdot S = 1575N$.

In addition, the stacks displacement in their $-30V \rightarrow +120V$ operating range at room temperature is estimated from capacitance measurements as shown on Fig. 5.7. They can achieve higher displacements than given in the specifications, with a total range around $15\mu m$ so that strains above 1.5% could be achieved for $1mm$ long samples. These measurements also show hysteresis, originating from the field dependent reorientation of the polarized crystallites.

Strained sample

Strains over 1% can only be achieved if all the stress σ is transmitted to the sample into strain ε. To maximize the transmission, the sample clamping is of paramount importance. We glue our samples with $STYCAST\ 2850FT$, a two component epoxy that is known for its strength, and good behavior at cryogenic temperatures. To ensure good adhesion of the stycast on the sample surface that has very low roughness, we scratch both sides of the surface with a diamond tip.

Although the Young modulus of the Stycast is high, it does not transmit all the stress of the piezostacks into strain in the sample. We follow Ref. [235] in assuming that some finite length of the Stycast is strained and that the length of the sample that is strained is longer than the unglued part of the sample of length L by a load transfer of length 2λ. A simplified version of this situation is shown on Fig. 5.8b where only the top and bottom Stycast layers are assumed to play a role in the bonding between sample and clamp. Strain is assumed to be completely uniaxial $\varepsilon(y)$.

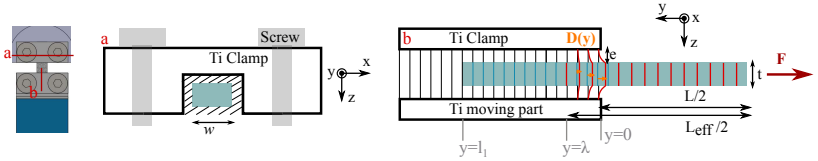

Figure 5.8: Sketch of sample clamping with two differents views as shown on the left. **a** Thanks to the clamp design, the Stycast organizes homogeneously on all sides of the sample. **b** Sketch of the side view of the sample clamping showing loss of applied stress into strain in the Stycast, along the length λ.

In that case, the strain in the sample varies along y starting at

$y = 0$. The force within the sample at position y is :

$$F(y) = E_{sample} wt\varepsilon = E_{sample} wt \frac{dD(y)}{dy} \tag{5.1}$$

where D(y) is the local displacement with respect to the unstrained situation. The Stycast close to the sample follows the same local displacement $D(y)$ at $z = e$ where e is the thickness of the Stycast between the sample and the clamp or the moving part of the cell, and no displacement at $z = 0$ upon straining over the width w. An infinitesimal variation of the strain over the (y, z) range can be approximated to be linear $\sim \frac{D(y)}{e}$, on both sides (hence the factor 2 in equation 5.2). One can thus write

$$\frac{dF(y)}{dy} \sim 2wC_S \frac{D(y)}{e} \tag{5.2}$$

where $C_S \sim 6GPa$ [235] is the shear elastic constant of the Stycast. Putting together equation 5.1 and 5.2 yields to the differential equation

$$E_{sample} t \frac{d^2D(y)}{dx^2} = 2C_S \frac{D(y)}{e} \tag{5.3}$$

which solution shows that $D(y)$ follows an exponential law that decays in y over the length

$$\lambda = \sqrt{\frac{E_{sample} \cdot t \cdot e}{2C_S}} \tag{5.4}$$

In the case of our typical SiC samples, a thickness of Stycast around 0.1mm yields $\lambda \sim 1.1$mm. That means that for an expected strain of 1%, the effective strain applied for a 1mm long sample is in fact 0.31% ($\varepsilon_{eff} = \varepsilon_{expected} \frac{L_{ech}}{L_{eff}}$)). As reducing too much e can result in the failure of the stycast for high strains, this loss of efficiency can be mainly avoided by reducing the thickness t of the sample to minimize the load λ.

The stress strain curve of Stycast is much more favorable at cryogenic temperatures as was shown by T. Hashimoto *et al.* [241] and reported on Fig. 5.9. As the Young modulus is expected to be multiplied by a factor over four, λ is expected to be lower than half its length at $300K$. Following with our 1mm long sample example, the effective strain would be 0.47% instead of 0.31%.

To increase the applied strain, the most efficient way is to reduce t the thickness of our samples which is about 350μm for typical SiC wafers. One must however remain in the limit where the aspect ratio is such that the sample does not buckle : $\frac{L}{t} < \frac{\pi}{\sqrt{3\epsilon}}$. For an aimed 1% strain in our 1mm long sample, one has to remain above $t = 56\mu$m, giving us a lot of room for improvement. For $t = 100\mu$m, the strain would reach 0.9% in the same conditions.

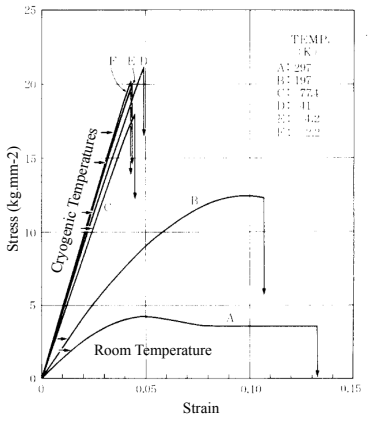

Figure 5.9: Stress-Strain curves of *STYCAST* 1266 for several temperatures. The Young modulus is increased by a factor over 4. The same behavior is expected for *STYCAST* 2850 because it is the same type of Stycast but with additional carbonic component that increases its strength.

Quantifying effective strain

At room temperatures, it is possible to estimate the strain effectively applied to the sample by performing digital image correlations between the unstrained and the strained situations. This is done using

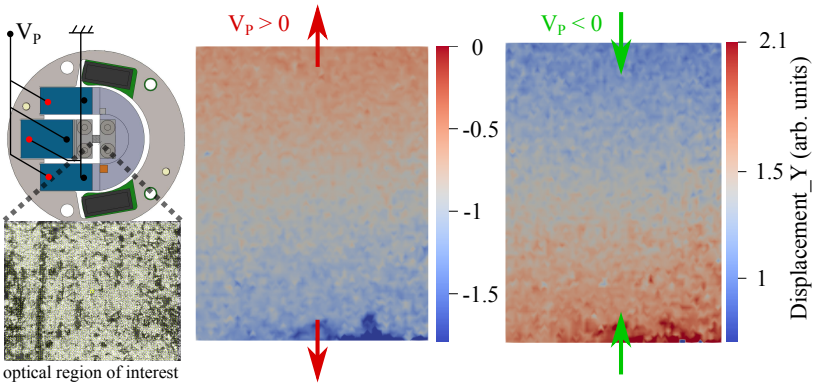

Figure 5.10: **Left** Optical image zoom on the clamped sample, covered with silver epoxy in order to help follow the pixels, and rasterized by in DICE [242] (yellow spots). **Right** Relative displacements along the strain axis between the unstrained image and the compressed (extended) sample as visualized by the green (red) arrows.

the software DICE [242] that performs the calculation in combination with Paraview [243] a data visualization tool. A correspondence between strain and applied voltage can thus be made.

5.4 *Strain effect in transistors*

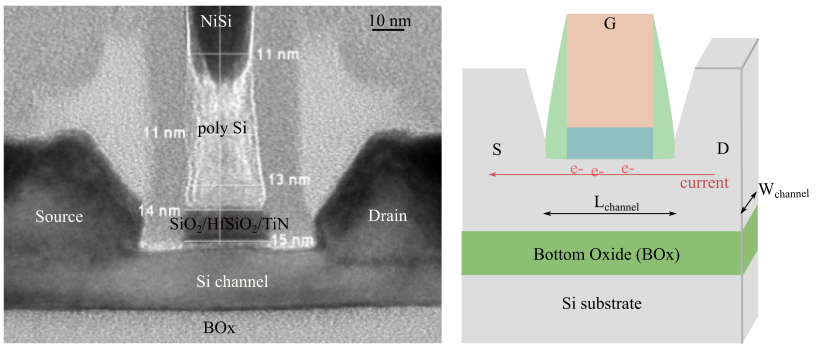

Figure 5.11: **Left** : TEM cut of a typical NMOS (n-doped MOSFET). **Right** : Sketch of a typical NMOS. The NMOS we measured had a channel length L = 0.1μm and width W = 0.06μm.

Our straincell can be useful to investigate strain effect in MOSFETs (Metal Oxide Semiconductor Field Effect Transistor). Such devices are designed to tune a current between two charge reservoirs, namely the source and the drain, through a channel of length L and width W as shown on Fig. 5.11. The current flow is controlled by a metallic gate below which charge carriers are accumulated upon application of a voltage. These are important components in electronics as they are the building blocks to operate the amplification of a signal by modulating the voltage of the gate, but also to operate calculations based on Boole calculations by defining two states 0 (current not flowing) and 1 (current flowing). The desirable technological reduction of the dimensions of transistors have reached its limits, as the gate length of transistor is now approaching 10nm. To pursue the improvement of performances on advanced technological devices, strain can be used as a tool to optimize the current flowing through the transistors channels. Strain has thus been introduced since 2003 by Intel, aiming at increasing the on-current of transistors. The understanding of the effect of strain is thus still important for

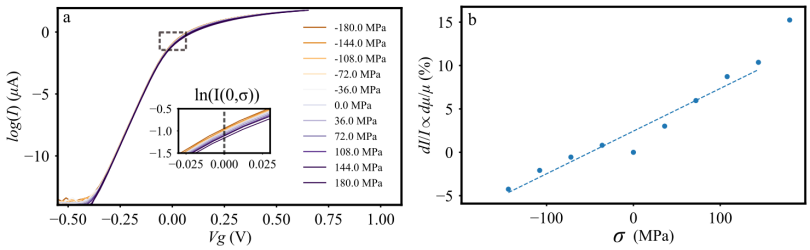

Figure 5.12: **a** Logarithm of the current flowing through the transistor channel, for several applied stresses. Stress is retrieved using DICE, and with the Young modulus of Silicon E_{Si} = 180GPa. The curves are shifted in order to align their threshold voltage V_t. The measured transistor is a NMOS of channel length L = 0.1μm and width W = 0.06μm. **b** Relative current $\frac{dI}{I} = \frac{I(V_g=0,\sigma=0)-I(V_g=0,\sigma)}{I(V_g=0,\sigma=0)} \propto \frac{d\mu}{\mu}$ changes as a function of stress in the system showing linear dependency.

further technological developments.

Strain can be introduced directly in the channel material during growth by several methods relying on the inclusion of Germanium atoms in the system, thereby changing the crystal parameter. This strain can be visualized by TEM methods [244]. Typical strains induced during fabrication reach 0.8% and induce mobility changes by changing the effective mass of the carriers [245].

Even lower amounts of strain can induce such mobility changes [246, 247]. At low strains, the relative mobility change $\frac{\Delta\mu}{\mu} \propto \frac{\Delta I}{I}$ linearily depends on the applied strain as shown by J. Pelloux Prayer *et al.* [247, 248] on SOI (silicon on insulator) nanowire transistors.

We reproduced their data by using our straincell. For each applied voltage on the piezostacks, we ramped the gate of the channel between the transistor's Source and Drain. At the threshold voltage V_t, the transistor opens and current starts to flow through the channel. Such a measurement for several applied strains is shown in Fig. 5.12a. By plotting the relative current as shown on Fig. 5.12b, we retrieve the linear dependence from Ref. [247]. Non-linearities in the data can also be noticed, and can be attributed to the piezostacks hysteresis and more marginally to artifacts on V_t.

The threshold voltage V_t slightly varies with strain, and the curves from Fig. 5.14a are offset accordingly. In our measurements however, this shift reaches over 100 mV as shown on Fig. 5.13, which cannot be attributed to strain effects only. Instead, V_t linearly decreases with increasing tension on the piezostacks. This variation is consistent with a variation of V_t upon a change of tension on the back of the sample, below the buried oxide (or *BOx*), that dopes the channel independently of V_G. What we observe is in fact a combined effect of strain and of voltage application on the BOx due to a leak of the voltage applied on the piezo to the back of the sample. This additional effect of doping below the BOx shifts V_t linearly [249], and thus it is mostly compensated by the shift we perform on each curve. In the future, the voltage on the BOx should be fixed with a voltage source to avoid artifacts.

The correspondence between applied voltage and applied strain can be done by digital correlation imaging as described in previous section and enables us to trace the mobility changes as a function of stress as shown on Fig. 5.12. For these first tests, we used only one voltage source applying opposite voltages on the outer and in-

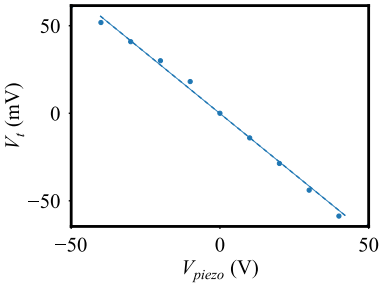

Figure 5.13: Threshold voltage V_t at which the transistor opens and lets current flow. It is strongly dependent on the voltage applied on the inner piezoactuator V_{piezo}, consistently with its linear dependency on the voltage applied to the *BOx* of the transistor.

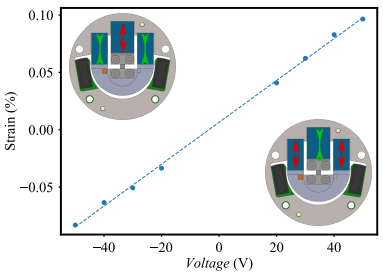

Figure 5.14: Surface strain as a function of the voltage applied on the piezoactuators. The strain is extracted from optical images analysed with digital image correlations. The average slope gives an efficiency of 0.002%/V. A slight nonlinearity can be noticed which comes from the piezoactuators hysteresis.

ner piezostacks which means we were limited by their depolarization voltage and we did not apply voltages above $\pm 50V$. With this limitation, as shown on Fig. 5.14, we find that we can apply a $\sim 0.2\%$ range of strains on the sample. For this range of applied tension, we expect a 5μm displacement and thus from equation 5.4 a $\pm 0.14\%$ effective strain on the sample. Higher strain could be achieved by applying higher voltages on the stacks, using two voltage sources. In addition, the sample we used were quite thick $t = 500\mu$m which could be significantly reduced to apply more strain.

These measurements open new perspectives. Indeed, with our strain cell, we have a higher resolution in strain than for the three point bending setup from Ref. [247], because we rely on longitudinal piezostacks where any voltage can be applied. Small non linearities in $\frac{\Delta I}{I}(\varepsilon)$ could thus be detected. In particular, tensile strains could be investigated much more easily, as they can be hard to achieve by bending method if one wants to measure MOSFETs at the same time due to the presence of bonding pads at the surface.

In addition, the low strains ($-0.1\% < \varepsilon < 0.1\%$) and high strains ($0.7\% < \varepsilon < 0.9\%$) regimes on MOSFETs have been investigated, but not intermediate strains which could be accessed here. Such strain measurements could also be performed with an additional variation of the BOx voltage.

Last, with our setup such measurements could be performed at cryogenic temperatures. In particular, measuring at low temperatures would permit to disentangle the effect of the phonons and the purely electronic effect in the mobility variations due to strain.

5.5 *Operating strain cell in cryogenic temperatures*

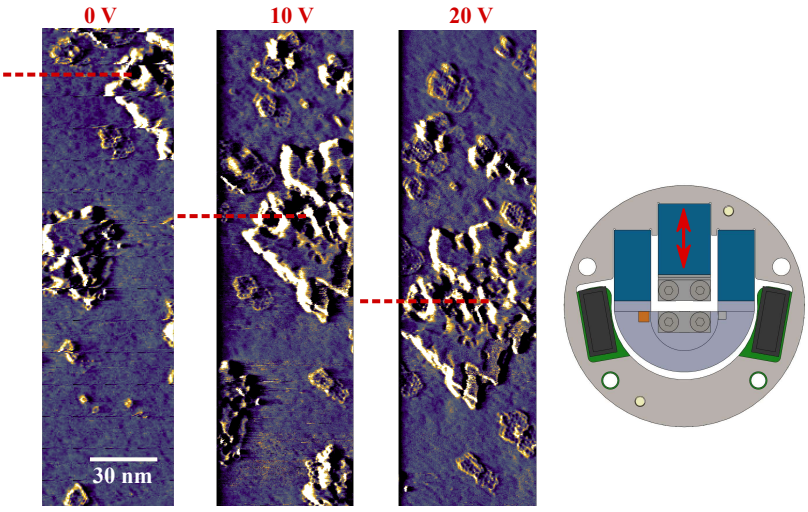

Figure 5.15: STM tracked displacement of the piezostacks depending on voltage at cryogenic temperatures. Each image is taken at different applied voltages on the inner piezostack. For each voltage, several images are taken to make sure drift originating from the piezostacks is negligible.

At cryogenic temperatures, we verify that STM measurements can be performed in our setup. All STM measurements from Chapter 4 were performed using our STM, with the sample clamped to our straincell setup.

In addition, we can quantify how much strain can in principle be applied to our samples at cryogenic temperatures by tracking the piezoactuators induced displacement using STM imaging. In Fig.5.15, we find that for a sample attached on both piezostacks, the displacement is around $5\text{nm}/V$, correponding to a total displacement range of about 0.8μm for a tension between -30 and $120V$. The piezoactuators specifications rather predict a 10 to 20% reduction in piezostack efficiency at cryogenic temperatures, which corresponds in our case to a 1.5μm to 3μm displacement range.

This reduced efficiency could be real or could be attributed to a loss of strain in the stycast, even at low temperatures. Strain relief processes occurring in the bulk, as noted by [220] could also be a source of discrepancy in the observed displacements. We verified that such strain relief process occurred in bulk $NbSe_2$ samples. Indeed, by performing transport measurements under strain we did not detect changes in the superconducting critical temperature as was reported in Ref. [250]. Instead, $NbSe_2$ flakes would wrinkle or be subject to various strain relief processes.

5.6 Conclusion and perpectives

In this Chapter, we have presented the design and testing of a strain cell compatible with a low temperature STM. This device enables one to use strain as a tool to tune the electronic properties of small samples. Strain effect on transistors has been demonstrated at room temperature with our strain cell. It offers promising perspectives to understand strain effect in such devices both at room temperature and cryogenic temperatures. At cryogenic temperatures, evidence of tunable strain is desirable, particularly given the strong effect of strain on twisted bilayers of graphene that was investigated in previous chapters, though experimental efforts still remain in that aspect. Other materials such as $MoSe_2$, $NbSe_2$ or $Fe_{1+x}Te$ could be investigated by STM under strain application.

Conclusion

Originally, twisted bilayers of graphene (TBLG) were measured at the surface of graphite, and then on graphene grown on SiC. The moiré in these systems remained a puzzling curiosity as the system behaved just like a graphene monolayer - it turned out this was due to the decoupling of the layers at high angles ($\sim 30°$). With the theoretical prediction of interesting behaviors in low angle TBLG, people turned to studying this lower angle regime. This led to prolific important experimental results, some of them being reviewed over Chapter 1, including the discovery of the superconducting state in magic angle TBLG.

At the same time, people started to realize that the twist angle between the layers was not the only tuning parameter of the system. In particular, L. Huder *et al.* gave the first demonstration that *heterostrain*, the relative strain between the layers, has significant importance. Using similar Scanning Tunnelling Microscopy and Spectroscopy (STM/STS) datas from the literature, and taking advantage of the ubiquitous native strain in TBLG samples, in Chapter 3 we systematically perform a careful analysis of the precise stacking between the layers and its link with the local electronic properties. This study is supported by systematic calculations of the electronic properties of TBLG commensurate cells that include varying heterostrain presented in Chapter 2. The method we use to produce these commensurate cells including heterostrain is very general and could be extended to other 2D materials. All in all, these results show that the flat bands of the system are sensitive to heterostrains as small as 0.1%, and establish the idea that close to the magic angle, uniaxial heterostrain is of paramount importance.

Uniaxial heterostrain is not the only type of strain that can have an influence on the moiré : biaxial heterostrain is also present in most samples although they are often smaller. Biaxial heterostrain could even produce a new type of moiré in graphene bilayers, that hasn't been studied so far. I show in Chapter 4 a first study on that matter, showing that biaxial strain can produce a new type of atomic relaxation, that we refer to as the *swirl* relaxation pattern. We also study the low energy properties of this swirl relaxation pattern and show that it features localized states at the center of the moiré but also near the domain walls of the relaxation. This measurement shows that not only the global electronic properties of the system are affected by stacking changes, but a local understanding of the

electronic properties can also be relevant as local stacking variations seem to affect them.

Finally, it is clear at the end of this manuscript that all the factors affecting the relative arrangement between the layers should be studied if we want to develop a detailed understanding of multilayered van der Waals materials. This is a far more complex task than considering a single parameter, but it is also an extraordinary opportunity to extend the tunability of these systems. The scientific community is thus starting to work on improving our control, not only on the twist, but also on the heterostrain parameter. We also have started to work on that path with the building of a new STM compatible with a strain cell, which we present in Chapter 5. We verify that this strain cell can be operated at room temperature, by measuring strain induced mobility changes in transistors, which opens perspectives in terms of such device engineering. We also verify that our setup can operate at cryogenic temperatures, which is very promising to performing STM measurements on extrinsically heterostrained graphene and other materials, 2D or not.

Conclusion en français

Les bicouches de graphène tournées (TBLG) ont à l'origine été mesurées à la surface du graphite, puis sur du graphène crû sur SiC. Le moiré dans ces systèmes est d'abord resté une curiosité étonnante car le système se comportait exactement comme une monocouche de graphène - il s'est avéré que cela était dû au découplage des couches à des angles élevés ($\sim 30^\circ$). Puis on s'est intéressé aux systèmes tournés à de faibles angles suite aux prédictions théoriques de comportements intéressants dans ce régime. Cela a conduit à de très nombreux importants résultats expérimentaux, dont certains sont passés en revue dans le chapitre 1, y compris la découverte de l'état supraconducteur dans les TBLG à l'angle magique.

Dans le même temps, la communauté scientifique a commencé à réaliser que l'angle entre les couches n'était pas le seul paramètre induisant une variation du système. En particulier, L. Huder *et al*. ont démontré pour la première fois que les hétérodéformations, c'est-à-dire les déformations relatives entre les couches, avaient une importance significative. En utilisant des données de microscopie et de spectroscopie à effet tunnel (STM/STS) similaires dans la littérature, et en tirant profit de la déformation intrinsèque qui est omniprésente dans les échantillons de TBLG, on réalise de façon systématique dans le chapitre 3 une analyse minutieuse de l'empilement précis entre les couches et de son lien avec les propriétés électroniques locales. Cette étude est appuyée par les calculs, présentés dans le chapitre 2, des propriétés électroniques de cellules commensurables de TBLG qui incluent une hétéroformation variable. La méthode que nous utilisons pour produire ces cellules commensurables incluant les hétérodéformations est très générale et pourrait être étendue à d'autres matériaux 2D. Dans l'ensemble, ces résultats montrent que les bandes plates du système sont sensibles aux hétérodéformations, même jusqu'à 0.1%, et établissent l'idée qu'à proximité de l'angle magique, les hétérodéformations uniaxiales sont d'une importance primordiale.

Les hétérodéformations uniaxiales ne sont pas le seul type de déformations qui peuvent avoir une influence sur le moiré : des hétérodéformations biaxiales peuvent également être présentes dans la plupart des échantillons, même si elles sont souvent plus faibles. Les hétérodéformations biaxiales peuvent même produire un nouveau type de moiré dans les bicouches de graphène, qui n'a pas été étudié jusqu'à présent. On présente au chapitre 4 une première

étude à ce sujet, montrant que la déformation biaxiale peut produire un nouveau type de relaxation atomique, que nous appelons relaxation en *tourbillon*. Nous étudions également les propriétés électroniques de basse énergie de ce mode de relaxation en tourbillon et montrons qu'il présente des états localisés au centre du moiré mais aussi près des parois du domaine de relaxation. Cette mesure montre que non seulement les propriétés électroniques globales du système sont affectées par des changements d'empilement, mais qu'une compréhension locale des propriétés électroniques peut également être pertinente car les variations locales d'empilement semblent les controller.

Finalement, il est clair à la fin de ce manuscrit que tous les facteurs affectant l'arrangement relatif entre les couches doivent être étudiés si nous voulons développer une compréhension précise des matériaux van der Waals multicouches. Il s'agit d'une tâche bien plus complexe que la prise en compte d'un seul paramètre, mais c'est aussi une opportunité extraordinaire d'étendre la versatilité de ces systèmes. La communauté scientifique commence donc à travailler non seulement sur l'amélioration du contrôle de l'angle entre les couches, mais aussi sur le contrôle des hétérodéformations dans le système. Nous avons également avancé sur cette voie avec la construction d'un nouveau microscope STM compatible avec une cellule de contrainte, que l'on présente dans le chapitre 5. On vérifie que cette cellule de contrainte peut fonctionner à température ambiante, en mesurant les changements de mobilité induits par la contrainte dans les transistors, ce qui ouvre des perspectives en termes d'ingénierie de ces dispositifs. On vérifie également que notre installation peut fonctionner à des températures cryogéniques, ce qui est très prometteur pour réaliser des mesures STM sur du graphène extrinsèquement hétérodéformé et sur d'autres matériaux, 2D ou non.

A
Scanning Transmission Electron Microscopy (STEM) of intercalated Gr/SiC

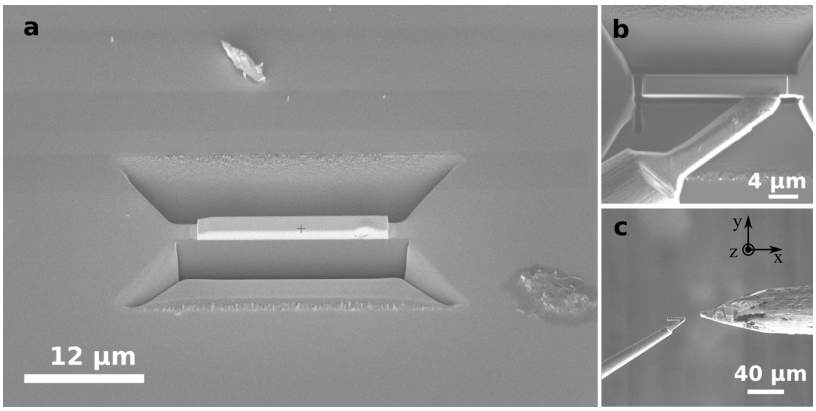

Figure A.1: Scanning Electron Microscope images of lamella preparation: **a** after deposition of an amorphous Carbon and Platinium protecting layers ; **b** lamella lift-out with Omniprobe micromanipulator ; **c** lamella transfer on the rotating needle.

In order to understand better the sample studied in Chapter 4, we collaborated with the group of Hanako Okuno from the LEMMA (Laboratory of Electron Microscopy and Material Advances) to perform Scanning Transmission Electron Microscopy (S-TEM). These measurements were performed by Djordje Došenović.

Such measurements rely on the fabrication of a very thin slide (or *lamella*) of the sample, normal to the surface, which is done using a Focused Ion Beam (FIB). The step by step fabrication of the TEM slide is shown on Figs. A.1 and A.2.

Using the FIB, the surface is first protected from the beam by depositing a layer of Platinium, in addition to amorphous carbon if necessary. This is done by directing the FIB in the region of interest while introducing a Platinium rich gaz in the chamber, therefore depositing Platinium layers on that precisely defined region of interest. The process also necessitates several steps of attachment and detachment to various supports in order to transfer the lamella to the final TEM grid. Such attachment processes of the lamella is done similarly by depositing Platinium where the sample is to be attached.

Then, the surface is etched into a thin slide by using the FIB in vacuum (Fig. A.1a). Before etching the last side of the slide, it is attached to a *micromanipulator* from the chamber, so that it can be

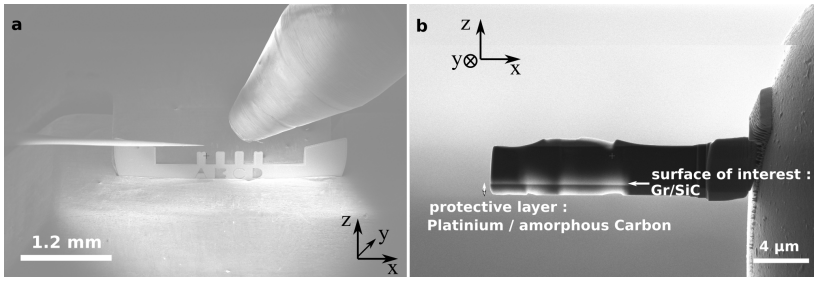

Figure A.2: MEB images of **a** transfer of the TEM slide on the TEM grid and **b** FIB back face thinning of the sample for TEM measurements.

detached from the surface without loosing it (Fig. A.1b). Next, (Fig. A.1c) it is attached to a rotating needle. Using this needle, the slide can be flipped upside-down for a backside thinning, which allows precise control of the final thickness of surface of interest, while leaving it mostly unaltered by the process.

It is then transferred to a TEM *grid* (Fig. A.2 a), where the final thinning down of the slide can take place (Fig. A.2 b). This step is critical for the TEM measurements.

Typical FIB slide thicknesses is $50 - 100nm$. The thinnest regions can be recognized as white regions in SEM images as shown on Fig. A.2 b, as they are transparent for accelerated electrons, and feature a low intensity signal coming from the secondary electrons only.

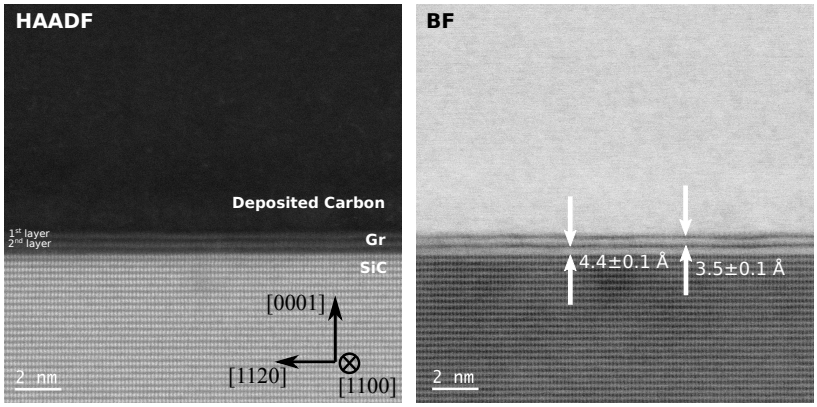

Figure A.3: Typical Transmission Electron Microscopy images showing High Angle Annular Dark Field (**a**) and Bright Field (**b**) contrasts.

The slide is then ready for TEM measurements : an electron beam is directed towards the region of interest and the transmitted electrons are collected on a screen that can be transformed into an image. The transmitted electrons having interacted with the atoms of the slide, the image gives a spatially resolved information on the structure at the atomic scale. Typical TEM images of our sample are shown on Fig. A.3. They enable to extract typical distances between the graphene layers ($0.35nm$) along with the relatively big distance between the SiC and the first graphene layer ($0.44nm$), thereby confirming the intercalated nature of our sample.

B
Annihilation of the swirl relaxation pattern

The swirl relaxation pattern studied in Chapter 4 annihilated itself after measuring it in STM for about one month and a half. Its annihilation means that its formation is metastable, and was perturbed by the many small perturbations that we regularly applied during the measurement campaign. In particular, tip interaction or slight thermal variations that can occur during the Helium transfers most likely caused its annihilation.

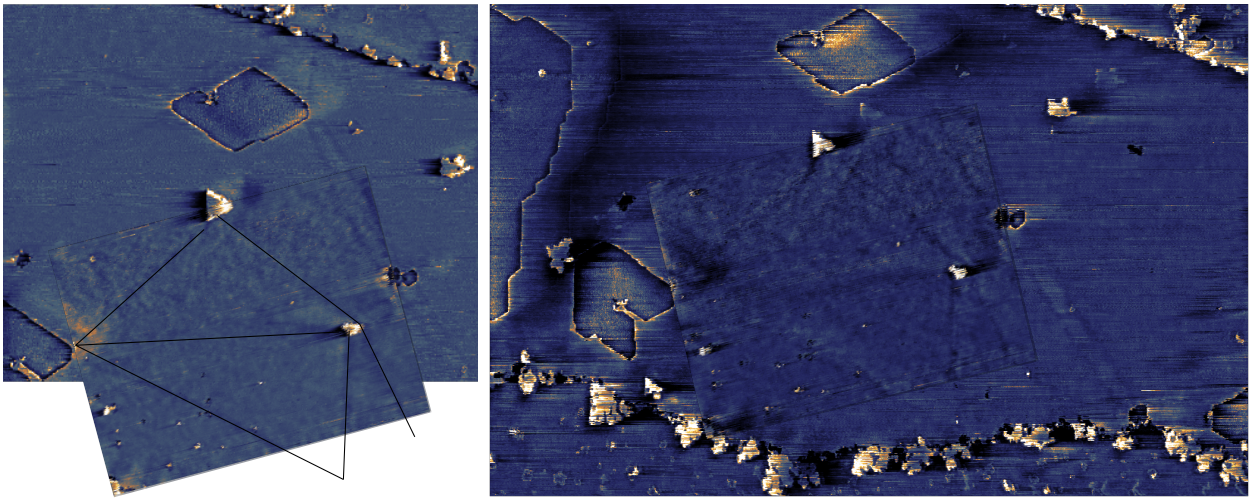

Figure B.1: STM images showing the fully annihilated structure. (V_b = $300mV$, I_t = $200pA$). These images are taken with a "dirty" tip that is affected by the measurement campaign (as can be seen from the double-tip features around the non intercalated regions). Zoom-ins are thus superimposed to improve the visualization of the DWs. Black lines on the left are guides to the eyes following the DWs that cross AB/BA regions between two non intercalated regions.

Measuring the destruction of the structure can still be of interest to us. Indeed, it gives us yet another experimental evidence that the system features no pinning of the layers to the substrate, for example in AA regions, and that the system does really originate from a relaxation effect.

The annihilation process occurred in two different steps :

-First, the clockwise rotating flower was pushed towards the non intercalated region on the right, pushing its right domain wall towards the nearest non intercalated region on the right.

-In a second step, the remaining swirl was pushed left, towards the closest non intercalated region on the left. This second annihilation occurred on a much shorter timescale than the first one (a few days

only), which means that the system was by then even less stable.

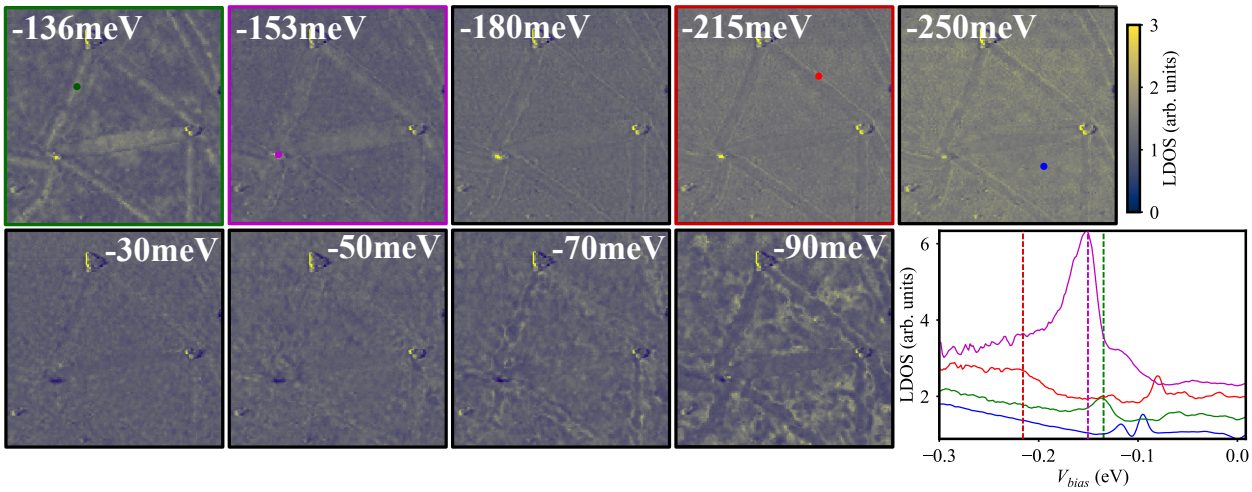

Figure B.2: STM images showing the annihilated structure. Setpoint is (V_b = $-300mV$, I_t = $250pA$).

At the end of the annihilation, only straight DW remain on the surface, as shown on Fig. B.1.

We were able to take a CITS measurement in between the two annihilation steps. The system in that configuration features only one anticlockwise rotating swirl, as shown on Fig. B.2 and that we discuss in more details in the following.

The CITS shown on Fig. B.2 shows that even in the single swirl configuration, the swirl relaxation pattern remains, and has similar features as the two-swirl system presented in Fig. 4.27.

The localization of the LDOS in AA region is shown by the purple curve. In AB regions, the blue curve averaged around the blue dot shows two peaks that correspond to the electric field induced gap opening. Between the maps $V_b = -136meV$ and $V_b = -250meV$, the edge states clearly get closer and closer to the DW center, as was previously observed. Last, localized states are still visible above charge neutrality, with disordered scattering features with lowering wavelength as the bias is sweeped away from charge neutrality.

Bibliography

[1] K. S. Novoselov, A. K. Geim, S. V. Morozov, D. Jiang, Y. Zhang, S. V. Dubonos, I. V. Grigorieva, and A. A. Firsov. Electric field effect in atomically thin carbon films. *Science*, 306(5696):666–669, 2004. doi: 10.1126/science.1102896. URL https://www.science.org/doi/abs/10.1126/science.1102896.

[2] C. Lee, X. Wei, J. Kysar, and J. Hone. Measurement of the elastic properties and intrinsic strength of monolayer graphene. *Science*, 321:385–388, 2008.

[3] K. S. Novoselov, Z. Jiang, Y. Zhang, S. V. Morozov, H. L. Stormer, U. Zeitler, J. C. Maan, G. S. Boebinger, P. Kim, and A. K. Geim. Room-temperature quantum hall effect in graphene. *Science*, 315(5817):1379–1379, 2007. doi: 10.1126/science.1137201. URL https://www.science.org/doi/abs/10.1126/science.1137201.

[4] Andrea Splendiani, Liang Sun, Yuanbo Zhang, Tianshu Li, Jonghwan Kim, Chi-Yung Chim, Giulia Galli, and Feng Wang. Emerging photoluminescence in monolayer mos2. *Nano Letters*, 10(4):1271–1275, 2010. ISSN 1530-6984, 1530-6992. doi: 10.1021/nl903868w. URL https://pubs.acs.org/doi/10.1021/nl903868w.

[5] Wing-Tat Pong and Colm Durkan. A review and outlook for an anomaly of scanning tunnelling microscopy (stm): superlattices on graphite. *Journal of Physics D: Applied Physics*, 38(21):R329–R355, 2005. ISSN 0022-3727, 1361-6463. doi: 10.1088/0022-3727/38/21/R01. URL https://iopscience.iop.org/article/10.1088/0022-3727/38/21/R01.

[6] Yuan Cao, V. Fatemi, Kenji Watanabe, Takashi Taniguchi, Efthimios Kaxiras, and Pablo Jarillo-Herrero. Magic-angle graphene superlattices: a new platform for unconventional superconductivity. *Nature*, 55:43–50, 2019.

[7] Matthew Yankowitz, Shaowen Chen, and Cory R. Dean. Tuning superconductivity in twisted bilayer graphene. *Science*, 363:1059–1064, 2019.

[8] L. Huder, A. Artaud, T. Le Quang, Guy Trambly de Laissardière, Claude Chapelier, and Vincent T. Renard. Electronic spectrum of twisted graphene layers under heterostrain. *Physical Review Letters*, 120:156405, 2018.

[9] A. H. Castro Neto, F. Guinea, N. M. R. Peres, K. S. Novoselov, and A. K. Geim. The electronic properties of graphene. *Rev. Mod. Phys.*, 81:109–162, 2009.

[10] G. Montambaux, F. Piechon, J.-N. Fuchs, and M. O. Goerbig. Merging of Dirac points in a two-dimensional crystal. *Physical Review B*, 80(15):153412, 2009. ISSN 1098-0121, 1550-235X. doi: 10.1103/PhysRevB.80.153412. URL http://arxiv.org/abs/0904.2117. arXiv: 0904.2117.

[11] P. R. Wallace. The band theory of graphite. *Physical Review*, 71(9):622–634, 1947. ISSN 0031-899X. doi: 10.1103/PhysRev.71.622. URL https://link.aps.org/doi/10.1103/PhysRev.71.622.

[12] Ken-ichi Sasaki and Katsunori Wakabayashi. Chiral gauge theory for the graphene edge. *Physical Review B*, 82(3):035421, 2010. ISSN 1098-0121, 1550-235X. doi: 10.1103/PhysRevB.82.035421. URL https://link.aps.org/doi/10.1103/PhysRevB.82.035421.

[13] M. I. Katsnelson, K. S. Novoselov, and A. K. Geim. Chiral tunnelling and the klein paradox in graphene. *Nature Physics*, 2(9):620–625, 2006. ISSN 1745-2473, 1745-2481. doi: 10.1038/nphys384. URL http://www.nature.com/articles/nphys384.

[14] M. V. Berry. Quantal phase factors accompanying adiabatic changes. *Proc. R. Soc. London Math. Phys. Eng. Sci.*, 392(45), 1984.

[15] A.V. Rozhkov, A.O. Sboychakov, A.L. Rakhmanov, and Franco Nori. Electronic properties of graphene-based bilayer systems. *Physics Reports*, 648:1–104, 2016. ISSN 03701573. doi: 10.1016/j.physrep.2016.07.003. URL https://linkinghub.elsevier.com/retrieve/pii/S0370157316301612.

[16] Jae-Kap Lee, Seung-Cheol Lee, Jae-Pyoung Ahn, Soo-Chul Kim, John Wilson, and Phillip John. The growth of aa graphite on (111) diamond. *The Journal of chemical physics*, 129:234709, 01 2009. doi: 10.1063/1.2975333.

[17] J. Borysiuk, J. Soltys, and J. Piechota. Stacking sequence dependence of graphene layers on sic(0001) experimental and theoretical investigation. *Journal of Applied Physics*, 109(9):093523, 2011. ISSN 0021-8979, 1089-7550. doi: 10.1063/1.3585829. URL http://aip.scitation.org/doi/10.1063/1.3585829.

[18] Andrey M. Popov, Irina V. Lebedeva, Andrey A. Knizhnik, Yurii E. Lozovik, and Boris V. Potapkin. Commensurate-incommensurate phase transition in bilayer graphene. *Physical Review B*, 84(4):045404, 2011. ISSN 1098-0121, 1550-235X. doi: 10.1103/PhysRevB.84.045404. URL https://link.aps.org/doi/10.1103/PhysRevB.84.045404.

[19] J.D. Bernal. The structure of graphite. *Proceedings of the Royal Society of London Series A*, 106(740):749–773, 1924. doi: 10.1098/rspa.1924.0101.

[20] R. De Gail. *Aspects topologiques des dérivés du graphène*. Condensed Matter thesis, Université Paris Sud, 2014.

[21] L. M. Malard, J. Nilsson, D. C. Elias, J. C. Brant, F. Plentz, E. S. Alves, A. H. Castro Neto, and M. A. Pimenta. Probing the electronic structure of bilayer graphene by raman scattering. *Phys. Rev. B*, 76:201401, Nov 2007. doi: 10.1103/PhysRevB.76.201401. URL https://link.aps.org/doi/10.1103/PhysRevB.76.201401.

[22] L. M. Zhang, Z. Q. Li, D. N. Basov, M. M. Fogler, Z. Hao, and M. C. Martin. Determination of the electronic structure of bilayer graphene from infrared spectroscopy. *Phys. Rev. B*, 78:235408, Dec 2008. doi: 10.1103/PhysRevB.78.235408. URL https://link.aps.org/doi/10.1103/PhysRevB.78.235408.

[23] Z. Q. Li, E. A. Henriksen, Z. Jiang, Z. Hao, M. C. Martin, P. Kim, H. L. Stormer, and D. N. Basov. Band structure asymmetry of bilayer graphene revealed by infrared spectroscopy. *Phys. Rev. Lett.*, 102:037403, Jan 2009. doi: 10.1103/PhysRevLett.102.037403. URL https://link.aps.org/doi/10.1103/PhysRevLett.102.037403.

[24] Edward McCann and Vladimir I. Fal'ko. Landau-level degeneracy and quantum hall effect in a graphite bilayer. *Physical Review Letters*, 96(8):086805, 2006. ISSN 0031-9007, 1079-7114. doi: 10.1103/PhysRevLett.96.086805. URL https://link.aps.org/doi/10.1103/PhysRevLett.96.086805.

[25] Edward McCann. Asymmetry gap in the electronic band structure of bilayer graphene. *Physical Review B*, 74(16):161403, 2006. ISSN 1098-0121, 1550-235X. doi: 10.1103/PhysRevB.74.161403. URL https://link.aps.org/doi/10.1103/PhysRevB.74.161403.

[26] Taisuke Ohta, Aaron Bostwick, Thomas Seyller, Karsten Horn, and Eli Rotenberg. Controlling the electronic structure of bilayer graphene. *Science*, 313(5789):951–954, 2006. ISSN 0036-8075, 1095-9203. doi: 10.1126/science.1130681. URL https://www.science.org/doi/10.1126/science.1130681.

[27] Yuan Cao, Valla Fatemi, Shiang Afng, Kenji Watanabe, Takashi Taniguchi, Efthimios Kaxiras, and Pablo Jarillo-Herrero. Correlated insulator behaviour at half-filling in magic-angle graphene superlattices. *Nature*, 556:80, 2019.

[28] Aaron L. Sharpe, Eli J. Fox, Arthur W. Barnard, Joe Finney, Kenji Watanabe, Takashi Taniguchi, M. A. Kastner, and David Goldhaber-Gordon. Emergent ferromagnetism near three-quarters filling in twisted bilayer graphene. *Science*, 365(6453):605–608, 2019. ISSN 0036-8075, 1095-9203. doi: 10.1126/science.aaw3780. URL https://www.science.org/doi/10.1126/science.aaw3780.

[29] Yuan Cao, Debanjan Chowdhury, Daniel Rodan-Legrain, Oriol Rubies-Bigorda, Kenji Watanabe, Takashi Taniguchi, T. Senthil, and Pablo Jarillo-Herrero. Strange metal in magic-angle graphene with near planckian dissipation. *Physical Review Letters*, 124(7):076801, 2020. ISSN 0031-9007, 1079-7114. doi: 10.1103/PhysRevLett.124.076801. URL https://link.aps.org/doi/10.1103/PhysRevLett.124.076801.

[30] Rui Lyu, Zachary Tuchfeld, Nishchhal Verma, Haidong Tian, Kenji Watanabe, Takashi Taniguchi, Chun Ning Lau, Mohit Randeria, and Marc Bockrath. Strange metal behavior of the hall angle in twisted bilayer graphene. *Phys. Rev. B*, 103:245424, Jun 2021. doi: 10.1103/PhysRevB.103.245424. URL https://link.aps.org/doi/10.1103/PhysRevB.103.245424.

[31] L. Van Hove. Occurence of singularities in the elastic frequency distribution of a crytals. *Phys. Rev. Letters*, 89(6):1190 1193, 1954.

[32] I. Brihuega, P. Mallet, G. Trambly de Laissardiere, M. M. Ugeda, L. Magaud, J. M. Gómez-Rodriguez, F. Yndurain, and J.-Y. Veuillen. Unraveling the intrinsic and robust nature of van hove singularities in twisted bilayer graphene by scanning tunneling microscopy and theoretical analysis. *Phys. Rev. Let.*, 109: 196802, 2012.

[33] Guohong Li, A. Luican, J. M. B. Lopes dos Santos, A. H. Castro Neto, A. Reina, J. Kong, and E. Y. Andrei. Observation of van hove singularities in twisted graphene layers. *Nat. Phys.*, 6(2):109 113, 2009.

[34] G. Trambly de Laissardiere, D. Mayou, and L. Magaud. Localization of dirac electrons in rotated graphene bilayers. *Nano Lett.*, 10:804–808, 2010.

[35] J. M. B. Lopes dos Santos, N. M. R. Peres, and A. H. Castro Neto. Graphene bilayer with a twist: Electronic structure. *Phys. Rev. Let.*, 99(256802), 2007.

[36] R. Bistritzer and A. H. MacDonald. Moiré bands in twisted double-layer graphene. *PNAS*, 108(30):12233 12237, 2011.

[37] J. M. B. Lopes dos Santos, N. M. R. Peres, and A. H. Castro Neto. Continuum model of the twisted bilayer. *Physical Review B*, 86(15):155449, 2012. ISSN 1098-0121, 1550-235X. doi: 10.1103/PhysRevB.86.155449. URL http://arxiv.org/abs/1202.1088. arXiv: 1202.1088.

[38] Zhen Bi, Noah F. Q. Yuan, and Liang Fu Fu. Designing flat band by strain. *arXiv*, 10146v, 2019.

[39] Mikito Koshino, Noah F.Q. Yuan, Takashi Koretsune, Masayuki Ochi, Kazuhiko Kuroki, and Liang Fu. Maximally localized wannier orbitals and the extended hubbard model for twisted bilayer graphene. *Physical Review X*, 8(3):031087, 2018. ISSN 2160-3308. doi: 10.1103/PhysRevX.8.031087. URL https://link.aps.org/doi/10.1103/PhysRevX.8.031087.

[40] Nguyen N. T. Nam and Mikito Koshino. Lattice relaxation and energy band modulation in twisted bilayer graphene. *Phys. Rev. B*, 96:075311, 2017.

[41] Manato Fujimoto and Mikito Koshino. Moiré edge states in twisted bilayer graphene and their topological relation to quantum pumping. *Physical Review B*, 103(15):155410, 2021. ISSN 2469-9950, 2469-9969. doi: 10.1103/PhysRevB.103.155410. URL https://link.aps.org/doi/10.1103/PhysRevB.103.155410.

[42] Dillon Wong, Yang Wang, J. Jung, S. Pezzini, A. M. DaSilva, H. Tsai, H. S. Jung, R. Khajeh, Y. Kim, J. Lee, S. Kahn, S. Tollabimazraehno, H. Rasool, K. Watanabe, T. Taniguchi, A. Zettl, S. Adam, Allan H. MacDonald, and Michael F. Crommie. Local spectroscopy of moiré-induced electronic structure in gate-tunable twisted bilayer graphene. *Phys. Rev. B*, 92(15), 2015.

[43] Stephen Carr, Shiang Fang, Pablo Jarillo-Herrero, and Efthimios Kaxiras. Pressure dependence of the magic twist angle in graphene superlattices. *Phys. Rev. B*, 98:085144, Aug 2018. doi: 10.1103/PhysRevB.98.085144. URL https://link.aps.org/doi/10.1103/PhysRevB.98.085144.

[44] Matthew Yankowitz, K. Watanabe, T. Taniguchi, Pablo San-Jose, and Brian J. LeRoy. Pressure-induced commensurate stacking of graphene on boron nitride. *Nature Communications*, 7(1):13168, 2016. ISSN 2041-1723. doi: 10.1038/ncomms13168. URL http://www.nature.com/articles/ncomms13168.

[45] Jeong Min Park, Yuan Cao, Kenji Watanabe, Takashi Taniguchi, and Pablo Jarillo-Herrero. Flavour hund's coupling, chern gaps and charge diffusivity in moiré graphene. *Nature*, 592(7852):43–48, 2021. ISSN 0028-0836, 1476-4687. doi: 10.1038/s41586-021-03366-w. URL http://www.nature.com/articles/s41586-021-03366-w.

[46] Zeyu Hao, A. M. Zimmerman, Patrick Ledwith, Eslam Khalaf, Danial Haie Najafabadi, Kenji Watanabe, Takashi Taniguchi, Ashvin Vishwanath, and Philip Kim. Electric field–tunable superconductivity in alternating-twist magic-angle trilayer graphene. *Science*, 371(6534):1133–1138, 2021. ISSN 0036-8075, 1095-9203. doi: 10.1126/science.abg0399. URL https://www.sciencemag.org/lookup/doi/10.1126/science.abg0399.

[47] Hyunjin Kim, Youngjoon Choi, Cyprian Lewandowski, Alex Thomson, Yiran Zhang, Robert Polski, Kenji Watanabe, Takashi Taniguchi, Jason Alicea, and Stevan Nadj-Perge. Spectroscopic signatures of strong correlations and unconventional superconductivity in twisted trilayer graphene. *arXiv:2109.12127 [cond-mat]*, 2021. URL http://arxiv.org/abs/2109.12127. arXiv: 2109.12127.

[48] Eslam Khalaf, Alex J. Kruchkov, Grigory Tarnopolsky, and Ashvin Vishwanath. Magic angle hierarchy in twisted graphene multilayers. *Physical Review B*, 100 (8):085109, 2019. ISSN 2469-9950, 2469-9969. doi: 10.1103/PhysRevB.100.085109. URL https://link.aps.org/doi/10.1103/PhysRevB.100.085109.

[49] Yiran Zhang, Robert Polski, Cyprian Lewandowski, Alex Thomson, Yang Peng, Youngjoon Choi, Hyunjin Kim, Kenji Watanabe, Takashi Taniguchi, Jason Alicea, Felix von Oppen, Gil Refael, and Stevan Nadj-Perge. Ascendance of superconductivity in magic-angle graphene multilayers, 2021. URL http://arxiv.org/abs/2112.09270. arXiv:2112.09270 [cond-mat].

[50] Alexandre Jaoui, Ipsita Das, Giorgio Di Battista, Jaime Díez-Mérida, Xiaobo Lu, Kenji Watanabe, Takashi Taniguchi, Hiroaki Ishizuka, Leonid Levitov, and Dmitri K. Efetov. Quantum critical behaviour in magic-angle twisted bilayer graphene. *Nature Physics*, 18(6):633–638, 2022. ISSN 1745-2473, 1745-2481. doi: 10.1038/s41567-022-01556-5. URL https://www.nature.com/articles/s41567-022-01556-5.

[51] U. Zondiner, A. Rozen, D. Rodan-Legrain, Y. Cao, R. Queiroz, T. Taniguchi, K. Watanabe, Y. Oreg, F. von Oppen, Ady Stern, E. Berg, P. Jarillo-Herrero, and S. Ilani. Cascade of phase transitions and dirac revivals in magic-angle graphene. *Nature*, 582(7811):203–208, 2020. ISSN 0028-0836, 1476-4687. doi: 10.1038/s41586-020-2373-y. URL http://www.nature.com/articles/s41586-020-2373-y.

[52] D. Wong and et al. Cascade of electronic transitions in magic-angle twisted bilayer graphene. *Nature*, 582:198, 2020.

[53] Youngjoon Choi, Hyunjin Kim, Yang Peng, Alex Thomson, Cyprian Lewandowski, Robert Polski, Yiran Zhang, Harpreet Singh Arora, Kenji Watanabe, Takashi Taniguchi, Jason Alicea, and Stevan Nadj-Perge. Correlation-driven topological phases in magic-angle twisted bilayer graphene. *Nature*, 589: 536, 2021.

[54] Kevin P. Nuckolls, Myungchul Oh, Dillon Wong, Biao Lian, Kenji Watanabe, Takashi Taniguchi, B. Andrei Bernevig, and Ali Yazdani. Strongly correlated chern insulators in magic-angle twisted bilayer graphene. *Nature*, 588:610, 2020.

[55] Youngjoon Choi, Hyunjin Kim, Cyprian Lewandowski, Yang Peng, Alex Thomson, Robert Polski, Yiran Zhang, Kenji Watanabe, Takashi Taniguchi, Jason Alicea, and Stevan Nadj-Perge. Interaction-driven band flattening and correlated phases in twisted bilayer graphene. *arXiv:2102.02209 [cond-mat]*, 2021. URL http://arxiv.org/abs/2102.02209. arXiv: 2102.02209.

[56] Yu Saito, Fangyuan Yang, Jingyuan Ge, Xiaoxue Liu, Takashi Taniguchi, Kenji Watanabe, J. I. A. Li, Erez Berg, and Andrea F. Young. Isospin pomeranchuk effect in twisted bilayer graphene. *Nature*, 592(7853):220–224, 2021. ISSN 0028-0836, 1476-4687. doi: 10.1038/s41586-021-03409-2. URL http://www.nature.com/articles/s41586-021-03409-2.

[57] Andrew T. Pierce, Yonglong Xie, Jeong Min Park, Eslam Khalaf, Seung Hwan Lee, Yuan Cao, Daniel E. Parker, Patrick R. Forrester, Shaowen Chen, Kenji Watanabe, Takashi Taniguchi, Ashvin Vishwanath, Pablo Jarillo-Herrero, and Amir Yacoby. Unconventional sequence of correlated chern insulators in magic-angle twisted bilayer graphene. *Nature Physics*, 2021. ISSN 1745-2473. doi: 10.1038/s41567-021-01347-4. URL https://www.nature.com/articles/s41567-021-01347-4.

[58] Robert Polski, Yiran Zhang, Yang Peng, Harpreet Singh Arora, Youngjoon Choi, Hyunjin Kim, Kenji Watanabe, Takashi Taniguchi, Gil Refael, Felix von Oppen, and Stevan Nadj-Perge. Hierarchy of symmetry breaking correlated phases in twisted bilayer graphene, 2022. URL http://arxiv.org/abs/2205.05225. arXiv:2205.05225 [cond-mat].

[59] M. Serlin, C. L. Tschirhart, H. Polshyn, Y. Zhang, J. Zhu, K. Watanabe, T. Taniguchi, L. Balents, and A. F. Young. Intrinsic quantized anomalous hall effect in a moiré heterostructure. *Science*, 367(6480):900–903, 2020. ISSN 0036-8075, 1095-9203. doi: 10.1126/science.aay5533. URL https://www.science.org/doi/10.1126/science.aay5533.

[60] Leon Balents, Cory R. Dean, Dmitri K. Efetov, and Andrea F. Young. Superconductivity and strong correlations in moiré flat bands. *Nature Physics*, 16 (7):725–733, 2020. ISSN 1745-2473, 1745-2481. doi: 10.1038/s41567-020-0906-9. URL http://www.nature.com/articles/s41567-020-0906-9.

[61] Thomas E. Beechem, Taisuke Ohta, Bogdan Diaconescu, and Jeremy T. Robinson. Rotational disorder in twisted bilayer graphene. *ACS Nano*, 8(2):1655–1663, 2014. ISSN 1936-0851, 1936-086X. doi: 10.1021/nn4059992. URL https://pubs.acs.org/doi/10.1021/nn405999z.

[62] A. Uri, S. Grover, Y. Cao, J. A. Crosse, K. Bagani, D. Rodan-Legrain, Y. Myasoedov, K. Watanabe, T. Taniguchi, P. Moon, M. Koshino, P. Jarillo-Herrero, and E. Zeldov. Mapping the twist-angle disorder and landau levels in magic-angle graphene. *Nature*, 581(7806):47–52, 2020. ISSN 1476-4687. doi: 10.1038/s41586-020-2255-3. URL https://www.nature.com/articles/s41586-020-2255-3.

[63] D. G. Purdie, N. M. Pugno, T. Taniguchi, K. Watanabe, A. C. Ferrari, and A. Lombardo. Cleaning interfaces in layered materials heterostructures. *Nature Communications*, 9(1):5387, 2018. ISSN 2041-1723. doi: 10.1038/s41467-018-07558-3. URL http://www.nature.com/articles/s41467-018-07558-3.

[64] Shahal Ilani. Flavor symmetry broken states and the pomeranchuk effect in matbg. *Capri School Lectures*, 2022. URL http://www.capri-school.eu/Capri22/lecture-notes-and-presentat/.

[65] Márton Szendrő, András Pálinkás, Péter Süle, and Zoltán Osváth. Anisotropic strain effects in small-twist-angle graphene on graphite. *Physical Review B*, 100(12):125404, 2019. ISSN 2469-9950, 2469-9969. doi: 10.1103/PhysRevB.100.125404. URL http://arxiv.org/abs/1908.09682. arXiv: 1908.09682.

[66] Justin H. Wilson, Yixing Fu, S. Das Sarma, and J. H. Pixley. Disorder in twisted bilayer graphene. *Phys. Rev. Research*, 2:023325, 2020. doi: 10.1103/PhysRevResearch.2.023325. URL https://link.aps.org/doi/10.1103/PhysRevResearch.2.023325.

[67] Jonathan S. Alden, Adam W. Tsen, Pinshane Y. Huang, Robert Hovden, Lola Brown, Jiwoong Park, David A. Muller, and Paul L. McEuen. Strain solitons and topological defects in bilayer graphene. *Proceedings of the National Academy of Sciences*, 110(28):11256–11260, 2013. ISSN 0027-8424. doi: 10.1073/pnas.1309394110. URL https://www.pnas.org/content/110/28/11256.

[68] Procolo Lucignano, Dario Alfè, Vittorio Cataudella, Domenico Ninno, and Giovanni Cantele. Crucial role of atomic corrugation on the flat bands and energy gaps of twisted bilayer graphene at the magic angle $\theta \sim 1.08^\circ$. *Physical Review B*, 99(19):195419, 2019. ISSN 2469-9950, 2469-9969. doi: 10.1103/PhysRevB.99.195419. URL https://link.aps.org/doi/10.1103/PhysRevB.99.195419.

[69] S. Amelinckx and P. Delavignette. Electron optical study of basal dislocations in graphite. *Journal of Applied Physics*, 31(12):2126–2135, 1960. ISSN 0021-8979, 1089-7550. doi: 10.1063/1.1735512. URL http://aip.scitation.org/doi/10.1063/1.1735512.

[70] S. R. Snyder, W. W. Gerberich, and H. S. White. Scanning-tunneling-microscopy study of tip-induced transitions of dislocation-network structures on the surface of highly oriented pyrolytic graphite. *PRB*, 47(16), 1993.

[71] P J Ouseph. Transformation of a graphite superlattice into triangular dislocations. *Phys. Rev. B*, 53(15):4, 1996.

[72] M M van Wijk, A Schuring, M I Katsnelson, and A Fasolino. Relaxation of moiré patterns for slightly misaligned identical lattices: graphene on graphite. *2D Materials*, 2(3):034010, 2015. ISSN 2053-1583. doi: 10.1088/2053-1583/2/3/034010. URL https://iopscience.iop.org/article/10.1088/2053-1583/2/3/034010.

[73] Fernando Gargiulo and Oleg V Yazyev. Structural and electronic transformation in low-angle twisted bilayer graphene. *2D Materials*, 5(1):015019, 2017. ISSN 2053-1583. doi: 10.1088/2053-1583/aa9640. URL https://iopscience.iop.org/article/10.1088/2053-1583/aa9640.

[74] V Hung Nguyen, D Paszko, M Lamparski, B Van Troeye, V Meunier, and J-C Charlier. Electronic localization in small-angle twisted bilayer graphene. *2D Materials*, 8(3):035046, 2021. ISSN 2053-1583. doi: 10.1088/2053-1583/ac044f. URL https://iopscience.iop.org/article/10.1088/2053-1583/ac044f.

[75] Francisco Guinea and Niels R. Walet. Continuum models for twisted bilayer graphene: Effect of lattice deformation and hopping parameters. *Physical Review B*, 99(20):205134, 2019. ISSN 2469-9950, 2469-9969. doi: 10.1103/PhysRevB.99.205134. URL https://link.aps.org/doi/10.1103/PhysRevB.99.205134.

[76] Jan H. Los, Luca M. Ghiringhelli, Evert Jan Meijer, and A. Fasolino. Improved long-range reactive bond-order potential for carbon. i. construction. *Physical Review B*, 72(21):214102, 2005. ISSN 1098-0121, 1550-235X. doi: 10.1103/PhysRevB.72.214102. URL https://link.aps.org/doi/10.1103/PhysRevB.72.214102.

[77] Thomas O'Connor, Jan Andzelm, and Mark O. Robbins. Airebo-m: A reactive model for hydrocarbons at extreme pressures. *The Journal of Chemical Physics*, 142(024903), 2015. doi: https://doi.org/10.1063/1.4905549.

[78] W. Ouyang, D. Mandelli, M. Urbakh, and O. Hod. Nanoserpents: Graphene nanoribbon motion on two-dimensional hexagonal materials. *Nano Letters*, 18: 6009, 2018.

[79] Tobias A. de Jong, Tjerk Benschop, Xingchen Chen, Eugene E. Krasovskii, Michiel J. A. de Dood, Rudolf M. Tromp, Milan P. Allan, and Sense Jan van der Molen. Imaging moiré deformation and dynamics in twisted bilayer graphene. *Nature Communications*, 13(1):70, 2022. ISSN 2041-1723. doi: 10.1038/s41467-021-27646-1. URL https://www.nature.com/articles/s41467-021-27646-1.

[80] T. A. de Jong, E. E. Krasovskii, C. Ott, R. M. Tromp, S. J. van der Molen, and J. Jobst. Intrinsic stacking domains in graphene on silicon carbide: A pathway for intercalation. *Physical Review Materials*, 2(10):104005, 2018. ISSN 2475-9953. doi: 10.1103/PhysRevMaterials.2.104005. URL https://link.aps.org/doi/10.1103/PhysRevMaterials.2.104005.

[81] Nathanael P. Kazmierczak, Madeline Van Winkle, Colin Ophus, Karen C. Bustillo, Stephen Carr, Hamish G. Brown, Jim Ciston, Takashi Taniguchi, Kenji Watanabe, and D. Kwabena Bediako. Strain fields in twisted bilayer graphene. *Nature Materials*, 2021. ISSN 1476-1122, 1476-4660. doi: 10.1038/s41563-021-00973-w. URL http://www.nature.com/articles/s41563-021-00973-w.

[82] Rebecca Engelke, Hyobin Yoo, Stephen Carr, Kevin Xu, Paul Cazeaux, Richard Allen, Andres Mier Valdivia, Mitchell Luskin, Efthimios Kaxiras, Minhyong Kim, Jung Hoon Han, and Philip Kim. Non-abelian topological defects and strain mapping in 2d moiré materials, 2022. URL http://arxiv.org/abs/2207.05276. arXiv:2207.05276 [cond-mat].

[83] Hyobin Yoo, Rebecca Engelke, Stephen Carr, Shiang Fang, Kuan Zhang, Paul Cazeaux, Suk Hyun Sung, Robert Hovden, Adam W. Tsen, Takashi Taniguchi, Kenji Watanabe, Gyu-Chul Yi, Miyoung Kim, Mitchell Luskin, Ellad B. Tadmor, Efthimios Kaxiras, and Philip Kim. Atomic and electronic reconstruction at the van der waals interface in twisted bilayer graphene. *Nature Materials*, 18(5):448–453, 2019. ISSN 1476-1122, 1476-4660. doi: 10.1038/s41563-019-0346-z. URL http://www.nature.com/articles/s41563-019-0346-z.

[84] Leo J. McGilly, Alexander Kerelsky, Nathan R. Finney, Konstantin Shapovalov, En-Min Shih, Augusto Ghiotto, Yihang Zeng, Samuel L. Moore, Wenjing Wu, Yusong Bai, Kenji Watanabe, Takashi Taniguchi, Massimiliano Stengel, Lin Zhou, James Hone, Xiaoyang Zhu, Dmitri N. Basov, Cory Dean, Cyrus E. Dreyer, and Abhay N. Pasupathy. Visualization of moiré superlattices. *Nature Nanotechnology*, 15(7):580–584, 2020. ISSN 1748-3387, 1748-3395. doi: 10.1038/s41565-020-0708-3. URL http://www.nature.com/articles/s41565-020-0708-3.

[85] Andreij C. Gadelha, Douglas A. A. Ohlberg, Cassiano Rabelo, Eliel G. S. Neto, Thiago L. Vasconcelos, João L. Campos, Jessica S. Lemos, Vinícius Ornelas, Daniel Miranda, Rafael Nadas, Fabiano C. Santana, Kenji Watanabe, Takashi Taniguchi, Benoit van Troeye, Michael Lamparski, Vincent Meunier, Viet-Hung Nguyen, Dawid Paszko, Jean-Christophe Charlier, Leonardo C. Campos, Luiz G. Cançado, Gilberto Medeiros-Ribeiro, and Ado Jorio. Localization of lattice dynamics in low-angle twisted bilayer graphene. *Nature*, 590(7846):405–409, 2021. ISSN 0028-0836, 1476-4687. doi: 10.1038/s41586-021-03252-5. URL http://www.nature.com/articles/s41586-021-03252-5.

[86] Yue Luo, Rebecca Engelke, Marios Mattheakis, Michele Tamagnone, Stephen Carr, Kenji Watanabe, Takashi Taniguchi, Efthimios Kaxiras, Philip Kim, and William L. Wilson. In situ nanoscale imaging of moiré superlattices in twisted van der waals heterostructures. *Nature Communications*, 11(1):4209, 2020. ISSN 2041-1723. doi: 10.1038/s41467-020-18109-0. URL https://www.nature.com/articles/s41467-020-18109-0.

[87] Dorri Halbertal, Nathan R. Finney, Sai S. Sunku, Alexander Kerelsky, Carmen Rubio-Verdú, Sara Shabani, Lede Xian, Stephen Carr, Shaowen Chen, Charles Zhang, Lei Wang, Derick Gonzalez-Acevedo, Alexander S. McLeod, Daniel Rhodes, Kenji Watanabe, Takashi Taniguchi, Efthimios Kaxiras, Cory R. Dean, James C. Hone, Abhay N. Pasupathy, Dante M. Kennes, Angel Rubio, and D. N. Basov. Moiré metrology of energy landscapes in van der waals heterostructures. *Nature Communications*, 12(1):242, 2021. ISSN 2041-1723. doi: 10.1038/s41467-020-20428-1. URL http://www.nature.com/articles/s41467-020-20428-1.

[88] Shengqiang Huang, Kyounghwan Kim, Dmitry K. Efimkin, Timothy Lovorn, Takashi Taniguchi, Kenji Watanabe, Allan H. MacDonald, Emanuel Tutuc, and Brian J. LeRoy. Topologically protected helical states in minimally twisted bilayer graphene. *Physical Review Letters*, 121(3):037702, 2018. ISSN 0031-9007, 1079-7114. doi: 10.1103/PhysRevLett.121.037702. URL https://link.aps.org/doi/10.1103/PhysRevLett.121.037702.

[89] Qi Zheng, Chen-Yue Hao, Xiao-Feng Zhou, Ya-Xin Zhao, Jia-Qi He, and Lin He. Tunable sample-wide electronic kagome lattice in low-angle twisted bilayer graphene. *Physical Review Letters*, 129(7):076803, 2022. ISSN 0031-9007, 1079-7114. doi: 10.1103/PhysRevLett.129.076803. URL https://link.aps.org/doi/10.1103/PhysRevLett.129.076803.

[90] Long-Jing Yin, Hua Jiang, Jia-Bin Qiao, and Lin He. Direct imaging of topological edge states at a bilayer graphene domain wall. *Nature Communications*, 7(1):11760, 2016. ISSN 2041-1723. doi: 10.1038/ncomms11760. URL http://www.nature.com/articles/ncomms11760.

[91] Long Ju, Zhiwen Shi, Nityan Nair, Yinchuan Lv, Chenhao Jin, Jairo Velasco, Claudia Ojeda-Aristizabal, Hans A. Bechtel, Michael C. Martin, Alex Zettl, James Analytis, and Feng Wang. Topological valley transport at bilayer graphene domain walls. *Nature*, 520(7549):650–655, 2015. ISSN 0028-0836, 1476-4687. doi: 10.1038/nature14364. URL http://www.nature.com/articles/nature14364.

[92] Peter Rickhaus, John Wallbank, Sergey Slizovskiy, Riccardo Pisoni, Hiske Overweg, Yongjin Lee, Marius Eich, Ming-Hao Liu, Kenji Watanabe, Takashi Taniguchi, Thomas Ihn, and Klaus Ensslin. Transport through a network of topological channels in twisted bilayer graphene. *Nano Letters*, 18(11):6725–6730, 2018. ISSN 1530-6984, 1530-6992. doi: 10.1021/acs.nanolett.8b02387. URL https://pubs.acs.org/doi/10.1021/acs.nanolett.8b02387.

[93] B. I. Halperin. Quantized hall conductance, current-carrying edge states, and the existence of extended states in a two-dimensional disordered potential. *Phys. Rev. B*, 25(2185), 1982.

[94] M. Z. Hasan and C. L. Kane. Colloquium : Topological insulators. *Reviews of Modern Physics*, 82(4):3045–3067, 2010. ISSN 0034-6861, 1539-0756. doi: 10.1103/RevModPhys.82.3045. URL https://link.aps.org/doi/10.1103/RevModPhys.82.3045.

[95] Ivar Martin, Ya. M. Blanter, and A. F. Morpurgo. Topological confinement in bilayer graphene. *Physical Review Letters*, 100(3):036804, 2008. ISSN 0031-9007, 1079-7114. doi: 10.1103/PhysRevLett.100.036804. URL https://link.aps.org/doi/10.1103/PhysRevLett.100.036804.

[96] Zhenhua Qiao, Jeil Jung, Qian Niu, and Allan H. MacDonald. Electronic highways in bilayer graphene. *Nano Letters*, 11(8):3453–3459, 2011. ISSN 1530-6984, 1530-6992. doi: 10.1021/nl201941f. URL https://pubs.acs.org/doi/10.1021/nl201941f.

[97] Fan Zhang, Allan H. MacDonald, and Eugene J. Mele. Valley chern numbers and boundary modes in gapped bilayer graphene. *Proceedings of the National Academy of Sciences*, 110(26):10546–10551, 2013. ISSN 0027-8424, 1091-6490. doi: 10.1073/pnas.1308853110. URL https://pnas.org/doi/full/10.1073/pnas.1308853110.

[98] Anthony R. Wright and Timo Hyart. Robust one-dimensional wires in lattice mismatched bilayer graphene. *Applied Physics Letters*, 98(25):251902, 2011. ISSN 0003-6951, 1077-3118. doi: 10.1063/1.3601851. URL http://aip.scitation.org/doi/10.1063/1.3601851.

[99] Abolhassan Vaezi, Yufeng Liang, Darryl H. Ngai, Li Yang, and Eun-Ah Kim. Topological edge states at a tilt boundary in gated multilayer graphene. *Physical Review X*, 3(2):021018, 2013. ISSN 2160-3308. doi: 10.1103/PhysRevX.3.021018. URL https://link.aps.org/doi/10.1103/PhysRevX.3.021018.

[100] Pablo San-Jose and Elsa Prada. Helical networks in twisted bilayer graphene under interlayer bias. *Physical Review B*, 88(12):121408, 2013. ISSN 1098-0121, 1550-235X. doi: 10.1103/PhysRevB.88.121408. URL https://link.aps.org/doi/10.1103/PhysRevB.88.121408.

[101] P. San-Jose, R. V. Gorbachev, A. K. Geim, K. S. Novoselov, and F. Guinea. Stacking boundaries and transport in bilayer graphene. *Nano Letters*, 14(4):2052–2057, 2014. ISSN 1530-6984, 1530-6992. doi: 10.1021/nl500230a. URL https://pubs.acs.org/doi/10.1021/nl500230a.

[102] Tao Hou, Yafei Ren, Yujie Quan, Jeil Jung, Wei Ren, and Zhenhua Qiao. Metallic network of topological domain walls. *Physical Review B*, 101(20):201403, 2020. ISSN 2469-9950, 2469-9969. doi: 10.1103/PhysRevB.101.201403. URL https://link.aps.org/doi/10.1103/PhysRevB.101.201403.

[103] Niels R Walet and Francisco Guinea. The emergence of one-dimensional channels in marginal-angle twisted bilayer graphene. *2D Materials*, 7(1):015023, 2019. ISSN 2053-1583. doi: 10.1088/2053-1583/ab57f8. URL https://iopscience.iop.org/article/10.1088/2053-1583/ab57f8.

[104] Dmitry K. Efimkin and Allan H. MacDonald. Helical network model for twisted bilayer graphene. *Physical Review B*, 98(3):035404, 2018. ISSN 2469-9950, 2469-9969. doi: 10.1103/PhysRevB.98.035404. URL https://link.aps.org/doi/10.1103/PhysRevB.98.035404.

[105] Aline Ramires and Jose L. Lado. Electrically tunable gauge fields in tiny-angle twisted bilayer graphene. *Physical Review Letters*, 121(14):146801, 2018. ISSN 0031-9007, 1079-7114. doi: 10.1103/PhysRevLett.121.146801. URL https://link.aps.org/doi/10.1103/PhysRevLett.121.146801.

[106] Haohao Shi, Zhen Zhan, Zhikai Qi, Kaixiang Huang, Edo van Veen, Jose Angel Silva-Guillen, Runxiao Zhang, Pengju Li, Kun Xie, Hengxing Ji, Mikhail I. Katsnelson, Shengjun Yuan, Shengyong Qin, and Zhenyu Zhang. Large-area, periodic, and tunable intrinsic pseudo-magnetic fields in low-angle twisted bilayer graphene. *Nature Communications*, 11(1):371, 2020. ISSN 2041-1723. doi: 10.1038/s41467-019-14207-w. URL http://www.nature.com/articles/s41467-019-14207-w.

[107] Ke-Ke Bai, Yi-Cong Wei, Jia-Bin Qiao, Si-Yu Li, Long-Jing Yin, Wei Yan, Jia-Cai Nie, and Lin He. Detecting giant electron-hole asymmetry in a graphene monolayer generated by strain and charged-defect scattering via landau level spectroscopy. *Physical Review B*, 92(12):121405, 2015. ISSN 1098-0121, 1550-235X. doi: 10.1103/PhysRevB.92.121405. URL https://link.aps.org/doi/10.1103/PhysRevB.92.121405.

[108] Si-Yu Li, Ying Su, Ya-Ning Ren, and Lin He. Valley polarization and inversion in strained graphene via pseudo-landau levels, valley splitting of real landau levels, and confined states. *Physical Review Letters*, 124(10):106802, 2020. ISSN 0031-9007, 1079-7114. doi: 10.1103/PhysRevLett.124.106802. URL https://link.aps.org/doi/10.1103/PhysRevLett.124.106802.

[109] Gerardo G Naumis, Salvador Barraza-Lopez, Maurice Oliva-Leyva, and Humberto Terrones. Electronic and optical properties of strained graphene and other strained 2d materials: a review. *Reports on Progress in Physics*, 80(9):096501, September 2017.

[110] Keun Soo Kim, Yue Zhao, Houk Jang, Sang Yoon Lee, Jong Min Kim, Kwang S. Kim, Jong-Hyun Ahn, Philip Kim, Jae-Young Choi, and Byung Hee Hong. Large-scale pattern growth of graphene films for stretchable transparent electrodes. *Nature*, 457(7230):706–710, 2009. ISSN 0028-0836, 1476-4687. doi: 10.1038/nature07719. URL http://www.nature.com/articles/nature07719.

[111] Wenzhong Bao, Feng Miao, Zhen Chen, Hang Zhang, Wanyoung Jang, Chris Dames, and Chun Ning Lau. Controlled ripple texturing of suspended graphene and ultrathin graphite membranes. *Nature Nanotechnology*, 4(9):562–566, September 2009. ISSN 1748-3387, 1748-3395. doi: 10.1038/nnano.2009.191. URL http://www.nature.com/articles/nnano.2009.191.

[112] S. V. Morozov, K. S. Novoselov, M. I. Katsnelson, F. Schedin, L. A. Ponomarenko, D. Jiang, and A. K. Geim. Strong suppression of weak localization in graphene. *Phys. Rev. Lett.*, 97:016801, Jul 2006. URL https://link.aps.org/doi/10.1103/PhysRevLett.97.016801.

[113] A. F. Morpurgo and F. Guinea. Intervalley scattering, long-range disorder, and effective time-reversal symmetry breaking in graphene. *Phys. Rev. Lett.*, 97:196804, Nov 2006. URL https://link.aps.org/doi/10.1103/PhysRevLett.97.196804.

[114] M. Ramezani Masir, D. Moldovan, and F. M. Peeters. Pseudo magnetic field in strained graphene: revisited. *Solid State Communications*, 175-176:76–82, 2013. ISSN 00381098. doi: 10.1016/j.ssc.2013.04.001. URL http://arxiv.org/abs/1304.0629. arXiv: 1304.0629.

[115] M. Oliva-Leyva and Gerardo G. Naumis. Understanding electron behavior in strained graphene as a reciprocal space distortion. *Physical Review B*, 88(8):085430, 2013. ISSN 1098-0121, 1550-235X. doi: 10.1103/PhysRevB.88.085430. URL https://link.aps.org/doi/10.1103/PhysRevB.88.085430.

[116] M. Oliva-Leyva and Gerardo G. Naumis. Generalizing the fermi velocity of strained graphene from uniform to nonuniform strain. *Physics Letters A*, 379 (40-41):2645–2651, 2015. ISSN 03759601. doi: 10.1016/j.physleta.2015.05.039.

[117] M. A. H. Vozmediano, M. I. Katsnelson, and F. Guinea. *Gauge fields in graphene*. arXiv, 1003.5179v2, 2010.

[118] T. M. G. Mohiuddin, A. Lombardo, R. R. Nair, A. Bonetti, G. Savini, R. Jalil, N. Bonini, D. M. Basko, C. Galiotis, N. Marzari, K. S. Novoselov, A. K. Geim, and A. C. Ferrari. Uniaxial strain in graphene by raman spectroscopy: g peak splitting, grüneisen parameters, and sample orientation. *Phys. Rev. B*, 79:205433, May 2009. doi: 10.1103/PhysRevB.79.205433. URL https://link.aps.org/doi/10.1103/PhysRevB.79.205433.

[119] Mingyuan Huang, Hugen Yan, Changyao Chen, Daohua Song, Tony F. Heinz, and James Hone. Phonon softening and crystallographic orientation of strained graphene studied by raman spectroscopy. *Proceedings of the National Academy of Sciences*, 106(18):7304–7308, 2009. ISSN 0027-8424. doi: 10.1073/pnas.0811754106. URL https://www.pnas.org/content/106/18/7304.

[120] R. de Gail, J.-N. Fuchs, M.O. Goerbig, F. Piéchon, and G. Montambaux. Manipulation of dirac points in graphene-like crystals. *Physica B: Condensed Matter*, 407(11):1948–1952, 2012. ISSN 09214526. doi: 10.1016/j.physb.2012.01.072. URL https://linkinghub.elsevier.com/retrieve/pii/S0921452612000774.

[121] V. M. Pereira, A. H. Castro Neto, and N. M. R. Peres. Tight-binding approach to uniaxial strain in graphene. *Phys. Rev. B*, 80(045401), 2009.

[122] M. Farjam and H. Rafii-Tabar. Comment on "band structure engineering of graphene by strain: First-principles calculations". *Phys. Rev. B*, 80:167401, Oct 2009. doi: 10.1103/PhysRevB.80.167401. URL https://link.aps.org/doi/10.1103/PhysRevB.80.167401.

[123] N. Levy, S. A. Burke, K. L. Meaker, M. Panlasigui, A. Zettl, F. Guinea, A. H. Castro Neto, and M. F. Crommie. Strain-induced pseudo–magnetic fields greater than 300 tesla in graphene nanobubbles. *Science*, 329(5991):544–547, 2010. ISSN 0036-8075, 1095-9203. doi: 10.1126/science.1191700. URL https://www.science.org/doi/10.1126/science.1191700.

[124] F. Guinea, M. I. Katsnelson, and A. K. Geim. Energy gaps and a zero-field quantum hall effect in graphene by strain engineering. *Nature Physics*, 6(1):30–33, 2010. doi: 10.1038/nphys1420. URL https://doi.org/10.1038/nphys1420.

[125] Shuze Zhu, Yinjun Huang, Nikolai N. Klimov, David B. Newell, Nikolai B. Zhitenev, Joseph A. Stroscio, Santiago D. Solares, and Teng Li. Pseudomagnetic fields in a locally strained graphene drumhead. *Physical Review B*, 90(7):075426, 2014. ISSN 1098-0121, 1550-235X. doi: 10.1103/PhysRevB.90.075426. URL https://link.aps.org/doi/10.1103/PhysRevB.90.075426.

[126] Lan Meng, Wen-Yu He, Hong Zheng, Mengxi Liu, Hui Yan, Wei Yan, Zhao-Dong Chu, Keke Bai, Rui-Fen Dou, Yanfeng Zhang, Zhongfan Liu, Jia-Cai Nie, and Lin He. Strain-induced one-dimensional landau level quantization in corrugated graphene. *Physical Review B*, 87(20):205405, 2013. ISSN 1098-0121, 1550-235X. doi: 10.1103/PhysRevB.87.205405. URL https://link.aps.org/doi/10.1103/PhysRevB.87.205405.

[127] Riju Banerjee, Viet-Hung Nguyen, Tomotaroh Granzier-Nakajima, Lavish Pabbi, Aurelien Lherbier, Anna Ruth Binion, Jean-Christophe Charlier, Mauricio Terrones, and Eric William Hudson. Strain modulated superlattices in graphene. *Nano Letters*, 20(5):3113–3121, 2020. ISSN 1530-6984, 1530-6992. doi: 10.1021/acs.nanolett.9b05108. URL https://pubs.acs.org/doi/10.1021/acs.nanolett.9b05108.

[128] Yuhang Jiang, Jinhai Mao, Junxi Duan, Xinyuan Lai, Kenji Watanabe, Takashi Taniguchi, and Eva Y. Andrei. Visualizing strain-induced pseudomagnetic fields in graphene through an hbn magnifying glass. *Nano Letters*, 17(5):2839–2843, 2017. ISSN 1530-6984, 1530-6992. doi: 10.1021/acs.nanolett.6b05228. URL https://pubs.acs.org/doi/10.1021/acs.nanolett.6b05228.

[129] Won-Jun Jang, Howon Kim, Yong-Ro Shin, Min Wang, Sung Kyu Jang, Minwoo Kim, Sungjoo Lee, Sang-Woo Kim, Young Jae Song, and Se-Jong Kahng. Observation of spatially-varying fermi velocity in strained-graphene directly grown on hexagonal boron nitride. *Carbon*, 74:139–145, 2014. ISSN 00086223. doi: 10.1016/j.carbon.2014.03.015.

[130] Hui Yan, Zhao-Dong Chu, Wei Yan, Mengxi Liu, Lan Meng, Mudan Yang, Yide Fan, Jiang Wang, Rui-Fen Dou, Yanfeng Zhang, Zhongfan Liu, Jia-Cai Nie, and Lin He. Superlattice dirac points and space-dependent fermi velocity in a corrugated graphene monolayer. *Physical Review B*, 87(7):075405, 2013. ISSN 1098-0121, 1550-235X. doi: 10.1103/PhysRevB.87.075405.

[131] Nuno J. G. Couto, Davide Costanzo, Stephan Engels, Dong-Keun Ki, Kenji Watanabe, Takashi Taniguchi, Christoph Stampfer, Francisco Guinea, and Alberto F. Morpurgo. Random strain fluctuations as dominant disorder source for high-quality on-substrate graphene devices. *Physical Review X*, 4(4):041019, 2014. ISSN 2160-3308. doi: 10.1103/PhysRevX.4.041019.

[132] Mark B. Lundeberg and Joshua A. Folk. Rippled graphene in an in-plane magnetic field: Effects of a random vector potential. *Physical Review Letters*, 105(14): 146804, 2010. ISSN 0031-9007, 1079-7114. doi: 10.1103/PhysRevLett.105.146804.

[133] Lujun Wang, Péter Makk, Simon Zihlmann, Andreas Baumgartner, David I. Indolese, Kenji Watanabe, Takashi Taniguchi, and Christian Schönenberger. Mobility enhancement in graphene by in situ reduction of random strain fluctuations. *Physical Review Letters*, 124(15):157701, 2020. ISSN 0031-9007, 1079-7114. doi: 10.1103/PhysRevLett.124.157701. URL http://arxiv.org/abs/1909.13484. arXiv: 1909.13484.

[134] Loic Huder. *Link between structural and electronic properties of moirés of graphene studied by scanning tunneling microscopy*. Condensed Matter Thesis, Université Grenoble Alpes, 2017.

[135] V. Hung Nguyen and P. Dollfus. Strain-induced modulation of dirac cones and va. *IOP Science*, 2(3), 2014.

[136] Choi Youngjoon, Kemmer Jeannette, Peng Yang, Thomson Alex, Arora Harpreet, Polski Robert, Zhang Yiran, Ren Hechen, Alicea Jason, Refael Gil, von Oppen Felix, Kenji Watanabe, Takashi Taniguchi, and Stevan Nadj-Perge. Electronic correlations in twisted bilayer graphene near the magic angle. *Nature Physics*, 15(1180):1174, 2019.

[137] Fernando de Juan, Mauricio Sturla, and Maria A. H. Vozmediano. Space dependent fermi velocity in strained graphene. *Physical Review Letters*, 108(22): 227205, 2012. ISSN 0031-9007, 1079-7114. doi: 10.1103/PhysRevLett.108.227205.

[138] Shang Liu, Eslam Khalaf, Jong Yeon Lee, and Ashvin Vishwanath. Nematic topological semimetal and insulator in magic-angle bilayer graphene at charge neutrality. *Physical Review Research*, 3(1):013033, 2021. ISSN 2643-1564. doi: 10.1103/PhysRevResearch.3.013033. URL https://link.aps.org/doi/10.1103/PhysRevResearch.3.013033.

[139] H Suzuura and T Ando. Phonons and electron-phonon scattering in carbon nanotubes. *Phys. Rev. B*, 65:235412, 2002.

[140] Zhen-Bing Dai, Yan He, and Zhiqiang Li. Effects of heterostrain and lattice relaxation on the optical conductivity of twisted bilayer graphene. *Physical Review B*, 104(4):045403, 2021. ISSN 2469-9950, 2469-9969. doi: 10.1103/PhysRevB.104.045403. URL https://link.aps.org/doi/10.1103/PhysRevB.104.045403.

[141] Daniel E. Parker, Tomohiro Soejima, Johannes Hauschild, Michael P. Zaletel, and Nick Bultinck. Strain-induced quantum phase transitions in magic angle graphene. *arXiv:2012.09885 [cond-mat]*, 2020. URL http://arxiv.org/abs/2012.09885. arXiv: 2012.09885.

[142] Yves H. Kwan, S. A. Parameswaran, and S. L. Sondhi. Twisted bilayer graphene in a parallel magnetic field. *Physical Review B*, 101(20):205116, 2020. ISSN 2469-9950, 2469-9969. doi: 10.1103/PhysRevB.101.205116. URL https://link.aps.org/doi/10.1103/PhysRevB.101.205116.

[143] Jianpeng Liu, Junwei Liu, and Xi Dai. Pseudo landau level representation of twisted bilayer graphene: Band topology and implications on the correlated insulating phase. *Physical Review B*, 99(15):155415, 2019. ISSN 2469-9950, 2469-9969. doi: 10.1103/PhysRevB.99.155415. URL https://link.aps.org/doi/10.1103/PhysRevB.99.155415.

[144] Naoto Nakatsuji and Mikito Koshino. Moire disorder effect in twisted bilayer graphene. *arXiv:2204.06177 [cond-mat]*, 2022. URL http://arxiv.org/abs/2204.06177. arXiv: 2204.06177.

[145] P. San-Jose, J. González, and F. Guinea. Non-abelian gauge potentials in graphene bilayers. *Physical Review Letters*, 108(21):216802, 2012. doi: 10.1103/PhysRevLett.108.216802. URL https://link.aps.org/doi/10.1103/PhysRevLett.108.216802. Publisher: American Physical Society.

[146] J. González. Confining and repulsive potentials from effective non-abelian gauge fields in graphene bilayers. *Physical Review B*, 94(16):165401, 2016. doi: 10.1103/PhysRevB.94.165401. URL https://link.aps.org/doi/10.1103/PhysRevB.94.165401. Publisher: American Physical Society.

[147] Ohad Antebi, Ady Stern, and Erez Berg. In-plane orbital magnetization as a probe for symmetry breaking in strained twisted bilayer graphene. *Physical Review B*, 105(10):104423, 2022. ISSN 2469-9950, 2469-9969. doi: 10.1103/PhysRevB.105.104423. URL http://arxiv.org/abs/2112.14785. arXiv:2112.14785 [cond-mat].

[148] J. M. Campanera, G. Savini, I. Suarez-Martinez, and M. I. Heggie. Density functional calculations on the intricacies of moiré patterns on graphite. *Physical Review B*, 75(23):235449, 2007. ISSN 1098-0121, 1550-235X. doi: 10.1103/PhysRevB.75.235449. URL https://link.aps.org/doi/10.1103/PhysRevB.75.235449.

[149] A. Artaud, L. Magaud, T. Le Quang, V. Guisset, P. David, C. Chapelier, and J. Coraux. Universal classification of twisted, strained and sheared graphene moiré superlattices. *Scientific Reports*, 6:25670, 2016.

[150] Yu Zhang, Zhe Hou, Ya-Xin Zhao, Zi-Han Guo, Yi-Wen Liu, Si-Yu Li, Ya-Ning Ren, Qing-Feng Sun, and Lin He. Correlation-induced valley splitting and orbital magnetism in a strain-induced zero-energy flatband in twisted bilayer graphene near the magic angle. *Physical Review B*, 102(8):081403, 2020. ISSN 2469-9950, 2469-9969. doi: 10.1103/PhysRevB.102.081403. URL https://link.aps.org/doi/10.1103/PhysRevB.102.081403.

[151] Gerd Binnig, Heinrich Rohrer, and E Weibel. Tunneling through a tunable vaccum gap. *Applied Physics Letters*, 59(40):178, 1982.

[152] Gerd Binnig and Heinrich Rohrer. Scanning tunneling microscopy—from birth to adolescence. *Reviews of Modern Physics*, 59(3):615–625, 1987. ISSN 0034-6861. doi: 10.1103/RevModPhys.59.615. URL https://link.aps.org/doi/10.1103/RevModPhys.59.615.

[153] G. Hörmandinger. Imaging of the cu(111) surface state in scanning tunneling microscopy. *Physical Review B*, 49(19):13897–13905, 1994. ISSN 0163-1829, 1095-3795. doi: 10.1103/PhysRevB.49.13897. URL https://link.aps.org/doi/10.1103/PhysRevB.49.13897.

[154] Kazuyuki Uchida, Shinnosuke Furuya, Jun-Ichi Iwata, and Atsushi Oshiyama. Atomic corrugation and electron localization due to moire patterns in twisted bilayer graphenes. *PHYSICAL REVIEW B*, page 9, 2014.

[155] Zhao Y. Rong and Pieter Kuiper. Electronic effects in scanning tunneling microscopy: Moiré pattern on a graphite surface. *Physical Review B*, 48(23):17427–17431, 1993. ISSN 0163-1829, 1095-3795. doi: 10.1103/PhysRevB.48.17427. URL https://link.aps.org/doi/10.1103/PhysRevB.48.17427.

[156] Klaus Hermann. Periodic overlayers and moiré patterns: theoretical studies of geometric properties. *Journal of Physics: Condensed Matter*, 24(31):314210, 2012. ISSN 0953-8984, 1361-648X. doi: 10.1088/0953-8984/24/31/314210. URL https://iopscience.iop.org/article/10.1088/0953-8984/24/31/314210.

[157] Diana A Cosma, John R Wallbank, Vadim Cheianov, and Vladimir I Fal. Moire pattern as a magnifying glass for strain and dislocations in van der waals heterostructures. *Faraday Discussions*, 173:137–143, 2014. ISSN 1359-6640. doi: 10.1039/C4FD00146J. URL http://dx.doi.org/10.1039/C4FD00146J.

[158] Márton Szendro, András Pálinkás, Péter Süle, and Zoltán Osváth. Anisotropic strain effects in small-twist-angle graphene on graphite. *Phys. Rev. B*, 100: 125404, Sep 2019. doi: 10.1103/PhysRevB.100.125404. URL https://link.aps.org/doi/10.1103/PhysRevB.100.125404.

[159] Jia-Bin Qiao, Long-Jing Yin, and Lin He. Twisted graphene bilayer around the first magic angle engineered by heterostrain. *Physical Review B*, 98(23): 235402, 2018. ISSN 2469-9950, 2469-9969. doi: 10.1103/PhysRevB.98.235402. URL https://link.aps.org/doi/10.1103/PhysRevB.98.235402.

[160] Alexander Kerelsky, L. McGilly, D. M. Kennes, L. Xian, M. Yankowitz, S. Chen, K. Watanabe, T. Taniguchi, J. Honeand C. Deanand A. Rubio, and A. N. Pasupathy. Maximized electron interactions at the magic angle in twisted bilayer graphene. *Nature*, 572:95–100, 2019.

[161] Yonglong Xie, Biao Lian, Berthold Jack, Xiaomeng Liu, Cheng-Li Chiu, Kenji Watanabe, Takashi Taniguchi, Andrei Bernevig, and Ali Yazdani. Spectroscopic signatures of many-body correlations in magic-angle twisted bilayer graphene. *Nature*, 572(91):101, 2019.

[162] Yuhang Jiang, Jinhai Mao, Xinyuan Lai, Kenji Watanabe, Takashi Taniguchi, Kristjan Haule, and Eva Y. Andrei. Charge order and broken rotational symmetry in magic-angle twisted bilayer graphene. *Nature*, 573(91), 2019.

[163] Zhiming Zhang, Rachel Myers, Kenji Watanabe, Takashi Taniguchi, and Brian J. LeRoy. Probing the wave functions of correlated states in magic angle graphene. *Phys. Rev. Research*, 2:033181, 2020. doi: 10.1103/PhysRevResearch.2.033181. URL https://link.aps.org/doi/10.1103/PhysRevResearch.2.033181.

[164] Tommaso Cea and Francisco Guinea. Band structure and insulating states driven by coulomb interaction in twisted bilayer graphene. *Phys. Rev. B*, 102: 045107, Jul 2020. doi: 10.1103/PhysRevB.102.045107. URL https://link.aps.org/doi/10.1103/PhysRevB.102.045107.

[165] G. Trambly de Laissardière, D. Mayou, and L. Magaud. Moiré bands in twisted double-layer graphene. *Phys. Rev. B*, 86:125413, 2012.

[166] Alexander Georgi, Peter Nemes-Incze, Ramon Carrillo-Bastos, Daiara Faria, Silvia Viola Kusminskiy, Dawei Zhai, Martin Schneider, Dinesh Subramaniam, Torge Mashoff, Nils M. Freitag, Marcus Liebmann, Marco Pratzer, Ludger Wirtz, Colin R. Woods, Roman V. Gorbachev, Yang Cao, Kostya S. Novoselov, Nancy Sandler, and Markus Morgenstern. Tuning the pseudospin polarization of graphene by a pseudomagnetic field. *Nano Letters*, 17(4):2240–2245, 2017. ISSN 1530-6984, 1530-6992. doi: 10.1021/acs.nanolett.6b04870. URL https://pubs.acs.org/doi/10.1021/acs.nanolett.6b04870.

[167] Claire Berger, Zhimin Song, Tianbo Li, Xuebin Li, Asmerom Y Ogbazghi, Rui Feng, Zhenting Dai, Alexei N Marchenkov, Edward H Conrad, Phillip N First, and Walt A de Heer. Ultrathin epitaxial graphite : 2d electron gas properties and a route toward graphene-based nanoelectronics. *J. Phys. Chem. B*, page 5, 2004.

[168] A.J. Van Bommel, J.E. Crombeen, and A. Van Tooren. Leed and auger electron observations of the sic(0001) surface. *Surface Science*, 48(2):463–472, 1975. ISSN 00396028. doi: 10.1016/0039-6028(75)90419-7. URL https://linkinghub.elsevier.com/retrieve/pii/0039602875904197.

[169] G. M. Rutter, N. P. Guisinger, J. N. Crain, E. A. A. Jarvis, M. D. Stiles, T. Li, P. N. First, and J. A. Stroscio. Imaging the interface of epitaxial graphene with silicon carbide via scanning tunneling microscopy. *Physical Review B*, 76(23): 235416, 2007. ISSN 1098-0121, 1550-235X. doi: 10.1103/PhysRevB.76.235416. URL https://link.aps.org/doi/10.1103/PhysRevB.76.235416.

[170] P Lauffer, K V Emtsev, R Graupner, Th Seyller, L Ley, S A Reshanov, and H B Weber. Atomic and electronic structure of few-layer graphene on sic(0001) studied with scanning tunneling microscopy and spectroscopy. *PHYSICAL REVIEW B*, page 10, 2008.

[171] A. Michon, L. Largeau, O. Mauguin, A. Ouerghi, S. Vézian, D. Lefebvre, E. Roudon, M. Zielinski, T. Chassagne, and M. Portail. Graphene growth using propane-hydrogen cvd on 6h-sic(0001): temperature dependent interface and strain. *physica status solidi c*, 9(2):175–178, 2012. ISSN 1862-6351, 1610-1642. doi: 10.1002/pssc.201100225. URL https://onlinelibrary.wiley.com/doi/10.1002/pssc.201100225.

[172] B. Jabakhanji, A. Michon, C. Consejo, W. Desrat, M. Portail, A. Tiberj, M. Paillet, A. Zahab, F. Cheynis, F. Lafont, F. Schopfer, W. Poirier, F. Bertran, P. Le Fèvre, A. Taleb-Ibrahimi, D. Kazazis, W. Escoffier, B. C. Camargo, Y. Kopelevich, J. Camassel, and B. Jouault. Tuning the transport properties of graphene films grown by cvd on sic(0001): Effect of in situ hydrogenation and annealing. *Physical Review B*, 89(8):085422, 2014. ISSN 1098-0121, 1550-235X. doi: 10.1103/PhysRevB.89.085422.

[173] Roy Dagher, Elisabeth Blanquet, Christian Chatillon, Timotée Journot, Marc Portail, Luan Nguyen, Yvon Cordier, and Adrien Michon. A comparative study of graphene growth on sic by hydrogen-cvd or si sublimation through thermodynamic simulations. *CrystEngComm*, 20(26):3702–3710, 2018. ISSN 1466-8033. doi: 10.1039/C8CE00383A. URL http://xlink.rsc.org/?DOI=C8CE00383A.

[174] Zouhour Ben Jabra, Isabelle Berbezier, Adrien Michon, Mathieu Koudia, Elie Assaf, Antoine Ronda, Paola Castrucci, Maurizio De Crescenzi, Holger Vach, and Mathieu Abel. Hydrogen-mediated cvd epitaxy of graphene on sic: Implications for microelectronic applications. *ACS Applied Nano Materials*, 4(5): 4462–4473, 2021. ISSN 2574-0970, 2574-0970. doi: 10.1021/acsanm.1c00082. URL https://pubs.acs.org/doi/10.1021/acsanm.1c00082.

[175] F. Varchon, P. Mallet, J.-Y. Veuillen, and L. Magaud. Ripples in epitaxial graphene on the si-terminated sic(0001) surface. *Physical Review B*, 77(23): 235412, 2008. ISSN 1098-0121, 1550-235X. doi: 10.1103/PhysRevB.77.235412. URL https://link.aps.org/doi/10.1103/PhysRevB.77.235412.

[176] C. Riedl, C. Coletti, T. Iwasaki, A. A. Zakharov, and U. Starke. Quasi-free-standing epitaxial graphene on sic obtained by hydrogen intercalation. *Physical Review Letters*, 103(24):246804, 2009. ISSN 0031-9007, 1079-7114. doi: 10.1103/PhysRevLett.103.246804. URL https://link.aps.org/doi/10.1103/PhysRevLett.103.246804.

[177] B. Kumar, M. Baraket, M. Paillet, J.-R. Huntzinger, A. Tiberj, A.G.M. Jansen, L. Vila, M. Cubuku, C. Vergnaud, M. Jamet, G. Lapertot, D. Rouchon, A.-A. Zahab, J.-L. Sauvajol, L. Dubois, F. Lefloch, and F. Duclairoir. Growth protocols and characterization of epitaxial graphene on sic elaborated in a graphite enclosure. *Physica E: Low-dimensional Systems and Nanostructures*, 75: 7–14, 2016. ISSN 13869477. doi: 10.1016/j.physe.2015.07.022. URL https://linkinghub.elsevier.com/retrieve/pii/S1386947715301296.

[178] Wei Chen, Hai Xu, Lei Liu, Xingyu Gao, Dongchen Qi, Guowen Peng, Swee Ching Tan, Yuanping Feng, Kian Ping Loh, and Andrew Thye Shen Wee. Atomic structure of the 6h–sic(0001) nanomesh. *Surface Science*, 596 (1-3):176–186, 2005. ISSN 00396028. doi: 10.1016/j.susc.2005.09.013. URL https://linkinghub.elsevier.com/retrieve/pii/S003960280500988X.

[179] Victor W. Brar, Yuanbo Zhang, Yossi Yayon, Taisuke Ohta, Jessica L. McChesney, Aaron Bostwick, Eli Rotenberg, Karsten Horn, and Michael F. Crommie. Scanning tunneling spectroscopy of inhomogeneous electronic structure in monolayer and bilayer graphene on sic. *Applied Physics Letters*, 91 (12):122102, 2007. ISSN 0003-6951, 1077-3118. doi: 10.1063/1.2771084. URL http://aip.scitation.org/doi/10.1063/1.2771084.

[180] Chaofei Liu and Jian Wang. Spectroscopic evidence for electron correlations in epitaxial bilayer graphene with interface-reconstructed superlattice potentials. *Chinese Physics Letters*, 39(7):077301, 2022. ISSN 0256-307X, 1741-3540. doi: 10.1088/0256-307X/39/7/077301. URL https://iopscience.iop.org/article/10.1088/0256-307X/39/7/077301.

[181] Konstantin V. Emtsev, Aaron Bostwick, Karsten Horn, Johannes Jobst, Gary L. Kellogg, Lothar Ley, Jessica L. McChesney, Taisuke Ohta, Sergey A. Reshanov, Jonas Röhrl, Eli Rotenberg, Andreas K. Schmid, Daniel Waldmann, Heiko B. Weber, and Thomas Seyller. Towards wafer-size graphene layers by atmospheric pressure graphitization of silicon carbide. *Nature Materials*, 8(3):203–207, 2009. ISSN 1476-1122, 1476-4660. doi: 10.1038/nmat2382. URL https://www.nature.com/articles/nmat2382.

[182] K.I. Bolotin, K.J. Sikes, Z. Jiang, M. Klima, G. Fudenberg, J. Hone, P. Kim, and H.L. Stormer. Ultrahigh electron mobility in suspended graphene. *Solid State Communications*, 146(9-10):351–355, 2008. ISSN 00381098. doi: 10.1016/j.ssc.2008.02.024. URL https://linkinghub.elsevier.com/retrieve/pii/S0038109808001178.

[183] C. Virojanadara, A.A. Zakharov, R. Yakimova, and L.I. Johansson. Buffer layer free large area bi-layer graphene on sic(0001). *Surface Science*, 604(2):L4–L7, 2010. ISSN 00396028. doi: 10.1016/j.susc.2009.11.011. URL https://linkinghub.elsevier.com/retrieve/pii/S0039602809007250.

[184] J. Kunc, M. Rejhon, and P. Hlídek. Hydrogen intercalation of epitaxial graphene and buffer layer probed by mid-infrared absorption and raman spectroscopy. *AIP Advances*, 8(4):045015, 2018. ISSN 2158-3226. doi: 10.1063/1.5024132. URL http://aip.scitation.org/doi/10.1063/1.5024132.

[185] Junko Ishii, Shigenori Matsushima, and Masamichi Naitoh. Electronic and structural properties of h-intercalated graphene-sic (0001) interface. *Japanese Journal of Applied Physics*, 58(3):035001, 2019. ISSN 0021-4922, 1347-4065. doi: 10.7567/1347-4065/aafb4a. URL https://iopscience.iop.org/article/10.7567/1347-4065/aafb4a.

[186] Andrew L Walter, Ki-Joon Jeon, Aaron Bostwick, Florian Speck, Markus Ostler, Thomas Seyller, Luca Moreschini, Yong Su Kim, Young Jun Chang, Karsten Horn, and Eli Rotenberg. Highly p-doped epitaxial graphene obtained by fluorine intercalation. *Appl. Phys. Lett.*, page 4, 2011.

[187] B Premlal, M Cranney, and F Vonau. Surface intercalation of gold underneath a graphene monolayer on sic(0001) studied by scanning tunneling microscopy and spectroscopy. *Appl. Phys. Lett.*, page 4, 2009.

[188] Xinran Wang, Xiaolin Li, Li Zhang, Youngki Yoon, Peter K. Weber, Hailiang Wang, Jing Guo, and Hongjie Dai. N-doping of graphene through electrothermal reactions with ammonia. *Science*, 324(5928):768–771, 2009. ISSN 0036-8075, 1095-9203. doi: 10.1126/science.1170335. URL https://www.science.org/doi/10.1126/science.1170335.

[189] Zhou-jun Wang, Mingming Wei, Li Jin, Yanxiao Ning, Liang Yu, Qiang Fu, and Xinhe Bao. Simultaneous n-intercalation and n-doping of epitaxial graphene on 6h-sic(0001) through thermal reactions with ammonia. *Nano Research*, 6(6):399–408, 2013. ISSN 1998-0124, 1998-0000. doi: 10.1007/s12274-013-0317-7. URL http://link.springer.com/10.1007/s12274-013-0317-7.

[190] Gregory M. Rutter, Suyong Jung, Nikolai N. Klimov, David B. Newell, Nikolai B. Zhitenev, and Joseph A. Stroscio. Microscopic polarization in bilayer graphene. *Nature Physics*, 7(8):649–655, 2011. ISSN 1745-2473, 1745-2481. doi: 10.1038/nphys1988. URL http://www.nature.com/articles/nphys1988.

[191] Alexander Kerelsky, Carmen Rubio-Verdú, Lede Xian, Dante M. Kennes, Dorri Halbertal, Nathan Finney, Larry Song, Simon Turkel, Lei Wang, Kenji Watanabe, Takashi Taniguchi, James Hone, Cory Dean, Dmitri N. Basov, Angel Rubio, and Abhay N. Pasupathy. Moiréless correlations in abca graphene. *Proceedings of the National Academy of Sciences*, 118(4):e2017366118, 2021. ISSN 0027-8424, 1091-6490. doi: 10.1073/pnas.2017366118. URL http://www.pnas.org/lookup/doi/10.1073/pnas.2017366118.

[192] Dorri Halbertal, Simon Turkel, Christopher J. Ciccarino, Jonas Hauck, Nathan Finney, Valerie Hsieh, Kenji Watanabe, Takashi Taniguchi, James Hone, Cory Dean, Prineha Narang, Abhay N. Pasupathy, Dante M. Kennnes, and D. N. Basov. Unconventional nonlocal relaxation dynamics in a twisted graphene moire superlattice. *arXiv*, 2022. URL http://arxiv.org/abs/2208.10399.

[193] Martina Corso, Laura Fernández, Frederik Schiller, and José Enrique Ortega. Au(111)-based nanotemplates by gd alloying. *ACS Nano*, 4(3):1603–1611, 2010. ISSN 1936-0851, 1936-086X. doi: 10.1021/nn9013455. URL https://pubs.acs.org/doi/10.1021/nn901345s.

[194] B. Lalmi, J. C. Girard, E. Pallecchi, M. Silly, C. David, S. Latil, F. Sirotti, and A. Ouerghi. Flower-shaped domains and wrinkles in trilayer epitaxial graphene on silicon carbide. *Scientific Reports*, 4(1):4066, 2015. ISSN 2045-2322. doi: 10.1038/srep04066. URL http://www.nature.com/articles/srep04066.

[195] Jan Ravnik, Igor Vaskivskyi, Yaroslav Gerasimenko, Michele Diego, Jaka Vodeb, Viktor Kabanov, and Dragan D. Mihailovic. Strain-induced metastable topological networks in laser-fabricated tas2 polytype heterostructures for nanoscale devices. *ACS Applied Nano Materials*, 2(6):3743–3751, 2019. ISSN 2574-0970, 2574-0970. doi: 10.1021/acsanm.9b00644. URL https://pubs.acs.org/doi/10.1021/acsanm.9b00644.

[196] Kaihui Li, Feiping Xiao, Wen Guan, Yulong Xiao, Chang Xu, Jinding Zhang, Chenfang Lin, Dong Li, Qingjun Tong, Si-Yu Li, and Anlian Pan. Morphology deformation and giant electronic band modulation in long-wavelength ws2 moiré superlattices. *Nano Letters*, 22(14):5997–6003, 2022. doi: 10.1021/acs.nanolett.2c02418. URL https://pubs.acs.org/doi/10.1021/acs.nanolett.2c02418.

[197] J V Barth, R J Behm, and G Ertl. structural transformations of the au(111) surface induced by alkali metal adsorption. *Surface Science Letters*, 302:8, 1994.

[198] C. Günther, J. Vrijmoeth, R. Q. Hwang, and R. J. Behm. Strain relaxation in hexagonally close-packed metal-metal interfaces. *Physical Review Letters*, 74(5): 754–757, 1995. ISSN 0031-9007, 1079-7114. doi: 10.1103/PhysRevLett.74.754. URL https://link.aps.org/doi/10.1103/PhysRevLett.74.754.

[199] E. Starodub, S. Maier, I. Stass, N. C. Bartelt, P. J. Feibelman, M. Salmeron, and K. F. McCarty. Graphene growth by metal etching on ru(0001). *Physical Review B*, 80(23):235422, 2009. ISSN 1098-0121, 1550-235X. doi: 10.1103/PhysRevB.80.235422. URL https://link.aps.org/doi/10.1103/PhysRevB.80.235422.

[200] Silong Quan, Linghui He, and Yong Ni. Tunable mosaic structures in van der waals layered materials. *Physical Chemistry Chemical Physics*, 20(39):25428–25436, 2018. ISSN 1463-9076, 1463-9084. doi: 10.1039/C8CP04360D. URL http://xlink.rsc.org/?DOI=C8CP04360D.

[201] Tobias A. de Jong, Luuk Visser, Johannes Jobst, Ruud M. Tromp, and Sense Jan van der Molen. Stacking domain morphology in epitaxial graphene on silicon carbide, 2022. URL http://arxiv.org/abs/2207.14623. arXiv:2207.14623 [cond-mat].

[202] J A Snyman. Computed epitaxial monolayer structures iii. two-dimensional model: zero average strain monolayer structures in the case of hexagonal interfacial symmetry. *Surface Science*, page 20, 1980.

[203] Shuai Shao, Jian Wang, Amit Misra, and Richard G. Hoagland. Spiral patterns of dislocations at nodes in (111) semi-coherent fcc interfaces. *Scientific Reports*, 3(1):2448, 2013. ISSN 2045-2322. doi: 10.1038/srep02448. URL http://www.nature.com/articles/srep02448.

[204] Shuyang Dai, Yang Xiang, and David J. Srolovitz. Twisted bilayer graphene: Moiré with a twist. *Nano Letters*, 16(9):5923–5927, 2016. ISSN 1530-6984, 1530-6992. doi: 10.1021/acs.nanolett.6b02870. URL https://pubs.acs.org/doi/10.1021/acs.nanolett.6b02870.

[205] Songsong Zhou, Jian Han, Shuyang Dai, Jianwei Sun, and David J. Srolovitz. van der waals bilayer energetics: Generalized stacking-fault energy of graphene, boron nitride, and graphene/boron nitride bilayers. *Physical Review B*, 92(15):155438, 2015. ISSN 1098-0121, 1550-235X. doi: 10.1103/PhysRevB.92.155438. URL https://link.aps.org/doi/10.1103/PhysRevB.92.155438.

[206] Tawfiqur Rakib, Pascal Pochet, Elif Ertekin, and Harley T. Johnson. Corrugation-driven symmetry breaking in magic-angle twisted bilayer graphene. *Communications Physics*, 5(1):242, 2022. ISSN 2399-3650. doi: 10.1038/s42005-022-01013-y. URL https://www.nature.com/articles/s42005-022-01013-y.

[207] Pascal Pochet, Brian C. McGuigan, Johann Coraux, and Harley T. Johnson. Toward moiré engineering in 2d materials via dislocation theory. *Applied Materials Today*, 9:240–250, 2017. ISSN 23529407. doi: 10.1016/j.apmt.2017.07.007. URL https://linkinghub.elsevier.com/retrieve/pii/S2352940717302305.

[208] Donald W Brenner, Olga A Shenderova, Judith A Harrison, Steven J Stuart, Boris Ni, and Susan B Sinnott. A second-generation reactive empirical bond order (rebo) potential energy expression for hydrocarbons. *Journal of Physics: Condensed Matter*, 14(4):783–802, 2002. ISSN 0953-8984, 1361-648X. doi: 10.1088/0953-8984/14/4/312. URL https://iopscience.iop.org/article/10.1088/0953-8984/14/4/312.

[209] Eduardo V. Castro, K. S. Novoselov, S. V. Morozov, N. M. R. Peres, J. M. B. Lopes dos Santos, Johan Nilsson, F. Guinea, A. K. Geim, and A. H. Castro Neto. Biased bilayer graphene: Semiconductor with a gap tunable by the electric field effect. *Physical Review Letters*, 99(21):216802, 2007. ISSN 0031-9007, 1079-7114. doi: 10.1103/PhysRevLett.99.216802. URL https://link.aps.org/doi/10.1103/PhysRevLett.99.216802.

[210] Paola Gava, Michele Lazzeri, A. Marco Saitta, and Francesco Mauri. Ab initio study of gap opening and screening effects in gated bilayer graphene. *Physical Review B*, 79(16):165431, 2009. ISSN 1098-0121, 1550-235X. doi: 10.1103/PhysRevB.79.165431. URL https://link.aps.org/doi/10.1103/PhysRevB.79.165431.

[211] A. B. Kuzmenko, I. Crassee, D. van der Marel, P. Blake, and K. S. Novoselov. Determination of the gate-tunable band gap and tight-binding parameters in bilayer graphene using infrared spectroscopy. *Physical Review B*, 80(16):165406, 2009. ISSN 1098-0121, 1550-235X. doi: 10.1103/PhysRevB.80.165406. URL https://link.aps.org/doi/10.1103/PhysRevB.80.165406.

[212] Yuanbo Zhang, Victor W. Brar, Feng Wang, Caglar Girit, Yossi Yayon, Melissa Panlasigui, Alex Zettl, and Michael F. Crommie. Giant phonon-induced conductance in scanning tunnelling spectroscopy of gate-tunable graphene. *Nature Physics*, 4(8):627–630, 2008. ISSN 1745-2473, 1745-2481. doi: 10.1038/nphys1022. URL http://www.nature.com/articles/nphys1022.

[213] N. Avraham, J. Reiner, A. Kumar-Nayat, N. Morali, R. Batabyal, and Y. Binghai. Quasiparticle interference studies of quantum materials. *Adv. Mater.*, 30(41), 2018. doi: 10.1002/adma.201707628.

[214] Suyong Jung, Gregory M. Rutter, Nikolai N. Klimov, David B. Newell, Irene Calizo, Angela R. Hight-Walker, Nikolai B. Zhitenev, and Joseph A. Stroscio. Evolution of microscopic localization in graphene in a magnetic field from scattering resonances to quantum dots. *Nature Physics*, 7(3):245–251, 2011. ISSN 1745-2473, 1745-2481. doi: 10.1038/nphys1866. URL http://www.nature.com/articles/nphys1866.

[215] L. E. F. Foa Torres, V. Dal Lago, and E. Suárez Morell. Crafting zero-bias one-way transport of charge and spin. *Physical Review B*, 93(7):075438, 2016. ISSN 2469-9950, 2469-9969. doi: 10.1103/PhysRevB.93.075438. URL https://link.aps.org/doi/10.1103/PhysRevB.93.075438.

[216] Matías Berdakin, Esteban A. Rodríguez-Mena, and Luis E. F. Foa Torres. Spin-polarized tunable photocurrents. *Nano Letters*, 21(7):3177–3183, 2021. ISSN 1530-6984, 1530-6992. doi: 10.1021/acs.nanolett.1c00420. URL https://pubs.acs.org/doi/10.1021/acs.nanolett.1c00420.

[217] F. K. Men, W. E. Packard, and M. B. Webb. Si(100) surface under an externally applied stress. *Physical Review Letters*, 61(21):2469–2471, 1988. ISSN 0031-9007. doi: 10.1103/PhysRevLett.61.2469. URL https://link.aps.org/doi/10.1103/PhysRevLett.61.2469.

[218] M. Göken, H. Vehoff, and P. Neumann. Atomic force microscopy investigations of loaded crack tips in nial. *Journal of Vacuum Science and Technology B*, 14(1157), 1996. doi: 10.1116/1.588420. URL https://avs.scitation.org/doi/abs/10.1116/1.588420.

[219] W. F. Oele, J. W. J. Kerssemakers, and J. Th. M. De Hosson. In situ generation and atomic scale imaging of slip traces with atomic force microscopy. *Review of Scientific Instruments*, 68(12):4492–4497, 1997. ISSN 0034-6748, 1089-7623. doi: 10.1063/1.1148419. URL http://aip.scitation.org/doi/10.1063/1.1148419.

[220] Oliver Schaff, Andreas K. Schmid, Norm C. Bartelt, Juan de la Figuera, and Robert Q. Hwang. In-situ stm studies of strain-stabilized thin-film dislocation networks under applied stress. *Materials Science and Engineering: A*, 319-321:914–918, 2001. ISSN 09215093. doi: 10.1016/S0921-5093(01)00977-7. URL https://linkinghub.elsevier.com/retrieve/pii/S0921509301009777.

[221] D Fujita, M Kitahara, K Onishi, and K Sagisaka. An atomic resolution scanning tunneling microscope that applies external tensile stress and strain in an ultrahigh vacuum. *Nanotechnology*, 19(2):025705, 2008. ISSN 0957-4484, 1361-6528. doi: 10.1088/0957-4484/19/02/025705. URL https://iopscience.iop.org/article/10.1088/0957-4484/19/02/025705.

[222] Y. Nahas, F. Berneau, J. Bonneville, C. Coupeau, M. Drouet, B. Lamongie, M. Marteau, J. Michel, P. Tanguy, and C. Tromas. An experimental uhv afm-stm device for characterizing surface nanostructures under stress/strain at variable temperature. *Review of Scientific Instruments*, 84(10):105117, 2013. ISSN 0034-6748. doi: 10.1063/1.4826555. URL https://aip.scitation.org/doi/10.1063/1.4826555. Publisher: American Institute of Physics.

[223] Chi Ming Yim, Christopher Trainer, Ramakrishna Aluru, Shun Chi, Walter N. Hardy, Ruixing Liang, Doug Bonn, and Peter Wahl. Discovery of a strain-stabilised smectic electronic order in LiFeAs. *Nature Communications*, 9(1):2602, 2018. ISSN 2041-1723. doi: 10.1038/s41467-018-04909-y. URL http://www.nature.com/articles/s41467-018-04909-y.

[224] Jiun-Haw Chu, Hsueh-Hui Kuo, James G. Analytis, and Ian R. Fisher. Divergent nematic susceptibility in an iron arsenide superconductor. *Science*, 337(6095): 710–712, 2012. ISSN 0036-8075, 1095-9203. doi: 10.1126/science.1221713. URL https://www.science.org/doi/10.1126/science.1221713.

[225] Shang Gao, Felix Flicker, Raman Sankar, He Zhao, Zheng Ren, Bryan Rachmilowitz, Sidhika Balachandar, Fangcheng Chou, Kenneth S. Burch, Ziqiang Wang, Jasper van Wezel, and Ilija Zeljkovic. Atomic-scale strain manipulation of a charge density wave. *Proceedings of the National Academy of Sciences*, 115(27): 6986–6990, 2018. ISSN 0027-8424, 1091-6490. doi: 10.1073/pnas.1718931115. URL http://www.pnas.org/lookup/doi/10.1073/pnas.1718931115.

[226] Chi Ming Yim, Soumendra Nath Panja, Christopher Trainer, Craig Topping, Christoph Heil, Alexandra S. Gibbs, Oxana V. Magdysyuk, Vladimir Tsurkan, Alois Loidl, Andreas W. Rost, and Peter Wahl. Strain-stabilized (pi, pi) order at the surface of fe(1+x)te. *Nano Letters*, 21(7):2786–2792, 2021. ISSN 1530-6984, 1530-6992. doi: 10.1021/acs.nanolett.0c04821. URL https://pubs.acs.org/doi/10.1021/acs.nanolett.0c04821.

[227] L. Wang. Magic continuum in twisted bilayer wse2. *arXiv*, 1910.12147, 2019.

[228] Yuan Hou, Shuai Zhang, Qunyang Li, Luqi Liu, Xiaoping Wu, and Zhong Zhang. Evaluation local strain of twisted bilayer graphene via moiré pattern. *Optics and Lasers in Engineering*, 152:106946, 2022. ISSN 01438166. doi: 10.1016/j.optlaseng.2022.106946. URL https://linkinghub.elsevier.com/retrieve/pii/S014381662200001X.

[229] Lujun Wang, Simon Zihlmann, Andreas Baumgartner, Jan Overbeck, Kenji Watanabe, Takashi Taniguchi, Péter Makk, and Christian Schönenberger. In-situ strain tuning in hbn-encapsulated graphene electronic devices. *Nano Letters*, 19(6):4097–4102, 2019. ISSN 1530-6984, 1530-6992. doi: 10.1021/acs.nanolett.9b01491. URL http://arxiv.org/abs/1904.06737. arXiv: 1904.06737.

[230] Vincent Pasquier, Alessandro Scarfato, Jose Martinez-Castro, Antoine Guipet, and Christoph Renner. Tunable biaxial strain device for low dimensional materials, 2022. URL http://arxiv.org/abs/2205.13864. arXiv:2205.13864 [cond-mat].

[231] Mäelle Kapfer, Bjarke S. Jessen, Megan E. Eisele, Matthew Fu, Dorte R. Danielsen, Thomas P. Darlington, Samuel L. Moore, Nathan R. Finney, Ariane Marchese, Valerie Hsieh, Paulina Majchrzak, Zhihao Jiang, Deepnarayan Biswas, Pavel Dudin, José Avila, Kenji Watanabe, Takashi Taniguchi, Søren Ulstrup, Peter Bøggild, P. J. Schuck, Dmitri N. Basov, James Hone, and Cory R. Dean. Programming moire patterns in 2d materials by bending, 2022. URL http://arxiv.org/abs/2209.10696. arXiv:2209.10696 [cond-mat].

[232] Tara Peña, Shoieb A Chowdhury, Ahmad Azizimanesh, Arfan Sewaket, Hesam Askari, and Stephen M Wu. Strain engineering 2d mos2 with thin film stress capping layers. *2D Materials*, 8(4):045001, 2021. ISSN 2053-1583. doi: 10.1088/2053-1583/ac08f2. URL https://iopscience.iop.org/article/10.1088/2053-1583/ac08f2.

[233] Tara Peña, Aditya Dey, Shoieb A Chowdhury, Ahmad Azizimanesh, Wenhui Hou, Carla L Watson, Hesam Askari, and Stephen M Wu. Moiré engineering in 2d heterostructures with process-induced strain. *arXiV*, page 28, 2022.

[234] J-Y Veuillen, F Hiebel, L Magaud, P Mallet, and F Varchon. Interface structure of graphene on sic: an ab initio and stm approach. *Journal of Physics D: Applied Physics*, 43(37):374008, 2010. ISSN 0022-3727, 1361-6463. doi: 10.1088/0022-3727/43/37/374008. URL https://iopscience.iop.org/article/10.1088/0022-3727/43/37/374008.

[235] Clifford W. Hicks, Mark E. Barber, Stephen D. Edkins, Daniel O. Brodsky, and Andrew P. Mackenzie. Piezoelectric-based apparatus for strain tuning. *Review of Scientific Instruments*, 85(6):065003, 2014. ISSN 0034-6748, 1089-7623. doi: 10.1063/1.4881611. URL http://aip.scitation.org/doi/10.1063/1.4881611.

[236] Drew Edelberg, Hemant Kumar, Vivek Shenoy, Héctor Ochoa, and Abhay N. Pasupathy. Tunable strain soliton networks confine electrons in van der waals materials. *Nature Physics*, 16(11):1097–1102, 2020. ISSN 1745-2481. doi: 10.1038/s41567-020-0953-2. URL https://www.nature.com/articles/s41567-020-0953-2.

[237] H.-H. Kim, S. M. Souliou, M. E. Barber, E. Lefrançois, M. Minola, M. Tortora, R. Heid, N. Nandi, R. A. Borzi, G. Garbarino, A. Bosak, J. Porras, T. Loew, M. König, P. J. W. Moll, A. P. Mackenzie, B. Keimer, C. W. Hicks, and M. Le Tacon. Uniaxial pressure control of competing orders in a high-temperature superconductor. *Science*, 362(6418):1040–1044, 2018. ISSN 0036-8075, 1095-9203. doi: 10.1126/science.aat4708. URL https://www.sciencemag.org/lookup/doi/10.1126/science.aat4708.

[238] A. Pustogow, Yongkang Luo, A. Chronister, Y.-S. Su, D. A. Sokolov, F. Jerzembeck, A. P. Mackenzie, C. W. Hicks, N. Kikugawa, S. Raghu, E. D. Bauer, and S. E. Brown. Constraints on the superconducting order parameter in sr2ruo4 from oxygen-17 nuclear magnetic resonance. *Nature*, 574(7776):72–75, 2019. ISSN 0028-0836, 1476-4687. doi: 10.1038/s41586-019-1596-2. URL http://www.nature.com/articles/s41586-019-1596-2.

[239] Paul Malinowski, Qianni Jiang, Joshua J. Sanchez, Joshua Mutch, Zhaoyu Liu, Preston Went, Jian Liu, Philip J. Ryan, Jong-Woo Kim, and Jiun-Haw Chu. Suppression of superconductivity by anisotropic strain near a nematic quantum critical point. *Nature Physics*, 16(12):1189–1193, 2020. ISSN 1745-2473, 1745-2481. doi: 10.1038/s41567-020-0983-9. URL https://www.nature.com/articles/s41567-020-0983-9.

[240] P.I. Pi piezoelectric solutions catalog. URL https://www.pi-usa.us/fileadmin/user_upload/pi_us/files/catalogs/PI_Piezoelectric_Solutions_Catalog.pdf.

[241] Tatsuo Hashimoto and Akira Ikushima. Mechanical properties of stycast-1266 at low temperatures. *Review of Scientific Instruments*, 51(3):378–379, 1980. ISSN 0034-6748, 1089-7623. doi: 10.1063/1.1136224. URL http://aip.scitation.org/doi/10.1063/1.1136224.

[242] DZ Turner. Digital image correlation engine (dice) reference manual. *Sandia Report*, SAND2015-10606 O, 2015. URL http://dicengine.github.io/dice/.

[243] Ahrens, James, Geveci, Berk, Law, and Charles. Paraview: An end-user tool for large data visualization. *Elsevier*, 2005. URL https://www.paraview.org/.

[244] David Cooper, Thibaud Denneulin, Jean-Paul Barnes, Jean-Michel Hartmann, Louis Hutin, Cyrille Le Royer, Armand Béché, and Jean-Luc Rouvière. Strain mapping with nm-scale resolution for the silicon-on-insulator generation of semiconductor devices by advanced electron microscopy. *Journal of Applied Physics*, 112(12):124505, 2012. ISSN 0021-8979, 1089-7550. doi: 10.1063/1.4767925. URL http://aip.scitation.org/doi/10.1063/1.4767925.

[245] Remi Coquand, Mikaël Casse, Sylvain Barraud, David Cooper, Virginie Maffini-Alvaro, Marie-Pierre Samson, Stephane Monfray, Frédéric Boeuf, Gérard Ghibaudo, Olivier Faynot, and Thierry Poiroux. Strain-induced performance enhancement of trigate and omega-gate nanowire fets scaled down to 10-nm width. *IEEE Transactions on Electron Devices*, 60(2):727–732, 2013. ISSN 0018-9383, 1557-9646. doi: 10.1109/TED.2012.2231684.

[246] J. W. Pan, P. W. Liu, T. Y. Chang, W. T. Chiang, C. H. Tsai, Y. H. Lin, C. T. Tsai, G. H. Ma, S. C. Chien, and S. W. Sun. Mobility and strain effects on /(110) sige channel pmosfets for high current enhancement. pages 1–4, 2006. doi: 10.1109/IEDM.2006.346812. URL http://ieeexplore.ieee.org/document/4154231/.

[247] J. Pelloux-Prayer, M. Casse, S. Barraud, P. Nguyen, M. Koyama, Y.-M. Niquet, F. Triozon, I. Duchemin, A. Abisset, A. Idrissi-Eloudrhiri, S. Martinie, J.-L. Rouviere, H. Iwai, and G. Reimbold. Study of the piezoresistive properties of nmos and pmos 10um-gate soi nanowire transistors: Scalability effects and high stress level. pages 20.5.1–20.5.4, 2014. doi: 10.1109/IEDM.2014.7047090. URL http://ieeexplore.ieee.org/document/7047090/.

[248] Johan Pelloux-Prayer. *Etude expérimentale des effets mécaniques et géométriques sur le transport dans les transistors nanofils à effet de champ*. Sciences de l'ingénieur / Micro et nanotechnologies / Microélectronique, 2017.

[249] Jean-Philippe Noel, Olivier Thomas, Marie-Anne Jaud, Olivier Weber, Thierry Poiroux, Claire Fenouillet-Beranger, Pierrette Rivallin, Pascal Scheiblin, François Andrieu, Maud Vinet, Olivier Rozeau, Frédéric Boeuf, Olivier Faynot,

and Amara Amara. Multi-v_t utbb fdsoi device architectures for low-power cmos circuit. *IEEE Transactions on Electron Devices*, 58(8):2473–2482, 2011. ISSN 0018-9383, 1557-9646. doi: 10.1109/TED.2011.2155658. URL http://ieeexplore.ieee.org/document/5887404/.

[250] Andrew Wieteska, Ben Foutty, Zurab Guguchia, Felix Flicker, Ben Mazel, Lyuwen Fu, Shuang Jia, Chris Marianetti, Jasper van Wezel, and Abhay Pasupathy. Uniaxial strain tuning of superconductivity in 2h-nbse2. *arXiv:1903.05253 [cond-mat]*, 2019. URL http://arxiv.org/abs/1903.05253. arXiv: 1903.05253.